
THE UNIVERSITY *of* EDINBURGH

# Resistance to HER2-targeted therapies in HER2-positive breast cancer

Natasha Tracey


THE UNIVERSITY
*of* EDINBURGH

Doctor of Philosophy
The University of Edinburgh
2018

# Abstract

Breast cancer accounts for 522,000 deaths worldwide each year and is the most common cancer in women. It is classified according to the cell of origin and its expression of several receptors: oestrogen and progesterone receptors, and human epidermal growth factor receptor 2 (HER2).

Historically, HER2-positive breast cancers had a worse survival prognosis than oestrogen or progesterone receptor-positive cancers, but the development of HER2-targeted therapies led to significant survival improvements. Despite this, patients often present with *de novo* resistance, or will develop acquired resistance to targeted therapies.

Several resistance mechanisms have been identified but attempts to target them have failed. Thus, it is of paramount importance to identify the mechanisms used, to prevent development of resistance or resensitise tumours to HER2-targeted therapies. Objectives of this study were: to understand the link between epithelial to mesenchymal transition (EMT) and loss of HER2, seen in a model of acquired resistance to the HER2-targeted therapy, sapatinib, and to characterise and validate tumours from a sapatinib-treated spontaneous mouse model of HER2-positive breast cancer.

The EMT-linked transcription factor ZEB1 was associated with acquired resistance to sapatinib in tumours that had undergone EMT and concurrently lost HER2. Generation of drug resistant cell lines failed to recapitulate the *in vivo* phenotype. Transient overexpression of ZEB1 *in vitro* did not induce clear EMT or loss of HER2, despite a trend towards lower HER2 expression. However, we found that treatment of cells with *ERBB2* shRNA, the gene encoding HER2, increased levels of ZEB1 and enhanced migration, but did not induce overt EMT. This may be the result of differing PTEN status between *in vivo* and *in vitro* models.

Treatment of a spontaneous mouse model of HER2-positive breast cancer with sapatinib revealed that progressing tumours had an increase in proteins associated with cellular iron homeostasis. Further investigation revealed increased heme oxygenase-1 (HO-1), iron exporter ferroportin and altered iron storage.

To ascertain if modulation of dietary iron intake could affect the development of resistance to sapatinib, mice were given a control or iron-deficient diet and treated with vehicle or sapatinib. This showed that in sapatinib-treated mice fed an iron-deficient diet, HO-1 was not increased as in tumours from mice fed a iron-low control diet.

We looked at the possibility of HER2-targeting therapies inducing ferroptosis, an iron-dependent form of cell death. Sapatinib-treated tumours from mice on a iron-low control

diet had increased cyclooxygenase 2 (COX2), a marker of ferroptosis, which was not seen in sapatinib-treated tumours from mice on an iron-deficient diet. Additionally, *in vitro* drug treatments with HER2-targeting agents showed that SKBR3 cell death could be rescued by iron chelation.

HO-1 overexpression in SKBR3 cells revealed increased autophagic flux and resistance to HER2-targeted therapies. Inhibition of autophagy reversed resistance, rendering them susceptible to sapatinib- and lapatinib-induced cell death. Further, increased autophagic flux was seen in all progressive tumours on sapatinib. The increased resistance to sapatinib in mice fed an iron-deficient diet was also associated with increased autophagic flux, although this was HO-1-independent.

Taken together, the results presented here provide a novel mechanism of cell death induced by HER2-targeting agents *in vitro* and *in vivo*. We have shown that increased HO-1 and reducing dietary iron can affect the development of resistance to sapatinib, which is reliant on autophagy induction. Further, inhibiting autophagy can resensitise cells to sapatinib and lapatinib treatment.

## Lay summary

The most common cancer in women is breast cancer: in 2012, there were 1.7 million new cases worldwide. Treatment is tailored according to what the cancer cells express on their surface. The main molecules are oestrogen receptor, progesterone receptor and human epidermal growth factor receptor 2 (HER2). For cancers driven by HER2, drugs have been designed that stop it signalling.

Although these drugs were revolutionary, up to 60% of patients don't respond initially and a further 70% of patients will stop responding within two years of treatment. These cancers are then classed as resistant. To overcome resistance, we need to understand how it develops in the first place. We used a mouse model that develops breast cancers driven by HER2 and treated it with a therapy targeting HER2, called sapatinib.

When we used this model to look at resistance acquired over time, we saw that cells in some of the resistant tumours had changed their shape and expression of different molecules. Rather than being rounded they had become more elongated and 'spindle' shaped, indicating that they had undergone a process called epithelial to mesenchymal transition (EMT). As well as this, they had lost expression of HER2.

By looking at how this process was driven, we found a molecule called ZEB1 was increased in these tumour cells and was maintaining the spindle shape and EMT. By overexpressing ZEB1 in cells, we found that it did not result in the same loss of HER2 seen in the mouse model. Conversely, when we modelled loss of HER2, we saw some features related to EMT increased, including ZEB1 expression and migration.

To look at resistance another way, we treated mice with sapatinib continuously, rather than cyclically as was used to develop acquired resistance. By doing this, we found that tumours from sapatinib-treated mice had changes in cellular iron homeostasis. This manifested as increases in some molecules which regulate cellular iron and iron deposits outside of cells.

Because of these results, we looked at whether altering dietary iron intake could affect the development of resistance in the mouse model. Mice given an iron-deficient diet developed tumours which progressed on sapatinib more rapidly and were less likely to respond to treatment than mice on a iron-low control diet.

Next, we looked at the possibility that HER2-targeted therapies were inducing a form of iron-dependent cell death called ferroptosis. Sapatinib-treated mice on a iron-low control diet had higher expression of a marker of ferroptosis, COX2, than mice on the iron-deficient diet. By looking in cells, we saw increased oxidation of lipids after

treatment with HER2-targeted therapies. Additionally, death induced by these therapies could be rescued by removing iron from the environment.

When we overexpressed a molecule seen in the tumours from mice fed a iron-low control diet, HO-1, we found that they were resistant to HER2-targeted therapies and ferroptosis. In the mouse models and in cells, expression of HO-1 was associated with a recycling process in cells called autophagy, meaning self-eating. This process was also seen in mice fed an iron-deficient diet, although it was independent of HO-1 expression. Inhibiting autophagy was able to resensitise cells to HER2-targeted therapies and ferroptosis.

Overall, we have shown a new way that HER2-targeted therapies can cause cell death, which can be modulated by dietary iron. Exploiting this could help patients to avoid resistance developing or allow new therapies to be developed targeting HO-1 and autophagy.

## Declaration

I declare that this thesis has been composed by myself and describes my own research unless where acknowledged in the text. No part of this thesis has been submitted for any other degree or professional qualification.

Natasha Tracey

December 2018

# Acknowledgements

Firstly, I would like to thank Val Brunton for her guidance over the last 3 years. She has pushed me to question every piece of data and interpretation, making me the scientist I am today. I would also like to thank Morwenna Muir for her support with the animal experiments, without which I would have gotten absolutely no lab work done, and Helen Creedon who started this project.

Thanks also to members of the 3rd floor lab, both past and present and particularly the members of the Gammoh Group for their help interpreting my autophagy data. A special thanks to my 1st floor office ladies: Joanne Simpson, Kristel Sepp and Georgia Dodd, who have always been available for discussion and deliberation over tea and wine. Joanne has also proofread and commented on every piece of writing I've put in front of her, which was quite a lot, and not once asked for anything in return. She truly is an angel.

During my PhD I had the pleasure to work with Judith Zich and Tesh Patel, both of whom encouraged me to carry on when I wanted to give in. An extra thanks to Tesh for providing me with beer whenever needed, which was more often than I'd care to admit. Thanks also to Sonia Wojciechowska for supporting me over the 4 years I've been in Edinburgh, helping to make some important decisions and always having alcohol at the ready.

Finally, I would like to extend my thanks to Ryan and my Mum, for always listening to me complaining about things without needing any explanation of what on earth I was actually on about. I couldn't have done this without your love and support.

# Contents

# List of Figures

# List of Tables

# Abbreviations

**Table 1.** List of abbreviations

| Abbreviation | Meaning |
|---|---|
| 3-MA | 3-methyladenine |
| ADCC | Antibody-dependent cell-mediated cytotoxicity |
| ANOVA | Analysis of variance |
| BCA | Bicinchoninic acid |
| BSA | Bovine serum albumin |
| CI | 95% confidence interval |
| CST | Cell Signaling Technologies |
| CT | Cycle threshold |
| DAB | 3,3-Diaminobenzidine |
| DAPI | 4,6-diamidino-2-phenylindole |
| DFO | Deferoxamine |
| DFS | Disease-free survival |
| DMEM | Dulbeccos modified eagle medium |
| DMSO | Dimethyl sulfoxide |
| DNA | Deoxyribonucleic acid |
| ECL | Enhanced chemiluminescence |
| ECOG | Eastern Cooperative Oncology Group |
| EDTA | Ethylenediaminetetraacetic acid |
| EGTA | Ethylene glycol-bis($\beta$-aminoethyl ether)-N,N,N,N-tetraacetic acid |
| EMT | Epithelial-to-mesenchymal transition |
| ER | Oestrogen receptor |
| FACS | Fluorescence activated cell sorting |
| FBS | Foetal bovine serum |
| FDA | Food and drug administration |
| FID | Functional iron deficiency |
| Flox | Flanked by lox |
| GEMM | Genetically engineered mouse model |
| GFP | Green fluorescent protein |
| GI50 | Growth inhibition 50% |
| GO | Gene ontology |
| GSH | Reduced glutathione |
| GSSG | Oxidised gluthathione |
| HEPES | 4-(2-hydroxyethyl)-1-piperazineethanesulfonic acid |
| HPLC | High performance liquid chromatography |
| HR | Hazard ratio |
| HRP | Horse radish peroxidase |
| IDC | Invasive ductal carcinoma |

Continued on the next page

Continued from previous page

| Abbreviation | Meaning |
|---|---|
| IF | Immunofluorescence |
| IHC | Immunohistochemistry |
| IQR | Interquartile range |
| IRES | Internal ribosome entry site |
| KM | Kaplan-Meier |
| LapR-A/B | Lapatinib resistant A or B cell line |
| LB | Luria-Bertani |
| LC-MS/MS | Liquid chromatography tandem mass spectroscopy |
| LFQ | Label free quantification |
| LIP | Labile iron pool |
| LR | Lapatinib resistant |
| MMTV | Mouse mammary tumour virus |
| MP | Molecular Probes |
| mRNA | Messenger RNA |
| MS | Mass spectrometry |
| NIC | Neu-IRES-Cre |
| NK | Natural killer |
| NS | Not significant |
| NSCLC | Non-small cell lung cancer |
| ORR | Overall response rate |
| PBS | Phosphate buffered saline |
| PBST | Phosphate buffered saline tween |
| PCR | Polymerase chain reaction |
| pCR | Pathological complete response |
| PE | phosphatidylethanolamine |
| PEM | PIPES EGTA $MgCl_2$ buffer |
| PFA | Paraformaldehyde |
| PFS | Progression-free survival |
| PIPES | Piperazine-N,N-bis(2-ethanesulfonic acid) |
| PMSF | Phenylmethane sulfonyl fluoride |
| po | *Per os* (orally) |
| PR | Progesterone receptor |
| qd | *Quaque die* (once daily) |
| qPCR | Quantitative PCR |
| RFI | Relative fluorescence intensity |
| RFS | Recurrence-free survival |
| RIPA | Radioimmunoprecipitation assay |
| RNA | Ribonucleic acid |
| ROI | Region of interest |
| ROS | Reactive oxygen species |
| RPPA | Reverse phase protein array |

Continued on the next page

Continued from previous page

| **Abbreviation** | **Meaning** |
|---|---|
| RT | Room temperature |
| RTK | Receptor tyrosine kinase |
| SapR-A/B | Sapatinib resistant A or B cell line |
| SCB | Santa Cruz Biotech |
| SD | Standard deviation |
| SDS | Sodium dodecyl sulfate |
| shRNA | Short hairpin ribonucleic acid |
| TBS | Tris-buffered saline |
| TBST | Tris-buffered saline tween |
| TFA | Trifluoro acetic acid |
| TGS | Tris glycine saline |
| TME | Tumour microenvironment |
| TR | Trastuzumab resistant |
| Tris | Trisaminomethane |
| WB | Western blot |
| Z-VAD-FMK | Benzyloxycarbonyl-phenylalanyl-alanyl-fluoromethyl ketone |

# Chapter 1

# Introduction

## 1.1 Breast Cancer

Worldwide, breast cancer is the most common cancer in women; in 2012, there were 1.7 million new cases and 522,000 deaths.[1] It is a heterogeneous disease which can be ductal or lobular in origin.[2] Invasive ductal carcinoma (IDC), originating from the cells lining the ducts, accounts for 80% of all diagnosed breast cancers.[3] Molecular characterisation of IDC allows treatment to be tailored to specific subtypes of IDC, due to their different protein expression profiles (table 1.1).[1,4]

The luminal A and B subtypes are hormone receptor positive (table 1.1; oestrogen receptor (ER)+, progesterone receptor (PR)+).[4] Ki67, a proliferation index marker, is also used to categorise tumours to molecular classifications and is an indicator of proliferating cells.[4] The luminal A and B subtypes have better outcomes than human epidermal growth factor receptor 2 (HER2) and basal/triple negative subtypes, as they can be treated with hormone therapies.[1] Selective oestrogen receptor modulators are most commonly used in pre-menopausal women, whereas aromatase inhibitors, which inhibit oestrogen production, are used in post-menopausal women.[4]

Triple negative cancers tend to be basal-like, lacking expression of hormone receptors and HER2. These cancers have poorer survival rates than hormone receptor-positive and HER2-positive cancers.[4] Treatment focuses on chemo- and radiotherapy.[3] However, many *BRCA1/2* mutant breast cancers have a basal/triple negative pathology and are more responsive to cisplatin-based chemotherapy and poly(ADP-ribose) polymerase (PARP) inhibitors than *BRCA* wild-type tumours.[6,7]

The HER2 subtype of breast cancer is characterised by high levels of HER2 on the cell surface. This accounts for approximately 15-20% of breast cancers.[2,4] Prior to HER2-targeted therapies, these tumours had a worse prognosis than luminal cancers. However, survival rates have improved.[1]

**Table 1.1.** Molecular classification of invasive ductal carcinoma

| Subtype | Protein Expression Profile |
|---|---|
| Luminal A | ER+ and/or PR+, HER2-, $Ki67^{low}$ |
| Luminal B | ER+ and/or PR+, HER2±, $Ki67^{high}$ |
| Basal/Triple negative | ER-, PR-, HER2- |
| HER2 | ER-, PR-, HER2+ |

ER: oestrogen receptor; HER2: human epidermal growth factor receptor 2; PR: progesterone receptor; Allison[4], Hammond et al.[5]

## 1.2 HER2 signalling pathways

HER2 is a member of the human epidermal growth factor receptor (EGFR) family which consists of four members (HER1, HER2, HER3 and HER4). They have structural homology: an extracellular ligand binding domain with four regions, a transmembrane domain and an intracellular tyrosine kinase domain (fig 1.1).[8]

Once ligand is bound to the extracellular domain, the receptors dimerise. Although EGFR (HER1), HER3 and HER4 all have known ligands, none have been identified for HER2.[9] Upon ligand binding to EGFR, HER3 or HER4, the receptors undergo a conformational change, revealing their dimerisation arms and allowing them to form dimers with other family members. Ligands for each receptor are detailed in table 1.2. HER2 is in a fixed formation which mimics the ligand-bound conformation of the other family members, with the dimerisation arm exposed.[10] Due to this, HER2 is the preferential binding partner for other HER family members.[10]

When dimerised, the receptors undergo autophosphorylation at tyrosine residues on the intracellular domain, although HER3 does not possess tyrosine kinase activity and thus can't form homodimers.[12] From this, downstream signalling pathways such as phosphoinositide 3-kinase (PI3K)/protein kinase B (AKT) and mitogen-activated protein kinase (MAPK) are activated (fig 1.1).[13] Under normal physiological conditions, HER2 forms heterodimers due to its lack of ligand binding, but when overexpressed it is able to form homodimers and signal in a ligand-independent manner.[10]

Both EGFR and HER2 are stabilised by the protein chaperone heat shock protein 90 (HSP90). Clients of HSP90 include a wide range of kinases, steroid receptors and

**Table 1.2.** EGFR family ligand binding specificity

| | Receptor | | | |
|---|---|---|---|---|
| **Ligand** | **EGFR** | **HER2** | **HER3** | **HER4** |
| EGF | + | | | |
| TGF-$\alpha$ | + | | | |
| Amphiregulin | + | | | |
| HB-EGF | + | | | |
| Betacellulin | + | | | + |
| Epigen | + | | | + |
| Epiregulin | + | | | + |
| NRG-1 | | | + | + |
| NRG-2 | | | + | + |
| NRG-3 | | | | + |
| NRG-4 | | | | + |
| Tomoregulin | | | | + |
| Neuroglycan C | | | + | |

Abbreviations: EGF: epidermal growth factor; TGF-$\alpha$: transforming growth factor $\alpha$; HB-EGF: heparin-binding EGF-like growth factor; NRG: neuregulin. Wieduwilt and Moasser[11]

transcription factors.[14] Although studies have shown that HER2 is more reliant on HSP90 for its continued expression than EGFR, HSP90 prevents signalling through HER2 homodimers.[15–17]

### 1.2.1 PI3K/AKT pathway

Phosphorylation of HER family members results in the activation of the PI3K family. PI3Ks are heterodimers consisting of catalytic and regulatory subunits.[13] Class I PI3Ks, the main class to have a role in cancer progression, convert phosphatidylinositol 4,5-bisphosphate ($PIP_2$) to phosphatidylinositol 3,4,5-trisphosphate ($PIP_3$).[18] This process is reversed by phosphatase and tensin homolog (PTEN), which dephosphorylates $PIP_3$ back to $PIP_2$ (fig 1.1).[19]

$PIP_3$ binds to AKT, resulting in its phosphorylation by phosphoinositide-dependent kinase 1 (PDK1) and mammalian target of rapamycin complex 2 (mTORC2).[20,21] AKT then activates downstream targets involved in proliferation, migration, protein synthesis and cell survival.[12,22]

AKT can be inactivated by dephosphorylation, a process which is carried out by protein phosphatase 2A (PP2A) and PH domain leucine-rich repeat protein phosphatases (PHLPP) 1 and 2.[23,24]

### 1.2.2 MAPK pathway

Three MAPK pathways have been documented, but activation through HER family members results in preferential activation of the extracellular signal-regulated kinase (ERK) pathway.[22] The ERK pathway is activated through the adapter protein growth factor receptor-bound protein 2 (GRB2) and a guanine nucleotide exchange factor, son of sevenless (SOS).[25] SOS catalyses guanosine diphosphate/guanosine triphosphate (GDP/GTP) exchange, thus activating RAS.[25] RAS binds to RAF, promoting its phosphorylation and dimerisation. Once phosphorylated, RAF activates MAPK/ERK kinase 1/2 (MEK1/2) and ERK1/2 (fig 1.1).[26]

Activated ERK1/2 can regulate cytosolic targets or translocate to the nucleus where it phosphorylates transcription factors. Cytosolic targets of ERK1/2 control migration, cell adhesion, and ion channels and receptors.[27] There is some cross-over between the MAPK and PI3K pathways; activated RAS is able to bind to and activate the p110 catalytic subunit of PI3K.[28]

The ERK pathway can be inhibited by Sprouty proteins, MAPK phosphatases and scaffolding proteins which regulate RAF localisation.[29–31] ERK also negatively regulates SOS and RAF by phosphorylation, reducing their activity.[22]

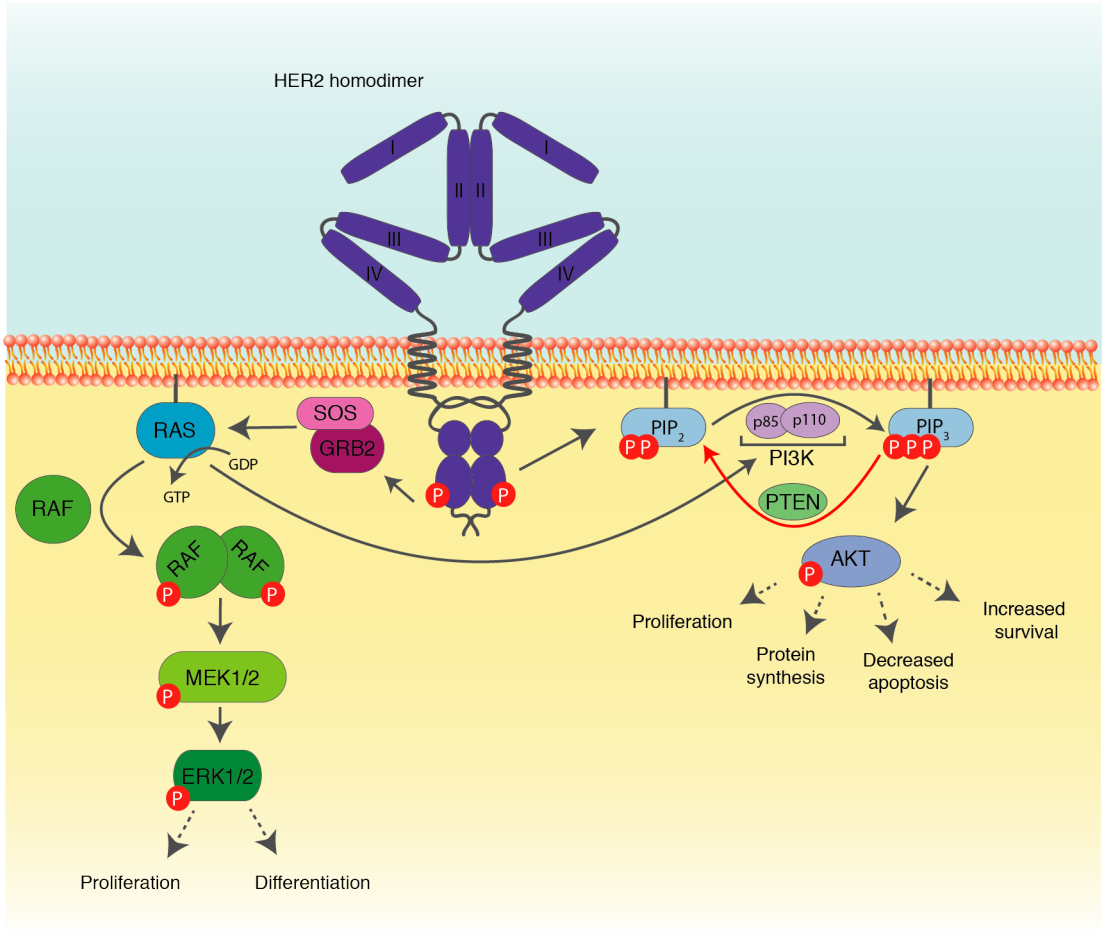


**Figure 1.1. Schematic representation of HER2 signalling pathways.** Once human epidermal growth factor 2 (HER2) forms a homo- or heterodimer, the C-terminal domain becomes transphosphorylated. Downstream signalling pathways, including phosphoinositide 3-kinase (PI3K)/protein kinase B (AKT) and mitogen-activated protein kinase (MAPK) pathways, become activated resulting in proliferation, differentiation, increased protein synthesis and survival and decreased apoptosis. Abbreviations: ERK1/2: extracellular signal-regulated kinase 1/2; GRB2: growth factor receptor-bound protein 2; GDP: guanosine diphosphate; GTP: guanosine triphosphate; MEK1/2 :MAPK/ERK kinase 1/2; $PIP_2$: phosphatidylinositol 4,5-bisphosphate; $PIP_3$: phosphatidylinositol 3,4,5-trisphosphate; P: phosphorylation; SOS: son of sevenless.

## 1.3 HER2 targeting agents

HER2-targeted therapies are monoclonal antibodies, targeting the extracellular domain of HER2, or small molecule tyrosine kinase inhibitors which specifically target the intracellular domain of HER2 (fig 1.2). All of these therapies work by preventing activation of HER2 and downstream signalling, amongst other mechanisms of action.[32–36]

The gold-standard treatment for HER2-positive breast cancer is the monoclonal antibody trastuzumab,[37] which irreversibly binds the extracellular domain, region IV, of the

protein. It does not prevent receptor dimerisation but inhibits activation of the PI3K/AKT and MAPK pathways.[32] Pertuzumab, another monoclonal antibody used in the treatment of HER2-positive breast cancer, has a complementary mechanism of action to trastuzumab; by irreversibly binding to extracellular domain II, it inhibits receptor dimerisation and prevents downstream signalling.[33,38]

Both trastuzumab and pertuzumab induce antibody-dependent cell-mediated cytotoxicity (ADCC).[33,39] Recruitment of Natural Killer (NK) cells to tumour cells results in CD16-mediated ADCC and cell death.[32] Additionally, HER2 internalisation and degradation can be triggered by trastuzumab, resulting in presentation of HER2 fragments to immune cells and tumour cell lysis.[40] Trastuzumab emtansine, an antibody-drug conjugate, relies on the internalisation of HER2 upon trastuzumab binding and its subsequent degradation, releasing emtansine. Emtansine is then able to act specifically on HER2-positive cells, binding to microtubules which inhibits their polymerisation, leading to cell cycle arrest and death.[41]

Lapatinib, sapatinib and neratinib are small molecule tyrosine kinase inhibitors which bind to EGFR and HER2.[34–36] Sapatinib and neratinib additionally bind to HER3 and HER4, respectively.[35,36] All three are competitive inhibitors of the ATP-binding pocket within the intracellular domain of HER family members. Of the tyrosine kinase inhibitors, only neratinib binds irreversibly as it forms covalent bonds, rather than the hydrogen bonds formed by lapatinib and sapatinib.[35,36,42] All three agents work by inhibiting phosphorylation of HER2 and its dimerisation partners, therefore inhibiting downstream pathway activation.[34–36] Pharmacokinetics of sapatinib and lapatinib in phase I studies showed similar distribution and plasma concentration after administration, with both molecules primarily being excreted through the faeces within 24 to 48 hours.[43,44] Lapatinib is mainly metabolised by CYP3A4 and CYP3A5. This information is not available for sapatinib, but it has been suggested it is partly metabolised by CYP2D6 *in vitro*.

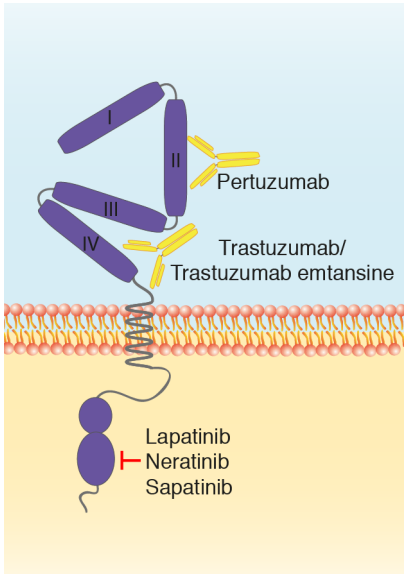


**Figure 1.2. Schematic representation of HER2-targeting agents.** Human epidermal growth factor 2 (HER2) consists of an extracellular domain, a single transmembrane domain and an intracellular domain. The extracellular domain is split into four regions. The first and third are associated with ligand binding in other HER family members, although there is no known ligand for HER2. The second region is involved in receptor dimerisation and is the target for monoclonal antibody pertuzumab. In other HER family members, the fourth region interacts with residues on the second region when the receptors are inactive. However, HER2 is always in an active state. Trastuzumab, a monoclonal antibody, binds to the fourth region, but this does not prevent HER2 dimerisation. Trastuzumab emtansine, an antibody-drug conjugate, retains the HER2-binding capacity of trastuzumab but results in cell cycle arrest and cytotoxicity once HER2 is internalised and degraded, as emtansine inhibits microtubule polymerisation. The intracellular region contains a catalytic tyrosine kinase domain and phosphorylation sites which activate intracellular signalling pathways. Small molecule inhibitors lapatinib, neratinib and sapatinib all bind to this intracellular region, preventing phosphorylation and downstream signalling.

### 1.3.1 Current treatment regimens

Currently, trastuzumab in combination with chemotherapy agent paclitaxel is the first-line treatment for patients with HER2-positive breast cancer in the neoadjuvant and adjuvant setting (before and after surgery, respectively).[37] Pertuzumab is approved in cases of recurrent or metastatic breast cancer in combination with trastuzumab and docetaxel.[45]

Trastuzumab and pertuzumab are not administered as single agents, as they have worse overall response rates (ORR) than chemotherapy alone.[46] In combination with chemotherapy regimens, there is a marked increase in ORR. Additionally, combined pertuzumab and trastuzumab with docetaxel gives greater ORR than either trastuzumab or pertuzumab in combination with docetaxel.[46,47]

Despite patients' disease progressing on trastuzumab, removing this from their treatment regimen can result in rapid proliferation and tumour regrowth.[48,49] Although continuation of trastuzumab treatment is commonplace worldwide, the UK's National Institute for Health and Care Excellence (NICE) does not approve continuation beyond progression.[50]

Lapatinib is indicated in cases of advanced or metastatic breast cancer in combination with capecitabine.[51] In metastatic, hormone receptor-positive disease, lapatinib has been indicated in combination with aromatase inhibitor letrozole, which has been shown to significantly enhance ORR.[52,53] In breast cancer that has progressed on trastuzumab therapy, combination therapy of lapatinib plus trastuzumab has been shown to prolong progression free survival (PFS) and overall survival (OS).[54]

However, treatment with trastuzumab emtansine, indicated in patients with recurrent disease or who have progressed on trastuzumab, has greater survival benefits compared with lapatinib and capecitabine.[55] Trastuzumab emtansine resulted in prolonged OS, PFS and ORR compared with lapatinib plus capecitabine.[56]

Neratinib has recently been indicated by the US Food and Drug Administration (FDA) for the treatment of early stage breast cancer after one year of trastuzumab-based adjuvant therapy.[57] However, it was rejected by the European Medicines Agency,[58] as results from a clinical trial showed it had a small effect in preventing recurrence but was associated with an increase in gastrointestinal side effects, leading to dose reductions and treatment discontinuation in many patients.[59]

Sapatinib is not currently indicated for treatment of HER2-positive breast cancer. Despite phase I studies indicating that sapatinib was well tolerated,[60,61] phase II studies failed to show an advantage of sapatinib in combination with paclitaxel compared with paclitaxel alone in patients with gastric cancer.[62] This is despite preclinical data showing good bioavailability and target inhibition.[36,63]

Recent guidance from NICE supports reassessment of hormone receptor and HER2 status after progression to guide further treatment options.[50] Prior to 2017, retesting was not indicated after progression. Loss of HER2 amplification at the primary site following neoadjuvant or chemotherapy has been shown to confer worse recurrence-free survival compared with those patients who maintain HER2-positivity.[64,65] Studies

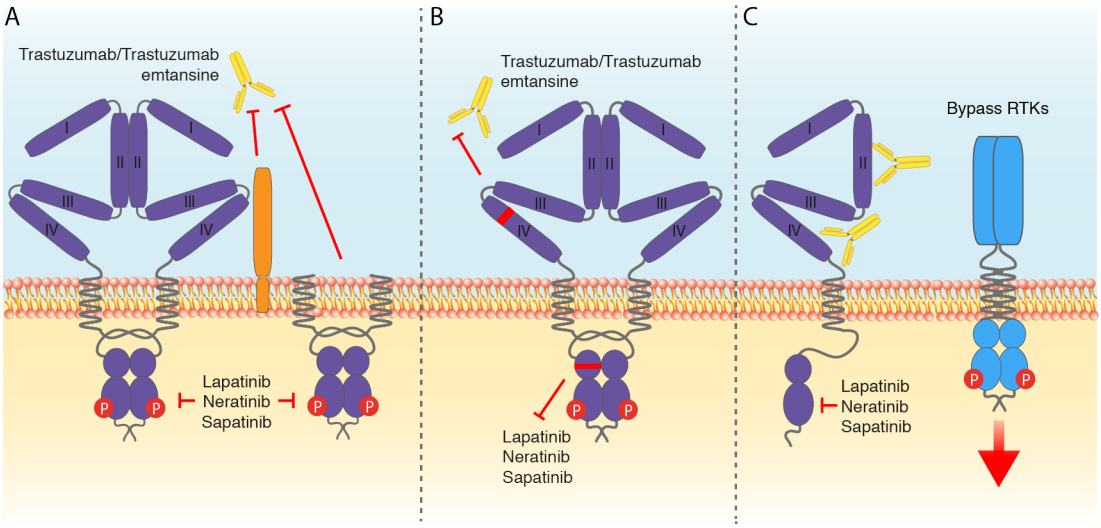


**Figure 1.3. Schematic representation of known resistance mechanisms to HER2-targeted agents.** **(A)** Epitope masking has been evidenced as a resistance mechanism against trastuzumab and pertuzumab. This may be by upregulating molecules with large extracellular domains or cleavage of the extracellular domain, resulting in p95 huamn epidermal growth factor receptor 2 (HER2). **(B)** Mutations within the regions bound by drugs can result in resistance and lack of inhibition. **(C)** Additionally, upregulation of other receptor tyrosine kinases (RTKs) can bypass HER2 inhibition, resulting in the same downstream pathways being activated.

have indicated that between 20–35% of patients with metastatic breast cancer have discordance between primary and metastatic sites,[66–68] but the effect this may have on survival times is not clear.[66,67]

## 1.4 Resistance mechanisms

Between 45–62% of patients present with *de novo* resistance to trastuzumab in the neoadjuvant setting.[69,70] Of those that initially respond to HER2-targeted therapies, up to 70% will develop acquired resistance to trastuzumab within two years of treatment commencing.[71] Depending on the mechanism of resistance, it may be possible to treat with other HER2-targeting therapies, such as lapatinib.[72] However, some patients with trastuzumab resistance are also lapatinib resistant.[73]

### 1.4.1 Epitope masking and lineage changes

Up to 50% of HER2-positive breast cancers have been shown to express the truncated form of HER2, p95.[74,75] High expression of this form of HER2 is an independent predictor of reduced disease-free survival (DFS), compared with patients with high expression of the full-length form of HER2.[74]

This isoform results from the cleavage of the extracellular domain of HER2. As a result of this, therapies targeting the extracellular domain (fig 1.3 A) are no longer able to bind to HER2.[74,75] Despite lacking the extracellular domain, p95 HER2 can dimerise with other HER family members and is constitutively active.[76] However, p95 HER2 has been shown to be sensitive to lapatinib, which targets the intracellular tyrosine kinase domain.[74,76]

Other mechanisms of epitope masking include the expression of proteins with large extracellular domains, such as mucin 4 (MUC4) or cluster of differentiation 44 (CD44). MUC4 is a large, *O*-glycosylated membrane-associated glycoprotein. In the JIMT-1 cell line, derived from a patient with HER2-positive, hormone receptor-negative breast cancer which was resistant to trastuzumab,[77] expression of MUC4 was associated with a reduction in the ability of trastuzumab to bind to HER2. Additionally, knockdown of MUC4 restored sensitivity to trastuzumab.[73]

JIMT-1 cells also have increased expression of CD44, a transmembrane receptor for hyaluron. When bound to CD44, hyaluron results in activation of RAS and PI3K pathways,[78] and decreases the binding capacity of trastuzumab for HER2 by blocking its epitope.[79]

CD44 is associated with increased stemness and a mesenchymal phenotype, which in turn is associated with increased expression of matrix metalloproteinases (MMPs). Expression of matrix metalloproteinases (MMPs) has been shown to result in cleavage of full-length HER2, giving rise to p95 HER2.[80] Moreover, expression of MMPs can initiate epithelial-to-mesenchymal transition (EMT).[81]

EMT is associated with increased invasion, metastasis and resistance to apoptosis.[82] In response to extracellular signals, EMT-related transcription factors, SLUG, SNAIL,

TWIST, zinc finger E-box binding homeobox 1 and 2 (ZEB1 and 2) orchestrate a switch to a mesenchymal phenotype.[83]

Although the canonical role of EMT is invasion and metastasis, several studies have shown that switching from an epithelial to a mesenchymal phenotype is associated with resistance to chemotherapy and targeted therapies.[84–91] Data from our own lab have linked EMT to loss of HER2 in a mouse model of HER2-positive breast cancer,[84] whilst Liu et al.[80] linked EMT to increased MMPs and cleavage of full-length HER2, as previously mentioned.

To overcome epitope masking of the extracellular domain, the small molecule tyrosine kinase inhibitors can be used, as cells remain sensitive to them.[74,76] However, JIMT-1 cells are resistant to both trastuzumab and lapatinib, which is likely due to their increased expression of CD44 leading to a mesenchymal phenotype. ZEB1 has been implicated in maintaining EMT and hence resistance to targeted therapies;[85,89] inhibiting ZEB1 *in vitro* and *in vivo* leads to cells being resensitised to targeted therapies.[85,89] Due to the range of mechanisms of resistance present in JIMT-1 cells, it is unclear if CD44 expression or EMT drives the resistance to lapatinib.

Some therapies targeting EMT have shown promising results in clinical trials. A novel liposomal miR-34a mimic, MRX34, has been shown to target 30 oncogenes across many pathways, including SNAIL-induced EMT and Notch signalling.[92] In a phase I study in advanced solid tumours, MRX34 showed good tolerability, although only 15% of patients had partial response or stable disease,[93] which is likely due to patients' EMT status not being assessed prior to therapy commencing.

Additionally, in EGFR overexpressing non-small cell lung cancer (NSCLC), resistance to targeted therapies erlotinib and gefitinib is often associated with EMT and driven by AXL. By inhibiting AXL, cells were resensitised to tyrosine kinase inhibitors and partial reversal of EMT was seen.[94,95] Clinical trials investigating several AXL inhibitors are currently ongoing.[96] However, EMT is a process that has inherent plasticity,[82] thus targeting EMT through one pathway may result in EMT maintenance through an unrelated signalling pathway.

### 1.4.2 Mutations in HER2

Several mutations have been identified in HER2 which result in it no longer being responsive to targeted therapies (fig 1.3 B). Most mutations affecting HER2 are point mutations, but insertion and deletion mutations have been identified in the extracellular domain (exon 16) and around the transmembrane domain (exon 20) (fig 1.4). These mutations can be broadly classified by the domain affected.

Fewer mutations affect the extracellular region of HER2, although two activating mutations have been identified in the second domain which is involved in receptor dimerisation.[97] D227G/H/V/Y (D227X) and S310F/Y (S310X) have been found in bladder and breast cancer, amongst others.[98,99] Both have been associated with resistance to lapatinib, but D227X does not induce resistance on its own. Rather, when combined with S310X it has been shown to enhance activation of HER2.[98] Conversely, S310X alone can induce resistance to lapatinib, neratinib and trastuzumab.[98,99]

Deletion of exon 16, named $\Delta$16, results in the constitutive activation of HER2. This mutation is found to be expressed in up to 39% of patients tumours.[100] Despite promoting the formation of disulfide bonds and stabilising HER2 dimerisation, $\Delta$16 does not prevent trastuzumab binding; in fact, patients with this mutation are more likely to respond to treatment and have decreased probability of tumour recurrence.[101]

Transmembrane domain mutations affecting HER2 have been found in NSCLC. These mutations are primarily insertions and deletions within exon 20. The transmembrane domain has been shown to promote receptor activation and autophosphorylation through a conformational change.[102] However, mutations in this region have been shown to remain sensitive to lapatinib, neratinib and trastuzumab.[103–106]

Of all HER2 mutations, 65% are in the catalytic tyrosine kinase domain.[107] Mutations in this region are associated with increased kinase activity and constitutive activation of HER2. As a result, these mutations are frequently associated with resistance to HER2-targeted therapies. However, some mutations are still sensitive to dual inhibition with trastuzumab and neratinib.[108] If mutations render HER2 resistant to targeted therapies,

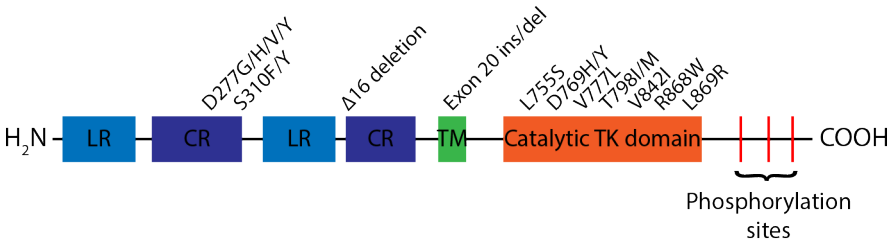


**Figure 1.4. Mutations identified within *ERBB2*.** Schematic representation of *ERBB2*, the gene encoding human epidermal growth factor receptor 2. Mutations identified from patient tumours and *in vitro* studies are included. LR: Receptor L domain; CR: Cysteine-rich region; TM: transmembrane; TK: tyrosine kinase; ins/del: insertion/deletion.

targeting downstream effectors or using non-targeted chemotherapy and radiotherapy may be used to treat patients.[108]

### 1.4.3 Downstream pathway mutations

Mutations in the PI3K and ERK pathways have consistently been shown to predict poor response to targeted therapies and worse PFS and OS.[22,109–113] Mutations in all of these pathways are able to overcome resistance to HER2-targeted therapies (fig 1.5).[109–111,113–115]

#### 1.4.3.1 PI3K pathway

The most common mutation in HER2-positive breast cancer is *PIK3CA*. This gene encodes the p110$\alpha$ catalytic subunit of PI3K.[114] In patient samples, 22% have mutations within *PIK3CA*.[107] These mutations are found within exons 9 and 20; mutations in exon 9 alter the ability of p85 to bind and inhibit the action of p110$\alpha$, whereas those in exon 20 alter the kinase domain, leading to constitutive activation and downstream signalling.[114] Additionally, amplification of *PIK3CA* has been found in 8.78% of breast cancers.[107]

Although mutations in the genes encoding *AKT1-3* are rare, they are amplified in 6-8% of breast cancers, with amplification of *AKT3* the most common.[107,116] Increased expression of *AKT* is associated with worse survival outcomes in breast cancer, but the mechanism for this without other pathway abberations is unclear.[110,116]

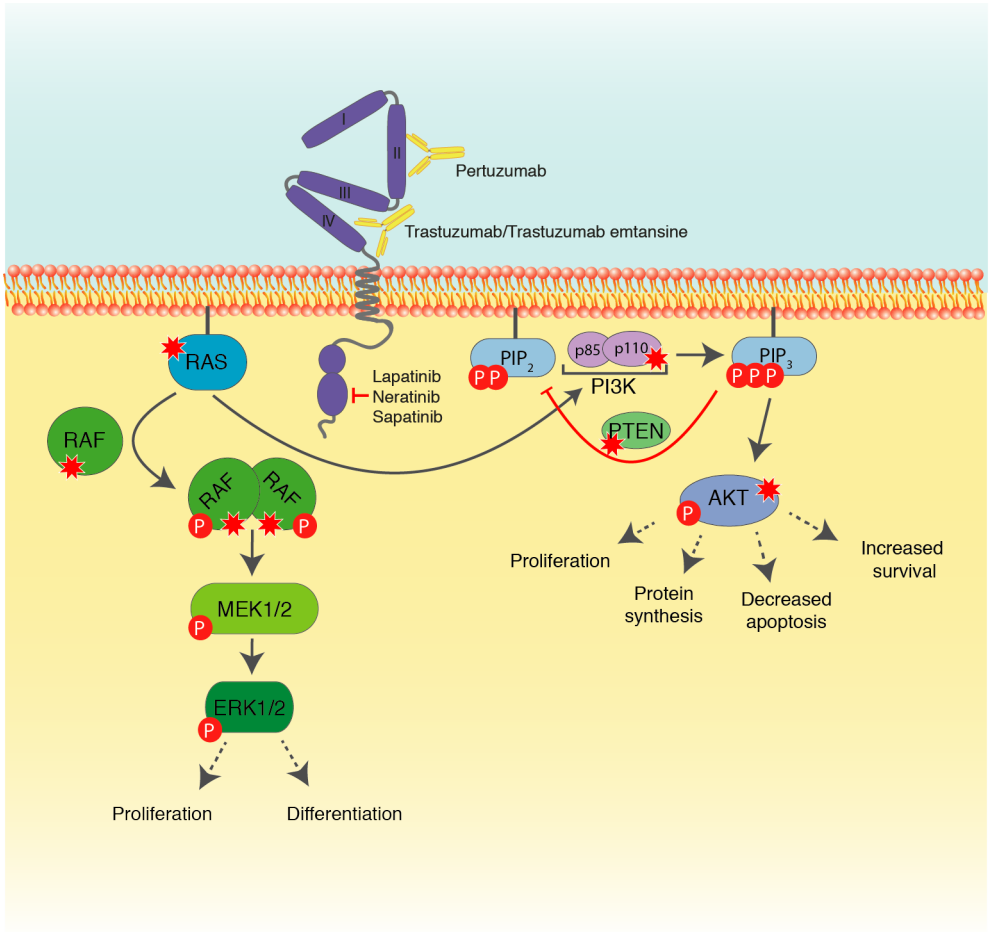


**Figure 1.5. Schematic representation of mutations downstream of HER2 found in breast cancer.** Proteins involved in the phosphoinositide 3-kinase (PI3K)/protein kinase B (AKT) and mitogen-activated protein kinase (MAPK) pathways are commonly mutated in in cancers. Activating mutations in PI3K, AKT, RAS and RAF result in downstream activation despite inhibition of HER2. Mutations in phosphatase and tensin homolog (PTEN) stop the dephosphorylation of phosphatidylinositol 3,4,5-triphosphate ($PIP_3$) to phosphatidylinositol 4,5-biphosphate ($PIP_2$). Common mutations depicted with red asterisk.

*PTEN* mutations have been reported in up to 55% of patients. The majority of these are monoallelic (40–50%), whereas 5% are biallelic.[117] An additional 5% of patients present with complete loss of *PTEN* at diagnosis,[109,115] which has been shown to independently predict survival outcomes and response to trastuzumab in HER2-positive breast cancers.[109,111,115] A reduction or loss of PTEN results in increased activation of the PI3K/AKT pathway through a lack of inhibition.[19,115]

#### 1.4.3.2 MAPK pathway

Mutations in the ERK pathway are less common in breast cancers than those in the PI3K pathway. However, the three *RAS* isoforms (*NRAS*, *KRAS*, *HRAS*) are found mutated in 6% and amplified in 17.67% of breast cancers.[107] All identified mutations within the *RAS* isoforms alter the GTPase-activating-protein-stimulated GTP hydrolysis activity, resulting in constitutive activation and downstream signalling.[112]

While *ARAF* and *BRAF* are found amplified in 5.89% and 6.79% of breast cancers respectively, only *BRAF* is found mutated in 2.5% of breast cancers.[107] Most *BRAF* mutations result in the inactive confirmation of the protein being destabilised. This results in the protein being in its active formation and further activation downstream of RAF.[113]

#### 1.4.3.3 Downstream pathway inhibition

Inhibitors targeting components of PI3K/AKT or MAPK pathways result in increased activation of the untargeted pathway, for example when co-treated with EGFR inhibitor gefitinib and a MEK inhibitor, breast cancer cells became more reliant on AKT activation for survival.[118] This finding translates to treatment of HER2-overexpressing lines: inhibition of PI3K in HER2-overexpressing breast cancer cells resulted in increased activation of MAPK signalling.[119] However, in some cases combining targeted therapies with MAPK inhibition can overcome resistance mechanisms.[120]

Vemurafenib, a tyrosine kinase inhibitor specifically targeting the $BRAF^{V600E}$ mutation, shows good efficacy initially.[121] However, within 12 months of treatment initiation, MAPK pathway inhibition is relieved by new activating mutations or expression of receptor tyrosine kinases (RTKs) to increase signalling via MAPK or PI3K/AKT pathways.[121] Thus, although downstream inhibition initially results in good responses, over time resistance to these new inhibitors can develop.

### 1.4.4 Bypass of HER2 inhibition

Upon inhibition of HER2, activation of downstream signalling pathways is halted. This results in a lack of proliferation, protein synthesis and decreased survival.[22] To overcome this, cells upregulate unrelated RTKs to maintain signalling through the PI3K/AKT and MAPK pathways (fig 1.3 C).[122–124]

*In vitro* studies utilising trastuzumab have shown increased expression of insulin-like growth factor 1 receptor (IGF1R), AXL and fibroblast growth factor receptor (FGFR).[122,124] This subset of RTKs were capable of maintaining downstream pathway activation, whereas other RTKs frequently implicated as bypass RTKs were unable to, despite being able to signal through these pathways.[122–124] This indicates that the ligands for these RTKs must be sufficiently available within the tumour microenvironment (TME) to maintain signal transduction.

Despite many RTKs being implicated in bypass of HER2 inhibition, activation of SRC has also been implicated in resistance. SRC is a non-receptor tyrosine kinase that interacts with many signalling pathways, including the PI3K/AKT and MAPK pathways. Activation of SRC has been shown to be a common node; downstream of several resistance pathways in response to trastuzumab and other targeted therapies.[120,125] However, targeting of SRC has proved ineffective, as resistance is quickly developed.[120,126,127]

Targeting RTKs that are overexpressed can be a valid treatment option *in vitro*. However, identifying overexpressed RTKs and their activation in patients is currently reliant on clinical remission after administration of additional targeted therapies. It is important to note that different patients may upregulate different RTKs, so a combination approach targeting several RTKs may be beneficial, but comes with increased side effects through the administration of several drugs.[22]

Cabozantinib, an RTK inhibitor, has been shown to be active against many RTKs which have been implicated in resistance and tumour biology. Its targets include MET, AXL, vascular endothelial growth factor receptor 2 (VEGFR2), RET, KIT and fms-like tyrosine kinase 3 (FLT3).[128] Carbozanitib has been approved for use in renal cell carcinoma and medullary thyroid cancer, with clinical trials showing improvements in

OS, PFS and ORR.[129,130] Treatment with cabozantinib has not been investigated in treatment-resistant HER2 breast cancer to date.

HSP90 inhibitors have shown great promise *in vitro* and in clinical trials.[131] As they are involved in the folding and stabilising of many tyrosine kinases, inhibition can result in the increased degradation of a range of pathways and RTKs that cells are reliant on for continued proliferation and survival.[14] In patients with progressive HER2-positive breast cancer treated with trastuzumab, HSP90 inhibitor 17-AAG resulted in a 24% ORR, with 57% of patients deriving clinical benefit, including disease stabilisation.[132] Despite showing promising results, further development was halted. To date, no HSP90 inhibitors have been approved by the FDA.

### 1.4.5 Altered iron homeostasis

Iron is involved in many biochemical pathways related to DNA synthesis and mitochondrial function.[133] An overview of the key proteins and pathways involved in cellular iron homeostasis can be seen in figure 1.6. Alterations in iron homeostasis have previously been linked to resistance to radiotherapy and chemotherapy in many cancer types and has been shown to have differing effects in treatment-resistant cancer models. The key signalling axis in iron homeostasis is the hepcidin-ferroportin axis, responsible for transporting ferric iron out of the cell.[134,135]

Several groups have reported that treatment with iron chelation regimens reversed resistance to targeted therapies and chemotherapy.[136–138] Furthermore, disruption of ferritin expression reversed resistance to radiotherapy and chemotherapy.[139,140] Conversely, many groups have reported increased iron storage, ferritin expression and reduced labile iron pools (LIPs) associated with resistance.[139,140,199] From the literature, it is evident that iron plays a varied role in the development of resistance to many therapies and may be cancer and model specific.

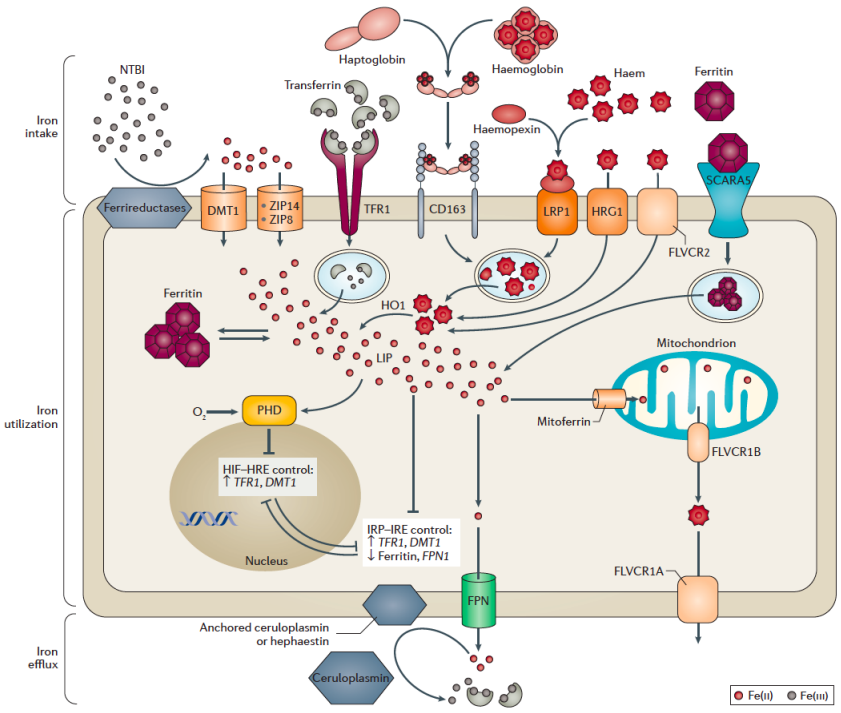


**Figure 1.6. Cellular iron homeostasis pathways.** Free ferric iron is reduced to ferrous iron by ferrireductases six transmembrane epithelial antigen of prostate (STEAP), cytochrome b reductase 1 (DYCTB) and ferric chelate reductase 1. Free ferrous iron can be transported into the cell by divalent metal-ion transporter 1 (DMT1), Zrt- and Irt-like protein 14 and 8 (ZIP14 and ZIP8). Transferrin-bound iron can only be taken up by transferrin receptor 1 (TFR1) endocytosis. Transferrin-bound iron is then released and reduced to ferric iron by DMT1. CD163 is a scavenger receptor which endocytoses haptoglobin-bound haemoglobin. After this, haemoglobin is degraded and haem transported into the cytoplasm. Pro-low-density lipoprotein receptor-related protein 1 (LRP1) can transport systemic haem complexed with haemopexin into the cytoplasm. Haem-responsive gene 1 protein homologue (HRG1) and feline leukaemia virus subgroup C receptor-related protein 2 (FLVCR2) can transport haem directly to be processed by heme oxygenase-1 (HO-1) to be released as ferrous iron. Ferritin, consisting of heavy and light chains, is broken down by scavenger receptor class A member 5 (SCARA5) which releases the ferric iron into the cytoplasm. The labile iron pool (LIP) consists of cytoplasmic ferrous iron which can be stored in ferritin or used in biochemical processes and enzymes. Expression of TFR1, DMT1, ferritin and ferroportin (FPN) is controlled by the LIP, via the post-transcriptional iron regulatory protein–iron-responsive element (IRP–IRE) regulatory system. The transcription of TFR1 and DMT1 can also be controlled by the hypoxia-inducible factor-hypoxia response element (HIF-HRE) regulatory system. In turn, prolyl-4-hydroxylase (PHD) regulates HIF expression and degradation under high oxygen conditions. Mitoferrin transfers iron to the mitochondria, where many of these processes take place. Mitochondrially produced haem is exported from mitochondria by FLVCR1B. Ferrous iron can be exported by ferroportin, then oxidised to ferric iron by ceruloplasmin or hephaestin. Intracellular haem can be exported directly by FLVCR1A. Reprinted by permission from RightsLink: Nature publishing group, *Nature Reviews Drug Discovery*, Crielaard et al. [134], 2017.

## 1.5 Mouse models of HER2-positive breast cancer

Mouse models are commonly used in preclinical drug development to provide information on the pharmacokinetics and pharmacodynamics of drugs *in vivo*. Use of mouse models also allows validation that drugs are able to hit the correct target, monitor potential side effects that may occur in humans, and assess appropriate concentrations relevant to disease treatment. The most commonly used mouse models of breast cancer are cell- or patient-derived xenografts, syngeneic mouse models and conventional, or conditional, genetically engineered mouse models (GEMMs).

### 1.5.1 Transplantation models

Ectopic cell-derived xenografts use cell lines implanted subcutaneously. Although this is a fast method which is not technically difficult,[141] the host must be immunocompromised and will only model advanced disease.[142]

Orthotopic cell-derived xenografts are more technically difficult, as cells must be injected into the mammary gland or fat pad. However, they offer benefits over ectopic xenografts as the cells are surrounded by the appropriate microenvironment.[143] Despite this, they only model advanced disease, as such, early events in tumourigenesis or the development of resistant phenotypes may not be studied as easily as in other models.[142]

Patient-derived xenografts are preferable over cell-derived xenografts, as the histological features and genetic profile of the original patient tumour can be maintained.[144] This model does have several disadvantages — it favours aggressive subtypes of breast cancer, has high costs associated with maintenance and requires access to fresh patient material.[142]

Allografts taken from a strain-matched host have advantages over xenografts, as both the tumour and microenvironment are derived from the same species, allowing the use of immunocompetent mice.[145] Using allografts requires advanced tumours for transplant, which is unsuitable for studing early events in tumourigenesis.[142] However, allografts

have been shown to recapitulate the histological features of human cancer more faithfully than cell-derived xenografts.[145,146]

### 1.5.2 Genetically engineered mouse models

Conventional GEMMs allow study of both early and late tumour progression, with a natural tumour microenvironment and immunocompetent mice. Expression of genes of interest under the control of mouse mammary tumour virus (MMTV) allows expression of transgenes to be confined to mammary tissues.[147] However, the genetics of these tumours are not truly representative of human disease states, with transgenes being expressed at higher levels than would be seen in patient tumours.

Conditional GEMMs share many advantages with conventional GEMMs, but are better able to represent genetic heterogeneity within tumours. Additionally, tumour initiation can be controlled, giving better spatial and temporal activation of oncogenes.[142,147,148]

### 1.5.3 MMTV-NIC mice

The MMTV-Neu model was first derived by Muller et al.[147], placing the activated rat *Neu* gene, encoding HER2 with a 16 amino acid in-frame deletion adjacent to the transmembrane domain, under the control of MMTV to ensure expression in the mammary tissues only.[147] These mice develop rapidly growing, invasive mammary tumours with a mean latency of 197 days.[147] To allow expression of two transgenes from the same bicistronic transcript, this model was altered to include an internal ribosome entry site (IRES) between *Neu* and a Cre recombinase under the expression of MMTV.[148] This gave rise to the MMTV-Neu-IRES-Cre (MMTV-NIC) model.

Disruption of *Pten* by flanking with loxP recombination sites (flox), ensuring expression of HER2 and PTEN deletion occurred simultaneously, accelerated tumour onset, from 197 days in MMTV-Neu mice to 43 days in MMTV-NIC-PTEN$^{flox/flox}$ mice.[149]

In Creedon et al.[84], MMTV-NIC-PTEN$^{+/-}$ mice were used, which have deletion of one *Pten* allele, giving rise to loss of heterozygosity to replicate human disease.[149] These mice develop tumours with a mean latency of 81 days.[84]

### 1.5.4 MMTV-NIC-PTEN$^{+/-}$ mice

Two derivatives of the MMTV-NIC-PTEN$^{+/-}$ model were used as part of this thesis. The MMTV-NIC-PTEN$^{+/-}$ model spontaneously develops up to 10 mammary tumours simultaneously and tumour growth has been characterised in Creedon et al.[150] Once tumours reached 0.1 cm$^3$, treatment with vehicle or sapatinib began. Treatment was continuous and mice sacrificed once any tumour reached 15 mm in any dimension. More in-depth analysis of resistance mechanisms within this model has not been investigated yet, but will be as part of this thesis.

To allow the development of acquired resistance to be studied in more detail, untreated tumours from MMTV-NIC-PTEN$^{+/-}$ mice were fragmented and implanted into the fourth mammary fat pad of FVB/N mice. Once tumours reached 0.1 cm$^3$, treatment with vehicle or sapatinib began. If tumours regressed below this, treatment was halted until tumours had reached 0.1 cm$^3$ again. This cyclical treatment continued until tumours no longer responded to treatment. Mice were sacrificed once the tumour reached 15 mm in any dimension. Initial characterisation of the tumours developed in this model has been previously described,[84,150] and will be followed up in this thesis.

## 1.6 Aims

Resistance to targeted therapies is a problem which occurs in all cancers. Despite advances in targeted and combination therapies, patients still develop resistance and their disease ultimately progresses. Targeting the resistance mechanisms currently identified has not resulted in many, if any, viable alternatives to prevent resistance developing in these patients. This thesis has focused on identifying novel mechanisms of resistance to HER2-targeted therapies and investigating how the development of resistance could be manipulated to prevent its occurrence.

The aims of this study were to:

- Understand the link between EMT and resistance to HER2-targeted therapy previously identified in the Brunton lab.[84]

- Use a mouse model of HER2-driven mammary cancer to identify novel mechanisms of resistance to HER2-targeted therapy.

# Chapter 2

# Materials & Methods

## 2.1 Materials

### 2.1.1 Buffers

The composition of all buffers and solutions used are listed below. Where water is used as a solvent, this was distilled. All chemicals were obtained from Sigma Aldrich (MO, USA), unless otherwise stated.

**Table 2.1.** List of buffers used

| Buffer | Composition |
|---|---|
| 0.1 M citric acid | 10.5 g $C_6H_8O_7.H_2O$, 500 ml water |
| 0.1 M sodium citrate | 14.7 g $C_6H_5Na_3O_7.2H_2O$, 500 ml water |
| 10 mM sodium citrate, pH 6 | 11.5 ml 0.1 M citric acid, 88.5 ml 0.1 M sodium citrate |
| 1 M NaCl | 29.22 g NaCl, 500 ml water |
| 1 M Tris HCl pH 8 | 60.57 g TRIS, 500 ml water and pH to 8 using 1 M HCl |
| 6X Laemmli sample buffer | 416 mM SDS, 47% (v/v) glycerol, 6 mM Tris (pH 6.8), 895 $\mu$M bromophenol blue in water. Prior to use, add 10% (v/v) $\beta$-mercaptoethanol |
| Blocking buffer - Immunofluorescence | 1.1% (w/v) bovine serum albumin (BSA), 0.2% (v/v) Triton X-100 in PBS |
| Blocking buffer - Western blotting | 5% (w/v) BSA in TBS-T (0.1%) |
| Fluorescent activated cell sorting (FACS) buffer | 1% (w/v) foetal bovine serum (FBS) in phosphate buffered saline (PBS) |
| Lipidomic reconstitution buffer | Acetonitrile/propan-2-ol/water (60:30:5) |
| Luria Bertani (LB) Broth | 1% (w/v) Bacto-tryptone, 0.5% (w/v) Bacto-yeast extract, 171 mM NaCl in water |
| Lysis buffer | 1.25 $\mu$M PMSF, 0.5 M NaF, 0.1 M $Na_3VO_4$, 0.1% (v/v) aprotinin in RIPA |
| Lysis buffer - Reverse Phase Protein Array (RPPA) | 1% (v/v) Triton X-100, 50 mM HEPES (pH 7.4) 150 mM NaCl, 1.5 mM $MgCl_2$, 1 mM EGTA, 100 mM NaF, 10 mM $Na_4P_2O_7$, 1 mM $Na_3VO_4$, 10% (v/v) glycerol, cOmplete$^{TM}$, EDTA-free Protease Inhibitor Cocktail and PhosSTOP$^{TM}$ (Roche). |

Continued on the next page

Continued from previous page

| Buffer | Composition |
|---|---|
| PEM Buffer | 0.1 M PIPES, 50 mM EGTA, 1 mM $MgCl_2$, 0.2% (v/v) Triton-X 100, 4% (v/v) paraformaldehyde in water |
| Phosphate buffered saline (PBS) | 136 mM NaCl, 2.6 mM KCl, 12 mM $Na_2HPO_4$, 1.76 mM $KH_2PO_4$ (pH 7.4) in water |
| RIPA | 50 mM Tris HCl (pH 8), 150 mM NaCl, 1% NP40, 0.5% $C_{24}H_{39}NaO_4$, 0.1% SDS in water |
| Scott's tap water | 41 mM $NaHCO_3$, 210 mM $MgSO_4$ in water |
| Tris buffered saline (TBS) | 50 mM Tris, 150 mM NaCl, 2 mM DTT in water |
| Tris Glycine SDS (TGS) buffer | 25 mM Tris, 192 mM glycine, 0.1% (w/v) SDS, pH 8.3 in water |
| Trypsin | 1 mM EDTA, 0.25% (v/v) trypsin (Gibco, Thermo Fisher Scientific, MA, USA) in PBS |
| Urea Lysis Buffer | 50 mM $NH_4HCO_3$, pH 7.4, 8 M urea, 100 mM NaF, 10 mM $Na_4P_2O_7$, 1 mM $Na_3VO_4$ in mass spectrometry grade water |

### 2.1.2 Antibodies

The antibodies used are listed in the table below, with typical dilutions for western blotting (WB), immunohistochemistry (IHC). All antibodies were diluted in the appropriate buffer for the purpose, i.e, for western blots, antibodies were diluted in western blotting blocking buffer. For immunofluorescence, all antibodies were used at 1/200 dilution.

#### Primary Antibodies

**Table 2.2.** List of primary antibodies used

| Antibody | Host | Catalog Nº | Company | WB | IHC |
|---|---|---|---|---|---|
| $\beta$-actin | Rabbit | 8457 | CST | 1/1000 | - |
| $\beta$-catenin | Mouse | 610154 | BD Biosciences | - | 1/800 |
| CD31 | Rabbit | ab28364 | Abcam | - | 1/400 |
| Ceruloplasmin | Rabbit | ab48614 | Abcam | - | 1/50 |
| Cleaved caspase-3 | Rabbit | 9664 | CST | - | 1/200 |

Continued on the next page

Continued from previous page

| Antibody | Host | Catalog Nº | Company | WB | IHC |
|---|---|---|---|---|---|
| COX2 | Rabbit | 12282 | CST | - | 1/600 |
| DMT-1 | Mouse | ab55735 | Abcam | - | 1/100 |
| E-Cadherin | Mouse | M3612 | Dako | - | 1/50 |
| EGFR | Rabbit | 4405 | CST | 1/1000 | - |
| Ferritin Heavy Chain | Rabbit | ab183781 | Abcam | 1/1000 | 1/400 |
| Ferritin Light Chain | Rabbit | ab69090 | Abcam | 1/1000 | 1/400 |
| Ferroportin | Rabbit | ab78066 | Abcam | - | 1/50 |
| Heme oxygenase-1 | Mouse | ab13248 | Abcam | 1/1000 | 1/250 |
| GPX4 | Rabbit | ab125066 | Abcam | - | 1/100 |
| HER2 | Rabbit | 2165 | CST | 1/1000 | 1/400 |
| HER3 | Rabbit | 4754 | CST | 1/1000 | - |
| Ki67 | Mouse | VP-K452 | Vector | - | 1/100 |
| LC3B | Mouse | 0231-100 | Nanotools | - | 1/100 |
| LC3B | Rabbit | L7543 | Sigma | 1/3000 | - |
| NCOA4 | Rabbit | PA5-39311 | Invitrogen | - | 1/50 |
| NRF2 | Rabbit | ab31163 | Abcam | - | 1/100 |
| p62 | Rabbit | 5114 | CST | 1/1000 | - |
| p62 | Rabbit | BML-PW9860 | Enzo | - | 1/1000 |
| Phospho AKT (Ser 473) | Rabbit | 4060 | CST | - | 1/50 |
| Phospho EGFR (Tyr1068) | Rabbit | 3777 | CST | 1/1000 | - |
| Phospho HER2 (Tyr1221/1222) | Rabbit | 2243 | CST | 1/1000 | - |
| Phospho HER3 (Tyr1289) | Mouse | 4791 | CST | 1/1000 | - |
| Phospho p44/42 MAPK (Thr202/Tyr404) | Rabbit | 4370 | CST | - | 1/250 |

Continued on the next page

Continued from previous page

| Antibody | Host | Catalog Nº | Company | WB | IHC |
|---|---|---|---|---|---|
| Phospho SMAD1/5 | Rabbit | 9516 | CST | 1/1000 | - |
| Phospho SMAD1/5/8 | Rabbit | AB3848-I | Merck | - | 1/50 |
| PTEN | Rabbit | 9188 | CST | - | 1/200 |
| SLUG | Rabbit | ab27568 | Abcam | - | 1/500 |
| SMAD1 | Rabbit | 6944 | CST | 1/1000 | - |
| SMAD5 | Rabbit | 12534 | CST | 1/1000 | - |
| SNAIL | Rabbit | ab180714 | Abcam | - | 1/5000 |
| Transferrin receptor | Rabbit | ab108985 | Abcam | - | 1/1000 |
| TWIST1 | Rabbit | sc-134136 | SCB | - | 1/250 |
| ZEB1 | Mouse | ab180905 | Abcam | - | 1/150 |
| ZEB2 | Rabbit | HPA003456 | Atlas | - | 1/250 |

CST: Cell Signaling Technologies; SCB: Santa Cruz Biotechnologies; MP: Molecular Probes

**Table 2.3.** List of primary antibodies used for fluorescence

| Antibody | Host | Catalog Nº | Company | FACS | IF |
|---|---|---|---|---|---|
| HER2-APC | Mouse | 324407 | BioLegend | 1/200 | - |
| Vimentin | Rabbit | 5741 | CST | - | 1/200 |

### Secondary Antibodies

**Table 2.4.** List of secondary antibodies used

| Antibody | Host | Catalog Nº | Company | WB | IF |
|---|---|---|---|---|---|
| Anti-Mouse | Horse | 7076 | CST | 1/5000 | - |
| Anti-Rabbit | Goat | 7074 | CST | 1/5000 | - |
| Anti-Mouse 546 | Goat | A-11003 | MP | - | 1/400 |
| Anti-Rabbit 488 | Chicken | A-21441 | MP | - | 1/400 |
| Phalloidin 594 | - | A12381 | Invitrogen | - | 1/250 |

CST: Cell Signaling Technologies; MP: Molecular Probes

### 2.1.3 Primers

Primers were designed using NCBI Primer Blast,[151] and made by Integrated DNA Technologies (IA, USA).

**Table 2.5.** List of primers used

| Target Gene | Species | Sequence (5'-3') |
|---|---|---|
| *β2m* | Mouse | F- GGGAAGCCGAACATACTGAA<br>R- TGCTTAACTCTGCAGGCGTAT |
| *Cp* | Mouse | F- ACTCCCATGTTGATGCTCCA<br>R- ACTTTCTCGGGTTCAGAGCA |
| *ERBB2* | Human | F- GGTGGTCTTTGGGATCCTCA<br>R- ACCTTCACCTTCCTCAGCTC |
| *ErbB2* | Mouse | F- GGCACTGTCTACAAGGGCAT<br>R- GAGGCGGGACACATATGGAG |
| *ErbB2* | Mouse | F- GGTGACACAGCTTATGCCCT<br>R- AGCTCATCCCCTTGGCAATC |
| *ERBB3* | Human | F- GAGGTGTGAGGTGGTGATGG<br>R- CGAATCCACTGCAGGAAGGA |
| *Fth* | Mouse | F- AACAGTGCTTGAACGGAACC<br>R- GTTGATCTGGCGGTTGATGG |
| *Ftl* | Mouse | F- TCAGCTCCTAGGACCAGTCT<br>R- AAGCCCAGAGAGAGGTAGGT |
| *GAPDH* | Human | F- CTGACTTCAACAGCGACACC<br>R- GTGGTCCAGGGGTCTTACTC |
| *Ho-1* | Mouse | F- TCCGCATACAACCAGTGAGT<br>R- GGACACCTGACCCTTCTGAA |
| *SNAI1* | Human | F- AGTGGTTCTTCTGCGCTACT<br>R- GTAGGGCTGCTGGAAGGTAA |
| *SNAI2* | Human | F- ATGAGGAATCTGGCTGCTGT<br>R- CTCTCTCTGTGGGTGTGTGT |
| *ZEB1* | Human | F- ACCAGACAGTGTTACCAGGG<br>R- CTCTTCAGGTGCCTCAGGAA |
| *ZEB2* | Human | F- AGGAATGACAAGCCCCATCA<br>R- GAGGGTTACTGTTGGGAGCT |

### 2.1.4 Plasmids

Short hairpin RNA (shRNA) and overexpression plasmids were obtained from S. Brabletz (University of Erlangen-Nuernberg, Germany), or purchased commercially.

**Table 2.6.** List of plasmids used

| Insert | Backbone | Reporter | Source |
|---|---|---|---|
| Empty Vector | pCI-Neo | None | - |
| Empty Vector | pCMV6 | GFP | - |
| Empty Vector | SMARTvector | TurboGFP | Dharmacon |
| *HO-1* | pCMV6 | GFP | Origene |
| sh*ERBB2* | SMARTvector | TurboGFP | Dharmacon |
| *ZEB1* | pCI-Neo | None | S. Brabletz |

GFP: Green fluorescent protein

### Releasing Open Reading Frame

To obtain empty vectors, plasmids containing open reading frames were digested in the conditions listed in table 2.7.

**Table 2.7.** Conditions for plasmid digestion

| Plasmid | Restriction Enzyme | Temperature | Time |
|---|---|---|---|
| *HO-1* | Acc65I/BsiWI | 37°C/ 55°C | 60 mins/ 60 mins |
| *ZEB1* | XbaI | 37°C | 60 mins |

Digested plasmids were then ligated with T4 DNA ligase (New England Biolabs, MA, USA) for 2 hours at room temperature (RT). Following ligation, OneShot TOP10 chemically competent *E. coli* were transformed and plasmids purified as stated in section 2.2.5.

## 2.2 Methods

### 2.2.1 Animal Models & Analysis

Animal husbandry and breeding were carried out by the staff of the Institute of Genetics and Molecular Medicine, University of Edinburgh. Genotyping was performed by Transnetyx (TN, USA) with the use of ear notch tissue from at least 14-day old mice. All animal experiments were carried out in compliance with UK Home Office guidelines by Morwenna Muir unless otherwise indicated.

Mice were housed in conventional Techniplast 1144 cages with shavings, Kleenex® tissues for nest material, cardboard tubes and aspen chew sticks. The light cycle was 12 hours on, 12 hours off (7:00–19:00). Mice were given Rat and Mouse No. 1 Maintenance diet (159 ppm Fe; Special Diet Services, Essex, UK), unless otherwise indicated. Mice were sacrificed using cervical dislocation and tissues were collected. Tissue was fixed overnight in neutral-buffered 10% formaldehyde (Surgipath, Europe), for later histological analysis, or flash frozen in liquid nitrogen and stored at -80°C until required.

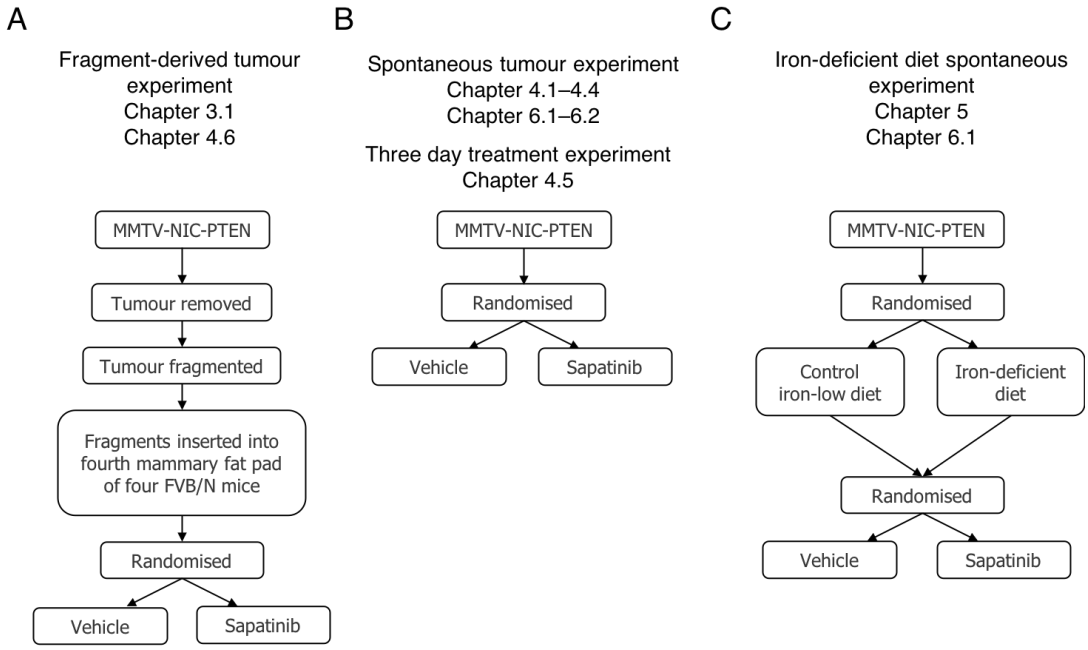


**Figure 2.1. Diagram of animal experiments. (A)** Tumours from MMTV-NIC-PTEN mice were removed and fragmented, then inserted into the fourth mammary fat pad of FVB/N mice. These mice were randomised to recieve vehicle or sapatinib and treated cyclically until tumours reached $\geq$15 mm in any direction. **(B)** MMTV-NIC-PTEN mice were allowed to develop tumours, with vehicle or sapatinib treatment beginning once tumours reached 0.1 $cm^3$ for spontaneous tumour experiments, or $0.3^3$ for three day treatment experiments. For spontaneous tumour experiments, mice were sacrificed once tumours reached $\geq$15 mm in any direction. For three day treatment experiments, mice were sacrificed two hours after the third dose. **(C)** MMTV-NIC-PTEN mice were allowed to develop tumours. Once a tumour was palpable, mice were randomised to receive a control, iron-low diet or an iron-deficient diet. After four days on diet, mice were randomised to receive vehicle or sapatinib treatment. Mice were sacrificed once any tumour reached $\geq$15 mm in any direction.

### Fragment-Derived Tumour Experiment

This experiment was carried out by Dr Helen Creedon. Tumours were collected from MMTV-NIC-PTEN$^{+/-}$ mice, washed in ice-cold PBS and cut into 1 mm$^3$ sections. These were centrifuged at 450 *g* and the supernatant removed prior to storage at -80°C. Fragments were defrosted at RT and inserted into the fourth mammary fat pad of FVB/N mice. Mice were dosed weekly with vehicle (1% Tween 80 in PBS) or sapatinib (100 mg/kg with 1% Tween 80 in PBS) by oral gavage. To generate resistant tumours, an intermittent drug schedule was performed. Tumours were allowed to grow to ≥0.1 cm$^3$ before starting treatment. Once tumours had regressed to ≤0.1 cm$^3$, treatment was stopped. Mice were sacrificed when tumours reached ≥15 mm in any direction. Summarised in fig 2.1 A.

### Spontaneous Tumour Experiment

Tumour measurements were carried out by Dr Helen Creedon. MMTV-NIC-PTEN$^{+/-}$ mice on an FVB/N background [148] were randomised to receive treatment with vehicle (1% Tween 80 in PBS) or sapatinib (100 mg/kg with 1% Tween 80 in PBS) by oral gavage. Mice were monitored twice weekly for palpable tumour development. Once tumours were ≥0.1 cm$^3$, treatment commenced. When tumours were ≥15 mm in any direction, mice were sacrificed. Summarised in fig 2.1 B.

### 3 Day Spontaneous Tumour Treatments

This experiment was carried out by Dr Helen Creedon. MMTV-NIC-PTEN$^{+/-}$ mice were randomised to receive treatment with vehicle (1% Tween 80 in PBS) or sapatinib (100 mg/kg with 1% Tween 80 in PBS) by oral gavage. Mice were monitored twice weekly for palpable tumour development. Once tumours were ≥0.3 cm$^3$, treatment commenced. Mice were sacrificed two hours after the third dose. Summarised in fig 2.1 B.

### Iron-Deficient Diet Spontaneous Tumour Experiment

MMTV-NIC-PTEN$^{+/-}$ mice were monitored twice weekly for palpable tumour development. Once a palpable tumour was detected, mice were randomised to receive a iron-low control diet (TD.80394, 49 ppm Fe; Envigo, NJ, USA), or an iron deficient diet (TD.80396, 2 ppm Fe; Envigo, NJ, USA). Four days after diet commenced, mice were randomised to receive vehicle (1% Tween 80 in PBS) or sapatinib (100 mg/kg with 1% Tween 80 in PBS) by oral gavage. When tumours were ≥15 mm in any direction, mice were sacrificed. Summarised in fig 2.1 C.

#### Immunohistochemistry

Sections of tumours were cut, 4 $\mu$m thick, using a microtome. These were placed on slides and dried on a hot plate at 55°C. Paraffin was removed by immersing slides in xylene for 5 minutes, followed by decreasing ethanol washes (100%, 100%, 80% and 50%) for 5 minutes each. Slides were rinsed in water, then heat-mediated antigen retrieval was performed in pH 6 citrate buffer. Following this, slides were left to cool, rinsed with water and washed in TBST (0.0025%) for 5 minutes. Slides were stained using Dako Envision DAB+ kit (Dako, Denmark) and counterstained with haemotoxylin for 2 minutes. Slides were dehydrated in increasing alcohol washes (50%, 80%, 100%, 100%) and cleared with xylene.

#### Immunohistochemical Analysis

Slides were imaged using a Nanozoomer (Hamamatsu, Japan). Once images were obtained, Definiens Architect Tissue Studio software (Definiens, Germany) was used to score the antibody staining. Analysis parameters were altered for each antibody depending on the intensity of staining. Region of interest (ROI) detection was performed to exclude non-tumour tissue and areas of necrosis from the analysis. Statistical analysis was performed on the scoring as described below (section 2.2.8).

#### Perls' Prussian Blue

Sections were prepared and rehydrated as described above (section 2.2.1). Slides were rinsed in water, then placed in 1% (w/v) potassium ferrocyanide (Perls' Prussian Blue) and incubated for 3 minutes at RT. Slides were rinsed in distilled water and then stained for 5 minutes in nuclear fast red. Slides were then rinsed in 4 changes of distilled water and dehydrated as described above (section 2.2.1).

### 2.2.2 Assay Kits

#### Iron Determination Assay

Total iron, $Fe^{2+}$ and $Fe^{3+}$ concentration was determined using an Iron Assay Kit (Abcam, Cambridge, UK). Samples were measured in duplicate and normalised to protein concentration, determined as stated in section 2.2.6.

#### Glucose 6 Phosphase Dehydrogenase Assay

Glucose 6 Phosphate Dehydrogenase activity was determined using a G6PD activity assay kit (Abcam, Cambridge, UK). Samples were measured in duplicate.

#### Glutathione Assay

Reduced and oxidised glutathione concentration was determined using a GSH/GSSG ratio detection assay kit (Abcam, Cambridge, UK). Samples were measured in duplicate.

#### Active caspase 3/7 Assay

Levels of active caspase 3 and 7 were determined using a Caspase-Glo 3/7 Assay (Promega, WI, USA). Samples were normalised to DMSO control.

### 2.2.3 Cell Culture Methods

#### Cell Culture

Human breast cancer cell line SKBR3 (American Type Culture Collection, VA, USA) was grown in Dulbecco's Modified Eagle's Medium (DMEM) supplemented with 2 mM L-glutamine and 10% foetal bovine serum (FBS; all Thermo Fisher Scientific, MA, USA). Cells were maintained at 37°C in a humidified atmosphere containing 5% $CO_2$. Sapatinib was obtained from AstraZeneca (Cambridge, UK), lapatinib from GlaxoSmithKline (Brentford, UK).

#### Generation of Resistant Lines

SKBR3 cells were exposed to increasing concentrations of sapatinib or lapatinib. The concentration was increased after two passages. Cells were classed as resistant when they grew in the highest concentration of drug used. Sapatinib resistant cells were maintained in 0.67 $\mu$M sapatinib. Lapatinib resistant cells were maintained in 5 $\mu$M lapatinib.

#### Generation of shRNA cell lines

HEK293T cells were seeded in a 6 well plate at a density of $2.5\text{x}10^5$. The following day, cells were transfected with 1 $\mu$g construct, 0.2 $\mu$g psPAX2 and 0.3 $\mu$g pMD2.G using lipofectamine 2000 (Thermo Fisher Scientific, MA, USA) to produce virus. From this point, cells were handled in Category 2 confinement.

**Table 2.8.** Drug concentrations used over 48 hour period to determine cell death.

| Drug | Concentration | Supplier |
|---|---|---|
| 3-Methyladenine | 5 mM | Sigma Aldrich |
| Bafilomycin A1 | 5 nM | Sigma Aldrich |
| Deferoxamine | 100 $\mu$M | Sigma Aldrich |
| Erastin | 10 $\mu$M | Sigma Aldrich |
| Ferrostatin | 5 $\mu$M | Sigma Aldrich |
| Lapatinib | 5 $\mu$M | GlaxoSmithKline |
| Sapatinib | 0.67 $\mu$M | AstraZeneca |
| Z-VAD-FMK | 20 $\mu$M | Abcam |

Z-VAD-FMK: benzyloxycarbonyl-phenylalanyl-alanyl-fluoromethyl ketone

One day after transfection, HEK293T cells were washed and medium replaced. On day 2, medium was collected from HEK293T cells, supplemented with an additional 10% FBS and filtered then added to target cells. Target cells were kept in Category 2 for 2 passages, then transferred back to normal tissue culture. Cells were grown in appropriate antibiotic for selection and FACS sorted.

### Drug Treatments

### Alamar Blue Assay

Cells were seeded on day -1. On day 0, one plate was taken as a day 0 measurement. A 1/10 concentration of Alamar Blue reagent (Invitrogen, CA, USA) was added to each well and incubated at 37°C for 2 hours and the plate read at 590 nm. Drugs were added to the remaining plates, which were incubated for 3 days to allow growth. After 3 days, Alamar Blue was added to each well and plates incubated for 2 hours at 37°C prior to reading at 590 nm. Data were normalised to DMSO controls.

### Cell Death Assay

Cells were seeded on day -1. On day 0, drugs were added into each well. Cells were incubated with drug (table 2.8) for 48 hours. After this time, cells were stained with 1 $\mu$g/ml propidium iodide (PI) and cell death assessed using a Tali Image-Based Cytometer (Invitrogen, CA, USA).

### Fluorescence Activated Cell Sorting (FACS)

Cells were washed with PBS and cell dissociation solution (Thermo Fisher Scientific, MA, USA) added for 5 minutes at 37°C. Cells were filtered through a 70 $\mu$m cell strainer, centrifuged at 500 $g$ for 5 minutes at 4°C, resuspended in PBS, transferred to a 96 well plate and centrifuged again. Cells were resuspended in 1 $\mu$g/ml PI and incubated for 30 minutes at 4°C, then centrifuged

again. Cells were resuspended in FC block (BD Biosciences, NJ, USA) in FACS buffer for 15 minutes minutes at RT. Target antibody was added, final concentration 1/400 in FACS buffer and incubated for 30 minutes at RT. Cells were centrifuged and washed three times with FACS buffer, then resuspended for analysis on the LSR Fortessa (BD Biosciences, NJ, USA).

For C11 BODIPY staining, cells were incubated with 2 $\mu$M C11 BODIPY for 30 minutes at 37°C, then washed twice and analysed on the LSR Fortessa (BD Biosciences, NJ, USA).

#### Immunofluorescence

Cells were cultured on sterile glass coverslips in 6 well plates. Cells were fixed in PEM buffer containing 4% paraformaldehyde (PFA) for 15 minutes at RT, then washed thrice in PBS. Blocking buffer was added for 1 hour at RT. After this, primary antibodies were added and incubated overnight at 4°C. Cover slips were washed thrice with TBST (0.1%) and incubated for 1 hour at RT with secondary antibodies and phalloidin. Cover slips were washed thrice in TBST (0.1%) then mounted on glass slides using VectaShield with DAPI (Vector Laboratories, CA, USA). Slides were then stored at -20°C until imaged.

### 2.2.4 Microscopy

#### Phase Contrast

Cells were imaged using a 10x objective on a Leica DMIL LED microscope (Leica, Germany) attached to a Retiga EX*i* FAST1394 camera (Q Imaging, BC, Canada).

#### Proliferation & Wound Healing Assays

Cells were seeded in a 96 well plate (Greiner Bio-One, Austria) then imaged in the IncuCyte ZOOM (Essen Bioscience, MI, USA) at 10x, every 3 hours. For wound healing assays, once cells were seeded, they were returned to 37°C incubator overnight then a wound was created using an IncuCyte WoundMaker (Essen Bioscience, MI, USA). After creation of a wound, cells were imaged in the IncuCyte ZOOM for 96 hours.

#### Confocal Microscopy

Cells fixed on glass coverslips were imaged using a 63x HCX PL Apo 1.4 NA Iris oil immersion objective on a Leica SP5 confocal microscope (Leica, Germany). Z stacks were taken for all images. Images shown are maximum intensity projection compressed Z stacks.

### 2.2.5 Nucleic Acid Methods

#### RNA Extraction

#### Cells

Cells were pelleted and lysed in Buffer RLT containing $\beta$-mercaptoethanol. The RNeasy Mini Kit (Qiagen, Germany) was used according to the manufacturers instructions.

#### Tissue

Tissue was homogenised using a pestle and mortar, then Buffer RLT containing $\beta$-mercaptoethanol was added. The RNeasy Mini Kit (Qiagen, Germany) was used according to the manufacturers instructions.

#### cDNA Synthesis

For each cell line or tissue, 1 $\mu$g of RNA was used to generate complementary deoxyribonucleic acid (cDNA). QuantiNova Reverse Transcription kit (Qiagen, Germany) was used, according to the manufacturers instructions.

#### Real Time PCR

For each reaction, 5 ng of cDNA was added. Each reaction was performed in triplicate. SYBR Select Master Mix (Applied Biosystems, CA, USA) was used according to the manufacturers instructions. Each PCR reaction included a $H_2O$ control to check for primer specificity. Primers were used at a final concentration of 200 nM. The following cycling conditions were used:

- Pre-incubation at 95°C/3 minutes
- 40 cycles of:
  - 95°C 5 seconds
  - 60°C 10 seconds
  - 72°C 10 seconds
- One dissociation cycle:
  - 95°C 15 seconds
  - 60°C 60 seconds
  - Increasing 0.3°C every 15 seconds, until 95°C is reached

Cycle threshold (CT) was determined by StepOne Real-Time PCR System software (Applied Biosystems, CA, USA).

#### Cloning

One Shot TOP10 Chemically Competent *E. coli* (Invitrogen, CA, USA) were used according to the manufacturers instructions. Transformed colonies were selected on plates containing appropriate antibiotic (Invitrogen, CA, USA). One colony from each plate was selected and transferred into 2 ml of LB broth containing 100 $\mu$g/ml antibiotic. After 2 hours shaking at 37°C, cultures were transferred to 200 ml LB broth containing 100 $\mu$g/ml ampicillin and left overnight at 37°C, while shaking.

#### Plasmid Purification

Cultures were centrifuged at 10000 $g$ for 15 minutes at 4°C to obtain a pellet. Following this, plasmid purification was carried out using the MaxiPrep kit (Qiagen, Germany) according to manufacturers instructions.

### 2.2.6 Protein Methods

#### Cell Lysates

Cells were grown in 15 cm dishes until 70% confluence was reached. Dishes were transferred to ice, medium removed and cells washed twice with ice cold PBS. Cells were lysed in lysis buffer then incubated on ice for 20 minutes, with occasional agitation. Lysates were centrifuged at 210000 $g$ for 15 minutes at 4°C and the supernatant transferred to a new microcentrifuge tube. Lysates were stored at -20°C.

For RPPA, RPPA lysis buffer was used in place of lysis buffer and the remainder of the procedure was the same.

For tumours, a fragment was cut from fresh frozen tumour and homogenised using the FastPrep-24 homogeniser in pre-cooled Lysing matrix-D tubes (MP Biomedicals, CA, USA). RPPA lysis buffer was added immediately after homogenisation and vials placed on ice for 30 minutes. Samples were centrifuged at 4°C for 10 minutes at 21000 $g$ and supernatant transferred to a microcentrifuge tube.

### Protein Concentration Determination

Protein concentration of lysates was determined using a bicinchoninic acid assay (BCA assay). Micro BCA Protein Assay Kit (Thermo Fisher Scientific, MA, USA) was used according to manual. Plates were read on a plate reader at 540 nm wavelength, each lysate was measured in triplicate.

For use in the Iron Determination Assay, protein concentration of lysates was determined using the Coomassie Plus Protein Assay (Thermo Fisher Scientific, MA, USA), according to manufacturers instructions. Plates were read on a plate reader at 595 nm wavelength, samples were measured in duplicate.

### Western Blotting

After determination of protein concentration as described above (section 2.2.6), 20 $\mu$g of cell lysate was added to 6X Laemmli buffer and denatured for 5 minutes at 95°C. Denatured proteins were loaded into 4-15% Mini-PROTEAN TGX precast gels (BioRad, Germany) and ran in a BioRad Mini-PROTEAN 3 gel chamber in TGS buffer at 180 V for 40 minutes.

Proteins were transferred to Trans-Blot Turbo Midi Nitrocellulose membranes (BioRad, Germany) by semi-dry blotting, using a Trans-Blot Turbo Transfer System (BioRad, Germany) at 25 V, 2.5 A for 7 minutes. Membranes were blocked in blocking buffer for 1 hour at RT before addition of primary antibody. Membranes were incubated with primary antibody overnight at 4°C before being washed with TBST (0.1%). Secondary antibodies were incubated with the membrane for 1 hour at RT, before washing a minimum of three times in TBST (0.1%). Bound antibodies were detected by chemiluminescence using Clarity ECL Substrate (BioRad, Germany) on the BioRad Gel Doc XR+, or by near-infrared fluorescence on the LI-COR Odyssey Sa Infrared Imaging System (LI-COR, NE, USA).

### Reverse Phase Protein Array

Cell and tumour lysates were prepared as described above (section 2.2.6). Lysates were serially diluted to produce a dilution series comprising four serial two-fold dilutions of each sample and spotted onto nitrocellulose-coated slides (Grace Bio-Labs, OR, USA) in triplicate under conditions of constant 70% humidity using the Aushon 2470 array platform (Aushon Biosystems, MA, USA). Slides were hydrated in blocking buffer (Thermo Fisher Scientific, MA, USA) and then incubated with validated primary antibodies (all 1/250). Bound antibodies were detected by incubation with anti-rabbit DyLight 800-conjugated secondary antibody (New England BioLabs, MA, USA).

An InnoScan 710-IR scanner (Innopsys, France) was used to read the slides and images were acquired at the highest gain without saturation of the fluorescence signal. The relative

fluorescence intensity (RFI) of each sample spot was quantified using Mapix software (Innopsys, France). The linear fit of the dilution series of each sample was determined for each primary antibody, from which median RFI was calculated. Signal intensities were normalised by global sample median normalisation.

### 2.2.7 Mass Spectrometry

#### Proteomics

A fragment was cut from fresh frozen tumour and homogenised in 300 $\mu$l of urea lysis buffer. Lysates were then sonicated and clarified by centrifugation at 20000 $g$ for 15 minutes at 4°C. Supernatant was transferred into low-bind microcentrifuge tubes (Eppendorf, Germany). Protein concentration determination was performed as above (section 2.2.6).

Samples were denatured with 8 mM dithiothreitol for 10 minutes at 50°C and alkylated with 16 mM iodoacetamide for 10 minutes at 37°C. Urea concentration was reduced to 2 M using 50 mM $NH_4HCO_3$ and samples digested with trypsin (1:200 enzyme:protein; Thermo Fisher Scientific, MA, USA) at 37°C overnight. Samples were clarified by centrifugation at 2500 $g$ for 5 minutes and acidified with 10% trifluoroacetic acid (TFA).

Stage tips[152] were prepared by inserting a plug of C18 material (Thermo Fisher Scientific, MA, USA) into a Greiner BioOne 200 $\mu$l capacity pipette tip. Stage Tips were activated with 30 $\mu$l MeOH and equilibrated with 50 $\mu$l 0.1% TFA. 10 $\mu$g of sample was added and incubated at RT for 30 seconds, then aspirated and washed twice with 50 $\mu$l 0.1% TFA. Stage Tips were stored at -20°C until analysis. Peptides were eluted with 80% acetonitrile, 0.1% TFA into a clean PCR plate, then dried in a vacuum concentrator. After this, samples were made up to 15 $\mu$l and analysis performed.

Analysis of samples was performed using a Q Exactive Plus instrument (Thermo Fisher Scientific, MA, USA) controlled by Xcalibur (Thermo Fisher Scientific, MA, USA). Peak lists were generated using MaxQuant.[153,154] MS data were searched against SwissProt, UniProt KB[155] using MaxQuant. LFQ ratio and $p$ values, generated using Wilcoxon-Mann-Whitney test, were calculated by MaxQuant.

#### Lipidomics

A fragment was cut from fresh frozen tumour and homogenised using a Dounce homogeniser. After this, 375 $\mu$l chloroform/methanol (1:2) solution was added and vortexed. Tubes were agitated vigorously for 40 minutes at 4°C. Chloroform and water (125 $\mu$l) were added sequentially and tubes vortexed after each addition. Tubes were centrifuged at 200 $g$ for 5 minutes at RT and the lower phase transferred into a flat-bottomed 2 ml glass vial (Sigma Aldrich, MO, USA)

using a glass Pasteur pipette. This was dried under nitrogen and stored at 4°C. To prepare samples for LC-MS/MS, lipidomic reconstitution buffer was used.

Once reconstituted, lipid extracts were separated on a Kinetex 1.7 u C18 100 Å column (Phenomenex, CA, USA) using a Thermo Ultimate BioRS HPLC maintained at 45°C. Separated lipids were eluted into a Q Exactive Plus instrument (Thermo Fisher Scientific, MA, USA) and acquired in positive-ion mode. Lipid identification was carried out as in Wills et al.[156]

### 2.2.8 Statistical Analysis

Statistical analyses were performed using GraphPad Prism (GraphPad Software, CA, USA). Data were assumed to have a non-normal distribution and tested accordingly. For statistical analysis of IHC, the percentage of positively stained cells was taken and the appropriate analysis performed on these data. For determination of growth inhibition 50% (GI50) values, data obtained from alamar blue assays were log transformed, normalised to DMSO controls and a curve fitted to the data points.

# Chapter 3

# Resistance to sapatinib is associated with a loss of HER2 and EMT *in vivo*

Loss of HER2 after neoadjuvant or chemotherapy has consistently been shown to correlate with a worse prognosis in patients with HER2-positive breast cancer.[64,65] *In vitro* studies of resistance to HER2-targeted therapies show that loss of HER2 is the result of cancer cells losing their reliance on HER2, instead becoming reliant on other RTKs.[122–124] Understanding the mechanism behind loss of HER2 and reversing it could enable tumours to become resensitised to HER2-targeted therapies.

Several studies have shown that loss of HER2 is associated with EMT in trastuzumab-resistant models *in vitro*.[90,157] These groups, and others, have evidenced a link between EMT and resistance to targeted therapies.[84,89–91,157–159] Furthermore, reversal of EMT restored the epithelial phenotype and sensitivity to targeted therapies.[89,91,158]

Previous research by the Brunton lab[84] showed concurrent loss of HER2 and induction of EMT as a result of the development of acquired resistance to sapatinib. Using tumour fragments derived from MMTV-NIC-PTEN$^{+/-}$, matched vehicle-treated and sapatinib-resistant fragment-derived tumours were developed in FVB/N mice. Half of the fragment-derived tumours made resistant to sapatinib displayed an epithelial phenotype and were phenotypically indistinguishable from vehicle-treated tumours. The remaining resistant fragment-derived tumours displayed a mesenchymal phenotype with loss of HER2.

It is currently unknown if the primary mechanism of resistance was loss of HER2 or EMT induction. Understanding of the mechanism of resistance would allow further research into resensitising tumours and overcoming resistance. Initial comparison and characterisation of sapatinib-resistant tumours can be seen in Creedon et al.[84]

This chapter will therefore explore the following aims:

- Identify the transcriptional regulation of EMT in sapatinib-resistant fragment-derived tumours.
- Clarify if the HER2 loss seen is at the transcriptional or protein level.
- Establish whether HER2 levels are altered by increased EMT.
- Assess if loss of HER2 induces a program of EMT.

## 3.1 Sapatinib-resistant fragment-derived tumours have undergone EMT and lost HER2

Detailed results for this chapter can be found in tables A.1–A.4.

EMT has been demonstrated to confer primary resistance to targeted therapies in HER2-positive breast cancer[158] and EGFR-positive NSCLC,[89] as well as chemoresistance in pancreatic cancer.[160]

Fragment-derived tumours made resistant to sapatinib showed two distinct phenotypes. Half of all sapatinib-resistant fragment-derived tumours had an epithelial morphology also seen in vehicle-treated fragment-derived tumours (fig 3.1 A and B) and had no expression of vimentin (fig 3.1 D and E; staining performed by Dr Helen Creedon), E-cadherin (fig 3.1 G and H; staining performed by Dr Helen Creedon) and HER2 (fig 3.5 A and B; staining performed by Dr Helen Creedon) similar to vehicle-treated fragment-derived tumours. The remaining tumours exhibited a spindle cell morphology associated with a mesenchymal phenotype (fig 3.1 C),[82] gained expression of vimentin (fig 3.1 F) and lost expression of E-cadherin (fig 3.1 I) and HER2 (fig 3.5 C).

### 3.1.1 EMT is maintained by ZEB1 and ZEB2 *in vivo*

To understand the mechanisms driving EMT at the transcriptional level, five EMT-related transcription factors were assessed by IHC. SLUG, SNAIL, TWIST, ZEB1 and ZEB2 are all known to play different roles in the induction and maintenance of EMT, with both distinct and overlapping functions. IHC analysis of these transcription factors revealed significantly increased levels of ZEB1 and ZEB2 in sapatinib-resistant EMT tumours, compared with vehicle-treated and sapatinib-resistant tumours with an epithelial phenotype (fig 3.2 A–H). No difference can be seen in levels of SLUG, SNAIL and TWIST, which were not broadly expressed in any of the tumours (fig 3.2 I–T).

As both ZEB1 and ZEB2 were upregulated in sapatinib-resistant fragment-derived tumours, KM-plotter[161] was interrogated for patients with HER2-positive breast cancer

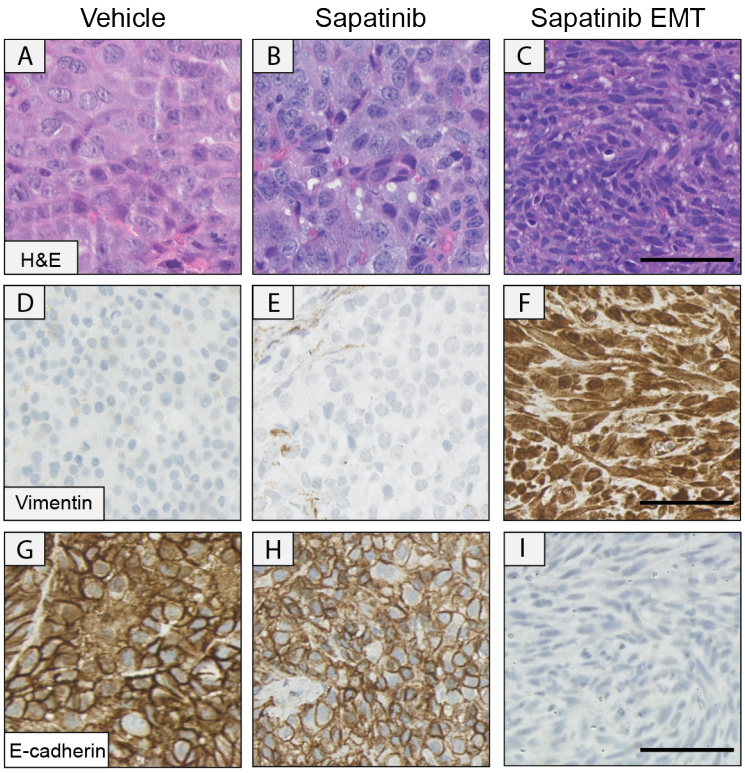


**Figure 3.1. Resistance to sapatinib is associated with epithelial-to-mesenchymal transition (EMT) in fragment-derived tumours. (A–C)** Representative haematoxylin and eosin (H&E) staining of tumours performed on MMTV-NIC-PTEN$^{+/-}$ fragment-derived tumours that had been inserted into the fourth mammary fat pad of FVB/N mice (vehicle: n=9; sapatinib: n=3; sapatinib EMT: n=4). Representative immunohistochemical (IHC) staining of **(D–F)** vimentin and **(G–I)** E-cadherin. Scale bar: 50 $\mu$m. Staining by Dr Helen Creedon.

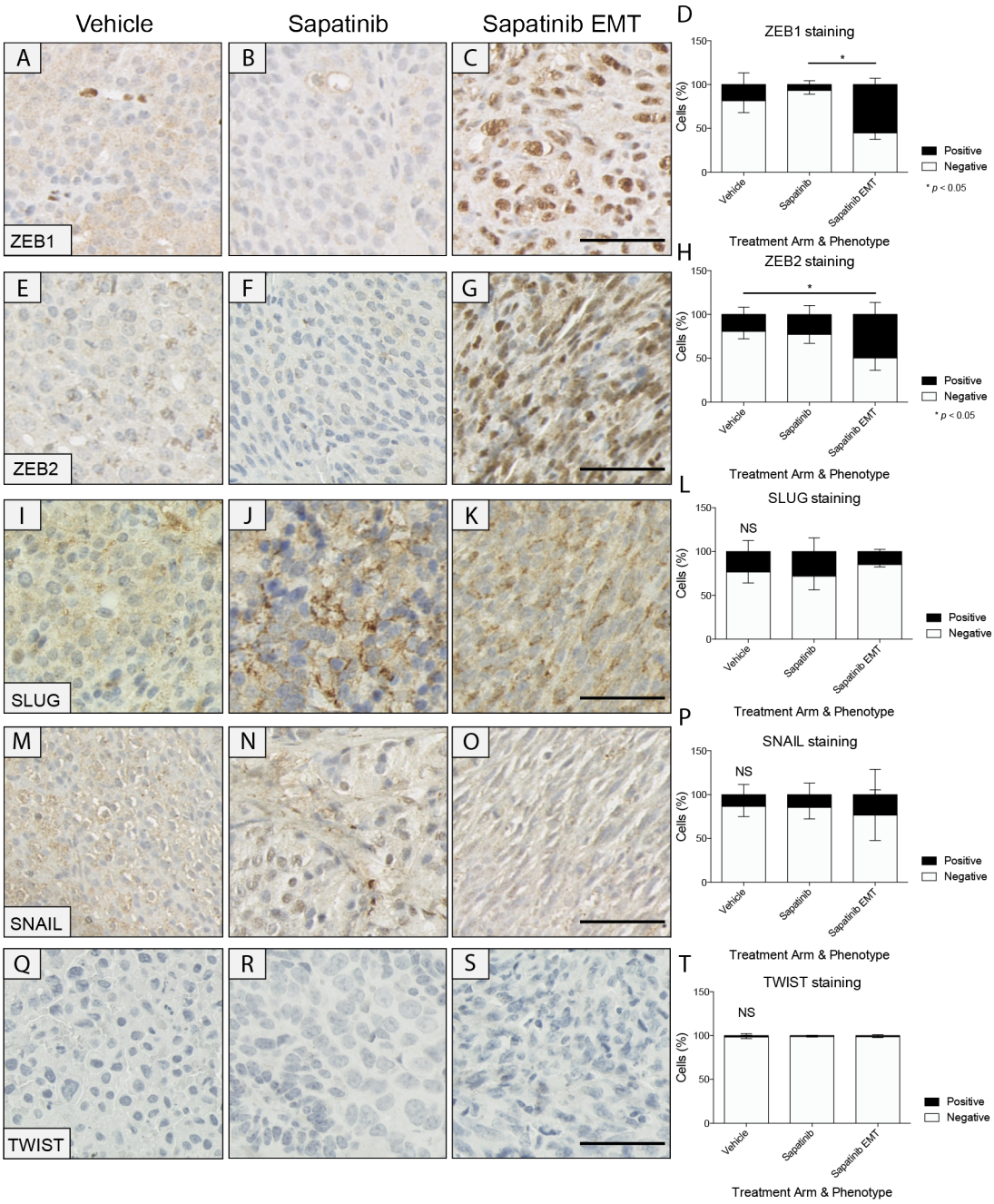


**Figure 3.2. Maintenance of the mesenchymal phenotype is a result of ZEB1 and ZEB2 expression.** Immunohistochemistry (IHC) was performed on sections of MMTV-NIC-PTEN$^{+/-}$ fragment-derived tumours that had been inserted into the fourth mammary fat pad of FVB/N mice. Representative IHC staining of **(A–C)** zinc finger E-box binding homeobox 1 (ZEB1; vehicle: n=8; sapatinib: n=3; sapatinib EMT: n=4), **(E–G)** zinc finger E-box binding homeobox 2 (ZEB2; vehicle: n=6; sapatinib: n=3; sapatinib EMT: n=2), **(I–L)** SLUG (vehicle: n=7; sapatinib: n=3; sapatinib EMT: n=3), **(M–O)** SNAIL (vehicle: n=8; sapatinib: n=3; sapatinib EMT: n=2) and **(Q–S)** TWIST (vehicle: n=5; sapatinib: n=3; sapatinib EMT: n=2). Scale bar: 50 $\mu$m. **(D, H, L, P and T)** Quantification of IHC staining by Definiens Architect. Vehicle was compared with both sapatnib phenotypes. Results presented as mean $\pm$ standard deviation. Kruskal-Wallis, Dunn's post-hoc test, not significant = NS, $p$<0.05=*. Detailed results can be found in table A.1.

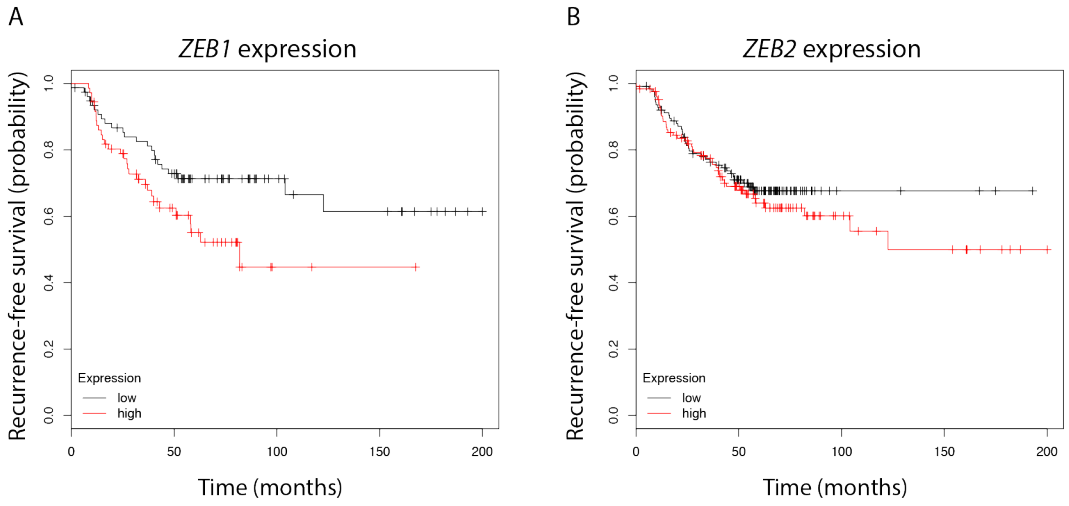


**Figure 3.3. Patients with high expression of *ZEB1* have worse recurrence-free survival.** Survival analysis based on high or low gene expression of **(A)** zinc finger E-box binding homeobox 1 (*ZEB1*) and **(B)** zinc finger E-box binding homeobox 2 (*ZEB2*) in all patients for whom these data were available with human epidermal growth factor receptor 2 (HER2)-positive breast cancer (n=150). Generated using www.kmplot.com.[161]

with high or low *ZEB1* or *ZEB2* expression levels, to ascertain the relevance to human disease.

This showed that patients with high expression of *ZEB1* had worse recurrence-free survival (RFS) than those with low expression (fig 3.3 A; median RFS: low: 44 months; high: 27.4 months; hazard ratio (HR): 1.8; $p$=0.036). However, no significant difference could be seen between patients with high and low expression of *ZEB2* (fig 3.3 B; median RFS: low: 37 months; high: 39 months; HR: 1.19; $p$=0.87).

To establish whether the results from sapatinib-resistant EMT tumours were consistent regarding EMT-related transcription factors and their impact on human disease, KM-plotter was also interrogated for expression levels of *SLUG*, *SNAIL* and *TWIST* from patients with HER2-positive breast cancer. This showed that patients with high levels of *SLUG*, *SNAIL* or *TWIST* had no survival disadvantage when compared with patients with low expression levels of these three genes (fig 3.4 A–C; *SLUG* median RFS: low: 44.17 months; high: 37 months; HR: 1.3; $p$=0.25; *SNAIL* median RFS: low: 40.56 months; high: 39 months; HR: 1.14; $p$=0.57; *TWIST* median RFS: low: 41.69 months; high: 39 months; HR: 1.28; $p$=0.27).

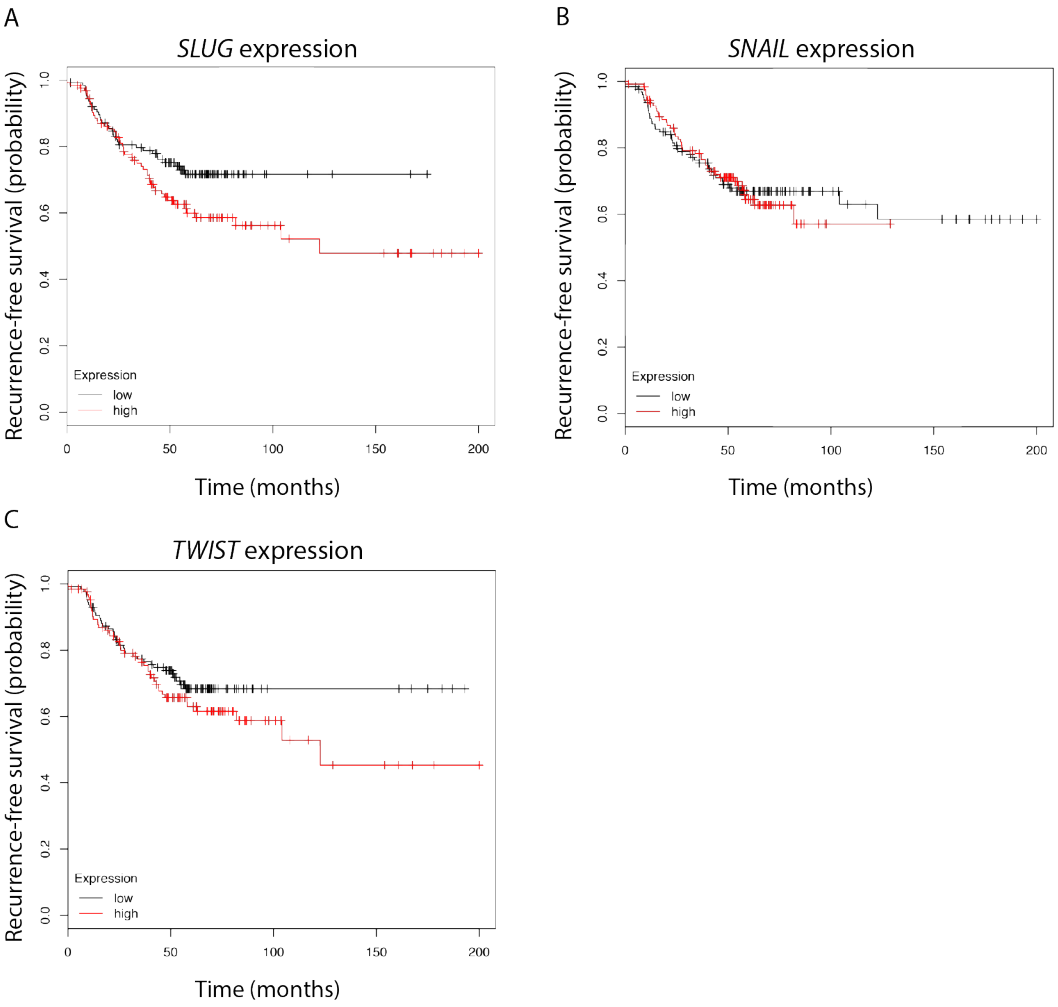


**Figure 3.4. Patients with high expression of *SLUG*, *SNAIL* and *TWIST* have no survival disadvantage.** Survival analysis based on high or low gene expression of **(A)** *SLUG*, **(B)** *SNAIL* or **(C)** *TWIST* in all patients for whom these data were available with human epidermal growth factor receptor 2 (HER2)-positive breast cancer (n=252). Generated using www.kmplot.com.[161]

### 3.1.2 Sapatinib-resistant fragment-derived tumours with EMT have no detectable HER2 protein

HER2 was assessed by western blotting and quantitative PCR (qPCR) to look for differences at the protein and transcript level, in order to better understand and confirm the loss of HER2 in half of the sapatinib-resistant fragment-derived tumours. This confirmed the loss of HER2 at the protein level, with no band detected in sapatinib-resistant EMT tumours, despite detection of HER2 in both the vehicle-treated and sapatinib-resistant epithelial fragment-derived tumours (fig 3.5 D).

QPCR analysis of mRNA from fragment-derived tumours showed significantly less *Erbb2* expression in sapatinib-resistant fragment-derived tumours which had undergone EMT, compared with vehicle-treated fragment-derived tumours. Sapatinib-resistant fragment-derived tumours with an epithelial morphology did not have a significant reduction in transcript levels, but there was a trend towards lower expression which was not significantly different from vehicle-treated fragment-derived tumours (fig 3.5 E).

## 3.2 Resistance *in vitro* is not associated with loss of HER2 or induction of EMT

To understand the relationship between HER2 loss and EMT, an *in vitro* model of resistance was developed. SKBR3 HER2-positive breast cancer cells were exposed to escalating doses of sapatinib or lapatinib. Once cells began to grow through the maximum drug concentration, they were classed as resistant. This was repeated, giving rise to two resistant cell lines per drug.

### 3.2.1 SKBR3 cells treated with escalating doses of sapatinib or lapatinib are resistant

To confirm resistance to sapatinib and lapatinib, the GI50 values of the cell lines maintained in each drug were determined (table 3.1). Resistant cell lines had higher

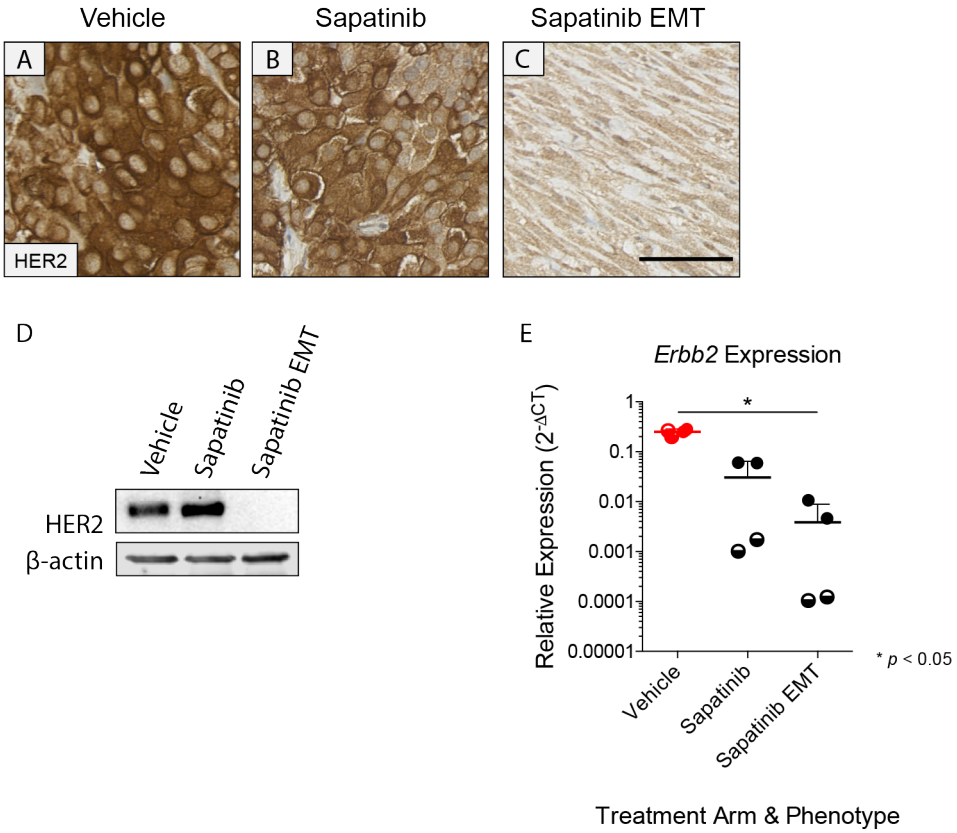


**Figure 3.5. Resistance to sapatinib is associated with EMT and loss of HER2 in fragment-derived tumours.** Representative immunohistochemical (IHC) staining of **(A–C)** human epidermal growth factor receptor 2 (HER2) performed on MMTV-NIC-PTEN$^{+/-}$ fragment-derived tumours that had been inserted into the fourth mammary fat pad of FVB/N mice. Scale bar: 50 $\mu$m. Staining by Dr Helen Creedon. **(D)** Representative western blot analysis of HER2 from two biological repeats. *B*-actin was used as a loading control. **(E)** Quantitative PCR analysis of the gene encoding HER2, erythroblastic oncogene B (*Erbb2*) mRNA transcript levels (vehicle: n=2; sapatinib: n=2; sapatinib EMT: n=2). Two primers targeting different regions of *Erbb2* were used and the results pooled. Results from the same tumour are grouped by symbol. Results presented as mean + standard deviation. Kruskal-Wallis test, Dunn's post-hoc test, $p$<0.05=*.

**Table 3.1.** GI50 values to sapatinib and lapatinib of parental SKBR3 cells and SKBR3 cells made resistant to sapatinib or lapatinib

| | **Drug** | |
|---|---|---|
| **Cell Line** | Sapatinib (M) | Lapatinib (M) |
| SKBR3 | $5.83 \times 10^{-12}$ | $1.12 \times 10^{-12}$ |
| SKBR3 SapR-A | $>3 \times 10^{-4}$ | $>3 \times 10^{-6}$ |
| SKBR3 SapR-B | $>3 \times 10^{-4}$ | $>3 \times 10^{-6}$ |
| SKBR3 LapR-A | $>3 \times 10^{-4}$ | $>3 \times 10^{-6}$ |
| SKBR3 LapR-B | $>3 \times 10^{-4}$ | $>3 \times 10^{-6}$ |

GI50 values than parental SKBR3 cells; in all cases their GI50 values could not be accurately calculated as they were greater than the highest assay concentration.

SKBR3 sapatinib-resistant and lapatinib-resistant cell lines are at least 10,000,000 times and 3,000,000 times more resistant to sapatinib and lapatinib, respectively, compared with parental SKBR3 cells. All cell lines are cross-resistant to sapatinib and lapatinib, to the same extent as cells made resistant to each drug (table 3.1). This indicates that all resistant cell lines have a mechanism of resistance that is not specific to sapatinib and lapatinib and has the potential to be applicable across all HER2-targeted tyrosine kinase inhibitors.

Resistant cell lines were maintained in either 0.67 $\mu$M sapatinib, or 5 $\mu$M lapatinib. These concentrations are lower than plasma concentrations identified in phase I clinical trials for sapatinib (240 mg oral dose: $C_{max}$: 1.345 $\mu$M; Tjulandin et al.[61]) and similar to those for lapatinib (1250 mg oral dose: $C_{max}$: 3.804–4.371 $\mu$M; Burris et al.[162], Simonelli et al.[163]).

Plasma concentrations of lapatinib are a poor indication of tumour concentrations, which have been shown to be 6 to 9 times higher in tumours.[164] The concentrations of sapatinib and lapatinib used have been shown to inhibit phospho-HER2 in SKBR3 cells,[165] as such they were deemed sufficient concentrations to class lines as resistant. Moreover, relevant lapatinib concentrations were not reached as the drug precipitates *in vitro* at higher concentrations.

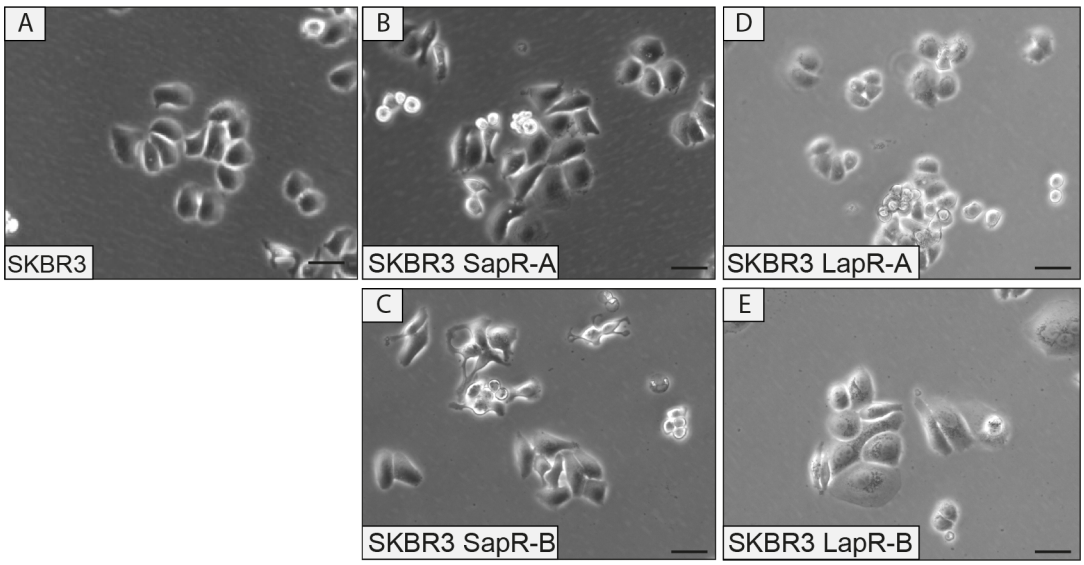


**Figure 3.6. Resistant SKBR3 cells are morphologically similar to parental SKBR3 cells.** SKBR3 human epidermal growth factor receptor 2 (HER2)-positive breast cancer cell line was exposed to increasing doses of sapatinib or lapatinib until cells were no longer inhibited. Cells were cultured in drug. Representative phase contrast images of **(A)** parental SKBR3 cells, **(B–C)** sapatinib-resistant (SapR-A/B) cells and **(D–E)** lapatinib-resistant (LapR-A/B) cells. Scale bar: 50 $\mu$m.

### 3.2.2 Sapatinib-resistant and lapatinib-resistant SKBR3 cells have no EMT phenotype

To assess if any morphological changes had taken place in response to exposure to sapatinib or lapatinib, phase contrast images of the cells were taken and compared (fig 3.6 A-E). All resistant cell lines maintained their epithelial morphology and no evidence of a spindle cell morphology, expected if EMT had occurred, could be seen.

EMT is characterised by increased levels of ZEB1, ZEB2, SLUG and SNAIL driving a program of transcriptional regulation, alone or in concert with each other.[82] Because of this, the transcript level of these genes was assessed by qPCR. No transcript could be detected for any of the four genes in parental SKBR3 or the four resistant lines (fig 3.7 A).

Increased proliferation and motility are key characteristics of EMT.[82] To determine whether the resistant lines had acquired these characteristics, proliferation and migration assays were carried out. Sapatinib-resistant and lapatinib-resistant cell lines showed significantly decreased proliferation when compared with parental SKBR3 cells (fig 3.8 A). Only SKBR3 LapR-B showed no difference in proliferation compared with SKBR3

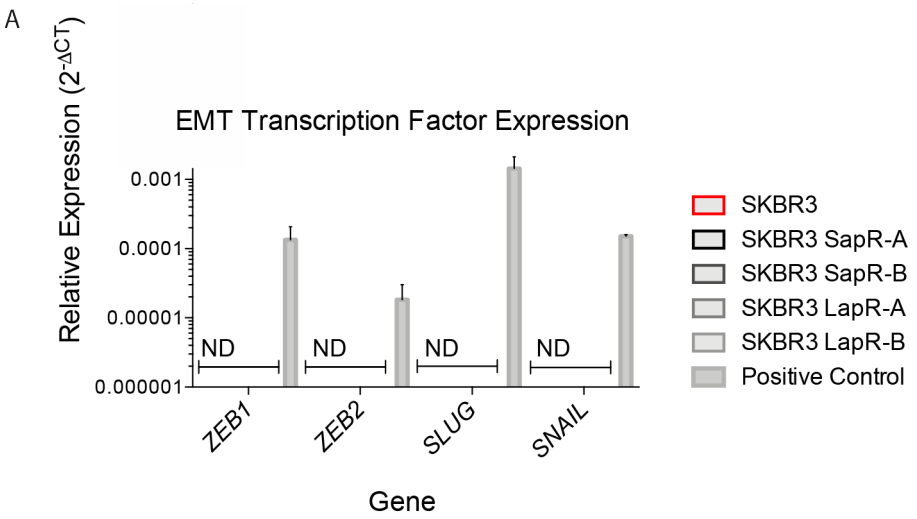


**Figure 3.7. Resistant SKBR3 cells have no detectable EMT-related transcription factors.** **(A)** Quantitative PCR analysis of parental and resistant SKBR3 cells of zinc finger E-box binding homeobox 1 (*ZEB1*), zinc finger E-box binding homeobox 2 (*ZEB2*), *SLUG* and *SNAIL* from three biological repeats. MDA-MB-231 cells were used as positive control. Results presented as mean + standard deviation. Not detected = ND.

cells. Parental SKBR3 cells showed a similar migratory capability compared with SapR-A, LapR-A and LapR-B cells. However, SapR-B cells had significantly greater migration when compared with SKBR3 cells (fig 3.9 A). Cells from all lines migrated collectively, rather than as single cells (fig 3.10 A–E).

A program of EMT results in decreased E-cadherin and increased vimentin.[82] SKBR3 cells have a homozygous deletion in the *CHD1* gene which encodes E-cadherin,[166] as such we were unable to look for changes in the expression of E-cadherin as a consequence of EMT. Immunofluorescence was undertaken to look for expression of vimentin. No expression of vimentin could be seen in the parental SKBR3 or resistant lines (fig 3.11 A and C–F), despite being detected in positive controls (fig 3.11 B).

### 3.2.3 Sapatinib-resistant and lapatinib-resistant SKBR3 cells have no loss of HER2

Resistant cell lines were assessed for any loss of HER2, as seen in the sapatinib-resistant fragment-derived tumours which had undergone EMT. No loss of HER2 could be seen in any of the resistant cell lines, but SKBR3 SapR-A showed decreased levels of HER3 by western blotting (fig 3.12 A). Despite being cultured in the presence of sapatinib,

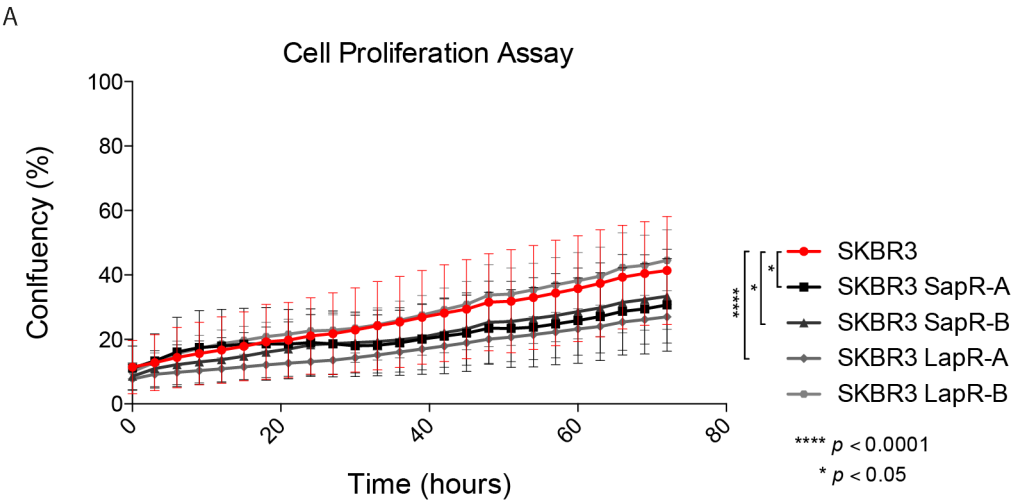


**Figure 3.8. Resistant SKBR3 cells do not have increased rates of proliferation. (A)** Rate of cell proliferation was measured in parental and resistant SKBR3 cells using the IncuCYTE ZOOM over a 72-hour period. Results presented as mean ± standard deviation, from three biological repeats. Friedman test, Dunn's post-hoc test, $p$<0.05=*, $p$<0.0001=****. Detailed results can be found in table A.2.

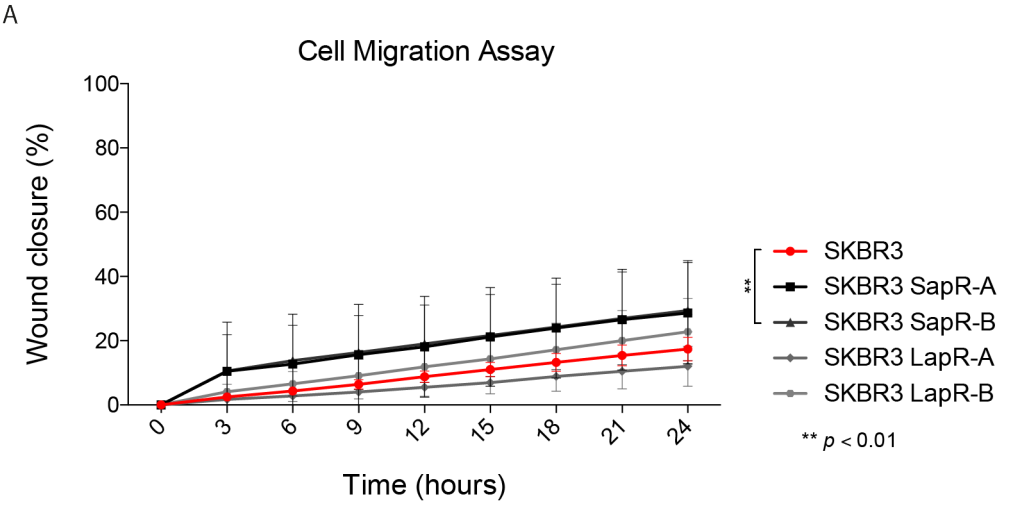


**Figure 3.9. Resistant SKBR3 cells migrate at a similar rate as SKBR3 cells. (A)** Rate of wound closure of parental and resistant SKBR3 cells was measured using the IncuCYTE ZOOM over a 24-hour period. Results presented as mean ± standard deviation, from three biological repeats. Friedman test, Dunn's post-hoc test, $p$<0.01=**. Detailed results can be found in table A.2.

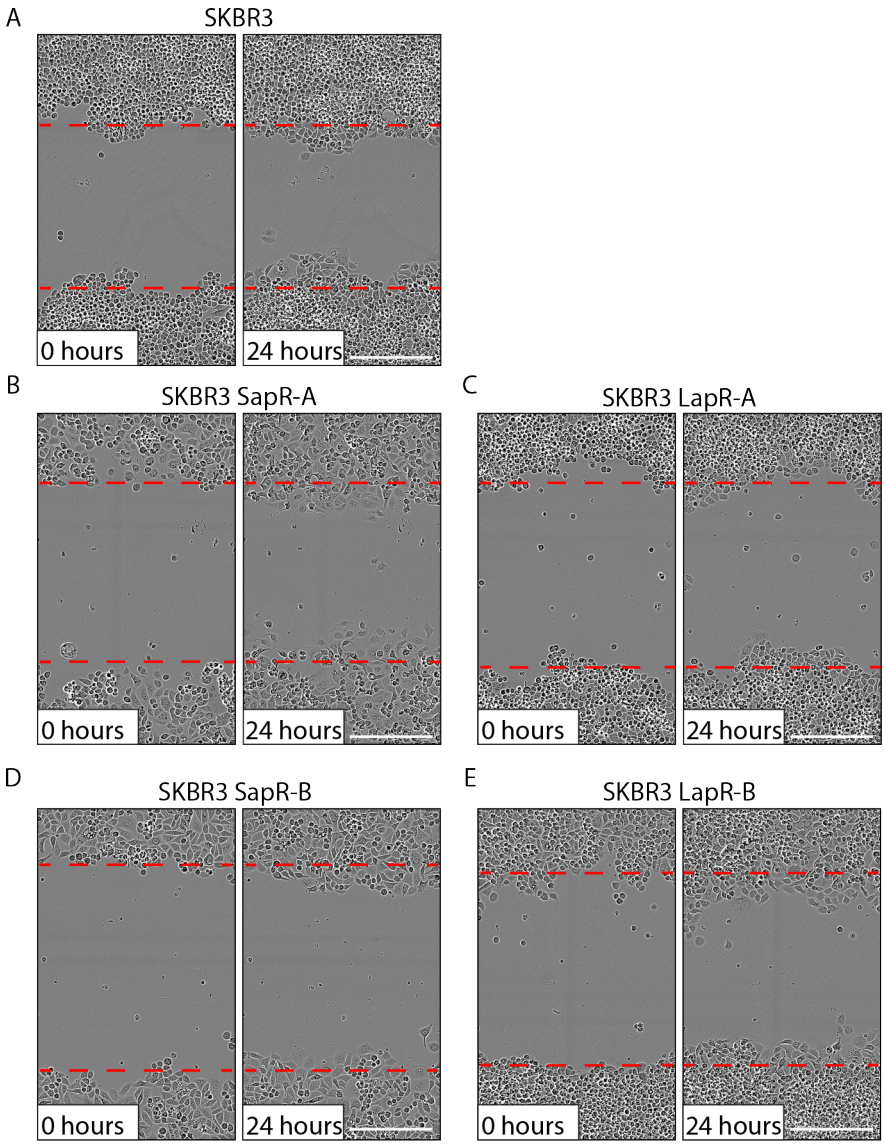


**Figure 3.10. Resistant SKBR3 cells migrate collectively.** Representative images, from three biological repeats, at 0 and 24 hours of **(A)** SKBR3, **(B, D)** SKBR3 sapatinib resistant (SapR-A and SapR-B), **(C, E)** SKBR3 lapatinib-resistant (LapR-A and LapR-B) cells. Scale bar: 300 $\mu$m. Red dashed lines represent the edge of the wound.

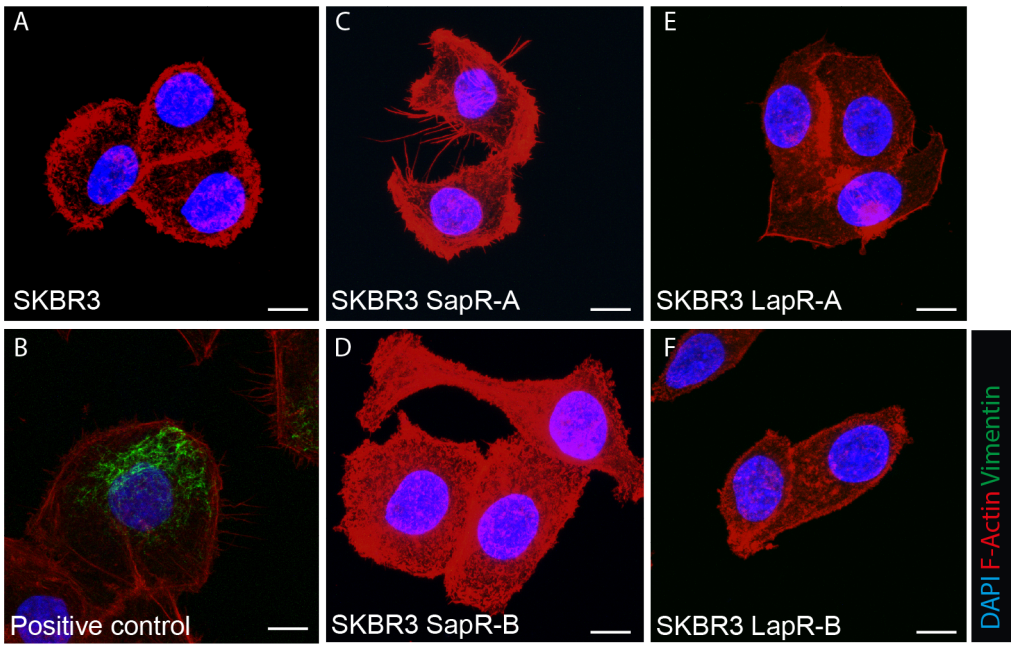


**Figure 3.11. Resistant SKBR3 cells have no expression of vimentin.** Representative images, from three biological repeats, of immunofluorescence staining of vimentin in **(A)** SKBR3 cells, **(B)** JIMT-1 positive-control cells, **(C–D)** sapatinib-resistant (SapR-A and SapR-B) and **(E–F)** lapatinib-resistant (LapR-A and LapR-B) SKBR3 cells. Images displayed as maximum intensity projection of Z stack. Scale bar: 10 $\mu$m.

HER2 and HER3 remained phosphorylated in both SKBR3 SapR-A and SapR-B, with levels of phospho-HER3 similar in resistant lines to that seen in parental SKBR3 cells.

This was not seen in LapR-A or LapR-B cells, which both had undetectable phospho-HER2 and phospho-HER3, despite lapatinib targeting only HER2 and EGFR. Total and phospho-EGFR remained undetectable in all cell lines. QPCR of all cell lines revealed no significant differences in the level of *ERBB2* transcript between parental SKBR3 and the resistant cell lines (fig 3.12 B).

Although HER2 protein levels were unaltered in the resistant cells when analysed by western blot, HER2 and HER3 phosphorylation was unaffected in SapR-A and SapR-B cells. To ascertain the cell surface expression of HER2 in the resistant cells, FACS was performed using an antibody targeting an extracellular epitope of HER2.

Unstained cells showed similar peak distribution, although LapR-A and LapR-B had higher levels of autofluorescence, caused by intracellular lapatinib.[167] Because of this, lapatinib-resistant cells were gated differently than SKBR3 and sapatinib-resistant cells. FACS of HER2-APC stained cells showed that parental SKBR3 cells had similar levels

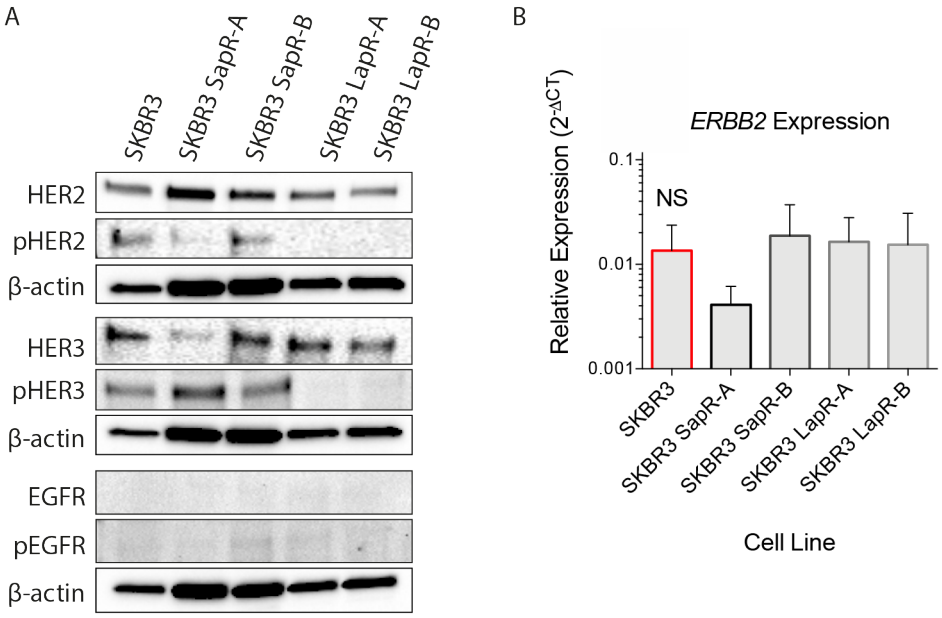


**Figure 3.12. Resistant SKBR3 cells show no loss of HER2. (A)** Representative western blots, from three biological repeats, of total and phospho-human epidermal growth factor receptor 2 (HER2), HER3 and epidermal growth factor receptor (EGFR). *B*-actin was used as a loading control. **(B)** Quantitative PCR analysis of the gene encoding HER2, erythroblastic oncogene B (*ERBB2*) transcript levels. Results presented as mean + standard deviation, from three biological repeats. Kruskal-Wallis test, Dunn's post-hoc test, not significant=NS. Detailed results can be found in table A.2.

of cells negative for cell surface HER2 compared with resistant sapatinib and lapatinib lines (fig 3.13 A–F).

## 3.3 Expression of *ZEB1* does not reduce levels of HER2

As the program of EMT *in vivo* was maintained by ZEB1, SKBR3 cells were transiently transfected with a plasmid containing an empty vector or *ZEB1* to induce EMT, as stable transfection is toxic (S Brabletz, January 2016, personal communication). Five days after transfection, *ZEB1*-overexpressing cells did not have a significantly different morphology compared with empty vector cells (fig 3.14 A and B). Despite this, SKBR3 *ZEB1*-overexpressing cells had a significant increase in levels of *ZEB1* transcript, which was undetectable in SKBR3 cells containing an empty vector (fig 3.14 C). No expression of *ZEB2*, *SLUG* and *SNAIL* could be detected in either *ZEB1*-overexpressing cells or SKBR3 empty vector cells.

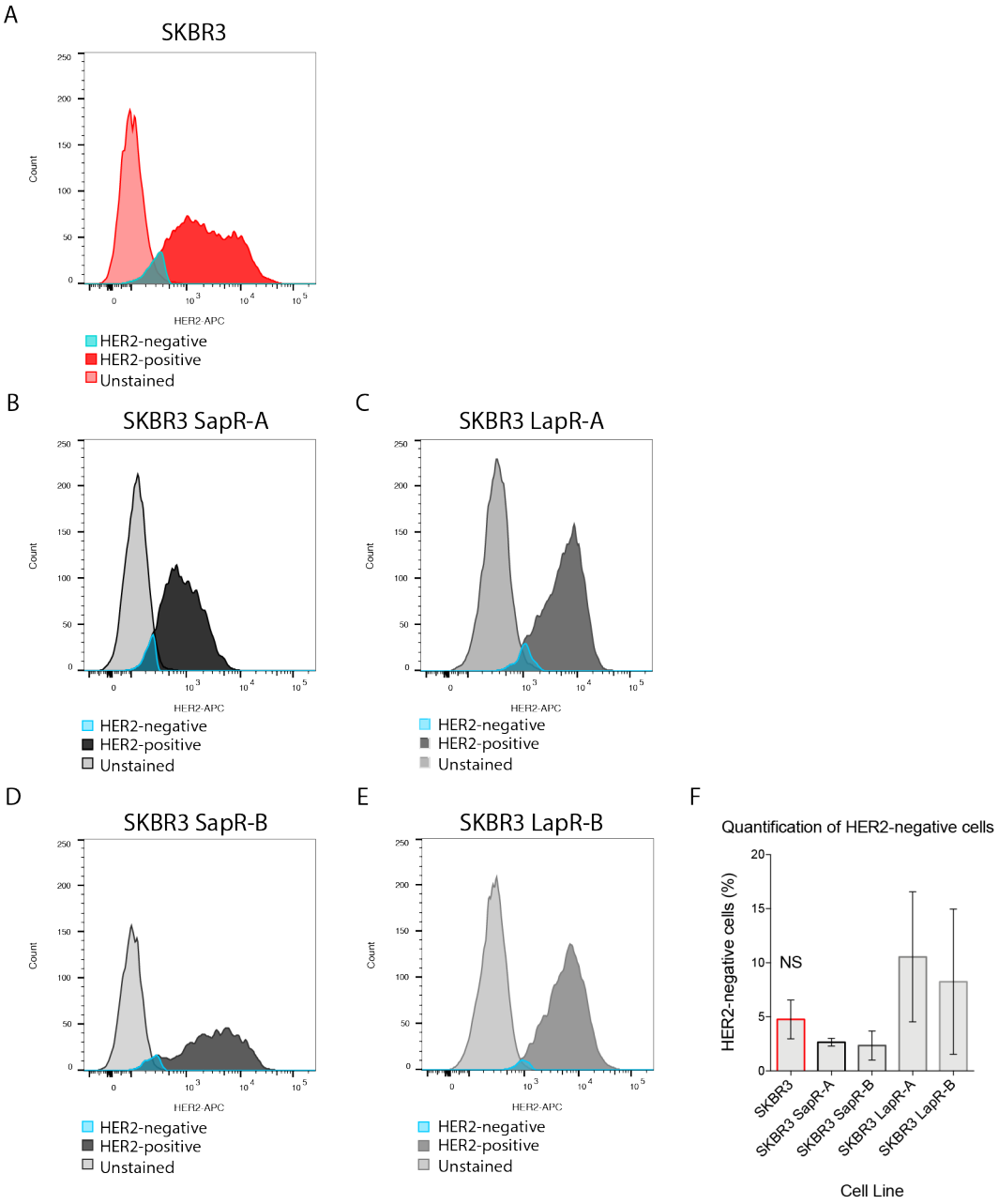


**Figure 3.13. Resistant SKBR3 cells have similar levels of cells negative for cell surface HER2.** Representative fluorescent activated cell sorting (FACS) plots of unstained and human epidermal growth factor receptor 2 (HER2)-stained **(A)** SKBR3 **(B and D)** sapatinib-resistant (SapR-A and SapR-B) cells and **(C and E)** lapatinib-resistant (LapR-A and LapR-B) cells. **(F)** Quantification of HER2-negative cells in parental, sapatinib-resistant or lapatinib-resistant SKBR3 cell lines. Results presented as mean ± standard deviation, from two biological repeats. Kruskal-Wallis test, Dunn's post-hoc test, not significant = NS. Detailed results can be found in table A.2.

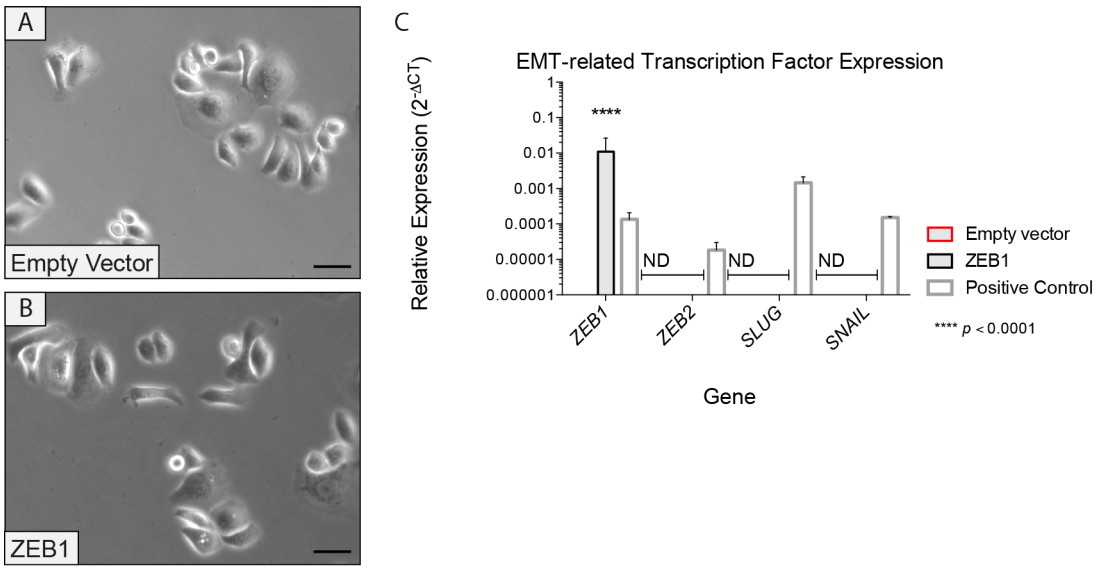


**Figure 3.14. SKBR3 cells overexpressing *ZEB1* do not have a mesenchymal morphology.** Representative phase contrast images of **(A)** SKBR3 cells containing empty vector and **(B)** SKBR3 zinc finger E-box binding homeobox 1 (*ZEB1*)-overexpressing cells. Scale bar: 50 $\mu$m. **(C)** Quantitative PCR analysis, from three biological repeats, of *ZEB1*, *ZEB2*, *SLUG* and *SNAIL* in SKBR3 cells containing empty vector or overexpressing *ZEB1*. MDA-MB-231 cells were used as positive control. Results presented as mean + standard deviation. Multiple *t*-tests, Sidak-Bonferroni correction, not detected = ND, $p$<0.0001=****.

To see if levels of HER2 were affected by the increase in *ZEB1*, cells were assessed by qPCR and western blot for HER2 and phospho-HER2. QPCR revealed no significant difference in levels of *ERBB2* transcript between empty vector cells and *ZEB1*-overexpressing cells (fig 3.15 A). Furthermore, no significant reduction could be seen in levels of HER2, or phospho-HER2 by western blot in *ZEB1*-overexpressing cells (fig 3.15 B-D).

## 3.4 Loss of HER2 does not induce a full program of EMT

As no loss of HER2 was observed in resistant SKBR3 lines and expression of *ZEB1* did not result in loss of HER2, we then asked if loss of HER2 was sufficient to induce EMT. SKBR3 cells were stably transfected with either non-target or *ERBB2* shRNA.

To see if loss of HER2 had any morphological effect on the cells, phase contrast images were taken and compared. These images showed that cells containing *ERBB2* shRNA did not have a cobblestone morphology as distinct as non-target shRNA cells (fig 3.16 A and B). However, they did still form cell-cell contacts and did not have an overt spindle cell morphology.

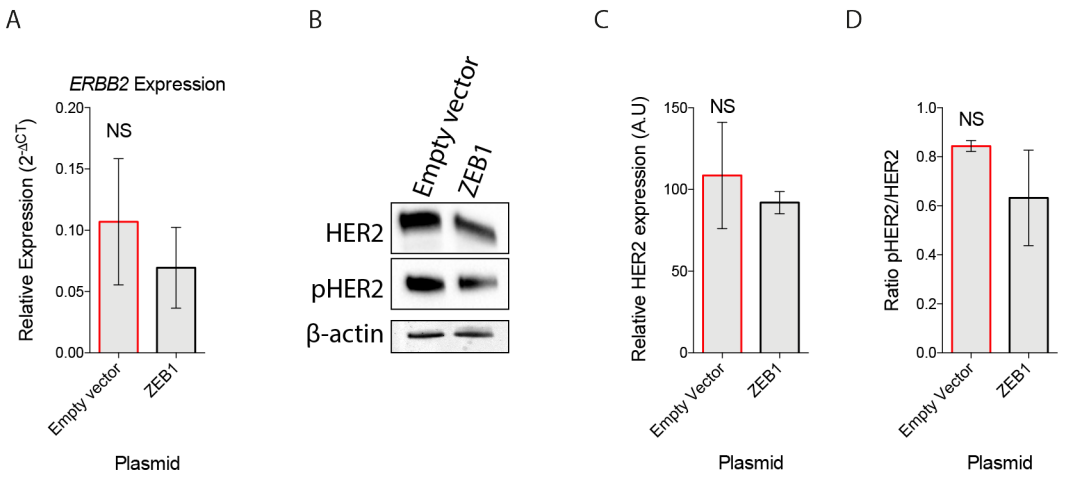


**Figure 3.15. SKBR3 cells overexpressing *ZEB1* do not have a reduction in HER2 or phospho-HER2 levels. (A)** Quantitative PCR analysis, from three biological repeats, of the gene encoding HER2, erythroblastic oncogene B (*ERBB2*) in SKBR3 cells containing empty vector or overexpressing zinc finger E-box binding homeobox 1 (*ZEB1*). Results presented as mean ± standard deviation (SD). Mann-Whitney test, not significant= NS. **(B)** Representative western blot analysis, from three biological repeats, of HER2 and phospho-HER2. *B*-actin was used as a loading control. **(C)** Quantification of HER2 protein expression (arbitrary unit: A.U), normalised to $\beta$-actin. Results presented as mean ± SD. Mann-Whitey test, not significant = NS. **(D)** Quantification of phospho-HER2:HER2 ratio, normalised to $\beta$-actin. Results presented as mean ± SD. Mann-Whitney test, not significant = NS. Detailed results can be found in table A.3.

To confirm successful gene silencing, levels of HER2 were assessed by western blotting and qPCR. Other HER family members were also assessed to see if there had been a switch to utilising other RTKs in the same family. Assessment of HER family members by western blot revealed no detectable HER2 or phospho-HER2 in *ERBB2* shRNA treated cells (fig 3.16 C). Analysis by qPCR showed a significant reduction in the transcript level of *ERBB2* (fig 3.16 D).

As a concurrent loss of HER3 and phospho-HER3 could be seen in *ERBB2* shRNA cells by western blotting (fig 3.16 C), qPCR was performed to check if the *ERBB2*-targeted shRNA was having off-target effects on *ERBB3*. This showed no reduction in *ERBB3* transcript levels (fig 3.16 D).

To determine if loss of HER2 resulted in a program of EMT, SKBR3 cells treated with non-target or *ERBB2* shRNA were analysed by qPCR for EMT-related transcription factors. Both non-target and *ERBB2* shRNA cells showed similar levels of *ZEB2* and *SNAIL* (fig 3.17 A). However, *ERBB2* shRNA-treated cells had significantly increased *ZEB1* and *SLUG* transcript levels (fig 3.17 A). These results indicate that loss of HER2 has had some effect in increasing mesenchymal properties in SKBR3 cells.

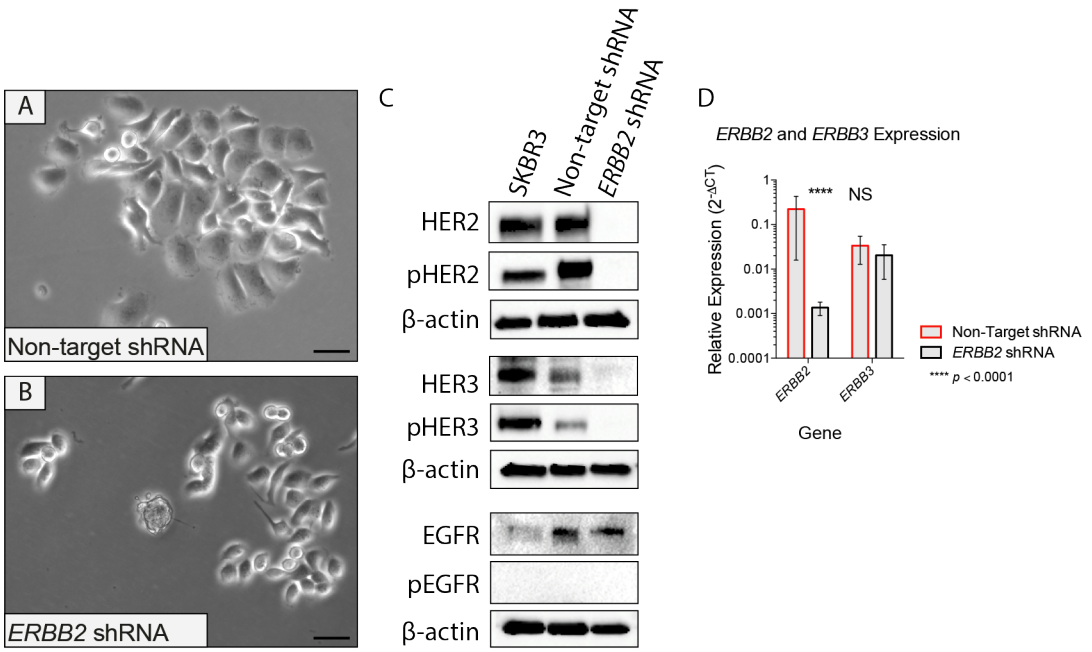


**Figure 3.16. Loss of HER2 does not change cell morphology, or reliance on other HER family members.** Representative phase contrast images of **(A)** non-target shRNA and **(B)** *ERBB2* shRNA treated cells. Scale bar: 50 $\mu$m. **(C)** Representative western blot analysis, from three biological repeats, of total and phospho-human epidermal growth factor receptor 2 (HER2), HER3 and epidermal growth factor receptor (EGFR) in SKBR3 cells treated with non-target shRNA, *ERBB2* shRNA or untreated. *B*-actin was used as a loading control. **(D)** Representative qPCR analysis, from three biological repeats, of *ERBB2* and *ERBB3* levels in SKBR3 cells treated with non-target shRNA or *ERBB2* shRNA. Results presented as mean $\pm$ standard deviation. Multiple two-tailed *t*-tests, Sidak-Bonferroni correction, not significant = NS, $p$<0.0001=****. Detailed results can be found in table A.4.

Cells that have undergone EMT are more proliferative, migratory and invasive.[82] To see whether *ERBB2* shRNA cells have these characteristics, proliferation and migration assays were used. This revealed that *ERBB2* shRNA cells proliferated significantly less than non-target shRNA cells (fig 3.18 A). However, *ERBB2* shRNA cells were significantly more migratory than non-target shRNA cells (fig 3.19 A). Both non-target and *ERBB2* shRNA cells moved collectively to close the wound (fig 3.19 B).

Vimentin is the main cytoskeletal protein in mesenchymal cells and is used as a marker of cells that have undergone EMT.[82] To identify any increase in cells expressing vimentin, immunofluorescence was used. Non-target and *ERBB2* shRNA cells had similar levels of vimentin (fig 3.20 A and B) when assessed by immunofluorescence. However, previous analysis of parental SKBR3 cells and resistant lines showed no expression of vimentin (fig 3.11). As vimentin is present in non-target and *ERBB2* shRNA lines, it may be due to the transfection process.

A

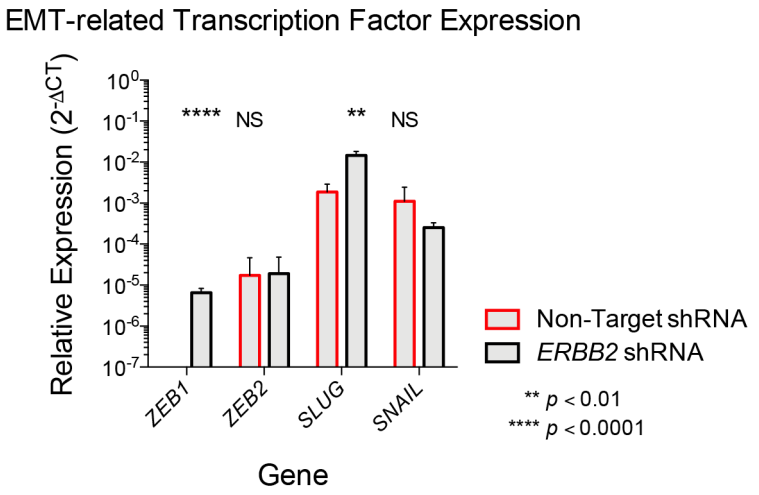


**Figure 3.17. Loss of HER2 alters expression of some EMT-related transcription factors.** **(A)** Quantitative PCR analysis, from three biological repeats, of zinc finger E-box binding homeobox 1 (*ZEB1*), *ZEB2*, *SLUG* and *SNAIL* in SKBR3 cells treated with *ERBB2* or non-target shRNA. Results presented as mean + standard deviation. Multiple two-tailed *t*-tests, Sidak-Bonferroni correction, not significant = NS, $p$<0.01=**, $p$<0.0001=****.Detailed results can be found in table A.4.

A

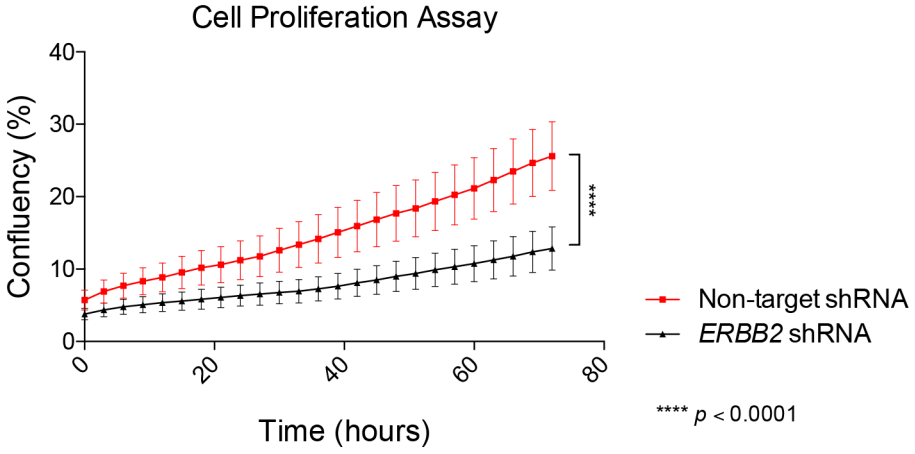


**Figure 3.18. Loss of HER2 reduces proliferation. (A)** Rate of cell proliferation of SKBR3 cells treated with non-target shRNA or *ERBB2* shRNA was measured using the IncuCyte ZOOM over a 72-hour period, from three biological repeats. Results presented as mean ± standard deviation. Two-tailed Wilcoxon matched-pairs signed-rank test, $p$<0.0001=****. Detailed results can be found in table A.4.

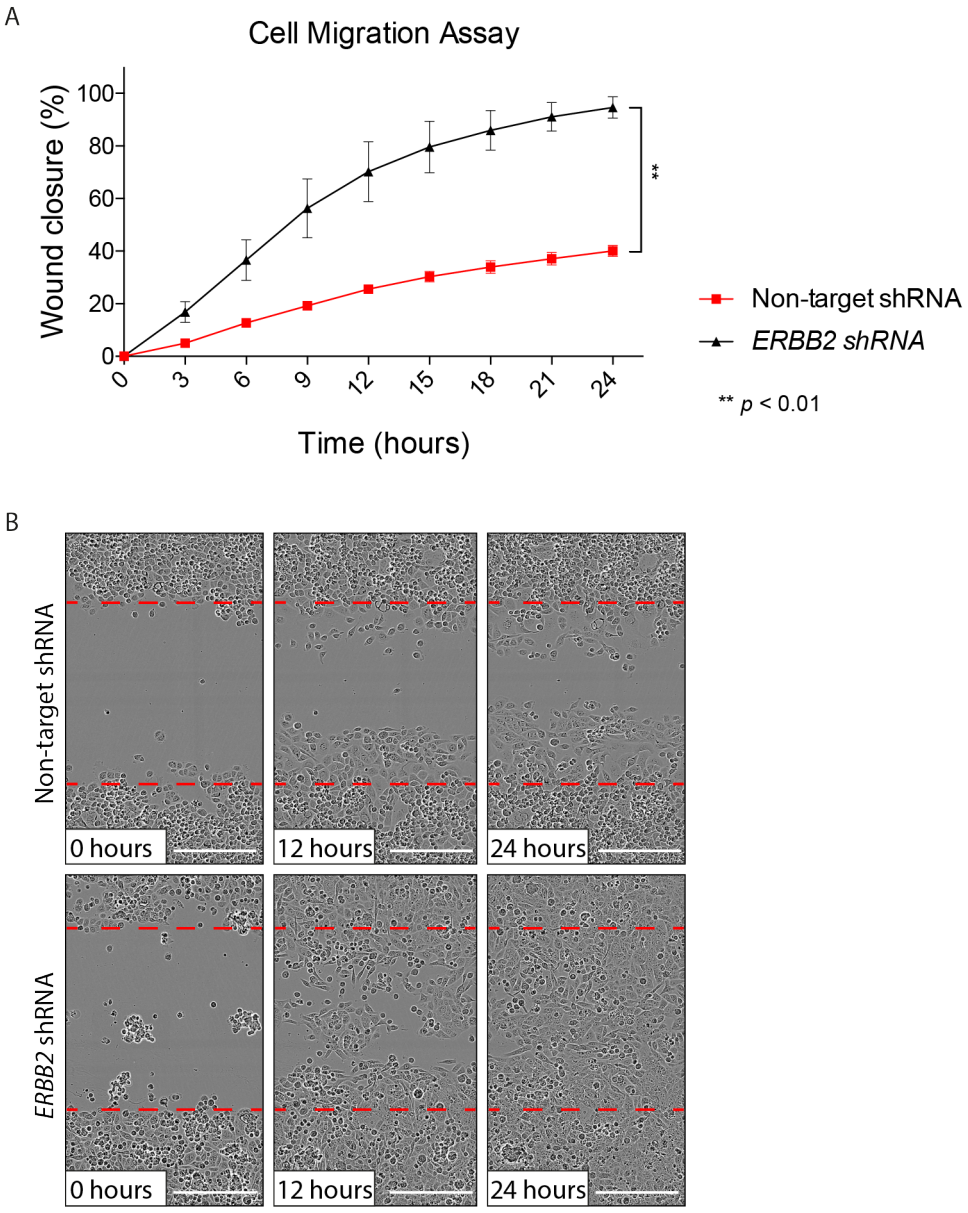


**Figure 3.19. Loss of HER2 increases migratory capacity.** SKBR3 human epidermal growth factor receptor 2 (HER2)-positive breast cancer cell line was treated with shRNA targeting the gene encoding HER2, erythroblastic oncogene B (*ERBB2*) or a non-target control shRNA. **(A)** Rate of wound closure was measured using the IncuCYTE ZOOM over a 24-hour period, from three biological repeats. Results presented as mean $\pm$ standard deviation. Two-tailed Wilcoxon matched-pairs signed-rank test, $p$<0.01=**. **(B)** Representative images at 0, 12 and 24 hours from non-target and *ERBB2* shRNA. Scale bar: 300 $\mu$m. Red dashed lines represent the edge of the wound. Detailed results can be found in table A.4.

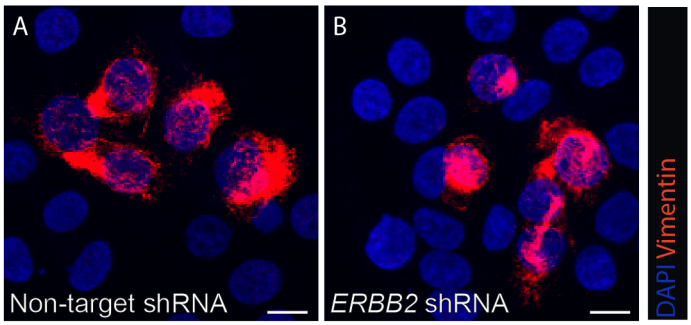


**Figure 3.20. Loss of HER2 does not increase the level of vimentin or N-cadherin.** SKBR3 human epidermal growth factor receptor 2 (HER2)-positive breast cancer cell line was treated with shRNA targeting the gene encoding HER2, erythroblastic oncogene B (*ERBB2*) or a non-target control shRNA. Representative immunofluorescence staining, from three biological repeats, of vimentin in SKBR3 cells treated with **(A)** non-target shRNA or **(B)** *ERBB2* shRNA. Images displayed as maximum intensity projection of Z stack. Scale bar: 10 $\mu$m.

## 3.5 Discussion

Previous work by Creedon et al.[84] evidenced a link between EMT and loss of HER2 in a fragment-derived tumour mouse model in response to the development of sapatinib resistance. This *in vitro* analysis evidences that short-term overexpression of ZEB1 alone is not sufficient to result in a loss of HER2 and that loss of HER2 is not sufficient to induce a full program of EMT, but was able to give rise to some mesenchymal properties.

### 3.5.1 ZEB1 and ZEB2 maintained the mesenchymal phenotype in sapatinib-resistant fragment-derived tumours

Increased ZEB1 and ZEB2 can be seen in sapatinib-resistant tumours that had undergone EMT while other EMT-associated transcription factors were unaltered (fig 3.2 A–H). This indicates that ZEB1 and ZEB2 are required for EMT in these resistant tumours. However, tumours were collected at the time of sacrifice, as such it is unclear if EMT was initially driven and then maintained by ZEB1 and ZEB2, or whether other EMT transcription factors played a role in the initiation of EMT.

Transcriptional regulation of EMT can be the result of many different cellular pathways. In the MMTV-NIC mouse model, tumour-initiating, or stem, cells have increased TGF-$\beta$ signalling and EMT.[168] Increased signalling through the TGF-$\beta$ pathway can result in decreased expression of miR-200 family members and a loss of inhibition at the promoter regions of *ZEB1* and *ZEB2* allowing them to be transcribed.[169,170] Thus, the increase in ZEB1 and ZEB2 could be indicative of a higher proportion of tumour stem cells within the sapatinib-resistant EMT tumours, compared with the epithelial sapatinib-resistant tumours.

It is interesting to note that no significant difference could be seen in levels of nuclear ZEB1 between vehicle-treated and sapatinib-resistant tumours with an epithelial or mesenchymal phenotype, but a significant difference could be seen between the two resistant tumour phenotypes (fig 3.2 A–D). Analysis of ZEB1 staining in vehicle-treated tumours shows that the percentage of ZEB1-positive cells was between that seen in sapatinib-resistant epithelial and mesenchymal tumours.

The variation in ZEB1 expression in the vehicle-treated tumours could be indicative of heterogeneity within the implanted fragments. If two populations ($ZEB1^{high}$ and $ZEB1^{low}$) are present in the implanted tumours, $ZEB1^{high}$ may give a selective advantage in some circumstances, resulting in mesenchymal $ZEB1^{high}$ and epithelial $ZEB1^{low}$ tumours. Secretion of pro- or anti-EMT factors (fig 3.21) by stromal cell populations in different tumour regions may be driving the selection of the epithelial and mesenchymal phenotypes seen in sapatinib-resistant tumours.[83]

ZEB1 expression has been shown to confer resistance to radio-, chemo-, and targeted therapies.[85,171,172] This is consistent with our data which showed patients with high gene expression of *ZEB1* have worse RFS than patients with lower levels (fig 3.3 A).[161]

Published data[85,171,172] and the patient data presented here (fig 3.3 A) indicate that ZEB1 is a key transcription factor controlling a mesenchymal phenotype and therapy resistance, as seen in the sapatinib-resistant fragment-derived tumours which have undergone EMT. However, the process leading to increased ZEB1 and ZEB2 in the sapatinib-resistant tumours is not known, due to tumours being collected at sacrifice. If increased ZEB1 is the primary mechanism of resistance, development of better *in vitro* models will allow modulation of this for confirmation.

### 3.5.2 Linking EMT and HER2 loss

In Creedon et al.[84], concurrent loss of HER2 and EMT were seen (fig 3.1, 3.5). Although induction of EMT in response to targeted therapies has been shown in the literature,[80,85,87,89,91,122,173,174] EMT is not consistently induced in response to targeted therapies.[123,175–177] Despite being highly resistant to both sapatinib and lapatinib, none of the resistant lines replicated the mesenchymal phenotype seen *in vivo* (section 3.2).

In our models, overexpression of *ZEB1* did not result in any loss of HER2 protein or transcript (fig 3.15). However, these were short-term experiments; despite increased *ZEB1* transcript, other evidence supporting EMT was lacking. Studies evidencing EMT in response to HER2-targeted therapies utilised trastuzumab,[80,91,122] whereas our models of acquired resistance used the tyrosine kinase inhibitors sapatinib and lapatinib. Although, other studies have evidenced ZEB1 as a driver of resistance using

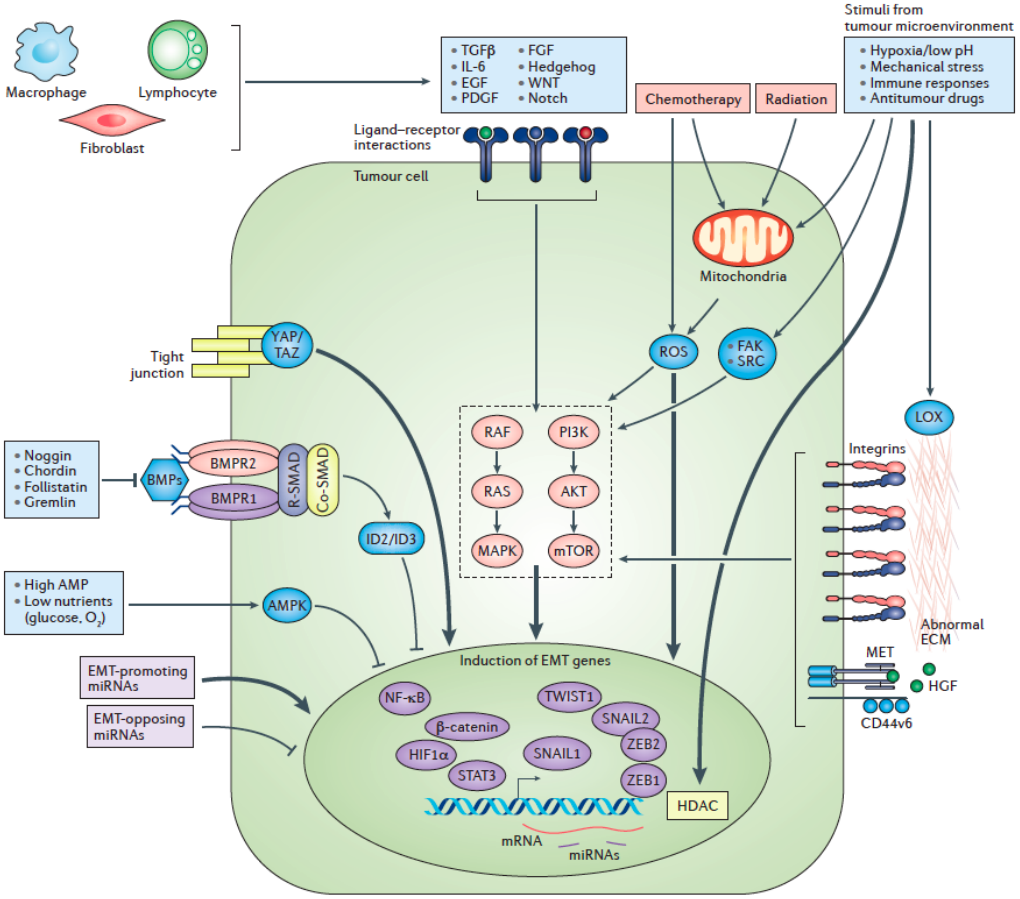


**Figure 3.21. EMT can be induced by stimuli from the tumour microenvironment.** The tumour microenvironment (TME) consists of cells such as fibroblasts and immune cells that are able to release cytokines which act on the tumour cells. Cellular pathways including phospho-inositide-3-kinase (PI3K)/AKT and mitogen-activated protein kinase (MAPK) can be activated. This can lead to activation of transcription factors signal transducer and activator of transcription 3 (STAT3), Yes-associated protein (YAP) and transcriptional co-activator with PDZ-binding motif (TAZ). Genes downstream of these proteins include epithelial to mesenchymal transition (EMT) transcription factors: SLUG, SNAIL, TWIST, zinc finger E-box binding homeobox 1 and 2 (ZEB1 and ZEB2). Cancer stem cell activity can be modulated by cytokines through MET and its receptor, CD44v6, which amplifies hepatocyte growth factor (HGF) signalling and transcription of EMT-associated genes. Cellular interaction with extracellular matrix (ECM) through integrins and other cell-adhesion proteins can also affect this signalling pathway. Conversely, bone morphogenetic proteins (BMPs) and AMP-activated protein kinase (AMPK) prevent EMT gene transcription. Micro-RNAs (miRNAs) can inhibit or support EMT dependent on their target genes. Abbreviations: BMPR: BMP receptor; Co-SMAD: common mediator SMAD; EGF: epidermal growth factor; FAK: focal adhesion kinase; FGF: fibroblast growth factor; HDAC: histone deacetylase; HIF-1$\alpha$: hypoxia-inducible factor 1$\alpha$; ID2: inhibitor of DNA binding 2; IL-6: interleukin-6; LOX: lysyl oxidase; NF-$\kappa$B: nuclear factor-$\kappa$B; PDGF: platelet-derived growth factor; ROS: reactive oxygen species; R-SMAD: receptor-regulated SMAD; SMAD: an acronym from the fusion of *C. elegans Sma* genes and the *D. melanogaster* mothers against decapentaplegic; TGF-$\beta$: transforming growth factor-$\beta$. Reprinted by permission from RightsLink: Nature publishing group, *Nature Reviews Drug Discovery*, Marcucci et al.[83], 2016.

*in vitro* models of acquired resistance to tyrosine kinase inhibitors and chemotherapeutic agents.[85,89] Thus, ZEB1 induction is not exclusive to resistance to targeted monoclonal antibodies.

Trastuzumab has a different mechanism of action to sapatinib and lapatinib; by targeting the extracellular domain of HER2, it inhibits downstream pathway signalling, induces ADCC and triggers HER2 internalisation.[32,39,40] However, sapatinib and lapatinib only inhibit phosphorylation of HER2, preventing downstream pathway activation.[34,36]

The additional actions of trastuzumab may encourage cells to undergo EMT *in vitro* without further stimulation by pro-inflammatory cytokines. Development of trastuzumab-resistant lines, or treatment of *ZEB1*-overexpressing cells with trastuzumab, may provide enough stimulus for cells to fully undergo EMT. However, as ZEB1 has been shown in response to other small molecule inhibitors, the question remains as to why resistant SKBR3 cells did not increase ZEB1, as seen *in vivo*.

Lapatinib has been shown to disrupt ERK and PI3K/AKT signalling through EGFR, resulting in suppression of EMT in squamous cell carcinoma.[178] Conversely, research by Kim et al.[173] evidenced that lapatinib resistance is associated with induction of EMT via Testican-1 signalling in gastric cancer. However in this instance, levels of HER2 and phospho-HER2 were maintained. From the conflicting results published, it is evident that the induction of EMT in response to targeting of HER family members is context specific and does not always correlate with downregulation of HER2 or EGFR.

Tumours with *PTEN* loss or *PIK3CA* mutations, leading to constitutive pathway activation,[109–111,114,115] have been shown to express EMT-like properties and increase expression of stem cell markers.[91,159] SKBR3 cells possess *PTEN*, whereas tumours from MMTV-NIC-PTEN$^{+/-}$ have reduced PTEN activity.[165] As a result of the reduced PTEN activity, PI3K/AKT signalling is increased in these tumours.[165,179] Therefore, the lack of concurrence between the *in vivo* and *in vitro* data may be due to the differing PTEN status of the models.

Increased expression of HER2 has been linked to EMT.[80,87,180] Liu et al.[80] found that activation of MMPs led to shedding of the extracellular domain and loss of membranous HER2, despite continued reliance on p95 HER2, which is evidenced by the sensitivity

of the cells to lapatinib. As HER2 overexpression can drive EMT and increase cancer stemness, we used SKBR3 cells to model this. However, development of resistant lines and overexpression of *ZEB1* failed to recapitulate the EMT seen *in vivo*.[84]

The data are contradictory: loss of HER2 due to EMT has also been shown.[90,157] Supporting the link between reduced HER2 expression and EMT, a recent meta-analysis showed that although HER2-positive breast cancers were more likely to be associated with decreased E-cadherin than luminal A or B subtypes, triple-negative breast cancers were significantly more likely than HER2-positive cancers to have decreased E-cadherin.[181]

Loss of HER2 after initial diagnosis has also been shown in primary breast cancers.[64,65] Both studies showed a loss of *ERBB2* DNA amplification, rather than at the protein or transcript level. The tumours analysed in Creedon et al.[84], and within this chapter, are derived from a genetically engineered mouse model, with *Erbb2* under the control of the MMTV promoter; ensuring HER2 becomes expressed and drives tumourigenesis only within mammary tissues.[147,148] We have confirmed that within this mouse model, there is complete loss of HER2 at the protein level (fig 3.5 C and D) in half of the sapatinib-resistant fragment-derived tumours. A significant decrease in *Erbb2* at the transcript level (fig 3.5 E) indicates that these tumours still possess the transgene, as *Erbb2* was detected in all tumours.

To explore loss of HER2 driving EMT, we knocked down *ERBB2* in SKBR3 cells. However loss of HER2 in SKBR3 cells did not result in a switch to an overt mesenchymal phenotype (section 3.4). Although, *ERBB2* shRNA cells had increased *ZEB1* and were more migratory, evidencing some mesenchymal properties (fig 3.17, 3.19). If the mesenchymal phenotype seen in the sapatinib-resistant tumours is reliant on cell-extrinsic factors, the full program of EMT would not occur despite loss of HER2.

### 3.5.3 Modelling resistance *in vitro*

As described above, in the MMTV-NIC-PTEN$^{+/-}$ model, resistance to sapatinib was associated with EMT and concurrent loss of HER2.[84] However, this was not recapitulated *in vitro* using the SKBR3 cell line (section 3.2). SKBR3 cells were chosen as they most accurately represent the molecular signature of the tumours generated in MMTV-NIC-

**Table 3.2.** HER2-positive cell lines

| Cell line | TR | LR | Additional Information |
|---|---|---|---|
| SKBR3 | - | - | - |
| AU565 | - | - | Derived from same patient as SKBR3 |
| HCC1569 | - | + | - |
| HCC1954 | + | - | - |
| HCC202 | - | + | - |
| JIMT-1 | + | + | - |
| KPL-4 | + | - | Inflammatory |
| MDA-MB-453 | + | + | Misidentified cell line |
| OCUB-1F | - | - | Non-adherent |
| SUM225 | + | - | - |
| UACC-893 | + | - | - |

TR: trastuzumab resistant; LR: lapatinib resistant. References: Tanner et al.[77], O'Brien et al.[182], Dai et al.[183], Ellison et al.[184], Jernström et al.[185], Sawada et al.[186]

PTEN$^{+/-}$ mice, which are *BRCA* wild-type and oestrogen receptor and progesterone receptor negative.[165] Other HER2-positive cell lines lacking oestrogen and progesterone receptors have been derived but have been shown to be *de novo* resistant to trastuzumab or lapatinib (table 3.2).[77,182–186] Due to this, they have limited utility in our experiments as matched, responsive lines are not available for comparison.

Two cell lines, AU565 and OCUB-1F, are not resistant to trastuzumab or lapatinib. However, AU565 and SKBR3 cells are derived from the same patient.[182] As such, they have the same molecular signature and react to drug treatments in similar ways.[182] Because of this, AU565 cells offer no advantage over SKBR3 cells. OCUB-1F cells are a non-adherent cell line and there is little information available in the literature regarding their sensitivity to targeted therapies, or their origin.[186] With this in mind, SKBR3 is the best *in vitro* model to replicate MMTV-NIC-PTEN$^{+/-}$ tumours.

Previous work in the Brunton lab generated cell lines derived from MMTV-NIC-PTEN$^{+/-}$ tumours.[187] However, these lines showed fluctuations in their expression of HER2 and no longer expressed the MMTV-NIC transcript. Additionally, alterations in the expression of cytokeratins and mesenchymal markers indicated that the cells were undergoing

lineage changes, without the addition of sapatinib or lapatinib.[187] Thus, use of these lines to study the relationship between HER2 loss and EMT in response to targeted therapies was not tenable.

Studies linking EMT and resistance to targeted therapies have shown that this is reliant on pro-inflammatory cytokines mediating a positive-feedback loop.[90,91,188] Increased expression of interleukin-6 (IL-6) or IL-1$\alpha$ through NF$\kappa$B and STAT3 signalling promote chronic inflammation which is necessary to support EMT and enhanced stemness (fig 3.21).[91,188] These cytokines can be produced by cancer cells themselves or, in *in vivo* models, by immune cells.[83,90,91]

Without the influence of pro-inflammatory cytokines *in vitro* our models are lacking the external signals which may be necessary for the induction of EMT. Co-culture experiments would better replicate the impact of the immune system and other cell types on cancer cells *in vitro*.[189,190] These systems better recapitulate the cross-talk between different cell types within a tumour. Cells within the microenvironment can exert a large influence on cell-fate decisions.[189] In particular, the release of cytokines by immune cells and fibroblasts can activate the TGF-$\beta$ pathway which can result in increased expression of ZEB1 (fig 3.21).[83,90,91]

Signals from the extracellular matrix can also influence cells to undergo EMT (fig 3.21). As the plastic used in 2D tissue culture is stiffer than the extracellular matrix, signalling pathways can be altered.[191] In contrast, 3D tissue scaffolds can be made of a variety of materials and have the ability to modulate substrate stiffness to better portray conditions *in vivo*.[192]

By utilising a co-culture or 3D culture technique, it may be possible to better recapitulate the EMT seen *in vivo* in response to sapatinib. As such, future research should employ these techniques to ascertain the effect they may have on EMT and HER2 loss *in vitro* in response to sapatinib.

### 3.5.4 Summary

We have shown that the EMT phenotype seen *in vivo* is maintained by ZEB1 expression; furthermore, patient data supports the translational relevance of the model. Additionally, we have shown that loss of HER2 is not sufficient to induce EMT in SKBR3 cells, despite bestowing some mesenchymal properties. Currently, it is still unclear how EMT and loss of HER2 are linked in the MMTV-NIC-PTEN$^{+/-}$ fragment-derived tumour mouse model.

Future studies should focus on the difference between the current *in vitro* and *in vivo* models and further elucidate the effect that PTEN loss may have on the development of HER2 loss and EMT in response to sapatinib treatment. Development of more relevant *in vitro* models, using co-culture or 3D cultures, will allow pathway manipulation to better understand the link between EMT and HER2 in the fragment-derived tumour mouse model.

# Chapter 4

# Sapatinib-treated tumours have perturbed iron storage

In the past decade, targeted therapies have resulted in major advances in the treatment of HER2-positive breast cancers. Despite this, up to 70% of patients will develop resistance to targeted therapies such as trastuzumab and lapatinib within two years.[71] Resistance to these therapies means that patients' disease will inevitably progress. If patients do progress on targeted therapies, chemotherapy becomes the only alternative. By uncovering pathways and mechanisms that resistant tumours are utilising to overcome targeted therapies, it is possible that these can be targeted to render the tumours sensitive to therapy once more.

To study resistance mechanisms within the primary tumour, a spontaneous mouse model of HER2-positive breast cancer was used. The MMTV-NIC-PTEN$^{+/-}$ mouse model develops multiple HER2-driven mammary tumours.[147,148] To understand resistance mechanisms behind HER2-targeted therapies, MMTV-NIC-PTEN$^{+/-}$ mice were treated with vehicle (1% Tween 80 in PBS; po, q.d.), or sapatinib (100 mg/kg, with 1% Tween 80 in PBS; po, q.d.) once a palpable tumour developed. Initial characterisation of untreated tumours and tumours treated with sapatinib for three days from this model has previously been undertaken and is detailed in Creedon et al.[84]

In this chapter, the following aims will be explored:

- Characterisation of a sapatinib-treated MMTV-NIC-PTEN$^{+/-}$ spontaneous tumour mouse model.
- Identify pathways which are differentially regulated in sapatinib-treated tumours.
- Validation of identified pathways and proteins *ex vivo*.
- Assess the similarity of resistance mechanisms between the fragment-derived tumour model and the spontaneous tumour model.

## 4.1 Sapatinib-treated mice have longer survival times despite similar tumour burden

Tumour development and measurements were performed by Dr Helen Creedon. Survival data up to 40 days after the first palpable tumour were assessed by Dr Helen Creedon,[165] and is included in Creedon et al.[84]. I performed all subsequent analysis presented in this chapter. Detailed results for this chapter can be found in tables A.5–A.8.

MMTV-NIC-PTEN$^{+/-}$ mice were monitored twice weekly for the development of palpable tumours. Vehicle-treated mice had a median survival time of 22 days after onset of treatment, compared with 71 days for sapatinib-treated mice (fig 4.1 A; HR: 0.3099; CI of ratio: 0.08970–1.070; $p$=0.0018). MMTV-NIC-PTEN$^{+/-}$ mice can develop up to 10 mammary tumours: mice treated with vehicle developed a median of six tumours each, whereas mice on sapatinib treatment developed a median of five tumours each (Mann-Whitney test; CI: $(-3)$–4; $p$=0.3175; NS).

Clinical disease progression is classified as a greater than 20% increase in tumour volume from baseline, whereas responsive disease is classed as a greater than 30% decrease in tumour volume.[193] Using these guidelines, 83% of all tumours from both treatment arms combined were classed as progressive (fig 4.1 B; vehicle: n=25 [92.59%]; sapatinib: n=17 [70.83%]). Two tumours were between 20% increase and 30% decrease in tumour volume (fig 4.1 B; vehicle: n=0 [0%]; sapatinib: n=2 [8.34%]) and were thus classified as stable.[193]

Several tumours that became palpable after treatment commenced showed pathological complete response (pCR) to treatment, with no palpable tumour detected (fig 4.1 B; vehicle: n=0 [0%]; sapatinib: n=5 [20.84%]). Two tumours had partial responses, greater than 30% regression, but less than 100% regression (fig 4.1 B; vehicle: n=1 [3.70%]; sapatinib: n=1 [4.17%]). No significant difference was seen between treatment groups when comparing the percentage volume change from baseline (Mann-Whitney test; $p$=0.0682; NS).

The index tumour was defined as the largest tumour at the time of sacrifice. Growth kinetics of the index tumours from each mouse (fig 4.1 C) showed that tumours from

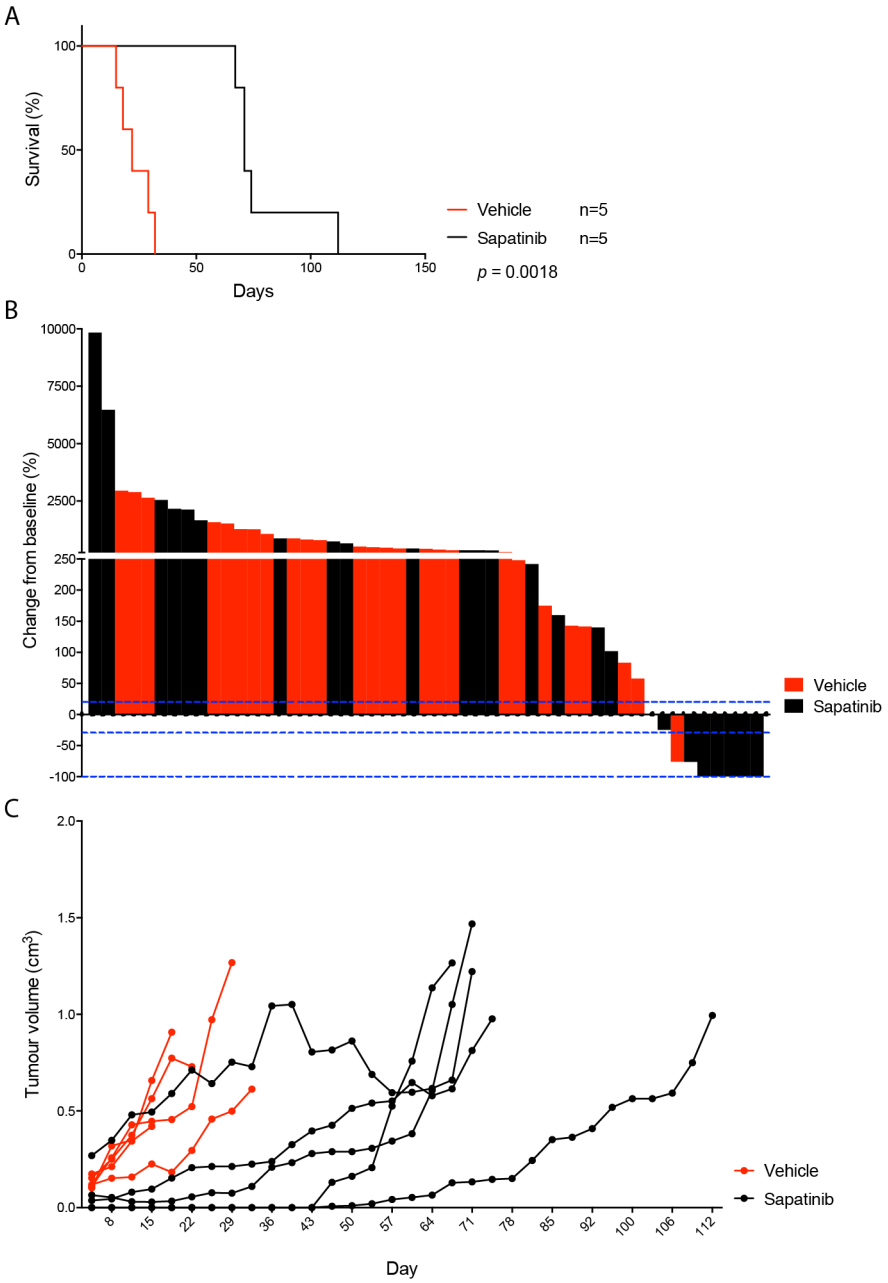


**Figure 4.1. Sapatinib increases survival time in MMTV-NIC-PTEN$^{+/-}$ mice.** **(A)** Kaplan-Meier survival curve showing survival time from start of treatment in MMTV-NIC-PTEN$^{+/-}$ mice treated with vehicle or sapatinib. Log-rank test, $p$=0.0018. **(B)** Waterfall plot showing volume change from baseline (%) of all MMTV-NIC-PTEN$^{+/-}$ tumours from mice treated with vehicle or sapatinib. Dotted blue lines represent 20% increase, 30% decrease and 100% decrease in tumour volume from baseline, respectively. Mann-Whitney test, $p$=0.0682. **(C)** Graph showing growth curves of index tumours in MMTV-NIC-PTEN$^{+/-}$ mice treated with vehicle or sapatinib from the onset of the first palpable tumour.

vehicle-treated mice grew rapidly after the initial tumour onset, whereas index tumours from sapatinib-treated mice had a longer period of latency after treatment commenced before rapid growth began. Subsequent analysis presented here has been performed on tumours progressing on vehicle or sapatinib treatment.

## 4.2 Spontaneous tumours have a mechanism of resistance distinct from that seen in fragment-derived tumours that have undergone EMT

### 4.2.1 Tumours from sapatinib-treated mice are morphologically similar to tumours from vehicle-treated mice

Previous data generated by the lab showed that 50% of the sapatinib-resistant tumours derived following implantation of MMTV-NIC-PTEN$^{+/-}$ tumour fragments exhibited a mesenchymal morphology, increased expression of mesenchymal markers and loss of HER2 (see chapter 3; Creedon et al.[84]). Haematoxylin and eosin staining shows resistant tumours from sapatinib-treated mice have a similar cellular morphology and tumour composition to those from vehicle-treated mice (fig 4.2 A–D, 4.2 E).

If tumours had undergone EMT a spindle cell morphology would be expected (fig 3.1 C; Creedon et al.[84]), but these cells exhibited a rounded, epithelial-like morphology. However, tumours from sapatinib-treated mice had a larger median cell area compared with vehicle-treated and untreated tumours (fig 4.2 E). Sapatinib-treated tumours also had a larger mean nuclear area (fig 4.2 F), compared with vehicle-treated tumours, although no significant difference can be seen between untreated and sapatinib-treated tumours.

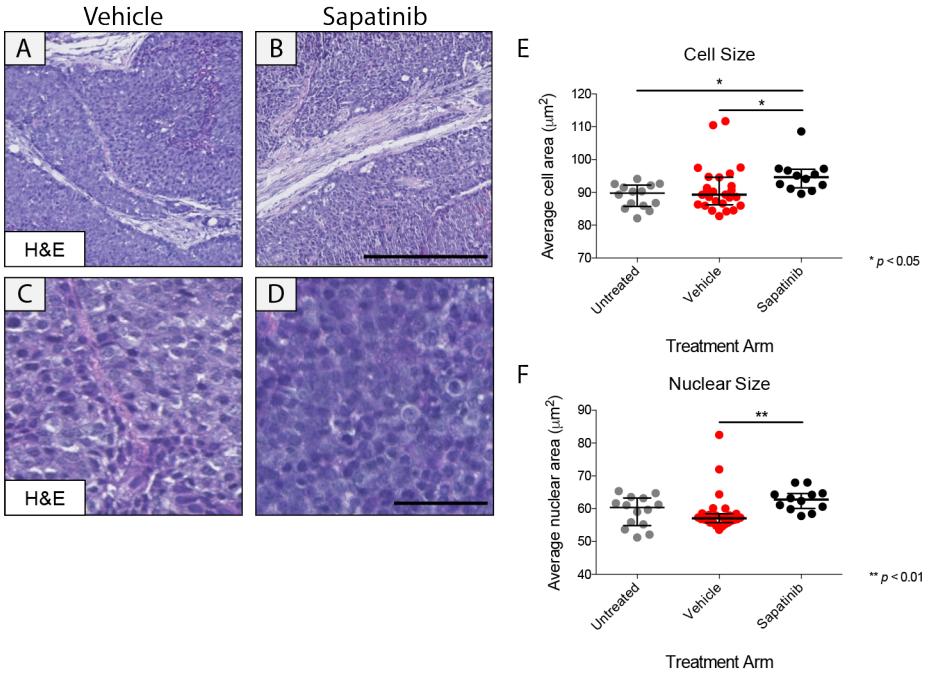


**Figure 4.2. Tumours from sapatinib-treated MMTV-NIC-PTEN$^{+/-}$ mice are morphologically similar to vehicle-treated mice.** Representative haematoxylin and eosin (H&E) staining of tumours from MMTV-NIC-PTEN$^{+/-}$ mice treated with vehicle (n=24) or sapatinib (n=11). **(A–B)** Scale bar: 250 $\mu$m and **(C–D)** scale bar: 50 $\mu$m. **(E)** Determination of mean cell area by Definiens Architect, compared with untreated tumours from MMTV-NIC-PTEN$^{+/-}$ mice (images not shown). Results presented as scatter plot with median $\pm$ IQR. Kruskal-Wallis test, Dunn's post-hoc test $p$<0.05=*. **(F)** Determination of mean nuclear area by Definiens Architect, compared with untreated tumours from MMTV-NIC-PTEN$^{+/-}$ mice (images not shown). Results presented as scatter plot with median $\pm$ interquartile range. Kruskal-Wallis test, Dunn's post-hoc test $p$<0.01=**. Detailed results can be found in table A.5.

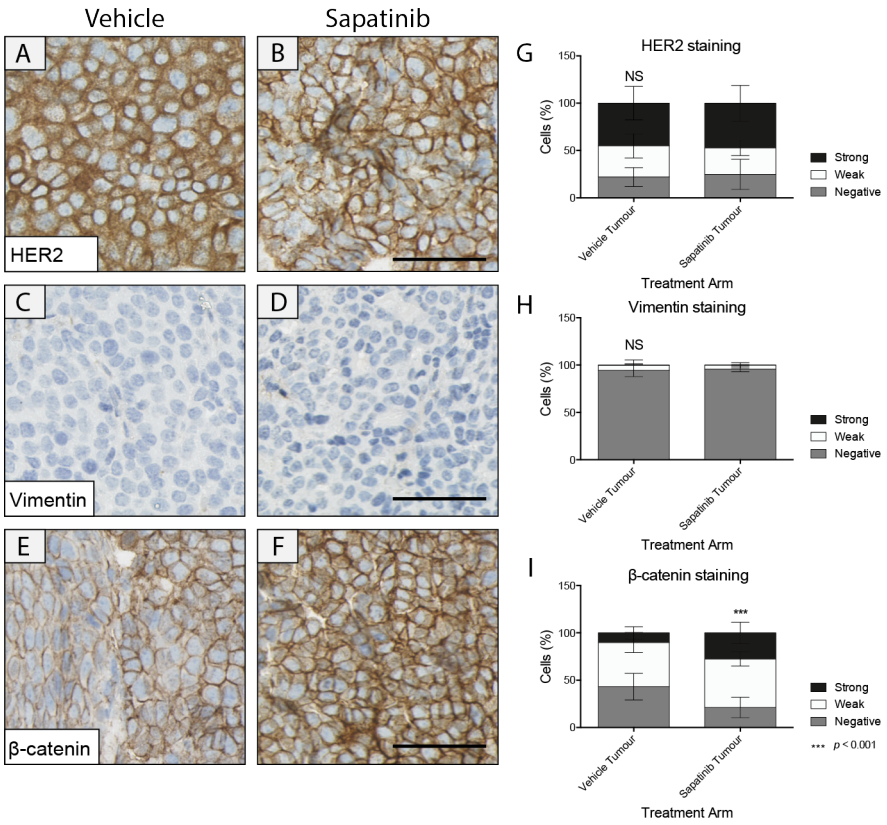


**Figure 4.3. Sapatinib-treated tumours from MMTV-NIC-PTEN$^{+/-}$ mice have no loss of HER2, or mesenchymal phenotype.** Immunohistochemistry (IHC) was performed on tumours from MMTV-NIC-PTEN$^{+/-}$ mice treated with vehicle or sapatinib. Representative IHC staining of **(A–B)** human epidermal growth factor receptor 2 (HER2) (vehicle: n=25; sapatinib: n=12), **(C–D)** vimentin (vehicle: n=23; sapatinib: n=11) and **(E–F)** $\beta$-catenin (vehicle: n=22; sapatinib: n=10). Scale bar: 50 $\mu$m. Quantification of **(G)** HER2, **(H)** vimentin and **(I)** $\beta$-catenin staining by Definiens Architect. Results presented as mean $\pm$ standard deviation. Two-tailed Mann-Whitney test, not significant = NS, $p$<0.001=***. Detailed results can be found in table A.5.

### 4.2.2 Sapatinib-treated tumours have no loss of HER2 or EMT associated protein expression

To further ascertain whether sapatinib-treated spontaneous tumours exhibit similar changes to sapatinib-resistant fragment-derived tumours that had developed acquired resistance (fig 3.1, 3.5), IHC was performed for HER2, vimentin and $\beta$-catenin. Unlike the sapatinib-treated fragment-derived tumours, sapatinib-treated spontaneous tumours showed similar numbers of HER2-positive cells as vehicle-treated spontaneous tumours (fig 4.3 A, B and G). Additionally, no increase in the number of vimentin positive cells, associated with a mesenchymal phenotype, was seen (fig 4.3 C and D). Sapatinib-treated tumours also showed increased numbers of $\beta$-catenin positive cells, associated with an epithelial phenotype, compared with vehicle-treated tumours (fig 4.3 E, F and H).

## 4.3 Alterations in key signalling axes indicate that sapatinib-treated tumours are utilising alternative pathways

### 4.3.1 Sapatinib-treated tumours have greater proliferation compared with vehicle-treated tumours

To assess if sapatinib-treated tumours had similar numbers of actively proliferating cells to vehicle-treated tumours, levels of Ki67 were assessed. This revealed that sapatinib-treated tumours had more Ki67-positive nuclei than vehicle-treated tumours (fig 4.4 A, B and E; median [CI]: vehicle: 21.97% [13.95–39.88]; sapatinib: 69.93% [29.32–91.19]; $p$=0.0006).

Previous work in the Brunton lab determined that MMTV-NIC-PTEN$^{+/-}$ mice developed tumours more quickly than MMTV-NIC-PTEN$^{+/+}$ and that those tumours with loss of PTEN had accelerated tumour progression.[84] To establish whether both treatment groups had similar expression of PTEN within tumours, IHC was performed. This confirmed that similar numbers of PTEN-positive cells can be seen across both vehicle-treated and sapatinib-treated tumours and that these cells did not express high levels of PTEN (fig 4.4 C, D and F).

### 4.3.2 Pathways downstream of HER2 are inhibited in tumours from sapatinib-treated MMTV-NIC-PTEN$^{+/-}$ mice

The PI3K/AKT and MAPK pathways are downstream of HER2 signalling. The activation of both pathways can result in increased proliferation due to their varied downstream targets (fig 1.1). Inhibition of HER2 by sapatinib has been shown to reduce signalling through these pathways *in vivo* after three days of treatment with sapatinib.[84] Dysregulation of signalling through the PI3K/AKT and MAPK pathways has been linked to resistance to HER2-targeted therapies.[109]

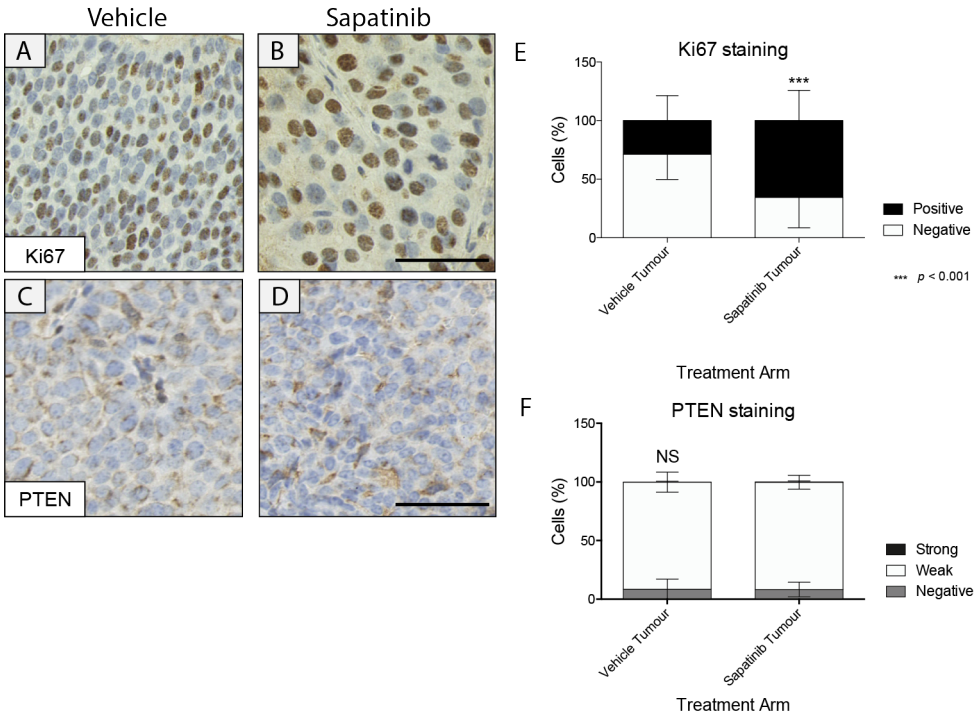


**Figure 4.4. Tumours from sapatinib-treated MMTV-NIC-PTEN$^{+/-}$ mice have greater proliferative potential than vehicle-treated tumours.** Representative immunohistochemical (IHC) staining of **(A–B)** Ki67 (vehicle: n=23; sapatinib: n=9) and **(C–D)** phosphatase and tensin homolog (PTEN; vehicle: n=24; sapatinib: n=12). Scale bar: 50 $\mu$m. Quantification of **(E)** Ki67 and **(F)** PTEN IHC staining by Definiens Architect. Results presented as mean $\pm$ standard deviation. Two-tailed Mann-Whitney test, not significant = NS, $p$<0.001=***. Detailed results can be found in table A.5.

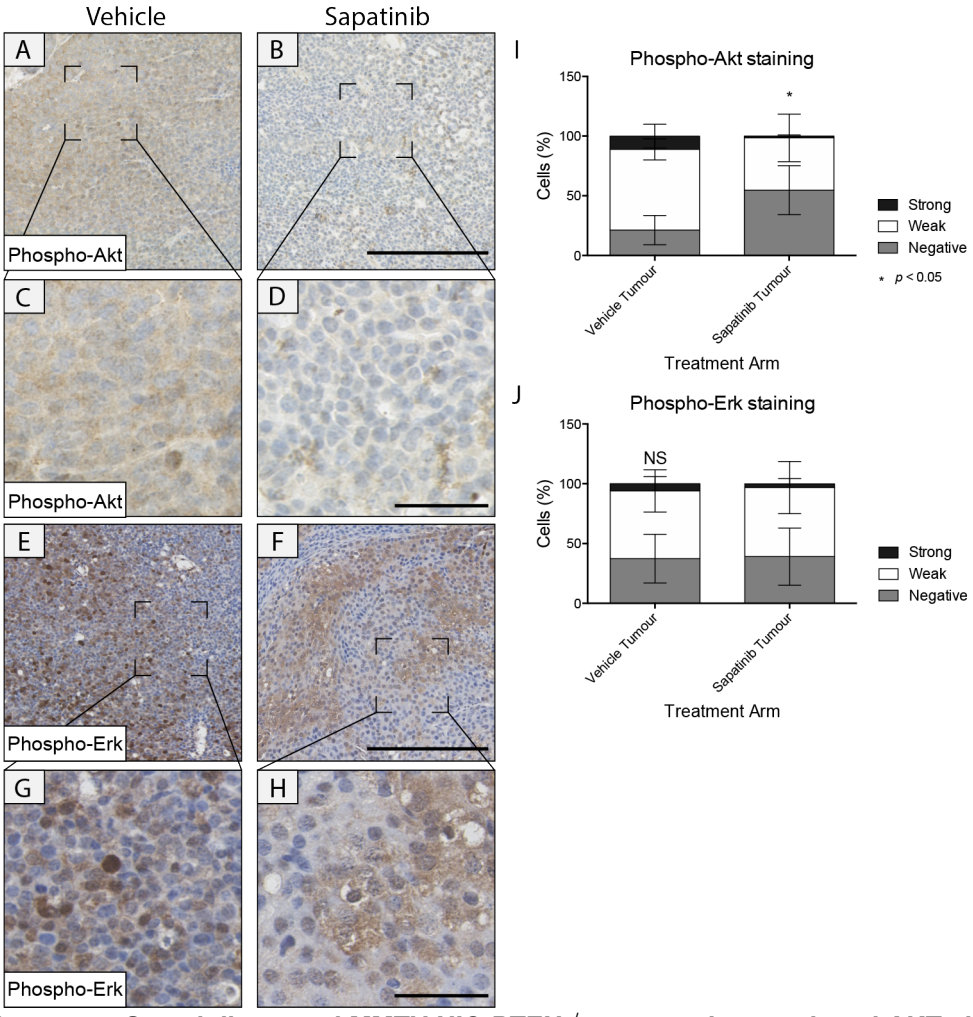


**Figure 4.5. Sapatinib-treated MMTV-NIC-PTEN$^{+/-}$ tumours have reduced AKT signalling.** Representative immunohistochemical (IHC) staining of **(A–D)** phosphorylated protein kinase B (phospho-AKT; vehicle: n=11; sapatinib: n=6) and **(E–H)** phosphorylated extracellular signal-regulated kinase-1 (phospho-ERK; vehicle: n=25; sapatinib: n=10). **(A–B, E–F)** Scale bar: 250 $\mu$m. **(C–D, G–H)** Scale bar: 50 $\mu$m. Quantification of **(I)** phospho-AKT and **(J)** phospho-ERK IHC staining by Definiens Architect. Results presented as mean $\pm$ standard deviation. Two-tailed Mann-Whitney test, not significant = NS, $p$<0.05=*. Detailed results can be found in table A.5.

To test if activation of these pathways was increased in the tumours, IHC was carried out for phospho-AKT and phospho-ERK. Levels of phospho-AKT were significantly reduced in sapatinib-treated tumours (fig 4.5 A–D and I). Meanwhile, no significant difference could be seen between treatment groups when comparing levels of phospho-ERK (fig 4.5 E–H and J). However, expression of phospho-ERK was highly variable across the tumours (fig 4.5 E and F), whereas phospho-AKT expression was more consistent across the whole tumour section (fig 4.5 A and B).

## 4.4 Pathway analysis reveals alterations in iron homeostasis

To assess differentially regulated pathways in sapatinib-treated tumours compared with vehicle-treated tumours, index tumours from both treatment arms were subjected to reverse phase protein array (RPPA) and proteomic analysis.

### 4.4.1 RPPA identifies increased phospho-SMAD1/5 in sapatinib-treated tumours

To identify any potential changes in pathways known to often be dysregulated in resistance, RPPA was used.[194] Key pathways investigated include AKT and MAPK signalling and those associated with transcriptional regulation, cell cycle and apoptosis. This revealed few changes in signalling pathways that were consistent across all sapatinib-treated index tumours (fig 4.6 A). Proteins that were significantly downregulated in sapatinib-treated tumours included downstream targets of EGFR and HER2 (fig 4.6 B) such as c-Myc, phospho-AKT and phospho-PLC-$\gamma$1. This result confirms previous quantification of IHC for phospho-AKT and phospho-ERK (fig 4.5 I and J) which showed significantly decreased phospho-AKT and no significant difference in levels of phospho-ERK.

Only phospho-SMAD1/5 (pSMAD1/5) was significantly upregulated in all sapatinib-treated tumours, compared with vehicle-treated tumours by RPPA. SMAD1 and SMAD5 are known to translocate to the nucleus when phosphorylated, in a complex with SMAD8, and initiate transcription of target genes.[195–197] To validate this finding, IHC was carried out. This revealed no significant difference in levels of nuclear pSMAD1/5/8 between the two treatment groups (fig 4.6 C–E).

Western blotting revealed an increase in pSMAD1/5 in sapatinib-treated tumours. However, these tumours also had higher levels of SMAD1 compared with vehicle-treated tumours, despite having lower levels of SMAD5 (fig 4.6 F). Quantification of these western blots by densitometry analysis revealed no significant difference between the

ratio of pSMAD1/5 to SMAD1 and SMAD5 between the two treatment groups (fig 4.6 G).

### 4.4.2 Sapatinib-treated tumours have dysregulated cellular iron homeostasis

Proteomic analysis by mass spectrometry (Section 2.2.7) revealed a small number of proteins that were significantly ($p<0.05$) and 2-fold differentially regulated between vehicle-treated and sapatinib-treated tumours (n=123, increased: n=34, decreased: n=89; fig 4.7 A; table B.1). However, gene ontology (GO) analysis of proteomic data revealed several proteins upregulated in sapatinib-treated tumours related to control of cellular iron homeostasis (n=4; fig 4.7 B; $p=0.019$). Fewer proteins involved in cellular redox homeostasis (n=6; $p=0.0017$), response to endoplasmic reticulum stress (n=7; $p=0.00028$) and protein folding (n=10; $p<0.00001$) were identified in sapatinib-treated tumours compared with vehicle-treated tumours (fig 4.7 B).

As cellular iron homeostasis was the only GO term upregulated in sapatinib-treated tumours compared with vehicle-treated tumours, it was decided that this represented a good avenue to investigate. To understand if the proteins identified by proteomics were located in the tumour tissue or the surrounding non-tumour tissue, including the stromal compartment, analysis was divided into tumour and non-tumour staining.

Further validation of the proteins identified and involved in cellular iron homeostasis by IHC confirmed increased ceruloplasmin (fig 4.8 A, B and I) in sapatinib-treated tumours. No significant difference could be seen in levels of ferritin heavy chain (fig 4.8 C, D and J) or ferritin light chain (fig 4.8 E, F and K). Heme oxygenase-1 was also significantly upregulated in sapatinib-treated tumours (HO-1; fig 4.8 E, F and K).

Ferritins and HO-1 are known to have roles in the nucleus.[199–201] As a result, we looked specifically at the nuclear expression of these proteins. The number of positive nuclei in tumour sections stained with ferritin heavy chain, ferritin light chain and HO-1 was quantified. This revealed no difference in levels of nuclear ferritin heavy chain (fig 4.9 A) or nuclear ferritin light chain (fig 4.9 B). However, there was a significant increase in nuclear HO-1 in sapatinib-treated tumours, but not in the non-tumour tissue (fig 4.9 C).

QPCR was performed to evaluate the regulation of ceruloplasmin, ferritin heavy and light chains, and HO-1 at the transcriptional level. This revealed no significant differences in transcript levels of ceruloplasmin, ferritin heavy chain, ferritin light chain and HO-1 between vehicle-treated and sapatinib-treated tumours (fig 4.10 A).

As cellular iron homeostasis was identified as upregulated by GO terms (fig 4.7 B), iron content and the location of ferric iron ($Fe^{3+}$) within the tumours was assessed. Using Perls' ferric iron stain revealed significantly increased ferric iron in the non-tumour tissue surrounding sapatinib-treated tumours (fig 4.11 A-C). Due to the presence of significant deposits of ferric iron in the non-tumourous tissue, an iron assay was performed to quantify levels of total iron, ferrous iron ($Fe^{2+}$) and ferric iron. This revealed no significant differences between vehicle-treated and sapatinib-treated tumours (fig 4.11 D).

As no difference could be seen in the quantity of different iron species between vehicle-treated and sapatinib-treated tumours, cellular iron importers and exporters were analysed. Transferrin receptor and divalent metal transporter 1 (DMT1) are the main iron importers, whereas ferroportin is the only iron exporter identified thus far.[134,202] Levels of these three proteins were assessed by IHC.

This analysis showed similar levels of the iron importers transferrin receptor and DMT1 (fig 4.12 A–D, G and H), but increased expression of the iron exporter ferroportin (fig 4.12 E, F and I).

## 4.5 Changes in iron storage proteins are seen in short-term treatments with sapatinib

To determine if the changes associated with cellular iron homeostasis seen in sapatinib-treated tumours growing through the drug could be seen in tumours soon after treatment, MMTV-NIC-PTEN$^{+/-}$ mice treated with vehicle (1% Tween 80 in PBS) or sapatinib (100 mg/kg with 1% Tween 80 in PBS) for three days, once tumours had reached $\geq$0.3 $cm^3$, were assessed by IHC.

This revealed that no increase in ceruloplasmin was present (fig 4.13 A, B and I). However, an increase could be seen in ferritin heavy chain (fig 4.13 C, D and J) and ferritin light chain (fig 4.13 E, F and K). No increase could be seen in HO-1 (fig 4.13 G, H and L).

To determine if similar changes in iron deposition and iron transporters could be seen from short-term treatments as is seen in long-term treatments, IHC was performed. This analysis revealed no difference in levels of ferric iron in the tumour or non-tumour cells (fig 4.14 A, B and I). Additionally, no difference could be seen in levels of transferrin receptor and DMT1 (fig 4.14 C–F, J and K). However, tumours treated for 3 days with sapatinib did show increased expression of ferroportin (fig 4.13 G, H and L).

## 4.6 Sapatinib-resistant fragment-derived tumours with an epithelial morphology do not have altered iron homeostasis

Sapatinib-resistant fragment-derived tumours had undergone EMT in 50% of cases (chapter 3). It is currently unknown what the mechanism of resistance is in the remaining 50% of tumours which are morphologically similar to vehicle-treated fragment-derived tumours. To ascertain if the mechanism of resistance is the same mechanism seen in sapatinib-treated spontaneous tumours, IHC was performed for the proteins identified by proteomics. This revealed no differences in the levels of ceruloplasmin, ferritin heavy and light chains, and HO-1 (fig 4.15).

Sapatinib-treated spontaneous tumours also showed increased iron deposits in the non-tumour compartment of the tissue. To confirm if the same could be seen in sapatinib-resistant fragment-derived tumours, Perls' ferric iron stain was performed. This showed no changes in levels of ferric iron in either the tumour tissue, or the non-tumour tissue (fig 4.16 A, B and I). Additionally, no changes could be seen in the levels of transferrin receptor, DMT1 or ferroportin in the tumours (fig 4.16).

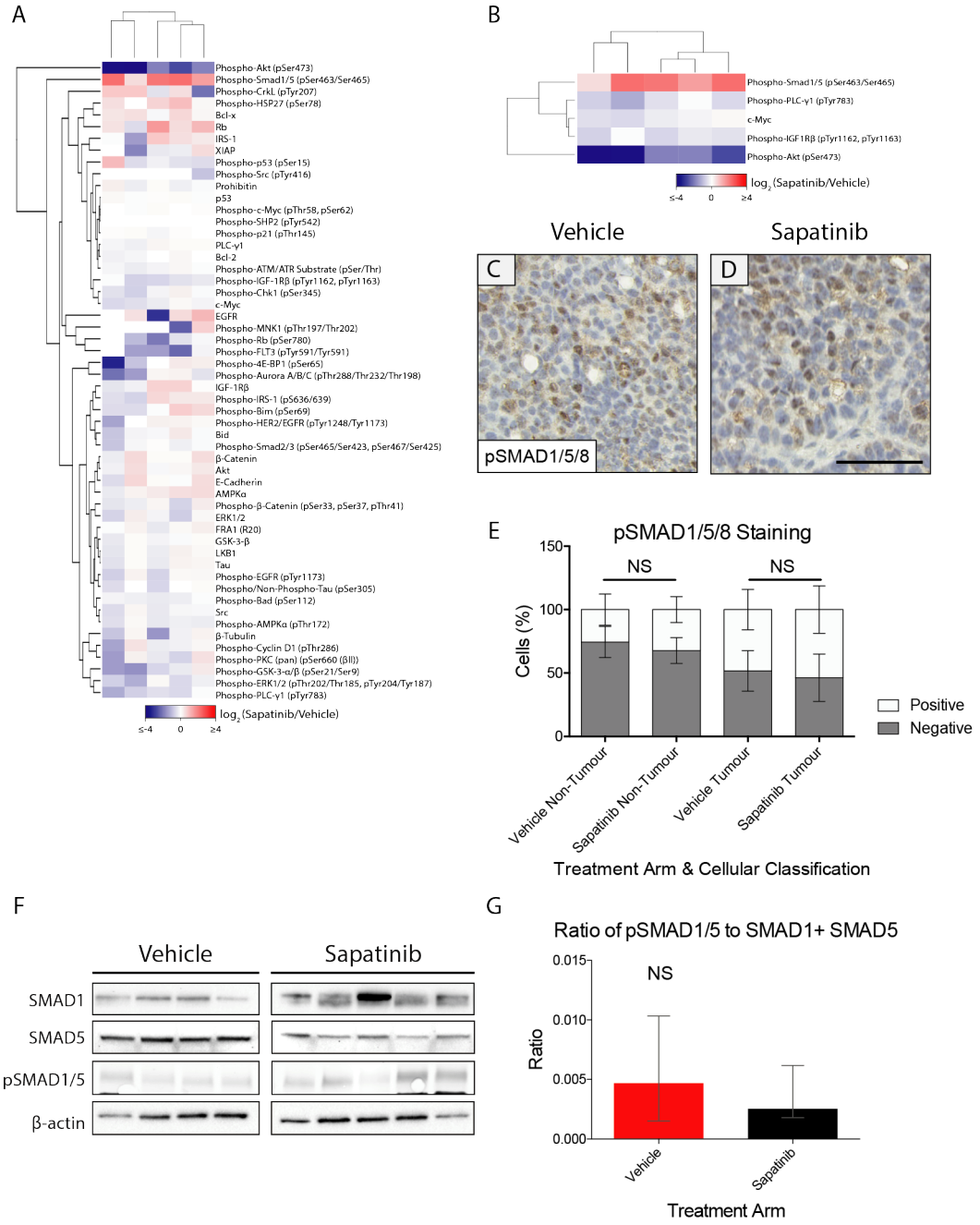


**Figure 4.6. Sapatinib-treated tumours have increased levels of phospho-SMAD1/5.** Heatmap of **(A)** all results and **(B)** significant results from reverse phase protein array (RPPA) analysis of index tumours from MMTV-NIC-PTEN$^{+/-}$ mice treated with vehicle (n=5) or sapatinib (n=5). Results presented as $\log_2$ fold change (sapatinib/vehicle). Multiple *t*-tests, Sidak-Bonferroni post-hoc test, $p<0.05$. **(C and D)** Representative immunohistochemical (IHC) staining of phosphorylated mothers against decapentaplegic homolog 1/5/8 (pSMAD1/5/8; vehicle: n=27; sapatinib: n=11). Scale bar: 50 $\mu$m. Quantification of **(E)** pSMAD1/5/8 IHC staining by Definiens Architect. Vehicle non-tumour was compared with sapatinib non-tumour, vehicle tumour was compared with sapatinib tumour. Results presented as mean $\pm$ standard deviation. Kruskal-Wallis test, Dunn's post-hoc test, not significant = NS. **(F)** Western blot analysis of SMAD1, SMAD5 and pSMAD1/5 in index tumours from MMTV-NIC-PTEN$^{+/-}$ mice treated with vehicle or sapatinib. *B*-actin was used as a loading control **(G)** Quantification of pSMAD1/5:SMAD1+SMAD5. Results presented as median $\pm$ interquartile range. Two-tailed Mann-Whitney test, not significant = NS. Detailed results can be found in table A.5 and table A.6.

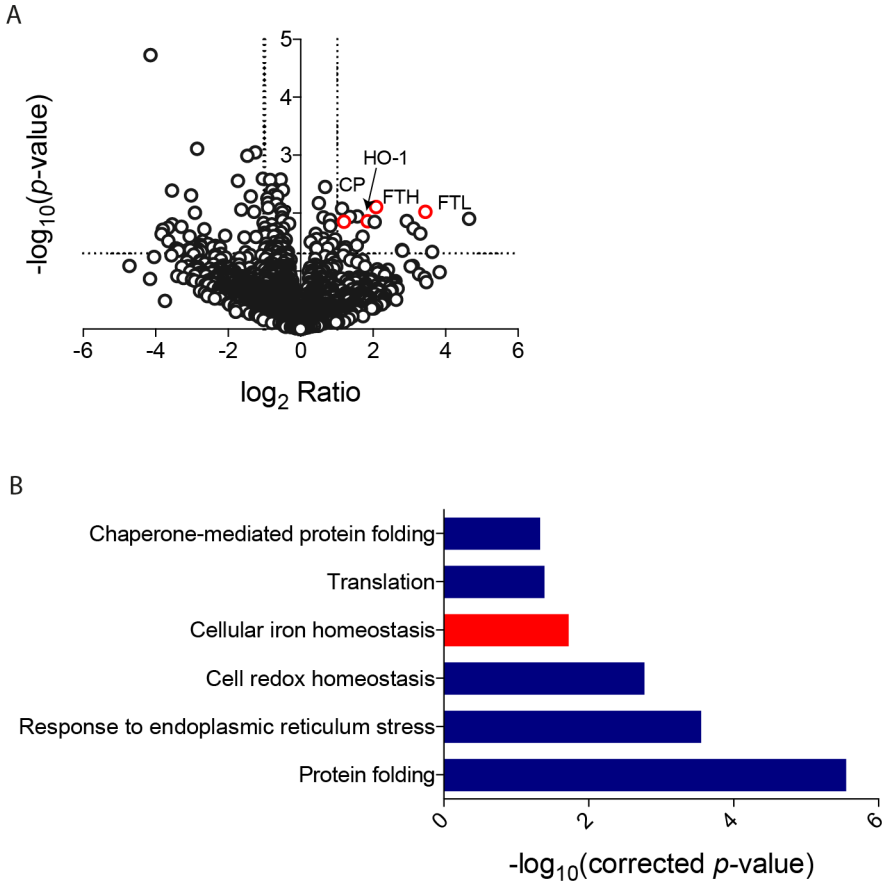


**Figure 4.7. Proteomics analysis reveals alterations in cellular iron homeostasis in sapatinib-treated tumours.** Index tumours from MMTV-NIC-PTEN$^{+/-}$ mice treated with vehicle (n=4) or sapatinib (n=5) were subject to liquid chromatography-tandem mass spectrometry (LC-MS/MS). Protein identification and quantitation were performed using MaxQuant. **(A)** Volcano plot of proteins identified by MaxQuant. Highlighted are proteins associated with cellular iron homeostasis, ferritin heavy chain (FTH), ferritin light chain (FTL), ceruloplasmin (CP) and heme oxygenase-1 (HO-1). Dotted lines represent $p$ of 0.05 and 2-fold ratio. **(B)** Bar chart showing significantly upregulated gene ontology (GO) terms related to proteins that were differentially regulated between vehicle-treated and sapatinib-treated tumours. Red bars represent GO terms upregulated in sapatinib-treated tumours, whereas blue bars represent those downregulated in sapatinib-treated tumours. Differentially regulated genes (table B.1) were selected as those which showed >2-fold change and $p<0.05$, as determined by MaxQuant, Wilcoxon-Mann-Whitney test. Benjamini-Hochberg corrected $p$-values and GO terms obtained from DAVID.[198]

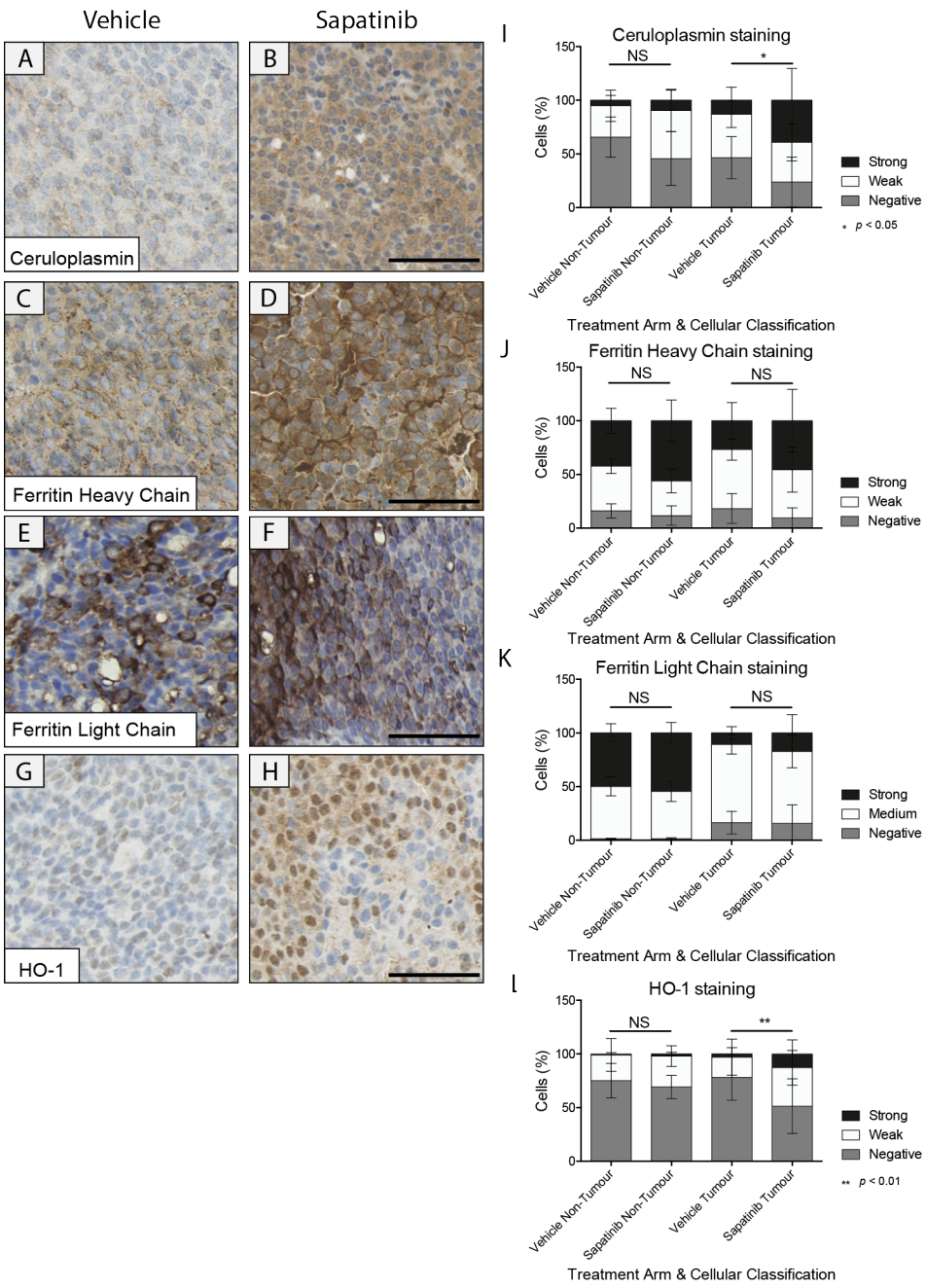


**Figure 4.8. Sapatinib-treated tumours from MMTV-NIC-PTEN$^{+/-}$ mice have increased ceruloplasmin and heme oxygenase-1.** Immunohistochemistry (IHC) was performed on tumours from MMTV-NIC-PTEN$^{+/-}$ mice treated with vehicle or sapatinib. Representative IHC staining of **(A–B)** ceruloplasmin (vehicle: n=20; sapatinib: n=12), **(C–D)** ferritin heavy chain (vehicle: n=18; sapatinib: n=10), **(E–F)** ferritin light chain (vehicle: n=23; sapatinib: n=10) and **(G–H)** heme oxygenase-1 (HO-1; vehicle: n=23; sapatinib: n=9). Scale bar: 50 $\mu$m. Quantification of cytoplasmic **(I)** ceruloplasmin, **(J)** ferritin heavy chain, **(K)** ferritin light chain and **(L)** HO-1 IHC staining by Definiens Architect. Vehicle non-tumour was compared with sapatinib non-tumour, vehicle tumour was compared with sapatinib tumour. Results presented as mean $\pm$ standard deviation. Kruskal-Wallis test, Dunn's post-hoc test, not significant = NS, $p$<0.05=* , $p$<0.01=**. Detailed results can be found in table A.6.

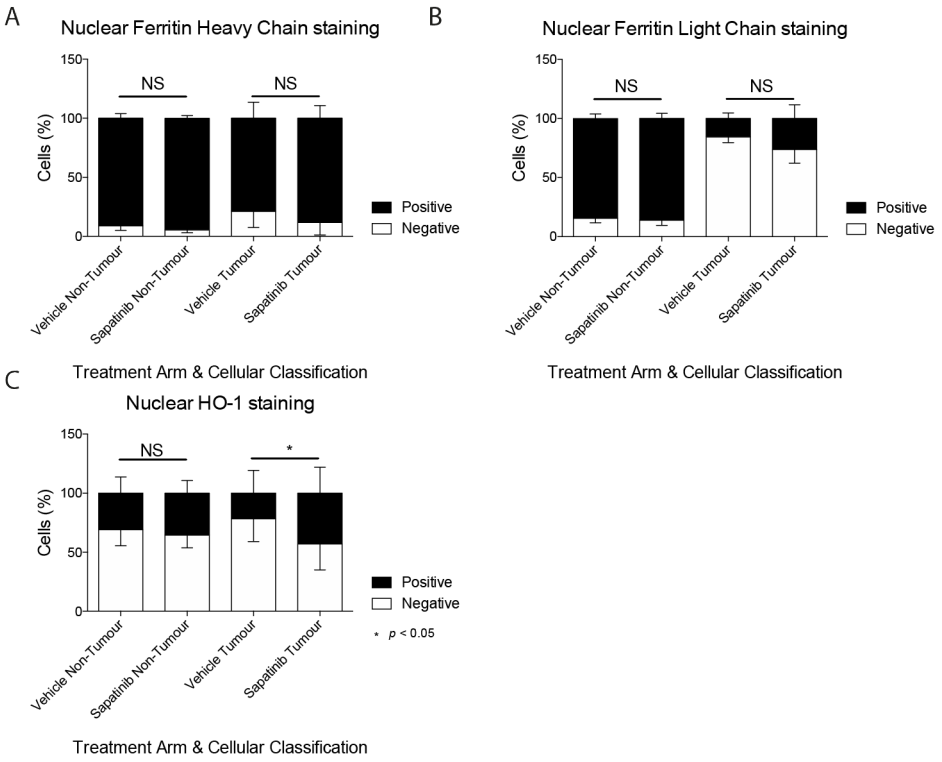


**Figure 4.9. Sapatinib-treated tumours from MMTV-NIC-PTEN$^{+/-}$ mice have increased nuclear heme oxygenase-1.** Immunohistochemistry (IHC) was performed on tumours from MMTV-NIC-PTEN$^{+/-}$ mice treated with vehicle or sapatinib. Quantification of nuclear **(A)** ferritin heavy chain, **(B)** ferritin light chain and **(C)** heme oxygenase-1 (HO-1) IHC staining by Definiens Architect. Vehicle non-tumour was compared with sapatinib non-tumour, vehicle tumour was compared with sapatinib tumour. Results presented as mean ± standard deviation. Kruskal-Wallis test, Dunn's post-hoc, not significant = NS, $p$<0.05=*. Detailed results can be found in table A.6.

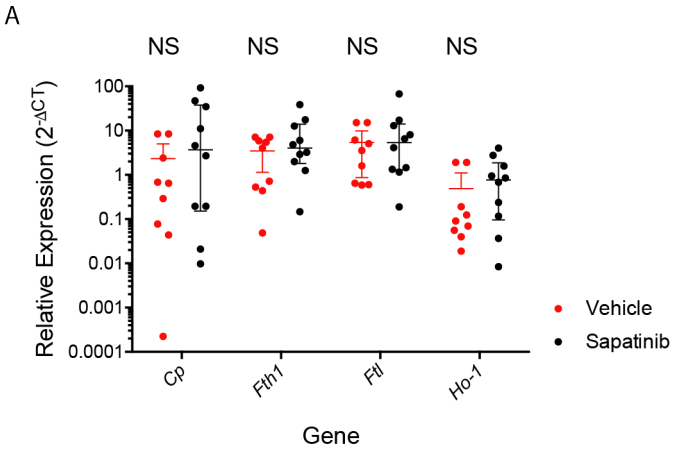


**Figure 4.10. No difference can be seen in levels of ceruloplasmin, heme oxygenase-1 or ferritin heavy and light chains at the transcript level. (A)** Quantitative PCR was performed on tumours from MMTV-NIC-PTEN$^{+/-}$ mice treated with vehicle (n=9) or sapatinib (n=10). Ceruloplasmin (*Cp*), ferritin heavy chain (*Fth*), ferritin light chain (*Ftl*) and heme oxygenase-1 (*Ho-1*) messenger RNA (mRNA) levels were analysed and normalised to levels of $\beta$-2 microglobulin (*B2m*) mRNA. Results presented as scatter plot with median ± interquartile range. Two-tailed Mann-Whitney tests, not significant = NS. Detailed results can be found in table A.5.

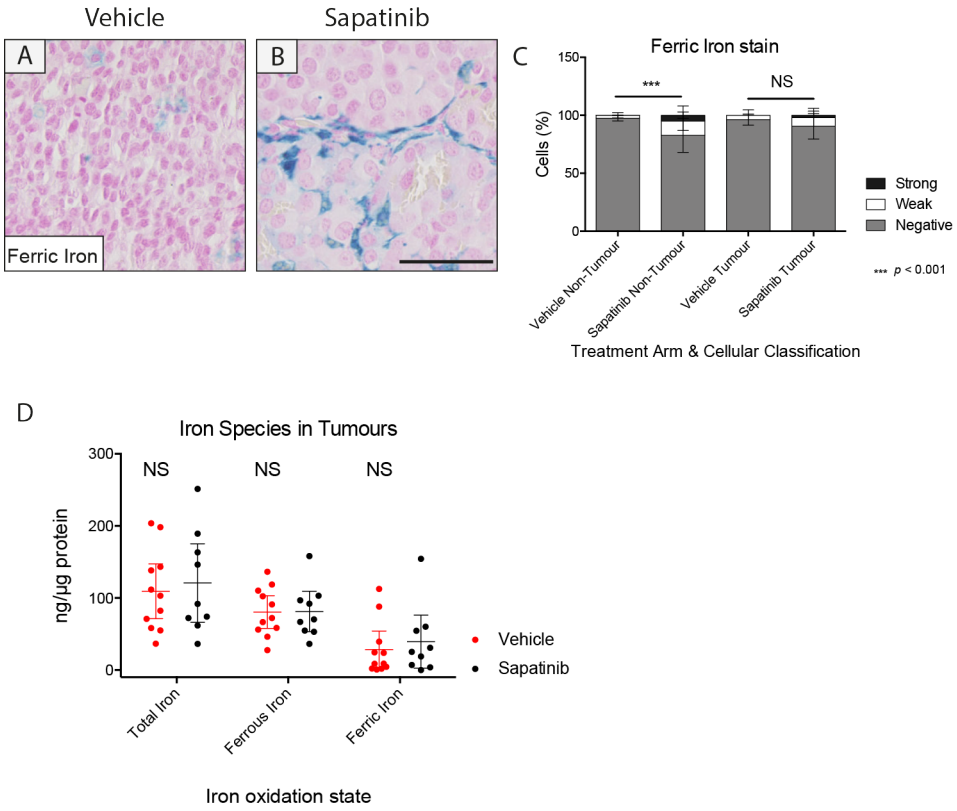


**Figure 4.11. Ferric iron deposits can be seen in the non-tumour tissue surrounding sapatinib-treated tumours.** Perls' ferric iron stain was performed on tumours from MMTV-NIC-PTEN$^{+/-}$ mice treated with vehicle (n=19) or sapatinib (n=10). **(A-B)** Representative Perls' ferric iron stain. Scale bar: 50 $\mu$m. Quantification of **(C)** Perls' ferric iron stain by Definiens Architect. Vehicle non-tumour was compared with sapatinib non-tumour, vehicle tumour was compared with sapatinib tumour. Results presented as mean $\pm$ standard deviation. Kruskal-Wallis test, Dunn's post-hoc test, not significant = NS, $p$<0.001=***. **(D)** An iron assay was performed on tumours from vehicle-treated (n=11) and sapatinib-treated (n=9) mice. Iron levels were normalised to protein content. Results presented as scatter plot with median $\pm$ interquartile range. Kruskal-Wallis test, Dunn's post-hoc test, not significant = NS. Detailed results can be found in table A.5 and table A.6.

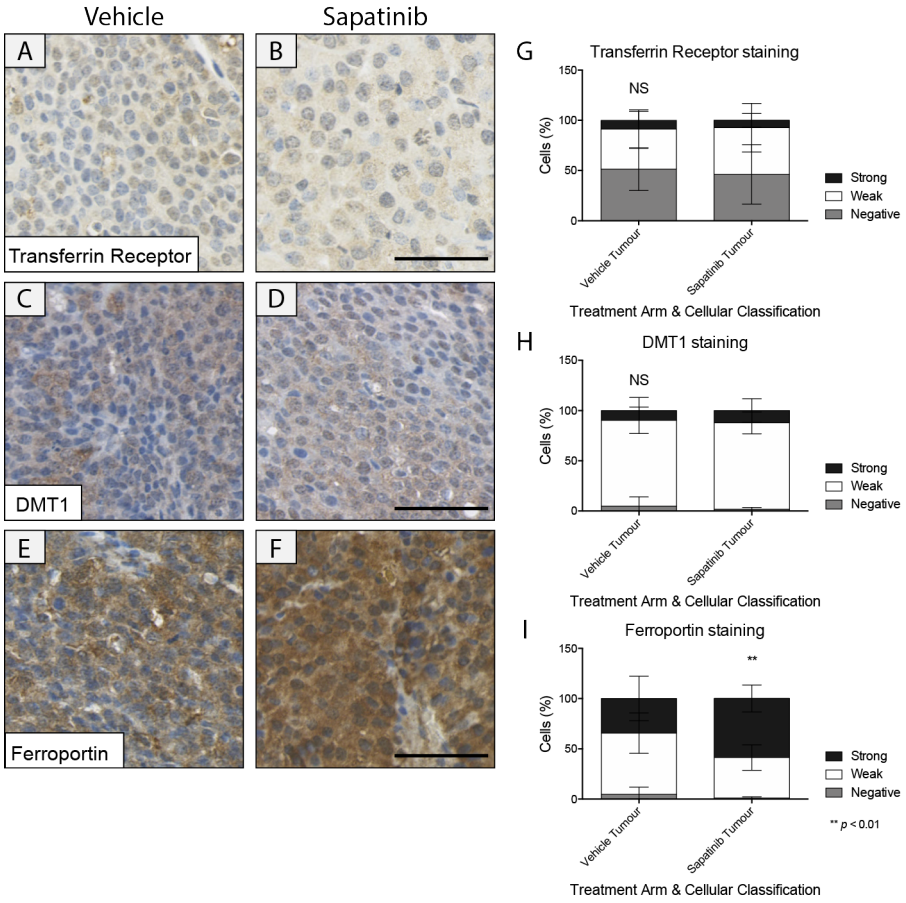


**Figure 4.12. Sapatinib-treated MMTV-NIC-PTEN$^{+/-}$ tumours have increased levels of iron exporter, ferroportin, in tumour cells.** Representative immunohistochemical (IHC) staining of **(A–B)** transferrin receptor (vehicle: n=26; sapatinib: n=11), **(C–D)** divalent metal transporter 1 (DMT1; vehicle: n=25; sapatinib: n=9) and **(E–F)** ferroportin (vehicle: n=25; sapatinib: n=11). Scale bar: 50 $\mu$m. Quantification of **(G)** transferrin receptor, **(H)** DMT1 and **(I)** ferroportin by Definiens architect. Results presented as mean $\pm$ standard deviation. Two-tailed Mann-Whitney test, not significant = NS, $p$<0.01=**. Detailed results can be found in table A.5.

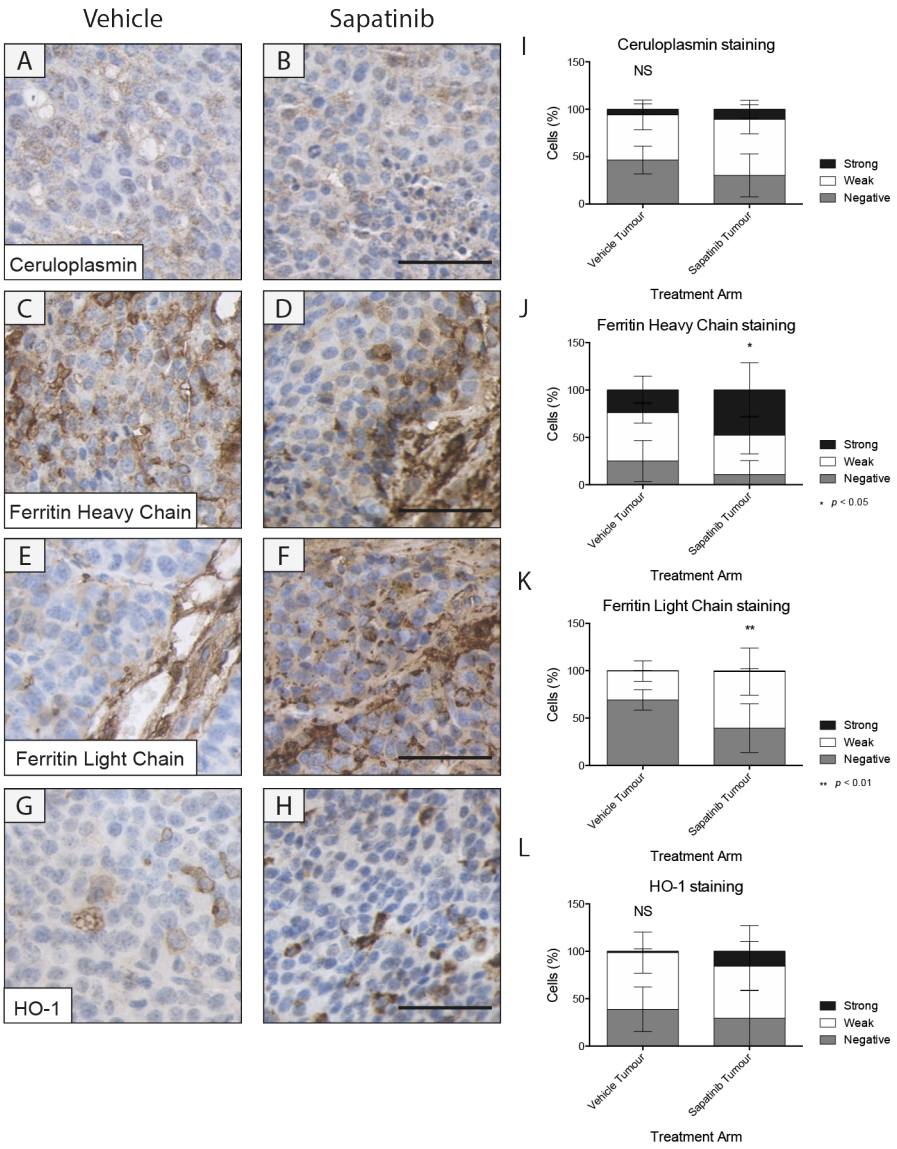


**Figure 4.13. Tumours treated with sapatinib for three days have increased ferritin.** Representative IHC staining of **(A–B)** ceruloplasmin (vehicle: n=8; sapatinib: n=19), **(C–D)** ferritin heavy chain (vehicle: n=8; sapatinib: n=15), **(E–F)** ferritin light chain (vehicle: n=8; sapatinib: n=19) and **(G–H)** heme oxygenase-1 (HO-1; vehicle: n=8; sapatinib: n=19). Scale bar: 50 $\mu$m. Quantification of **(I)** ceruloplasmin, **(J)** ferritin heavy chain, **(K)** ferritin light chain and **(L)** HO-1 by Definiens Architect. Results presented as mean $\pm$ standard deviation. Two-tailed Mann-Whitney test, not significant = NS, $p$<0.05=*, $p$<0.01=**. Detailed results can be found in table A.7.

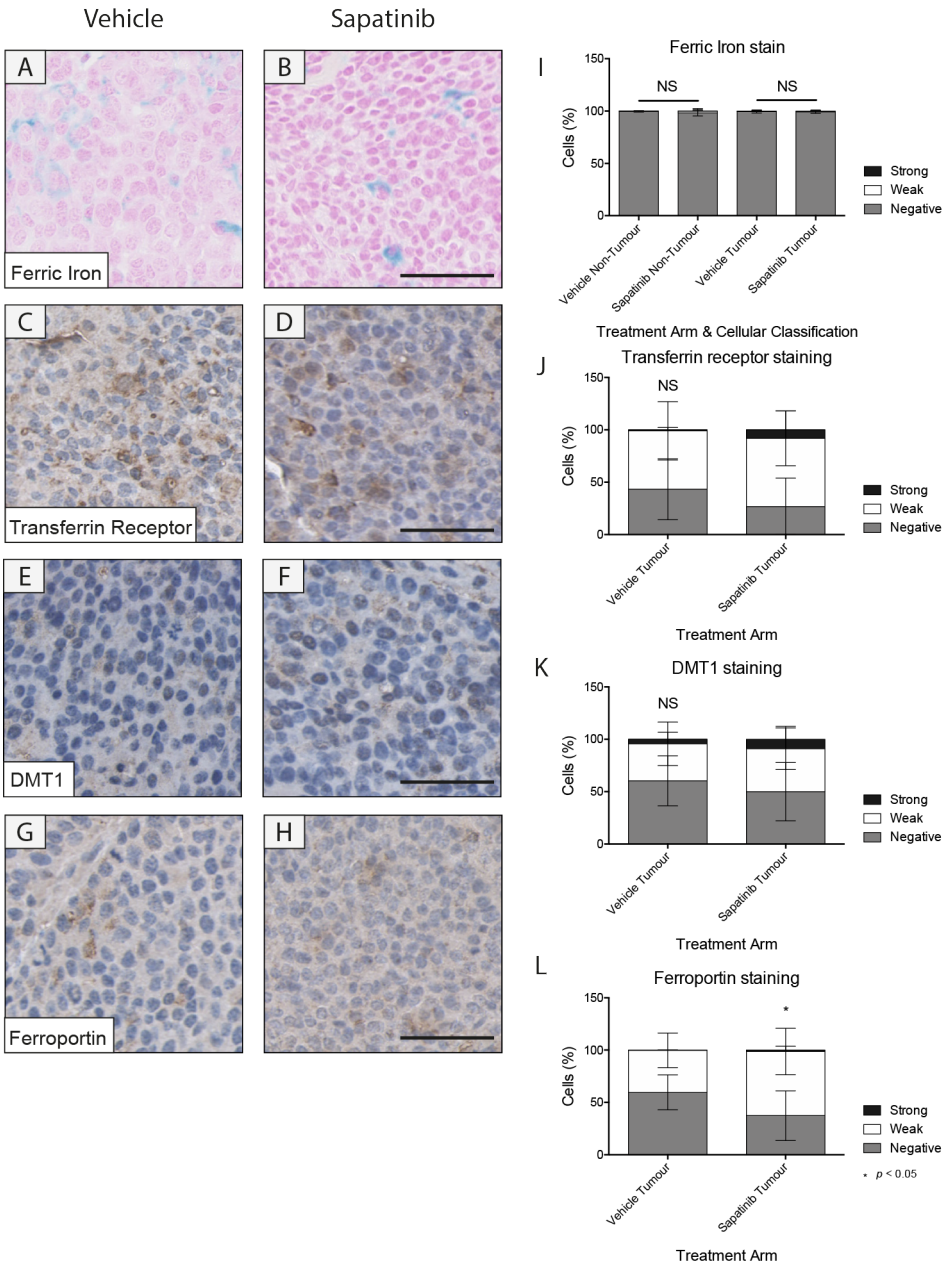


**Figure 4.14. Tumours treated with sapatinib for three days do not show differences in iron deposition but have increased iron exporter ferroportin. (A–B)** Representative Perls' ferric iron stain (vehicle: n=8; sapatinib: n=21). Representative immunohistochemical (IHC) staining of **(C–D)** transferrin receptor (vehicle: n=8; sapatinib: n=19), **(E–F)** divalent metal transporter 1 (DMT1; vehicle: n=8; sapatinib: n=19) and **(G–H)** ferroportin (vehicle: n=8; sapatinib: n=19). Scale bar: 50 $\mu$m. Quantification of **(I)** Perls' ferric iron stain by Definiens Architect. Vehicle non-tumour was compared with sapatinib non-tumour, vehicle tumour was compared with sapatinib tumour. Results presented as mean $\pm$ standard deviation (SD). Kruskal-Wallis test, Dunn's post-hoc test, not significant = NS. Quantification of **(J)** transferrin receptor, **(K)** DMT1 and **(L)** ferroportin by Definiens Architect. Results presented as mean $\pm$ SD. Two-tailed Mann-Whitney test, not significant = NS, $p$<0.05=*. Detailed results can be found in table A.5 and table A.7.

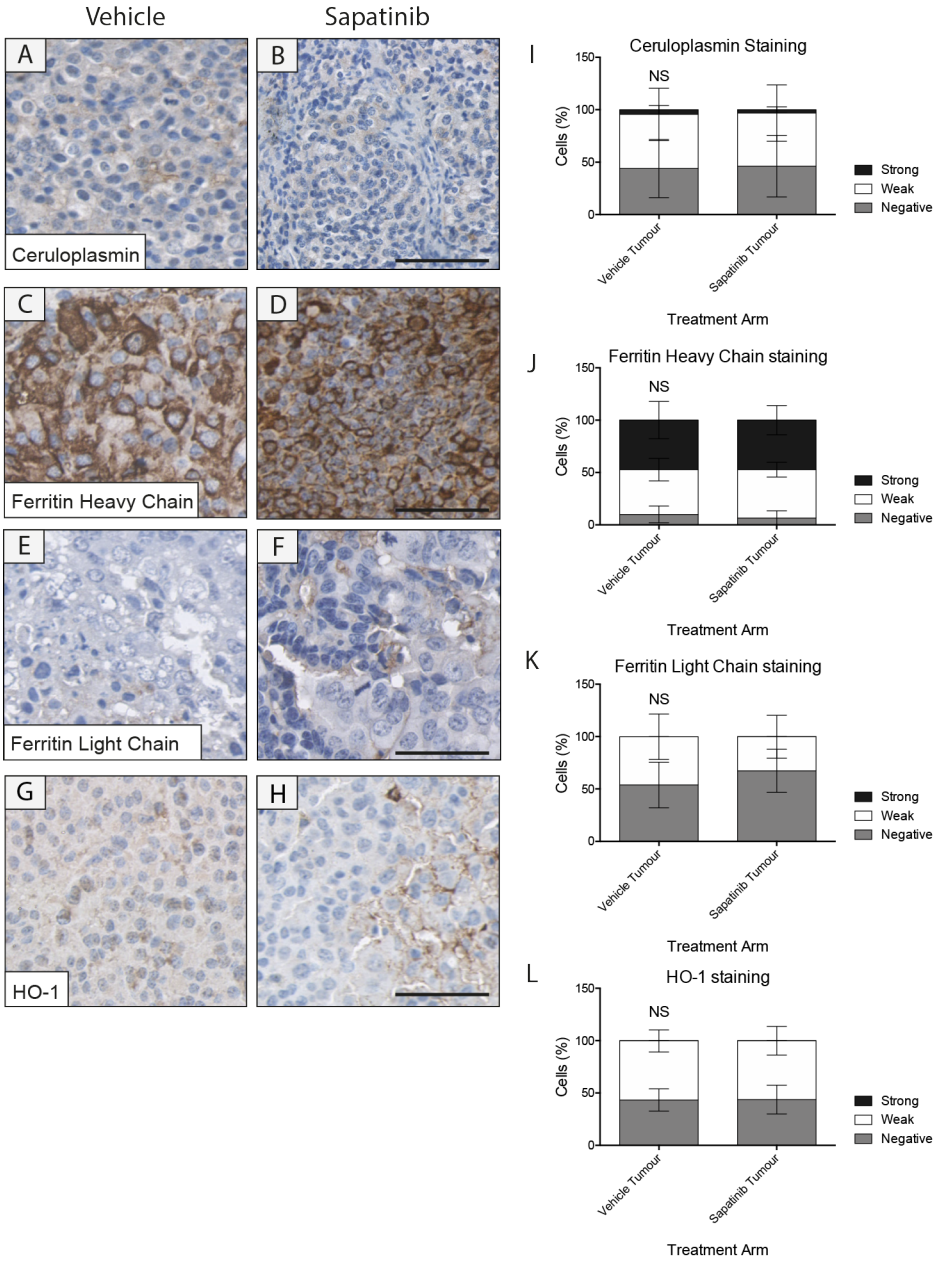


**Figure 4.15. Sapatinib-treated fragment-derived tumours that have not undergone EMT show no differences in proteins involved in iron homeostasis.** Representative immunohistochemical (IHC) staining of **(A–B)** ceruloplasmin (vehicle: n=9; sapatinib: n=3), **(C–D)** ferritin heavy chain (vehicle: n=5; sapatinib: n=2), **(E–F)** ferritin light chain (vehicle: n=7; sapatinib: n=3) and **(G–H)** heme oxygenase-1 (HO-1; vehicle: n=8; sapatinib: n=3). Scale bar: 50 $\mu$m. Quantification of **(I)** ceruloplasmin, **(J)** ferritin heavy chain, **(K)** ferritin light chain and **(L)** HO-1 by Definiens Architect. Results presented as mean $\pm$ standard deviation. Two-tailed Mann-Whitney test, not significant = NS. Detailed results can be found in table A.8.

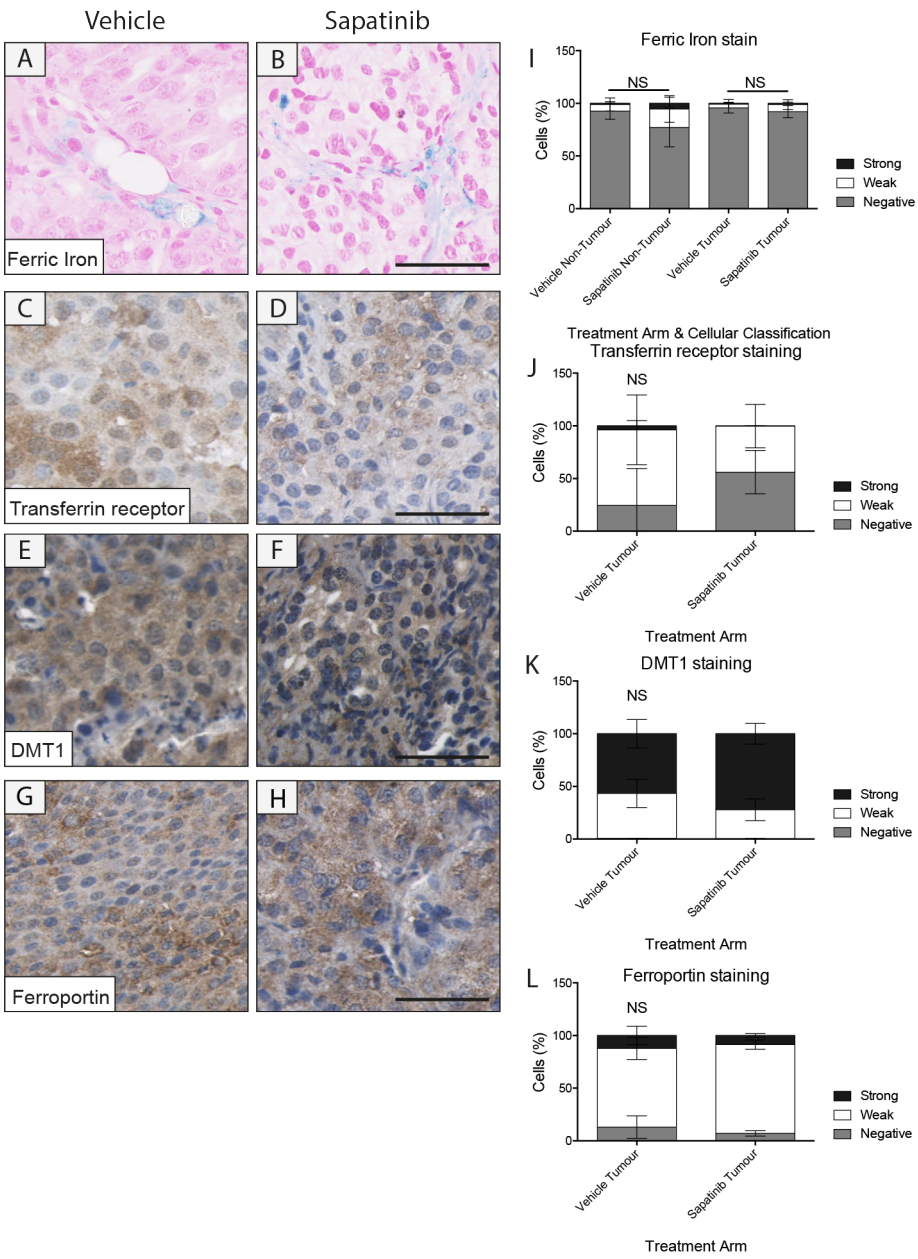


**Figure 4.16. Sapatinib-treated fragment-derived tumours that have not undergone EMT have no changes in ferric iron deposits or iron transporters.** Perls' ferric iron stain was performed on fragment-derived tumours resistant to sapatinib, or treated with vehicle. **(A–B)** Representative Perls' ferric iron stain (vehicle: n=8; sapatinib: n=3). Scale bar: 50 $\mu$m. Representative immunohistochemical (IHC) staining of **(C–D)** transferrin receptor (vehicle: n=6; sapatinib: n=3), **(E–F)** divalent metal transporter 1 (DMT1; vehicle: n=7; sapatinib: n=2) and **(G–H)** ferroportin (vehicle: n=6; sapatinib: n=2). Scale bar: 50 $\mu$m. Quantification of **(I)** Perls' ferric iron stain by Definiens Architect. Vehicle non-tumour was compared with sapatinib non-tumour, vehicle tumour was compared with sapatinib tumour. Results presented as mean $\pm$ standard deviation (SD). Kruskal-Wallis test, Dunn's post-hoc test, not significant = NS. Quantification of **(J)** transferrin receptor, **(K)** DMT1 and **(L)** ferroportin by Definiens Architect. Results presented as mean $\pm$ SD. Two-tailed Mann-Whitney test, not significant = NS. Detailed results can be found in table A.5 and table A.8.

## 4.7 Discussion

Using a GEMM of spontaneous HER2-driven breast cancer to study resistance mechanisms allows cell-intrinsic and cell-extrinsic factors that can influence the development of resistance to be studied.[203] This model accurately recapitulates the histopathology of human cancer, making findings more translatable to the clinic.[204] In this chapter, we have shown sapatinib-treated tumours from a mouse model of HER2-positive breast cancer have perturbed iron storage and increased expression of proteins associated with cellular iron homeostasis.

### 4.7.1 Mouse models of HER2-positive breast cancer

The most common model of HER2-positive breast cancer utilises oncogenic rat *Neu*, under the control of the MMTV promoter to ensure expression is localised to the mammary compartment.[147] MMTV-Neu mice develop rapidly growing mammary tumours, but the initial period before mice develop these tumours is a median 197 days. To overcome this, MMTV-NIC mice are utilised, simultaneously expressing *Neu* and Cre recombinase, with an IRES element, allowing the expression of other oncogenes of interest or inactivation of tumour suppressor genes, such as *Pten*.[149]

MMTV-NIC-PTEN$^{flox/flox}$ mice develop mammary tumours in 43 days, compared with 197 days with no loss of *Pten*.[149] In our model, MMTV-NIC-PTEN$^{+/-}$ mice develop tumours in a median of 102 days.[84] This longer latency period likely reflects the time taken to acquire a 'second hit' before tumour progression.[205] As mentioned in chapter 3, loss or reduction of PTEN results in worse progression-free survival and increased resistance to targeted therapies.[109] This resistance profile is seen in the MMTV-NIC-PTEN$^{flox/flox}$ model: the absence of PTEN renders tumours *de novo* resistant to trastuzumab and lapatinib, which can be targeted with AKT and MAPK inhibitors.[176,206] Using a heterozygous *Pten* model allows the investigation of resistance mechanisms in tumours that have retained some expression of PTEN (fig 4.4).

### 4.7.2 Modelling resistance to HER2-targeted therapies

Heterogeneity within tumours presents a unique challenge for clinicians.[207] Despite similar histopathology, tumours can be comprised of many different clones with different mutational landscapes.[208–211] Once treatment has begun, resistant clones may emerge and become the dominant clonal population within a tumour.[210] This may have occurred in this model, as strong HO-1 could be seen in some cells within tumours treated with sapatinib for three days, although the majority did not have increased expression and were comparable to vehicle-treated tumours (fig 4.13).

The intratumoural heterogeneity in the MMTV-NIC-PTEN$^{+/-}$ model is advantageous, as this more accurately reflects patients' disease.[209,211] Unlike the sapatinib-resistant fragment-derived tumour mouse model, sapatinib-treated spontaneous tumours did not undergo EMT (fig 4.3). This may also reflect different clonal populations within the tumour giving rise to different resistance mechanisms.[212] In particular, the different treatment regimens between the two models may have encouraged the development of different resistance mechanisms; in fragment-derived tumours, the cyclical treatment regimen allowed tumours time to recover from treatment and adapt over time. Meanwhile, the constant treatment of the spontaneous tumours did not allow for this. Thus, different clonal populations present in the fragment-derived and spontaneous tumours prior to treatment may have had selective advantages when exposed to the differing treatment regimens.

Due to the nature of the MMTV-NIC-PTEN$^{+/-}$ spontaneous tumour model, it is not possible to fully elucidate whether the resistance seen in these tumours is *de novo* or acquired resistance. The fragment tumour model (chapter 3) represents a model of acquired resistance; the treatment regimen used promotes the development of acquired resistance by allowing the tumours to grow after a period of response, until tumours no longer responded and grew through sapatinib treatment.[84]

It is possible that some tumour cells in the MMTV-NIC-PTEN$^{+/-}$ spontaneous model were *de novo* resistant.[213] However, the long latency period seen before rapid growth (fig 4.1 C) could be due to the time taken for the tumours to acquire resistance. With the data currently available, it is difficult to say if these tumours had *de novo* or acquired

resistance. Increases in some proteins associated with cellular iron homeostasis were seen after short-term treatment with sapatinib. These initial changes may represent *de novo* resistance in some clonal populations. However, changes associated with acquired resistance may begin soon after treatment initiation.

Signalling downstream of HER2 may have been necessary tumour cells to survival and failure to maintain signalling may have led to cell death and tumour regression in the tumours which responded to drug and were no longer palpable. However, due to the lack of tissue samples from responding or fully regressed tumours, it is not possible to conclude what differences may have lay between tumours which progressed and regressed. As each mouse is capable of developing up to ten tumours simultaneously, it can be difficult to fully assess each tumour which presents.

### 4.7.3 Increased cell size does not indicate apoptosis in sapatinib-treated tumours

Resistance to cancer therapies is classed as the failure of cancer cells to respond to a drug intended to kill or weaken them.[213] With this in mind, most sapatinib-treated tumours can be classed as resistant due to their progressive disease status (fig 4.1 B), as stated in Eisenhauer et al.[193].

Increased cell size (oncosis) could be seen in sapatinib-treated tumours, whereas vehicle-treated and untreated tumours did not have oncosis (fig 4.2 F). Oncosis can be caused by many things, but its relevance in cancer is still undetermined.[214] Cell size can be altered when cells are beginning to enter a cell death pathway.[215]

Apoptosis is associated with a smaller cell size, as cells begin to fragment and apoptotic bodies are phagocytosed.[216–218] Thus, it is reasonable to assume that cells in sapatinib-treated tumours are not undergoing apoptosis. However, without further investigation by assessing levels of cleaved caspase 3, associated with the irreversible stage of apoptotic cell death,[219] we are unable to definitively conclude whether sapatinib-treated tumours have reduced apoptosis or not.

Lapatinib acts by halting cell-cycle progression.[220] Treatment of BT474 and SKBR3 HER2 breast cancer cell lines with lapatinib have shown an increase in anti-apoptotic protein B-cell lymphoma-extra large (Bcl-xL).[221] Thus, it is reasonable to assume that sapatinib-treated tumours may have similar changes, evading regulated cell death. However, no significant changes could be seen in proteins associated with apoptosis by RPPA (fig 4.6).

Oncosis has been linked to non-apoptotic regulated cell death and is a morphological feature of necroptosis.[215] During necroptosis, organelle swelling, plasma membrane rupture and chromatin condensation can also be seen.[215,222] It is possible that sapatinib-treated cells have a larger size due to entering the reversible stage of necrosis. This will be investigated more fully in the following chapters. In another form of cell death, ferroptosis, one defining morphological feature is oncosis, as well as shrinking mitochondria and bioenergetic changes.[223]

In normal cells, increased nuclear size strongly correlates with polyploidy, but this correlation is not as strong in cancer cells.[214] However, in normal physiology and cancer, increased nuclear size does link more directly to overall cell size and cytoplasmic content. As cell size is increased, it is expected that nuclear size would also be increased in sapatinib-treated tumours due to the correlation between nuclear and cell size.[214]

### 4.7.4 Sapatinib is inhibiting pathways downstream of HER2

Previous work by Creedon et al.[84] has shown decreased phospho-AKT/AKT in both MMTV-NIC-PTEN$^{+/-}$ and MMTV-NIC-PTEN$^{+/+}$ mice treated with sapatinib for three days. These results are in accordance with the results in this chapter which show decreased phospho-AKT by IHC and RPPA (fig 4.5, 4.6). This is consistent with the expected pathway inhibition resulting from the inhibition of HER2 phosphorylation as a consequence of sapatinib treatment.

MAPK pathway signalling is often increased due to increased HER2 signalling. This is mainly, but not exclusively, activated upon EGFR/HER2 heterodimer signalling. RAS GTPase is activated by phosphorylated EGFR/HER2, resulting in a phosphorylation

cascade through RAF, MEK and ERK1/2. This then leads to transcriptional regulation of cell cycle progression by proteins such as c-MYC and CREB.[224]

Previous published data in the MMTV-NIC-PTEN$^{+/-}$ model showed decreased levels of phospho-ERK.[84] The results presented here show similar levels of phospho-ERK across all tumours (fig 4.5, 4.6). However, in Creedon et al.[84], changes were seen after short-term treatments, whereas the data presented here are from long-term treatment with sapatinib. It is likely that tumours initially responding to sapatinib would have decreased phospho-ERK and phospho-AKT signalling, but upon development of resistance, these signalling pathways may become active again.

In HER2-positive cell lines, high EGFR and low HER3 expression levels have been shown to correlate with enhanced MAPK pathway dependence and lower PI3K/AKT pathway signalling.[225] Using the same classifications used in Kirouac et al.[225], more dependence on the PI3K/AKT pathway compared with the MAPK pathway would be predicted in the MMTV-NIC-PTEN$^{+/-}$ model.

This supports the finding that levels of ERK phosphorylation did not change, as previous characterisation of 3-day treatments has shown undetectable levels of EGFR and no change in levels of HER3 after sapatinib treatment.[84,165] However, Kirouac et al.[225] did not investigate the signalling changes that may occur in HER2-positive breast cancers once treated with HER2-targeted therapies. Thus, it is difficult to fully predict which signalling changes may be utilised by our model using this classifier.

### 4.7.5 Resistance to sapatinib is associated with an iron storage phenotype in MMTV-NIC-PTEN$^{+/-}$ mice

As iron has been shown to be associated with increased tumour growth and cancer risk,[226–228] treatment with iron chelating agents would disrupt the pro-proliferative effects of iron. However, increased free iron within cells is key for ferroptosis to occur. In these circumstances, iron chelation would result in less ferroptotic cell death. The results presented in this chapter point towards altered iron storage as a mechanism to avoid cell death, with no evidence of lower proliferation in sapatinib-treated tumours despite extracellular iron deposition. Additionally, levels of iron were similar between treatment

groups when levels of iron species were assessed; this is likely due to the differences in technique: Perls' stain is performed on a fixed tissue section and assesses levels of free ferric iron, whereas the iron assay was performed on a piece frozen tissue and assesses all iron present in the sample.

Dysregulation of the hepcidin-ferroportin axis results in tissue-specific iron overload; decreased levels of hepcidin, HO-1 and ceruloplasmin have all shown similar iron deposition phenotypes.[135,229–231] On the contrary, our data show iron deposition with increased levels of HO-1, ceruloplasmin and ferroportin (fig 4.8, 4.11, 4.12). This highlights the differences that can occur in different pathologies and model systems. Of note is the location of the iron: in these studies, iron can be seen within the cells,[135,229,230] whereas in our model, the iron is deposited extracellularly (fig 4.11 A and B).Wu et al.[232] evidenced that increased resistance to cisplatin in ovarian cancer cell lines was associated with expression of NRF2. However, they noted NRF2 and ferroportin expression were inversely correlated. Additionally, overexpression of ferroportin reversed NRF2-induced resistance. These results contradict our own, which show increased HO-1, an NRF2 target gene,[233] and increased ferroportin.

### 4.7.6 Iron-associated proteins may protect cells from oxidative damage

Increased ferric iron deposits outside of the tumour cells may aid in avoiding ferroptosis, an iron-dependent form of cell death characterised by oncosis, lipid peroxidation and shrunken mitochondria.[223,234] HO-1 has been shown to protect against ferroptotic cell death,[235] and is part of the NRF2-induced oxidative stress response, resulting in the removal of reactive oxygen species (ROS).[233]

Despite having higher levels of ferric iron deposited in non-tumourous tissue, sapatinib-treated tumours may contain fewer ferritin and hemosiderin complexes which would not be identified by Perls' ferric iron stain.[236] This is evident when assessing the total iron species present in the tumours, as no difference could be seen between treatment groups in levels of total, ferrous or ferric iron (fig 4.11). Nuclear HO-1 has been previously linked to a reduction in the oxidative stress response via transcriptional activation of

several factors involved in the oxidative stress response and modulation of NRF2, a key transcriptional activator in response to increased oxidative stress.[200,237]

HO-1 could be acting to protect the cell from damage caused by ROS. GO terms identified as down-regulated in sapatinib-treated tumours compared with vehicle-treated tumours are indicative of reduced oxidative stress in sapatinib-treated tumours (fig 4.7). With this in mind, it is possible that nuclear HO-1 is protecting cells against damage from ROS. This will be further investigated in the following chapters.

Ceruloplasmin can be membrane bound or secreted and is involved in converting ferrous iron to ferric iron.[134] This supports the hypothesis that sapatinib-treated tumours have increased iron export through ferroportin (fig 4.12), which is also evidenced by the increased extracellular iron deposition seen in these tumours (fig 4.11).

As there are differences in where ferritin heavy and light chain are located within the cells, it is unlikely that the two subunits are forming ferritin complexes with ferric iron. This would result in free iron being available in the cells, which would cause damage to cellular components through the formation of hydroxyl radicals.[133,238]

### 4.7.7 Summary

To summarise, our data reveal a role for iron homeostasis *in vivo* in response to sapatinib. We have shown that mice treated with the HER2-targeted tyrosine kinase inhibitor, sapatinib, develop iron deposits in the surrounding non-tumour tissue and show increased levels of iron homeostasis related proteins, ceruloplasmin and HO-1, as well as the iron export protein ferroportin. Together, this may give rise to protection from oxidative stress and increased intracelluar ferrous iron induced by sapatinib treatment (fig 4.17).

Future studies will focus on the mechanistic role that HO-1 is playing with respect to resistance and examine the possibility of iron modulation to overcome resistance *in vivo*. Development of *in vitro* models of HO-1 overexpression and further investigation of HO-1's role *in vivo*, will allow a better understanding of the potential links between the proteins identified and perturbed iron homeostasis.

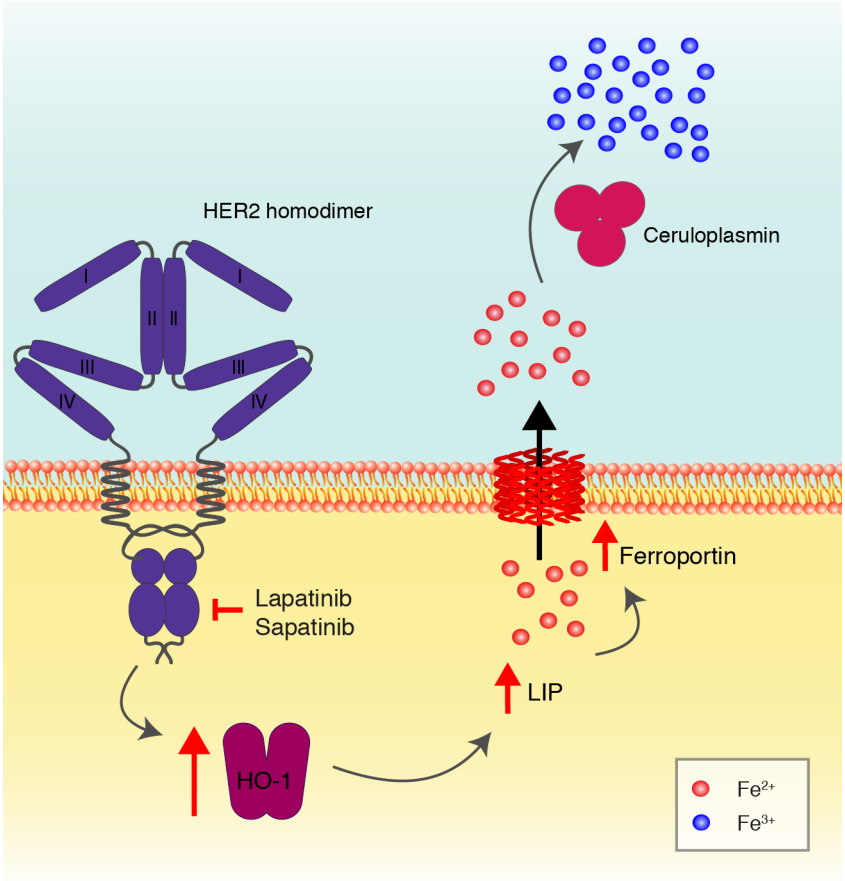


**Figure 4.17. Sapatinib-treated spontaneous tumours have increased HO-1, ferroportin and ceruloplasmin.** We hypothesise that after treatment with HER2-target tyrosine kinase inhibitors, heme oxygenase-1 (HO-1) becomes upregulated, increasing free iron in the labile iron pool (LIP). To avoid oxidative damage from free ferrous iron ($Fe^{2+}$), ferroportin transports the iron from the cell where it is converted to ferric iron ($Fe^{3+}$) by ceruloplasmin and deposited extracellularly.

# Chapter 5

# Altering dietary iron intake affects sapatinib resistance

Many cancer patients initially present with functional iron deficiency (FID), which may or may not be related to anaemia. These patients have worse Eastern Cooperative Oncology Group (ECOG) scores and survival outcomes than patients without FID at the time of diagnosis.[239] As sapatinib-treated tumours from MMTV-NIC-PTEN$^{+/-}$ displayed altered iron storage, we investigated the role that altered dietary iron may have on the development of resistance to sapatinib *in vivo*.

To study the effect of dietary iron intake, MMTV-NIC-PTEN$^{+/-}$ mice were randomised to receive a control or iron-deficient diet once a palpable tumour developed. After four days, mice were randomised to receive vehicle (1% Tween80 in PBS; p.o., q.d.) or sapatinib (100 mg/kg, with 1% Tween80 in PBS; p.o., q.d.).

This chapter will explore these subsequent aims:

- Characterise tumour growth and response to sapatinib in mice fed an iron-deficient diet.
- Assess changes associated with iron homeostasis seen in chapter 4.

## 5.1 Tumour growth is not impeded by an iron-deficient diet

Detailed results for this chapter can be found in tables A.9–A.10.

MMTV-NIC-PTEN$^{+/-}$ mice were randomised to receive a control or iron-deficient diet once a tumour was $\geq$0.1 cm$^3$. Four days after the diet commenced, mice were randomised to receive vehicle (1% Tween80 in PBS; p.o., q.d.) or sapatinib (100 mg/kg, with 1% Tween80 in PBS; p.o., q.d.). Once any tumour reached 15 mm in diameter, mice were sacrificed.

Vehicle-treated mice on a iron-low control diet had a median survival time similar to vehicle-treated mice on an iron-deficient diet (fig 5.1 A and B; median survival including censored: vehicle iron-low control diet: 21 days; vehicle iron-deficient diet: 22.5 days; NS; median tumour-related survival: vehicle iron-low control diet: 21 days; vehicle iron-deficient diet: 22.5 days; NS). Sapatinib-treated mice on both diets had a longer

median survival times than vehicle-treated mice (fig 5.1 A and B; median survival including censored: sapatinib iron-low control diet: 133 days; sapatinib iron-deficient diet: 56 days; NS; median tumour-related survival: sapatinib iron-low control diet: 82.5 days; sapatinib iron-deficient diet: 38 days; NS).

Although there was a trend towards decreased survival in sapatinib-treated mice on an iron-deficient diet, this was not significant. Due to this, we looked at growth of the individual tumours within the different cohorts. Growth kinetics of index tumours from each mouse sacrificed due to tumour burden shows that tumours from vehicle-treated mice in both diet arms grew rapidly after initial tumour onset (fig 5.2 A and B). Sapatinib-treated mice on a iron-low control diet had two distinct groups; those whose tumours grew through the drug treatment quickly and those with a longer period of latency before growing through the drug treatment (fig 5.2 C). Index tumours from sapatinib-treated mice on an iron-deficient diet had growth more similar to that seen in vehicle-treated mice, with no extended period of latency as seen in sapatinib-treated mice on a iron-low control diet (fig 5.2 D).

Based on guidelines set out in Eisenhauer et al.[193], 151 (86.78%) of all tumours were classed as progressive disease (fig 5.3 A; vehicle iron-low control diet: n=39 [95.12%]; vehicle iron-deficient diet: n=36 [92.31%]; sapatinib iron-low control diet: n=37 [77.08%]; sapatinib iron-deficient diet: n=39 [84.78%]). Nine tumours (5.17%) were between 20% increase in volume and a 30% decrease, classed as stable disease (vehicle iron-low control diet: n=2 [4.87%]; vehicle iron-deficient diet: n=2 [5.13%]; sapatinib iron-low control diet: n=2 [4.17%]; sapatinib iron-deficient diet: n=3 [6.52%]). Four tumours (2.30%) had partial responses to treatment (vehicle iron-low control diet: n=0 [0%]; vehicle iron-deficient diet: n=0 [0%]; sapatinib iron-low control diet: n=3 [6.25%]; sapatinib iron-deficient diet: n=1 [2.08%]). Ten tumours had pCR to treatment (vehicle iron-low control diet: n=0 [0%]; vehicle iron-deficient diet: n=1 [2.56%]; sapatinib iron-low control diet: n=6 [12.50%]; sapatinib iron-deficient diet: n=3 [6.52%]).

Analysis of the percentage volume change from baseline, when each tumour was first palpable, shows that there was a significant difference in tumour volume between vehicle-treated tumours from mice on a iron-low control diet and sapatinib-treated tumours from mice on both a iron-low control diet and an iron-deficient diet (fig 5.3 B). Vehicle-treated

A

i

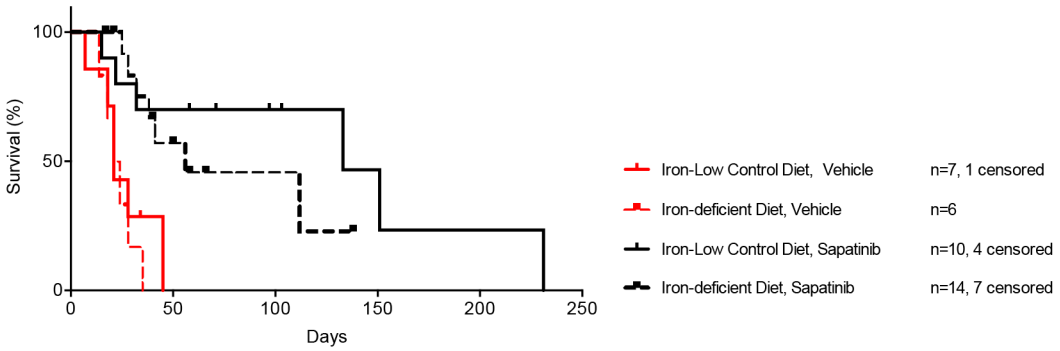


ii

| Group | | Group | Significance |
|---|---|---|---|
| Iron-Low Control Diet, Vehicle | vs | Iron-Deficient Diet, Vehicle | NS |
| | | Iron-Low Control Diet, Sapatinib | * |
| | | Iron-Deficient Diet, Sapatinib | ** |
| Iron-Deficient Diet, Vehicle | | Iron-Low Control Diet, Sapatinib | ** |
| | | Iron-Deficient Diet, Sapatinib | *** |
| Iron-Low Control diet, Sapatinib | | Iron-Deficient Diet, Sapatinib | NS |

B

i

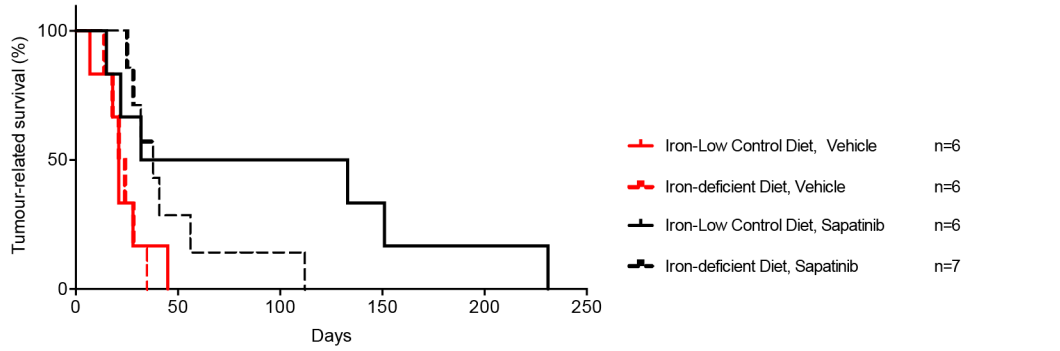


ii

| Group | | Group | Significance |
|---|---|---|---|
| Iron-Low Control Diet, Vehicle | vs | Iron-Deficient Diet, Vehicle | NS |
| | | Iron-Low Control Diet, Sapatinib | NS |
| | | Iron-Deficient Diet, Sapatinib | * |
| Iron-Deficient Diet, Vehicle | | Iron-Low Control Diet, Sapatinib | NS |
| | | Iron-Deficient Diet, Sapatinib | * |
| Iron-Low Control diet, Sapatinib | | Iron-Deficient Diet, Sapatinib | NS |

**Figure 5.1. An iron-deficient diet reduces survival time in sapatinib-treated mice.** MMTV-NIC-PTEN$^{+/-}$ mice on a control or iron-deficient diet were treated with vehicle or sapatinib. The diet began at the onset of the first palpable tumour. Drug treatment began four days after the diet commenced. **(A, i)** Kaplan-Meier curve showing survival time from the commencement of a control or iron-deficient diet in all randomised MMTV-NIC-PTEN$^{+/-}$ mice treated with vehicle or sapatinib. **(A, ii)** Log-rank test comparing each group within (A, i). Not significant = NS, $p$<0.05=*. **(B, i)** Kaplan-Meier curve showing survival time to tumour-related death from the commencement of a control or iron-deficient diet in MMTV-NIC-PTEN$^{+/-}$ mice treated with vehicle or sapatinib. **(B, ii)** Log-rank test comparing each group within (B, i). Not significant = NS, $p$<0.05=*, $p$<0.01=**, $p$<0.001=***.

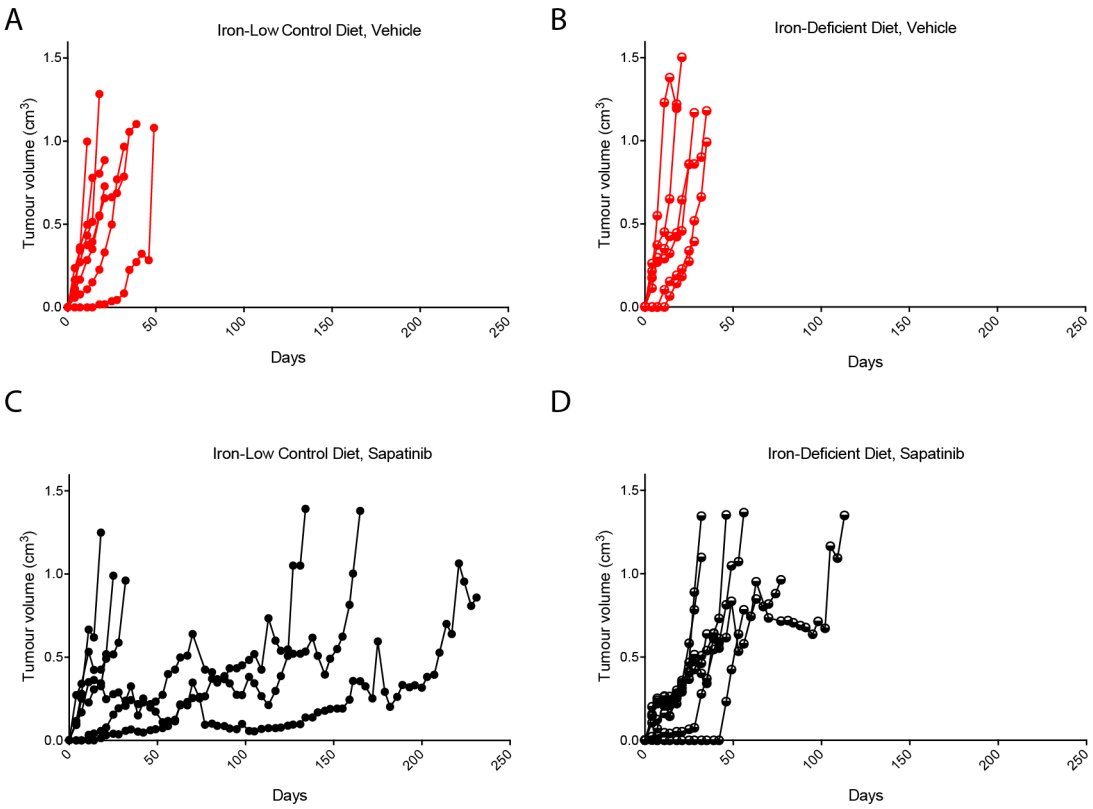


**Figure 5.2. Index tumours from sapatinib-treated mice on an iron-deficient diet have a shorter period of latency compared with sapatinib-treated mice on a iron-low control diet.** Graphs showing the growth curves of index tumours in MMTV-NIC-PTEN$^{+/-}$ mice on a control or iron-deficient diet, treated with vehicle or sapatinib. The diet began at the onset of the first palpable tumour. Drug treatment began four days after the diet commenced. **(A)** iron-low control diet, vehicle treatment (n=6). **(B)** Iron-deficient diet, vehicle treatment (n=6). **(C)** iron-low control diet, sapatinib treatment (n=6). **(D)** Iron-deficient diet, sapatinib treatment (n=7).

tumours from mice on an iron-deficient diet also showed significant differences when compared with sapatinib-treated tumours from mice on a iron-low control diet. However, there was no significant difference between vehicle-treated and sapatinib-treated tumours from mice on an iron-deficient diet.

Despite changes in tumour volume, there was no significant difference in the number of tumours that developed per mouse in each treatment group over the course of the experiment (fig 5.4 A; median number of tumours [CI]: vehicle iron-low control diet: 7 [4.40–9.26]; vehicle iron-deficient diet: 8 [3.78–9.22]; sapatinib iron-low control diet: 5 [1.00–8.00]; sapatinib iron-deficient diet: 4 [2.61–5.10]; NS). However, sapatinib-treated mice on a iron-low control diet had significantly more tumours with pCR or which had a decreasing volume for a minimum of seven days prior to sacrifice compared with vehicle-treated mice on a iron-low control diet, classed as responding (fig 5.4 B; median

A

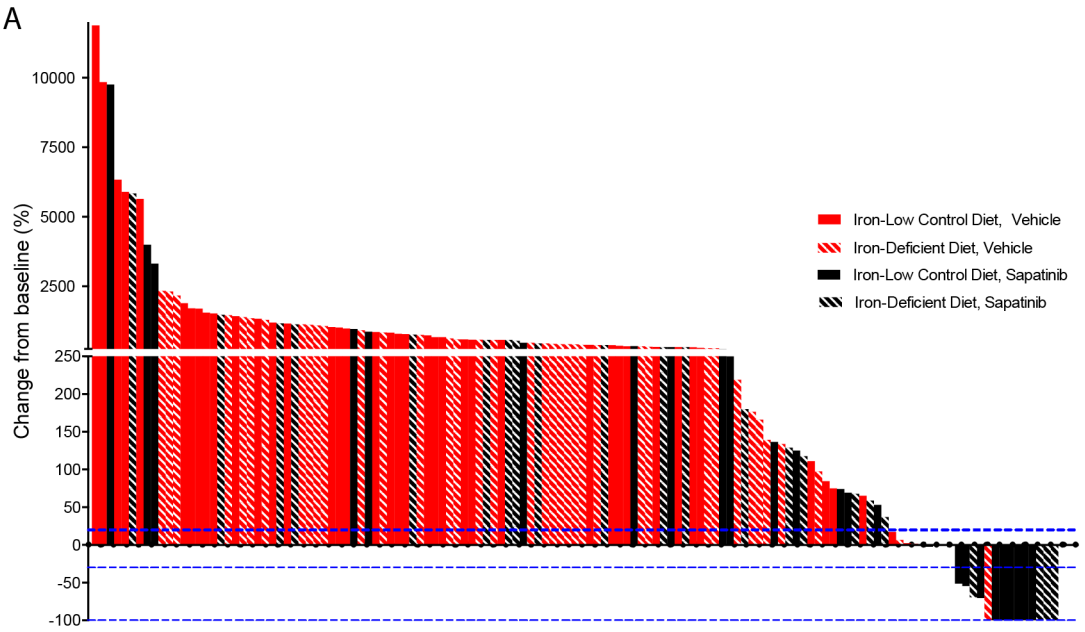


B

| Group | | Group | Significance |
|---|---|---|---|
| Iron-Low Control Diet, Vehicle | vs | Iron-Deficient Diet, Vehicle | NS |
| | | Iron-Low Control Diet, Sapatinib | *** |
| | | Iron-Deficient Diet, Sapatinib | ** |
| Iron-Deficient Diet, Vehicle | | Iron-Low Control Diet, Sapatinib | * |
| | | Iron-Deficient Diet, Sapatinib | NS |
| Iron-Low Control diet, Sapatinib | | Iron-Deficient Diet, Sapatinib | NS |

**Figure 5.3. An iron-deficient diet does not reduce change in tumour volume from baseline compared with a iron-low control diet.** MMTV-NIC-PTEN$^{+/-}$ mice on a control or iron-deficient diet were treated with vehicle or sapatinib. The diet began at the onset of the first palpable tumour. Drug treatment began four days after the diet commenced. **(A)** Waterfall plot showing volume change from baseline (%) of all tumours from MMTV-NIC-PTEN$^{+/-}$ mice on a control or iron-deficient diet, treated with vehicle or sapatinib, sacrificed due to tumour burden. Dotted blue lines represent 20% increase, 30% decrease and 100% decrease in tumour volume from baseline, respectively. **(B)** Kruskal-Wallis test, Dunns post-hoc test comparing tumour volume in each group from (A). Not significant = NS, $p$<0.05=*, $p$<0.01=**, $p$<0.001=***.

tumours [CI]: vehicle iron-low control diet: 0 [0–0]; vehicle iron-deficient diet: 0 [0–2]; sapatinib iron-low control diet: 3 [0–4]; sapatinib iron-deficient diet: 1 [0–2]; $p<0.05$). No significant difference could be seen between other groups.

To look for changes in iron due to the iron-deficient diet, an iron assay was performed to assess changes in the quantities of iron species present in serum. Despite not reaching significance, this showed a trend towards lower quantities of total and ferrous iron in both sapatinib- and vehicle-treated mice on an iron-deficient diet compared with mice on a iron-low control diet (fig 5.5).

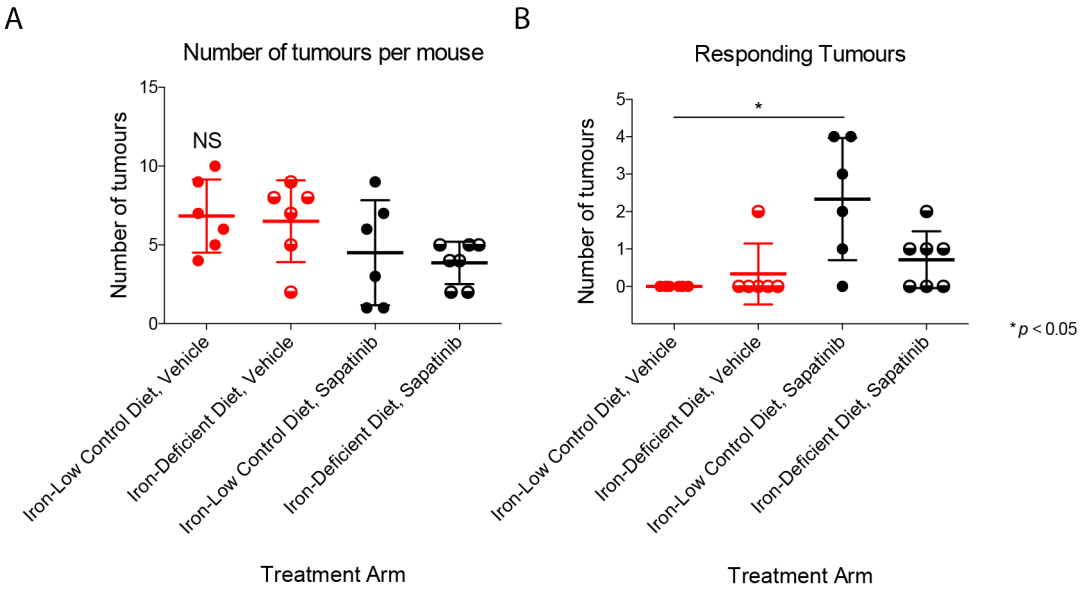


**Figure 5.4. Sapatinib-treated mice on an iron-deficient diet have fewer responding tumours than sapatinib-treated mice on a iron-low control diet.** MMTV-NIC-PTEN$^{+/-}$ mice on a control or iron-deficient diet were treated with vehicle or sapatinib (iron-low control diet, vehicle; n=6; iron-deficient diet, vehicle: n=6; iron-low control diet, sapatinib: n=6; iron-deficient diet, sapatinib: n=7). Drug treatment began four days after the diet commenced. **(A)** Graph showing the number of tumours developed in each treatment group, from the first palpable tumour to time of sacrifice. All groups compared with iron-low control diet, vehicle-treated mice. Results presented as scatter plot with mean ± standard deviation (SD). Kruskal-Wallis test, Dunn's post-hoc test, not significant = NS. **(B)** Graph showing the number of tumours per mouse during the whole treatment period that had fully regressed or had decreasing volume for a minimum of 7 days prior to sacrifice. All groups compared with iron-low control diet, vehicle-treated mice. Results presented as scatter plot with mean ± SD. Kruskal-Wallis test, Dunn's post-hoc test, $p$<0.05=*.

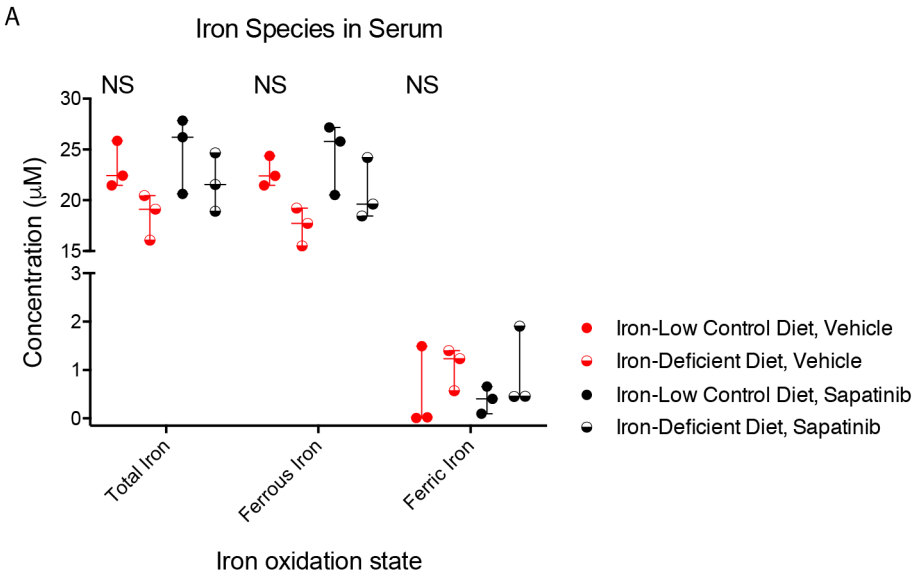


**Figure 5.5. MMTV-NIC-PTEN$^{+/-}$ mice on an iron-deficient diet have similar serum iron levels as mice on a iron-low control diet.** MMTV-NIC-PTEN$^{+/-}$ mice on a control or iron-deficient diet were treated with vehicle or sapatinib. Drug treatment began four days after the diet commenced. **(A)** An iron assay was performed on serum from mice in each treatment group (iron-low control diet, vehicle; n=3; iron-deficient diet, vehicle: n=3; iron-low control diet, sapatinib: n=3; iron-deficient diet, sapatinib: n=3). All groups compared with iron-low control diet, vehicle-treated mice. Results presented as scatter plot with median ± interquartile range. Kruskal-Wallis test, Dunn's post-hoc test, not significant = NS. Detailed results can be found in table A.9.

To summarise, an iron-deficient diet reduced survival time in sapatinib-treated mice but had no effect on tumour growth of vehicle-treated tumours. Additionally, sapatinib-treated mice on an iron-deficient diet had fewer responding tumours than sapatinib-treated mice on a iron-low control diet. Despite the iron-deficient diet, mice showed no significant changes in serum iron levels, but there was a trend towards lower total and ferrous iron.

## 5.2 Tumours responding to sapatinib treatment have changes in iron-related proteins and iron storage

Index tumours from MMTV-NIC-PTEN$^{+/-}$ mice on a control or iron-deficient diet treated with vehicle or sapatinib were analysed by IHC for proteins identified as being involved in cellular iron homeostasis (fig 4.7). This revealed no significant difference in levels of ceruloplasmin in sapatinib-treated tumours as seen in the previous *in vivo* experiment (fig 4.8). Furthermore, the iron-deficient diet had no significant effect on

ceruloplasmin levels. Sapatinib-treated tumours from mice on a iron-low control diet had increased staining, although this did not reach significance (fig 5.6 A–E and K).

Increased HO-1 was found in tumours from sapatinib-treated mice on a iron-low control diet, reflecting the previous *in vivo* experiment (fig 4.8). However, only the responding tumours had significantly increased HO-1, which most likely reflects the large variation within the progressing sapatinib-resistant tumours from these mice (fig 5.6 F–J and L). Index tumours from sapatinib-treated mice on an iron-deficient diet did not have increased HO-1. It was not possible to analyse responding tumours from sapatinib-treated mice on an iron-deficient diet, as material was only available from one tumour. No difference can be seen in levels of ferritin heavy chain (fig 5.7 A–E and K). Tumours from sapatinib-treated mice had a tendency towards increased ferritin light chain staining, but this was not significant (fig 5.7 F–J and L).

Perls' ferric iron stain was used to identify any changes in iron storage as seen in sapatinib-treated tumours (fig 4.11 A–C). This revealed that all sapatinib-treated tumours, on both diets, had increased iron deposition in non-tumour cells, as seen in the previous experiment (fig 5.8 A–J). However, only tumours responding to sapatinib had significantly increased iron within the tumour cells (fig 5.8 E and G). Interestingly, sapatinib-treated tumours from both diets had similar extracellular iron deposits. Despite the changes in iron deposition, no differences could be seen in levels of iron transporters. Levels of transferrin receptor, DMT1 and ferroportin were not significantly different between groups (fig 5.9 A–O, 5.10 A–C).

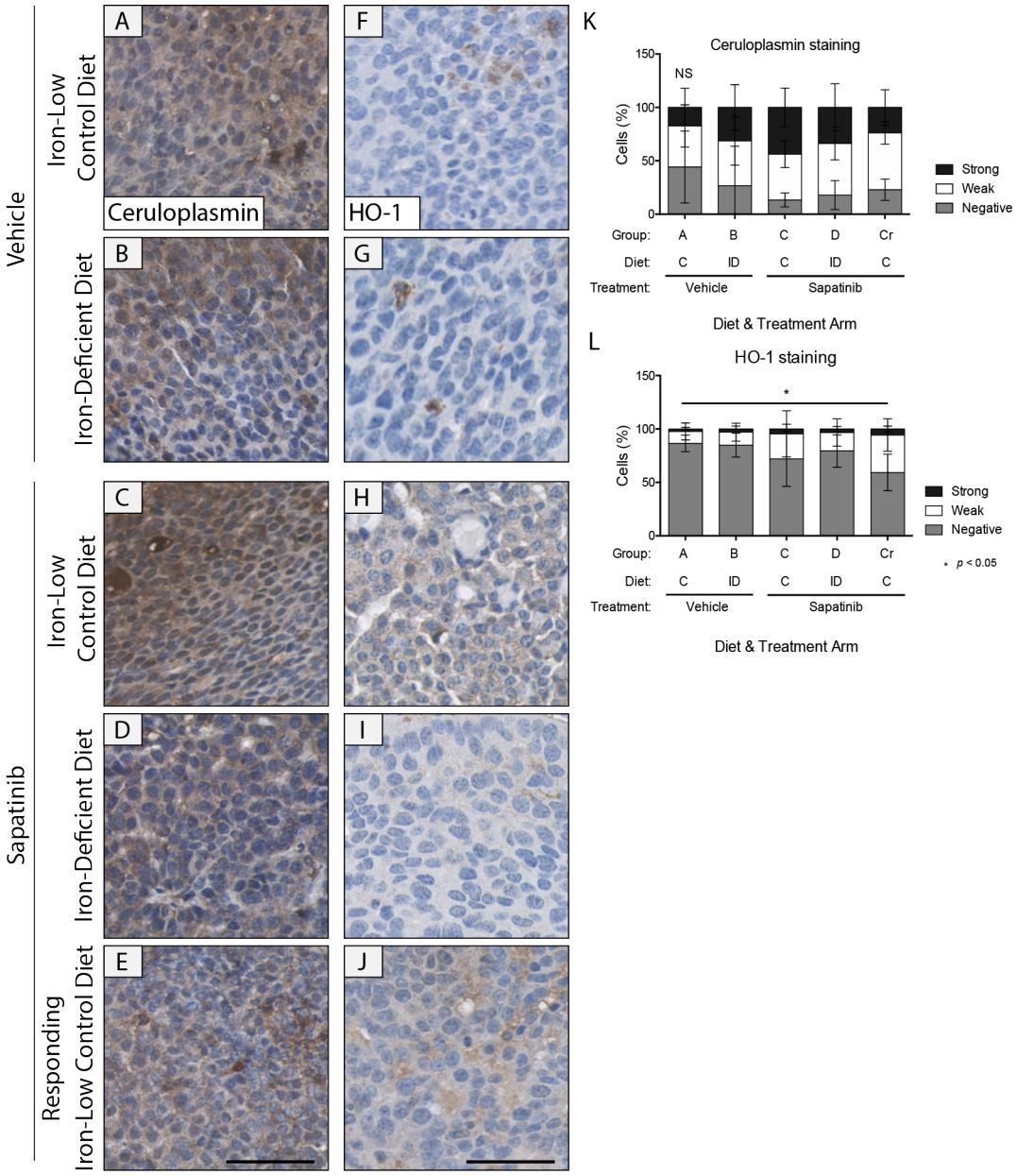


**Figure 5.6. Sapatinib-treated mice on an iron-deficient diet do not have increased HO-1.** MMTV-NIC-PTEN$^{+/-}$ mice on a control (C) or iron-deficient (ID) diet were treated with vehicle or sapatinib. Drug treatment began four days after the diet commenced. Representative immunohistochemical staining of **(A–E)** ceruloplasmin (iron-low control diet, vehicle; group A, n=6; iron-deficient diet, vehicle: group B, n=6; iron-low control diet, sapatinib: group C, n=5; iron-deficient diet, sapatinib: group D, n=5; responding tumours, iron-low control diet, sapatinib; group Cr, n=6) and **(F–J)** heme oxygenase-1 (Group A: n=6; Group B: n=5; Group C: n=6; Group D: n=7; Group Cr: n=6) in index tumours. Scale bar: 50 $\mu$m. Quantification of **(K)** ceruloplasmin and **(L)** HO-1 by Definiens Architect. All groups compared with iron-low control diet, vehicle-treated tumours. Results presented as mean $\pm$ standard deviation. Kruskal-Wallis test, Dunn's post-hoc test, not significant = NS, $p$<0.05=*. Detailed results can be found in table A.10.

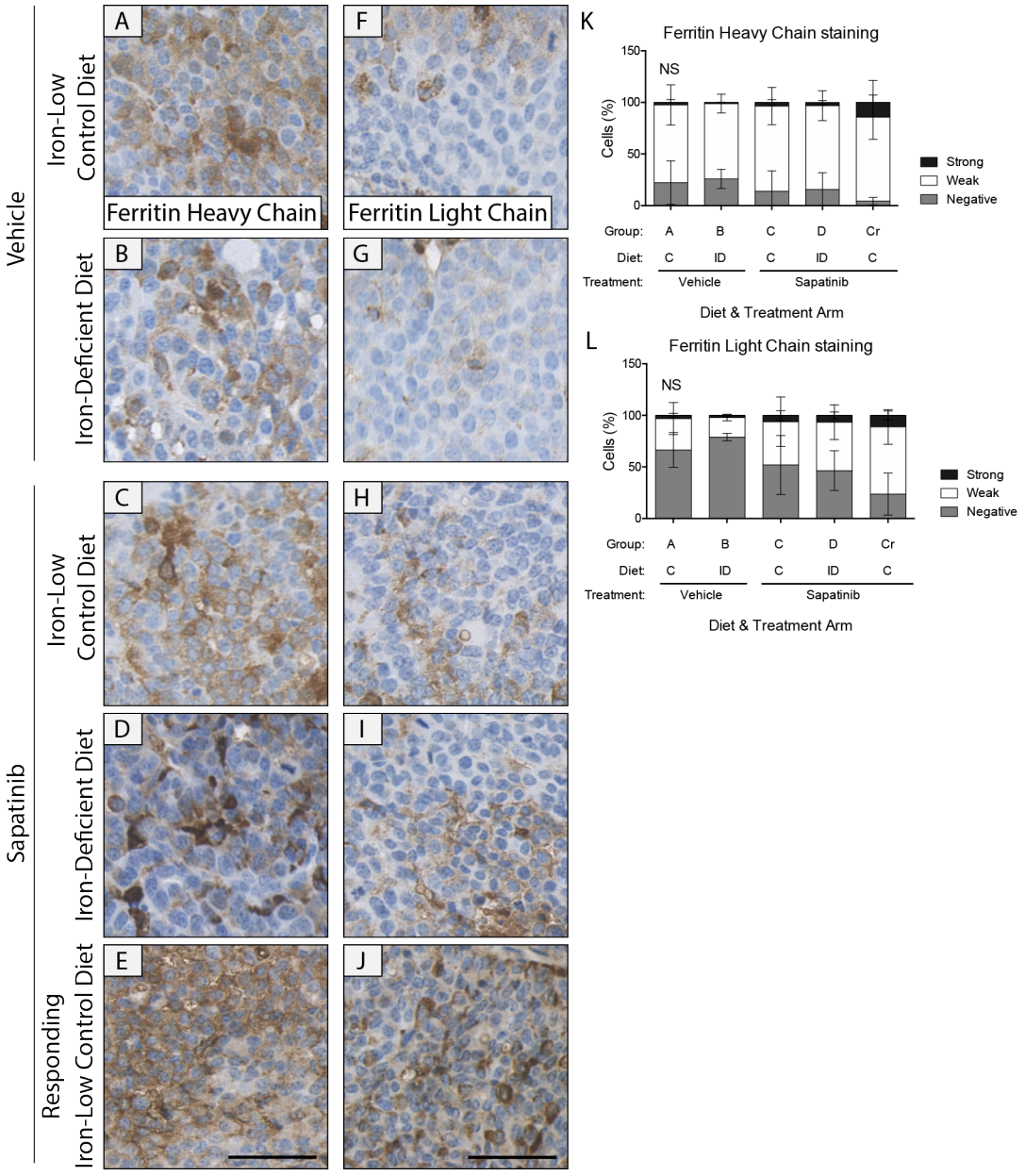


**Figure 5.7. Tumours from sapatinib-treated mice have increased ferritin light chain.** MMTV-NIC-PTEN$^{+/-}$ mice on a control (C) or iron-deficient (ID) diet were treated with vehicle or sapatinib. Drug treatment began four days after the diet commenced. Representative immunohistochemical staining of **(A–E)** ferritin heavy chain (iron-low control diet, vehicle; group A, n=6; iron-deficient diet, vehicle: group B, n=5; iron-low control diet, sapatinib: group C, n=6; iron-deficient diet, sapatinib: group D, n=6; responding tumours, iron-low control diet, sapatinib; group Cr, n=7) and **(F–J)** ferritin light chain (Group A: n=6; Group B: n=5; Group C: n=6; Group D: n=7; Group Cr: n=6) in index tumours. Scale bar: 50 $\mu$m. Quantification of **(K)** ferritin heavy chain and **(L)** ferritin light chain by Definiens Architect. All groups compared with iron-low control diet, vehicle-treated tumours. Results presented as mean $\pm$ standard deviation. Kruskal-Wallis test, Dunn's post-hoc test, not significant = NS. Detailed results can be found in table A.10.

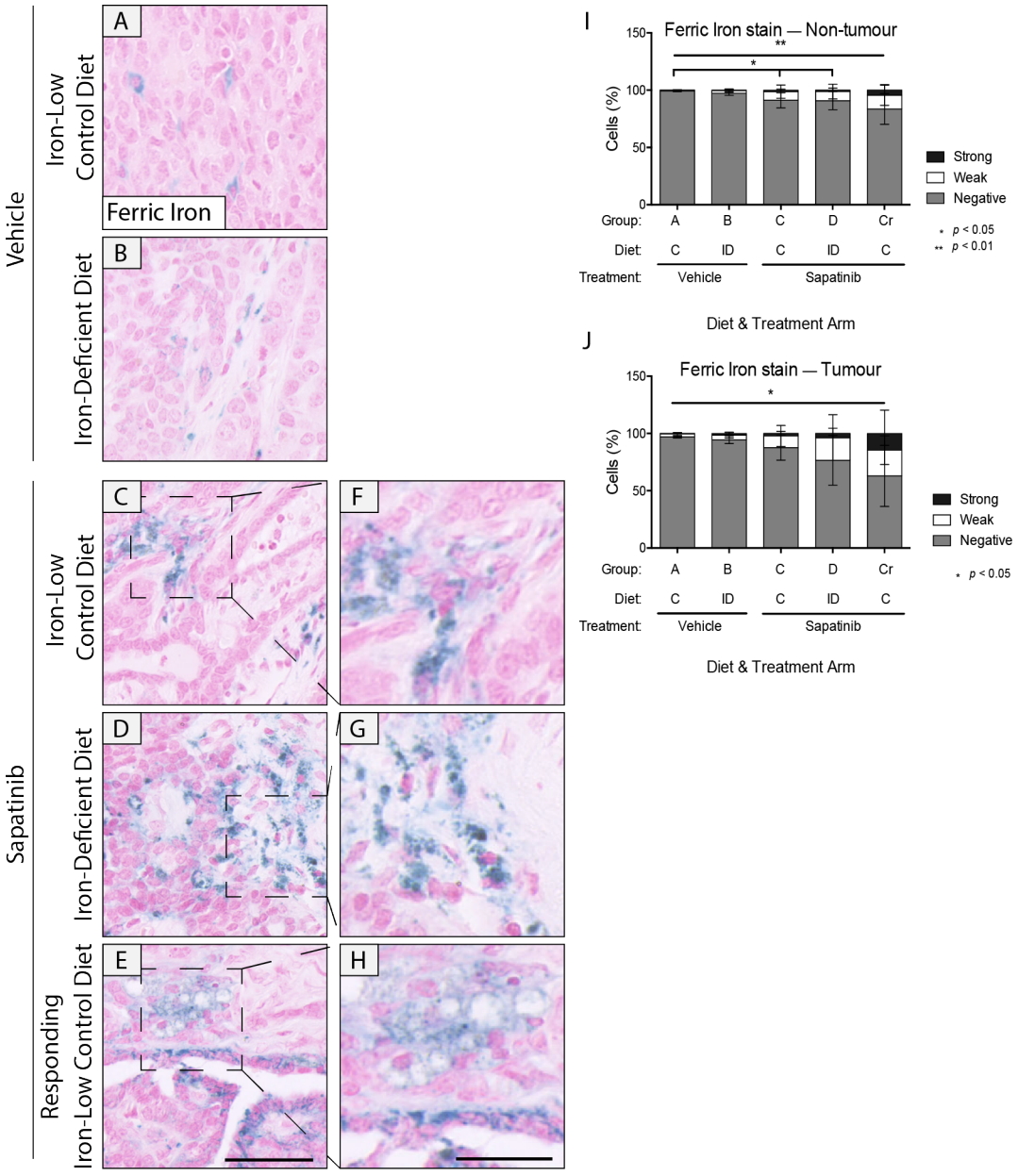


**Figure 5.8. Tumours from sapatinib-treated mice have altered iron storage.** MMTV-NIC-PTEN$^{+/-}$ mice on a control (C) or iron-deficient (ID) diet were treated with vehicle or sapatinib. Drug treatment began four days after the diet commenced. **(A–E)** Representative Perls' ferric iron stain (iron-low control diet, vehicle; group A, n=6; iron-deficient diet, vehicle: group B, n=5; iron-low control diet, sapatinib: group C, n=5; iron-deficient diet, sapatinib: group D, n=7; responding tumours, iron-low control diet, sapatinib; group Cr, n=8) in index tumours. Scale bar: 50 $\mu$m. **(F–H)** Representative example of extracellular iron deposition. Scale bar: 25 $\mu$m. Quantification of Perls' ferric iron stain by Definiens Architect in **(I)** non-tumour and **(J)** tumour. All groups compared with iron-low control diet, vehicle-treated tumours. Results presented as mean $\pm$ standard deviation. Kruskal-Wallis test, Dunn's post-hoc test, $p$<0.05=*, $p$<0.01=**. Detailed results can be found in table A.10.

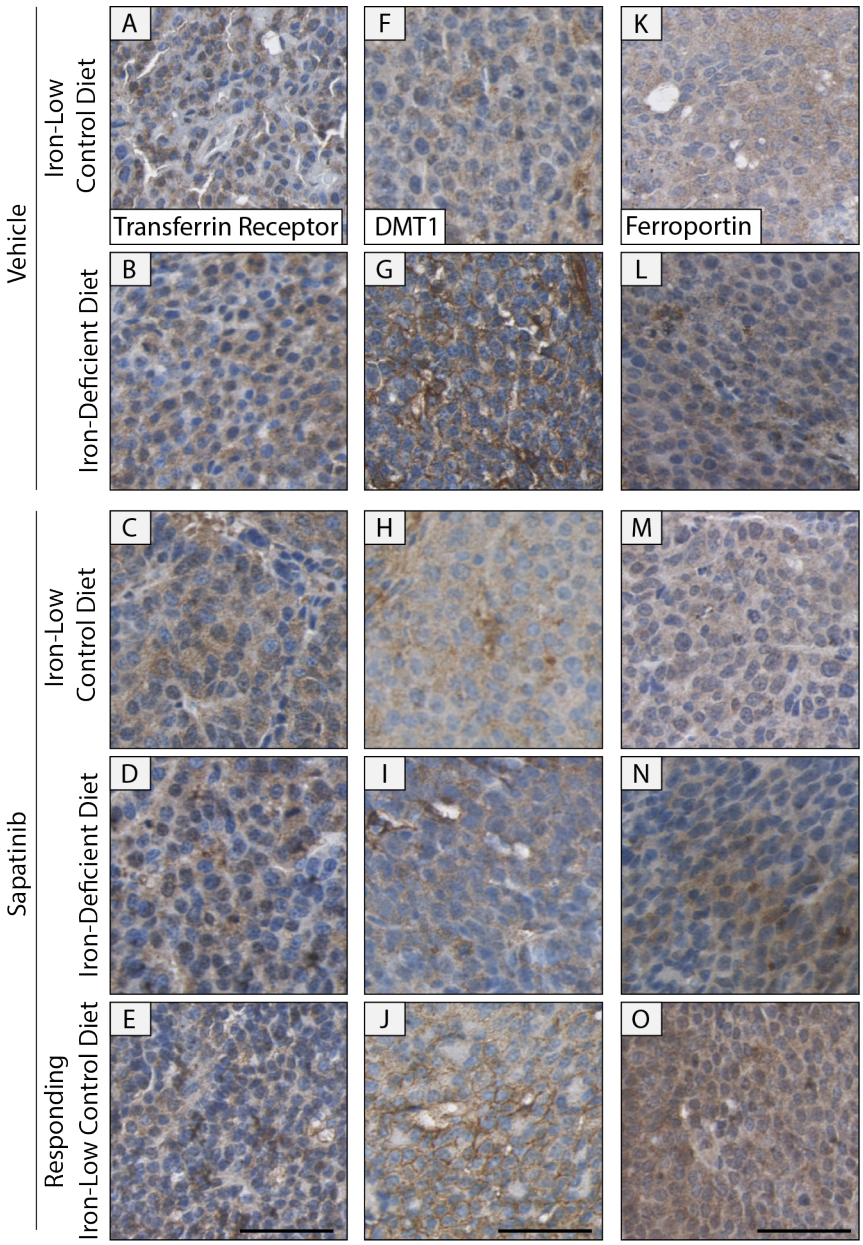


**Figure 5.9. Tumours from sapatinib-treated mice do not have differences in levels of iron transporters.** MMTV-NIC-PTEN$^{+/-}$ mice on a control (C) or iron-deficient (ID) diet were treated with vehicle or sapatinib. Drug treatment began four days after the diet commenced. Representative immunohistochemical staining of **(A–E)** transferrin receptor (iron-low control diet, vehicle; group A, n=6; iron-deficient diet, vehicle: group B, n=5; iron-low control diet, sapatinib: group C, n=6; iron-deficient diet, sapatinib: group D, n=5; responding tumours, iron-low control diet, sapatinib; group Cr, n=6), **(F–J)** divalent metal transporter-1 (DMT1; Group A: n=6; group B: n=4; group C: n=6; group D: n=5; group Cr: n=6) and **(K–O)** ferroportin (Group A: n=5; group B: n=5; group C: n=6; group D: n=4; group Cr: n=5). Scale bar: 50 $\mu$m. Detailed results can be found in table A.10.

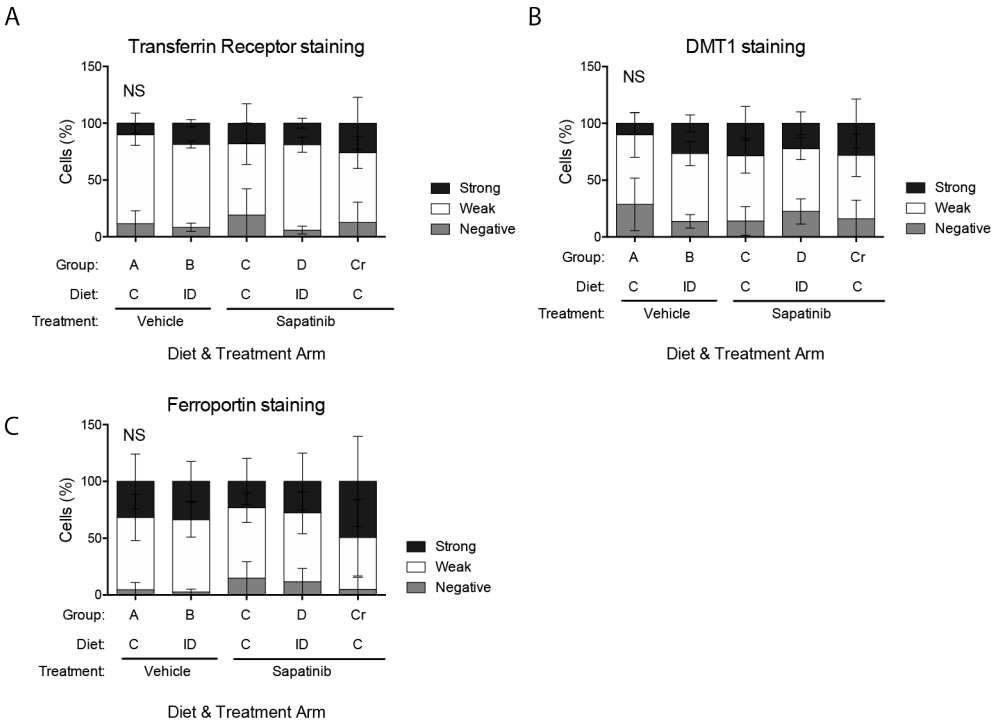


**Figure 5.10. Tumours from sapatinib-treated mice have varied levels of iron transporters.** MMTV-NIC-PTEN$^{+/-}$ mice on a control (C) or iron-deficient (ID) diet were treated with vehicle or sapatinib. Drug treatment began four days after the diet commenced. Quantification of **(A)** transferrin receptor, **(B)** DMT1 and **(C)** ferroportin staining by Definiens Architect (iron-low control diet, vehicle; group A; iron-deficient diet, vehicle: group B; iron-low control diet, sapatinib: group C; iron-deficient diet, sapatinib: group D; responding tumours, iron-low control diet, sapatinib; group Cr). All groups compared with iron-low control diet, vehicle-treated tumours. Results presented as mean $\pm$ standard deviation. Kruskal-Wallis test, Dunn's post-hoc test, not significant = NS.

## 5.3 Discussion

Iron is involved in many cellular processes including respiration, DNA synthesis and fatty acid metabolism, amongst other roles.[227,240] Here, we have shown that reducing dietary iron intake alters the development of resistance to sapatinib, negating the need for overexpression of HO-1, which is otherwise key in maintaining resistance.

### 5.3.1 Maintenance of serum iron levels can mask functional iron deficiency

Short-term treatment with an iron-deficient diet over a 3-day period has been shown to induce a non-anaemic iron-deficient state and alter hepatic gene expression, while long-

term treatment showed some changes similar to initial short-term treatments *in vivo*.[241] Other long-term treatments investigating the effect of iron-deficient diets on pathological conditions were associated with changes in ferritin levels and lipid peroxidation,[242,243] and increases in pro-angiogenic factors.[243]

Interestingly, long-term iron-deficient diets were not associated with differences in serum iron levels, suggesting tissue specific effects of iron deficiency, which is consistent with our data (fig 5.5). However, Kamei et al.[241] showed decreased serum iron after short-term treatments, indicating initial changes in iron availability that may induce compensatory mechanisms to maintain sufficient serum iron levels long-term. This is reflective of FID,[226] which is often seen in patients and is associated with worse progression-free survival.[239]

Despite no changes in iron-related proteins or serum iron levels evidenced (fig 5.6, 5.7), the development of resistance to sapatinib was able to be modulated by a change in diet. Although not significant, due to variation within the iron-low control diet sapatinib-treated arm, sapatinib-treated mice had survival times more similar to vehicle-treated mice (fig 5.1).

### 5.3.2 Restricting dietary iron did not impede tumour growth

Many studies have shown that increased iron availability can increase the rate of cell growth and cancer risk.[227,243–246] Similarly, iron deficiency has been shown to reduce tumourigenesis and continued tumour growth.[245,247,248] An iron-deficient diet did not impede tumourigenesis or tumour growth in MMTV-NIC-PTEN$^{+/-}$ mice (fig 5.4 A, 5.3). From this, it can be seen that reducing dietary iron intake has not had a deleterious impact on tumour initiation or progression in our study.

However, the diet used in chapter 4 contained 150 ppm of iron, whereas the matched iron-low control diet used in this chapter contained 49 ppm of iron. Although this is still greater than the 2 ppm iron in the iron-deficient diet, and within the normal range (35–350 ppm),[243] this difference between 'normal' and 'control' diets may explain the bimodal growth distribution in sapatinib-treated iron-low control diet mice (fig 5.2 C).

In this experiment, none of the iron-related proteins identified in chapter 4 were altered in response to an iron-deficient diet. This was likely due to different iron-low control diets used and the altered iron within the iron-low control diet compared with the normal diet. As such, all mice experienced some reduction in dietary iron intake, although those on the iron-deficient arms more so than the control arms.

### 5.3.3 Expression of HO-1 in response to sapatinib is affected by altering dietary iron

Although no changes in expression of ceruloplasmin or ferritins could be seen, we did see an effect on the response to sapatinib. Sapatinib-treated mice on an iron-deficient diet did not have increased HO-1 which was seen in tumours from sapatinib-treated mice on a iron-low control diet (fig 5.6). However, these tumours still showed similar levels of extracellular iron deposition as seen in tumours from sapatinib-treated iron-low control diet mice (fig 5.8).

Expression of HO-1 has been associated with the development of resistance to radio-, chemo- and targeted therapies.[249–256] This supports our data which show increased expression of HO-1 in sapatinib-treated tumours (fig 4.8). However, increased HO-1 was also seen in tumours responding to sapatinib-treatment (fig 5.6). As such, it is unclear how HO-1 is involved in the development and maintenance of resistance.

In tumours from sapatinib-treated mice on an iron-deficient diet, HO-1 was not increased (fig 5.6 H and L). Despite no increase in HO-1, all sapatinib-treated tumours had increased extracellular iron deposition, as seen in sapatinib-treated iron-low control diet mice (fig 5.8). Through its canonical role of heme breakdown,[257] and by increasing autophagic degradation of damaged iron-containing proteins,[249–251] HO-1 can increase the LIP.

Despite being able to increase the LIP, HO-1 is not responsible for extracellular iron deposition. It is likely that through increasing the LIP, other proteins acted to counteract this to prevent generation of excess ROS due to high levels of intracellular free iron.[133,238] Mice with reduced dietary iron intake showed small but insignificant changes in serum iron levels, consistent with the literature.[242,243] As such, and in keeping with the

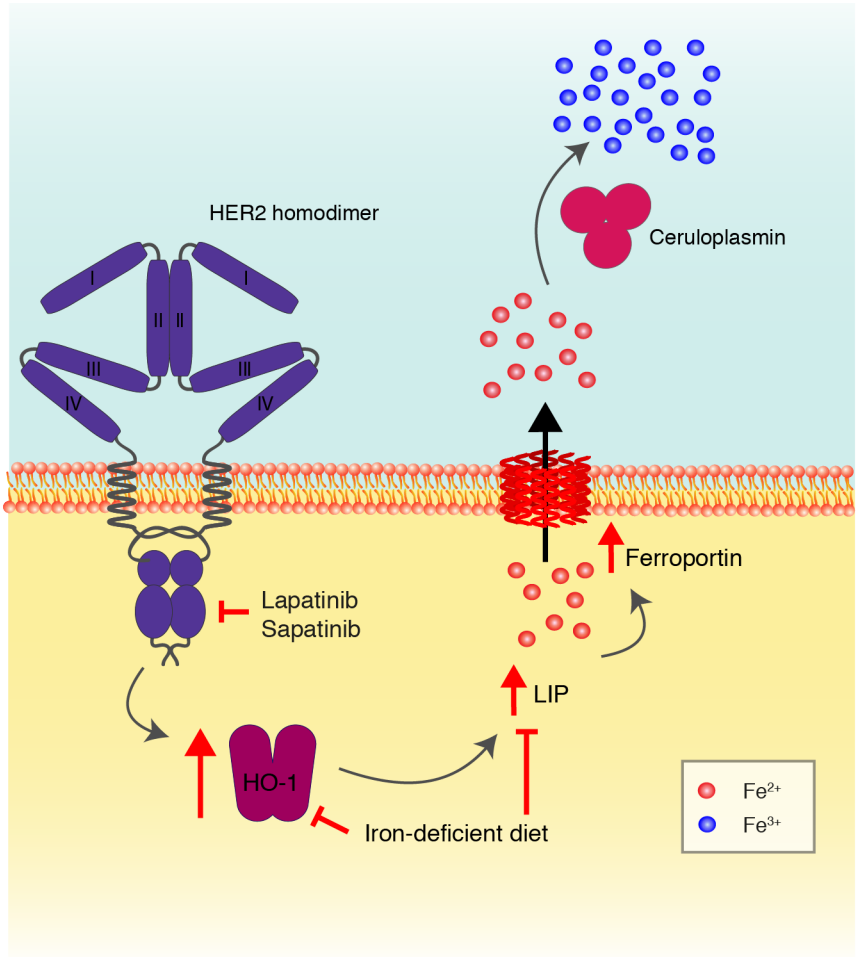


**Figure 5.11. An iron-deficient diet negates the need for increased expression of HO-1 to develop resistance to sapatinib.** We hypothesise that upon treatment with HER2-targeted tyrosine kinase inhibitors, heme oxygenase-1 (HO-1) becomes upregulated, increasing free iron in the labile iron pool (LIP). To avoid oxidative damage from free ferrous iron ($Fe^{2+}$), ferroportin transports the iron from the cell where it is converted to ferric iron ($Fe^{3+}$) by ceruloplasmin and deposited extracellularly. An iron-deficient diet reduces the amount of iron in the LIP, reducing oxidative damage making HO-1 unnecessary as there is less oxidative damage to respond to.

literature, reduced dietary iron intake would result in a reduced LIP.[242,258,259] This would result in less oxidative damage and increased autophagy to release iron from ferritin complexes.[260]

HO-1 may be required by the tumours to increase autophagy, which is also increased in iron-deficiency. If tumours on an iron-deficient diet have insufficient iron, this would result in increased autophagy without the need to increase expression of HO-1. Therefore, we hypothesise that increased HO-1 expression and reduced dietary iron have overlapping mechanisms in the development of resistance to sapatinib (fig 5.11).

### 5.3.4 Summary

Development of resistance can be affected by altering dietary iron intake *in vivo*. If these results translate to the clinic, increasing patients' dietary iron could represent a novel way to combat the development of resistance to HER2-targeted therapies without the addition of new drugs which may have additional side effects.

As HO-1 has been consistently increased in sapatinib-treated tumours, its role in maintaining resistance and the overlapping function of an iron-deficient diet should be the focus of further studies. As tumours responding to sapatinib also had increased HO-1, it will be important to identify what mechanism controls the switch between resistance and response. This will be investigated further in the following chapter.

# Chapter 6

# The role of HO-1 in resistance to sapatinib

The canonical role of HO-1 is the breakdown of haem groups into biliverdin, releasing carbon monoxide and iron in the process.[257] HO-1 is known to be involved in both autophagy and the oxidative stress response and has been shown in multiple cancer types to induce autophagy as a resistance mechanism.[249–251] An additional role for HO-1 is protection against ferroptotic cell death, thought to be associated with reaction to the oxidative stress response.[235] The accumulation of lipid peroxides, generated by hydroxyl radicals formed through the reaction of ferrous iron and hydrogen peroxide, leads cells to undergo ferroptosis.[133,238]

Sapatinib-treated tumours from MMTV-NIC-PTEN$^{+/-}$ mice exhibited changes in iron storage and increased expression of HO-1, as shown in chapter 4. When mice were given an iron-deficient diet and treated with sapatinib, HO-1 was no longer upregulated, but iron deposition was still seen (chapter 5).

With this in mind, the following chapter will explore these aims:

- Assess if increased HO-1 expression is associated with autophagy induction or increased oxidative stress.
- Determine if HER2-targeted therapies can induce ferroptosis.
- Elucidate the role of HO-1 on resistance to sapatinib and lapatinib *in vitro*.

## 6.1 Sapatinib-treated tumours have increased autophagic flux

Detailed results for this chapter can be found in tables A.11–A.14.

As HO-1 is known to induce autophagy,[249–251] we investigated if the increased HO-1 seen in sapatinib-treated tumours (fig 4.8 G, H and L) was associated with increased autophagy. Levels of autophagy-related proteins, sequestosome 1 (p62) and microtubule-associated proteins 1A/1B light chain 3B (LC3B), were assessed. p62 targets ubiquitinated proteins for autophagic degradation and is degraded during this process, thus when levels of autophagy are increased, levels of p62 are decreased.[261] Meanwhile, LC3B is present in

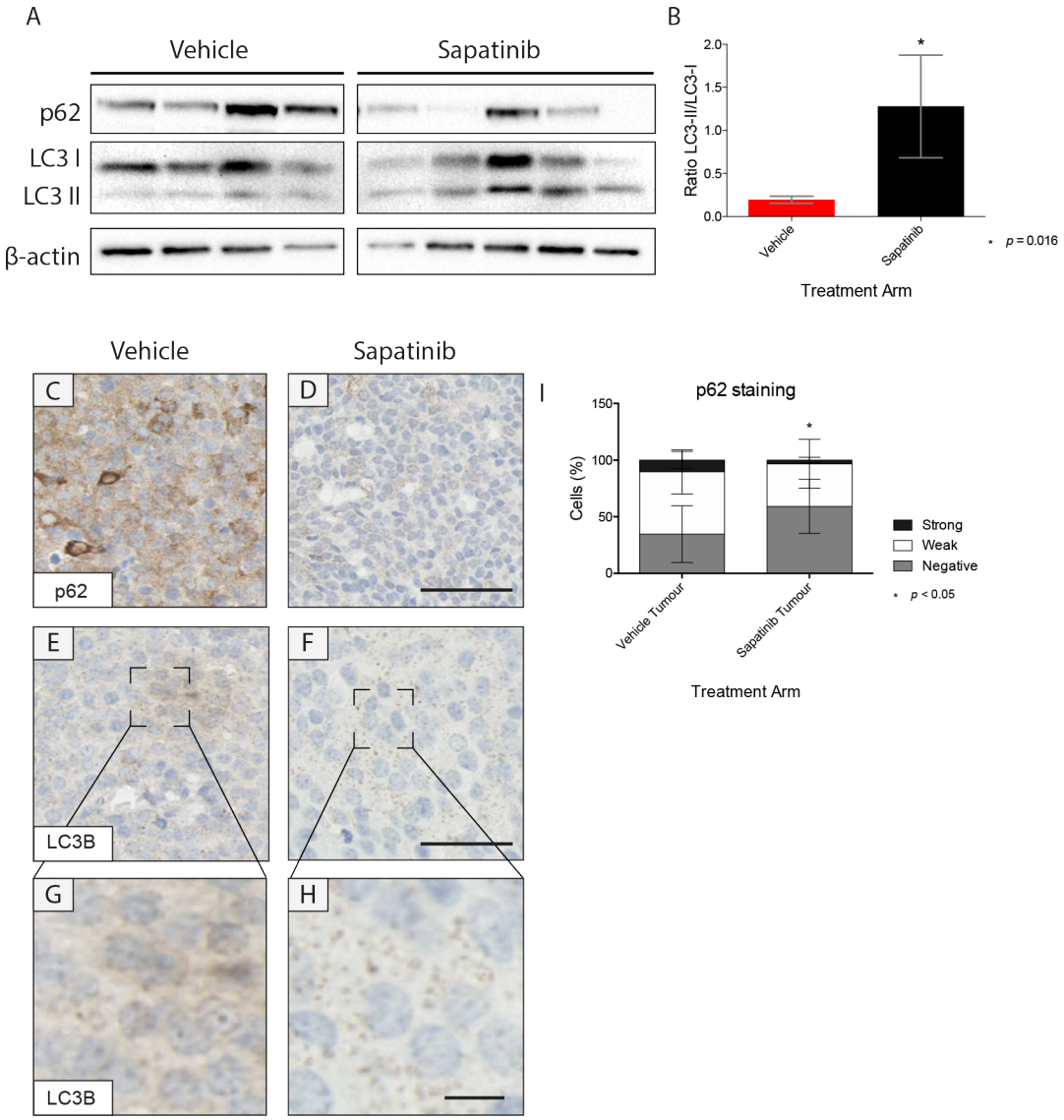


**Figure 6.1. Increased autophagic flux can be seen in MMTV-NIC-PTEN$^{+/-}$ tumours treated with sapatinib. (A)** Western blot analysis of sequestosome 1 (p62) and microtubule-associated proteins 1A/1B light chain 3B (LC3B) in index tumours from MMTV-NIC-PTEN$^{+/-}$ mice treated with vehicle (n=4), or sapatinib (n=5). *B*-actin was used as a loading control. **(B)** Quantification of LC3BII:LC3BI. Results presented as bar graph, mean $\pm$ standard deviation (SD). Two-tailed Mann-Whitney test, $p$=0.016. Representative immunohistochemical (IHC) staining of **(C–D)** p62 (vehicle: n=22; sapatinib: n=10) and **(E–F)** LC3B (vehicle: n=19; sapatinib: n=8). Scale bar: 50 $\mu$m. **(G–H)** Higher magnification of LC3B puncta. Scale bar: 10 $\mu$m. **(I)** Quantification of p62 by Definiens Architect. Results presented as mean $\pm$ SD, two-tailed Mann-Whitney test, $p$<0.05=*. Detailed results can be found in table A.12.

two forms: the cytosolic form, LC3B-I becomes conjugated to phosphatidylethanolamine (PE), forming LC3B-II which is recruited to autophagosomal membranes, appearing as puncta in cells.[262]

Western blot analysis revealed decreased p62 in sapatinib-treated tumours (fig 6.1 A) and increased autophagic flux, evidenced by an increased ratio of LC3BII to LC3BI (fig 6.1 A and B). To verify this result, levels of both proteins were assessed by IHC. This confirmed decreased p62 (fig 6.1 C, D and I) and increased LC3B-positive puncta in sapatinib-treated tumours (fig 6.1 E–H and J). A more diffuse staining can be seen in vehicle-treated tumours, as well as some puncta.

This was not reflected in tumours from mice on the iron-deficient diet experiment. Levels of p62 were comparable across treatments, except vehicle-treated mice on an iron-deficient diet which had increased levels of p62 compared with vehicle-treated iron-low control diet mice (fig 6.2 A–E and K, 6.3). However, there was a lot of variation within the sapatinib-treated iron-low control diet mice, which may reflect the two groups seen in the growth kinetics within this group (fig 5.2 C).

Interestingly, the p62 levels did not reflect the number of LC3B-positive puncta within the tumours (fig 6.2 F–J). Although, p62 is an indirect read out of autophagy, as it is under tight transcriptional and post-transcriptional control,[263] therefore it can be expected that p62 levels may not always correlate with the number of LC3B-positive puncta. Few puncta were seen in vehicle-treated mice on a iron-low control diet, but in tumours from vehicle-treated mice on an iron-deficient diet, many puncta could be seen. Some puncta could be seen in progressing tumours from sapatinib-treated mice on a iron-low control diet, but no puncta were detected in tumours responding to sapatinib.

Tumours from sapatinib-treated mice on an iron-deficient diet had many puncta, increased compared with vehicle-treated mice on the iron-deficient diet. Therefore, induction of autophagy may have occurred in mice on an iron-deficient diet to release iron from storage.[260] This may circumvent the need for HO-1 to increase autophagy as a mechanism of resistance. Furthermore, the cargo receptor for ferritin targeted for autophagic degradation is not p62, which may explain the lack of concordance between p62 and LC3B-positive puncta.

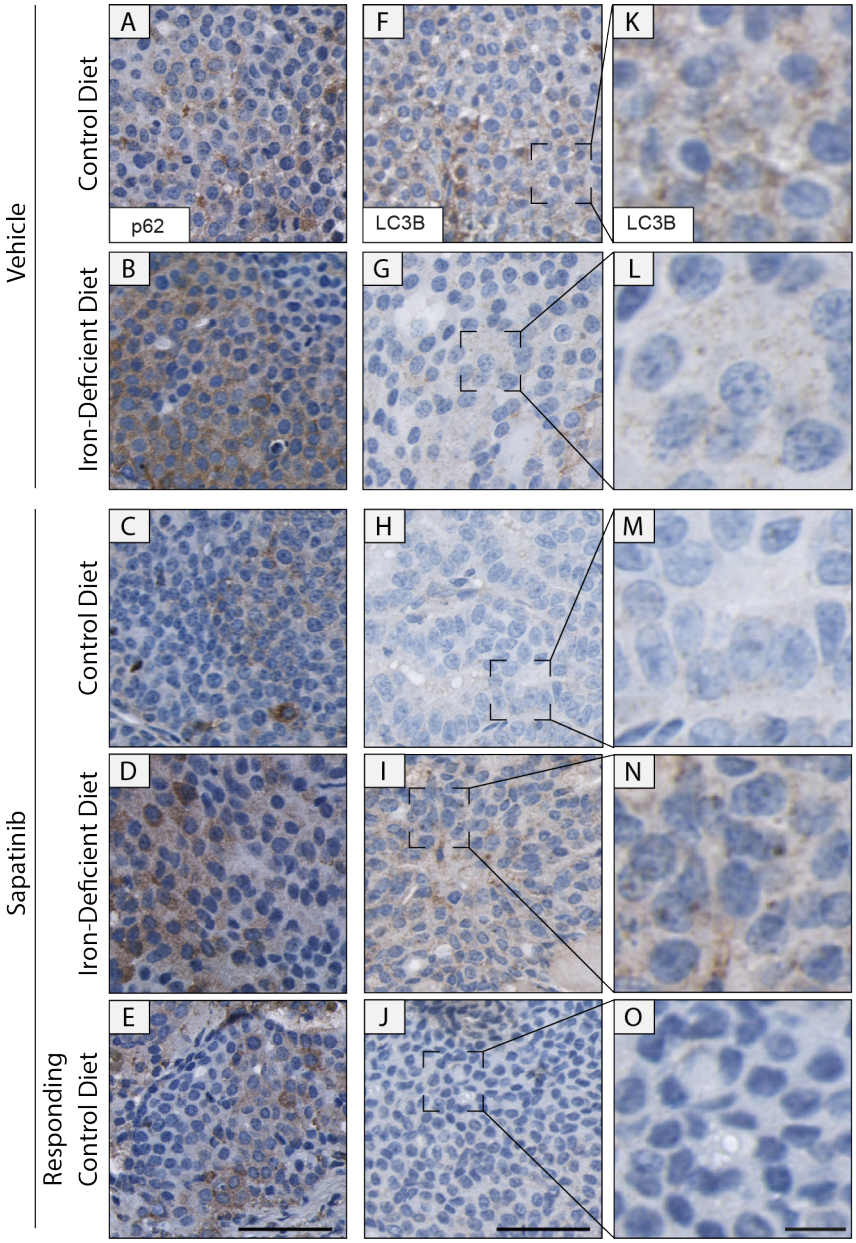


**Figure 6.2. Tumours responding to sapatinib do not have increased autophagic flux.** MMTV-NIC-PTEN$^{+/-}$ mice on a control (C) or iron-deficient (ID) diet were treated with vehicle or sapatinib. Drug treatment began four days after the diet commenced. Representative immunohistochemical staining of **(A–E)** sequestosome 1 (p62; iron-low control diet, vehicle; group A, n=5; iron-deficient diet, vehicle: group B, n=5; iron-low control diet, sapatinib: group C, n=6; iron-deficient diet, sapatinib: group D, n=4; responding tumours, iron-low control diet, sapatinib; group Cr, n=6) and **(F–J)** microtubule-associated proteins 1A/1B light chain 3B (LC3B; Group A: n=6; group B: n=4; group C: n=5; group D: n=6; group Cr: n=6). Scale bar: 50 $\mu$m. **(K–O)** Higher magnification of LC3B puncta. Scale bar: 10 $\mu$m. Detailed results can be found in table A.11.

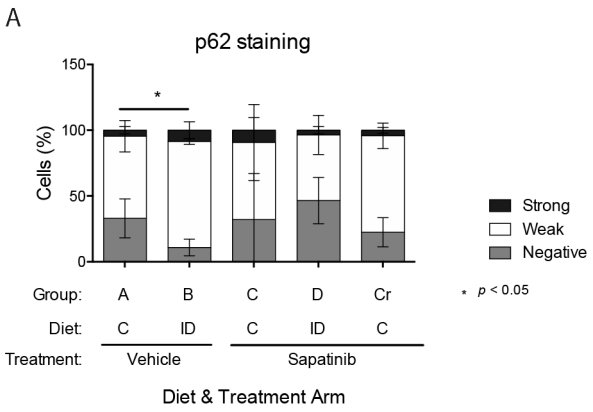


**Figure 6.3. Levels of p62 are not significantly different between treatment arms. (A)** Quantification of sequestosome 1 (p62; iron-low control diet, vehicle; group A, n=5; iron-deficient diet, vehicle: group B, n=5; iron-low control diet, sapatinib: group C, n=6; iron-deficient diet, sapatinib: group D, n=4; responding tumours, iron-low control diet, sapatinib; group Cr, n=6) in tumours from the iron-deficient diet experiment by Definiens Architect. All groups compared with iron-low control diet, vehicle-treated tumours. Results presented as mean $\pm$ standard deviation, Kruskal-Wallis test, Dunns post-hoc test, p<0.05=*.

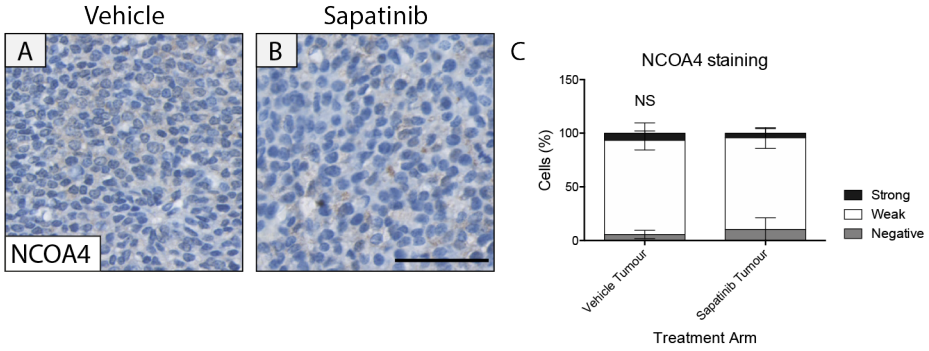


**Figure 6.4. Sapatinib-treated tumours do not have increased ferritinophagy.** Representative immunohistochemical staining of **(A–B)** nuclear receptor coactivator 4 (NCOA4) in tumours from vehicle- (n=23) and sapatinib-treated (n=9) MMTV-NIC-PTEN$^{+/-}$ mice. Scale bar 50 $\mu$m. **(C)** Quantification of NCOA4 staining by Definiens Architect. Results presented as mean $\pm$ standard deviation. Two-tailed Mann-Whitney test, not significant = NS. Detailed results can be found in table A.12.

To ascertain if increased autophagy has resulted in higher turnover of ferritin to release iron in mice on a normal diet, levels of nuclear receptor coactivator 4 (NCOA4), the cargo receptor for ferritin-specific autophagy,[264] were assessed in tumours from chapter 4. This showed no difference in NCOA4 levels between treatment groups (fig 6.4 A–C). This suggests that the increased autophagic flux and iron deposition in these tumours is not due to increased ferritin degradation.

Autophagy can be induced when there is reduced nutrient availability or increased oxidative stress.[265] To determine if the increased autophagy seen was correlated with insufficient blood flow causing a lack of nutrient availability or oxygen deprivation, the number of blood vessels within a tumour section was assessed using CD31 staining. This revealed no significant difference in the number of CD31-positive blood vessels, when normalised to the tumour section area, between the two treatment groups (fig 6.5 A–C).

In addition, there was no difference in expression of key regulators of vascularisation including vascular endothelial growth factor A (VEGFA; *Vegfa*; Hoeben et al.[266]) and its receptors, vascular endothelial growth factor receptor 1 and 2 (VEGFR1: *Flt1*; VEGFR2: *Kdr*; fig 6.5 D). Furthermore, levels of hypoxia-inducible factor-1$\alpha$ (*Hif1*$\alpha$) which can promote angiogenesis and thrombospondin 1 (*Thbs1*),[266] a potent inhibitor of angiogenesis, were not significantly different between treatment groups (fig 6.5 D).

## 6.2 Levels of oxidative stress are similar between sapatinib- and vehicle-treated tumours

Resistance to chemotherapy has been linked to induction of an oxidative stress response in breast cancer, neuroblastoma and squamous cell carcinoma.[252–254] Furthermore, several groups have shown increased oxidative stress after treatment with HER2-targeted therapies trastuzumab, pertuzumab and lapatinib.[267,268] HO-1 is intricately linked to the oxidative stress response and is a key effector of nuclear factor erythroid-2 related factor 2 (NRF2)-mediated maintenance of redox homeostasis.[269]

Cellular oxidative stress can be measured by the level of nicotinamide adenine dinucleotide phosphate (NADPH) available to provide reducing power. To measure this, we looked

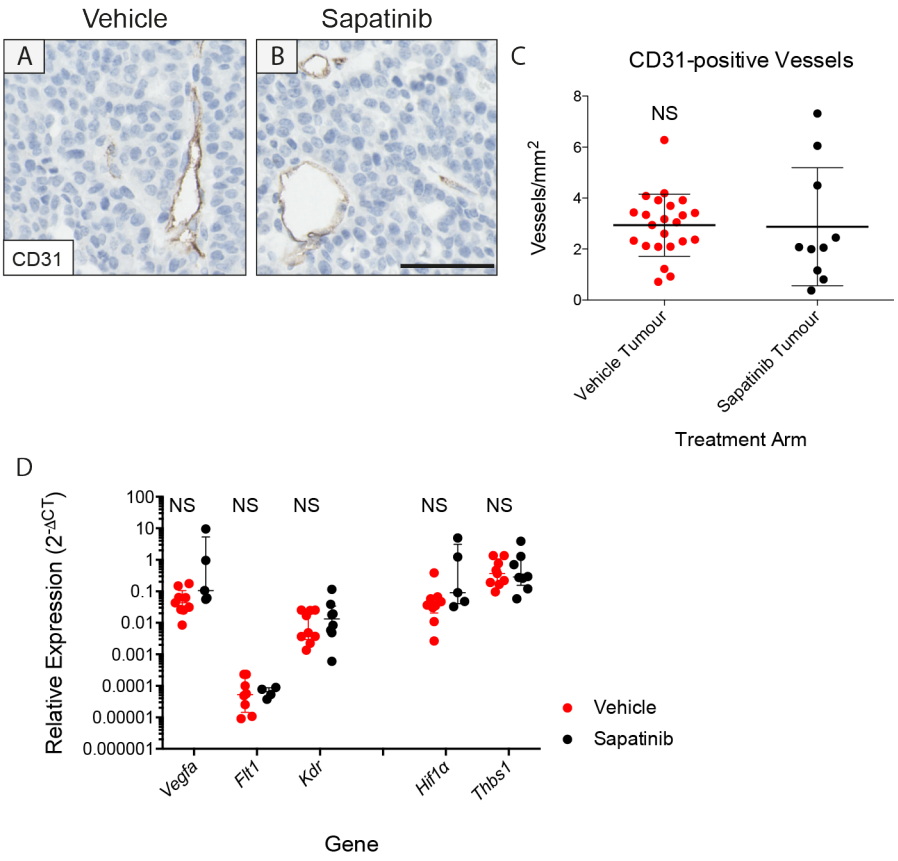


**Figure 6.5. No difference can be seen in the number of blood vessels in sapatinib-treated tumours compared with vehicle-treated tumours.** Representative immunohistochemical (IHC) staining of **(A–B)** cluster of differentiation 31 (CD31) in tumours from vehicle- (n=26) and sapatinib-treated (n=10) MMTV-NIC-PTEN$^{+/-}$ mice. Scale bar: 50 $\mu$m. **(C)** Quantification of CD31-positive vessels across whole sections by Definiens Architect, normalised to area. Results presented as median $\pm$ interquartile range (IQR). Unpaired two-tailed *t*-test, not significant = NS. **(D)** Quantitative PCR was performed on tumours from MMTV-NIC-PTEN$^{+/-}$ mice treated with vehicle (n=9) or sapatinib (n=9). Vascular endothelial growth factor A (*Vegfa*), vascular endothelial growth factor receptor 1 (*Flt1*), vascular endothelial growth factor receptor 2 (*Kdr*), hypoxia inducible factor 1$\alpha$ (*Hif1*$\alpha$) and thrombospondin 1 (*Thbs1*) mRNA levels were analysed and normalised to levels of $\beta$-2 microglobulin (*B2m*) mRNA. Results presented as scatter plot with median $\pm$ IQR. Two-tailed Mann-Whitney tests, not significant = NS. Detailed results can be found in table A.12.

at the activity of glucose-6-phosphate dehydrogenase (G6PDH) which catalyses the rate limiting step of the pentose phosphate pathway, responsible for maintaining cellular levels of NADPH.[270] This revealed that both sapatinib-treated and vehicle-treated tumours show similar levels of G6PDH activity (fig 6.6 A). Reduced glutathione (GSH) is another key cellular antioxidant; increased oxidised glutathione (GSSG) is indicative of oxidative stress.[271] To investigate this, we measured the ratio of GSH to GSSG. This revealed no significant difference between vehicle-treated and sapatinib-treated tumours (fig 6.6 B). Despite seeing no difference in the oxidative status of sapatinib-treated tumours

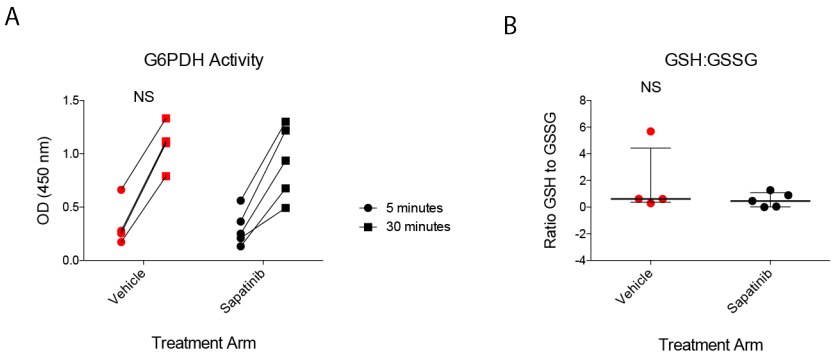


**Figure 6.6. Sapatinib-treated tumours have similar reducing capacity to vehicle-treated tumours.** Vehicle-treated (n=4) and sapatinib-treated (n=5) tumours were analysed using **(A)** a glucose-6-phosphate dehydrogenase (G6PDH) kinetic assay at 5 and 30 minutes to calculate G6PDH activity. Linear regression, not significant = NS. Vehicle-treated (n=4) and sapatinib-treated tumours (n=5) were analysed using **(B)** a thiol green indicator assay to determine the reduced glutathione to oxidised glutathione (GSH/GSSG) ratio. Results presented as scatter plot with median ± interquartile range. Two-tailed Mann-Whitney test, not significant = NS. Detailed results can be found in table A.12.

compared with vehicle-treated tumours, levels of glutathione peroxidase 4 (GPX4), which detoxifies lipid peroxides,[272] were increased (fig 6.7 A–C).

Lipid peroxidation is associated with increased cell death due to ferroptosis. Oxidation of PE species containing arachidonic- and adrenic acid (AA and AdA, respectively) drive cells towards ferroptotic cell death.[273–275] Despite increased GPX4, assessment of the oxidation state of PE species containing AA or AdA revealed no significant difference between the oxidation state of these lipids between vehicle- and sapatinib-treated tumours (fig 6.7 D). However, without comparing these results with those from tumours responding to sapatinib, it is difficult to conclude whether higher levels of GPX4 reduced lipid peroxidation to the same level as vehicle-treated tumours in response to sapatinib treatment.

As HO-1 and GPX4 are both NRF2-target genes, and increased in sapatinib-treated tumours (fig 4.8 G and H, 6.7 A and B), we assessed levels of nuclear NRF2. Despite NRF2 target genes being upregulated, analysis of NRF2 by IHC showed significantly reduced levels in sapatinib-treated tumours compared with vehicle-treated tumours (fig 6.8 A, B and E).

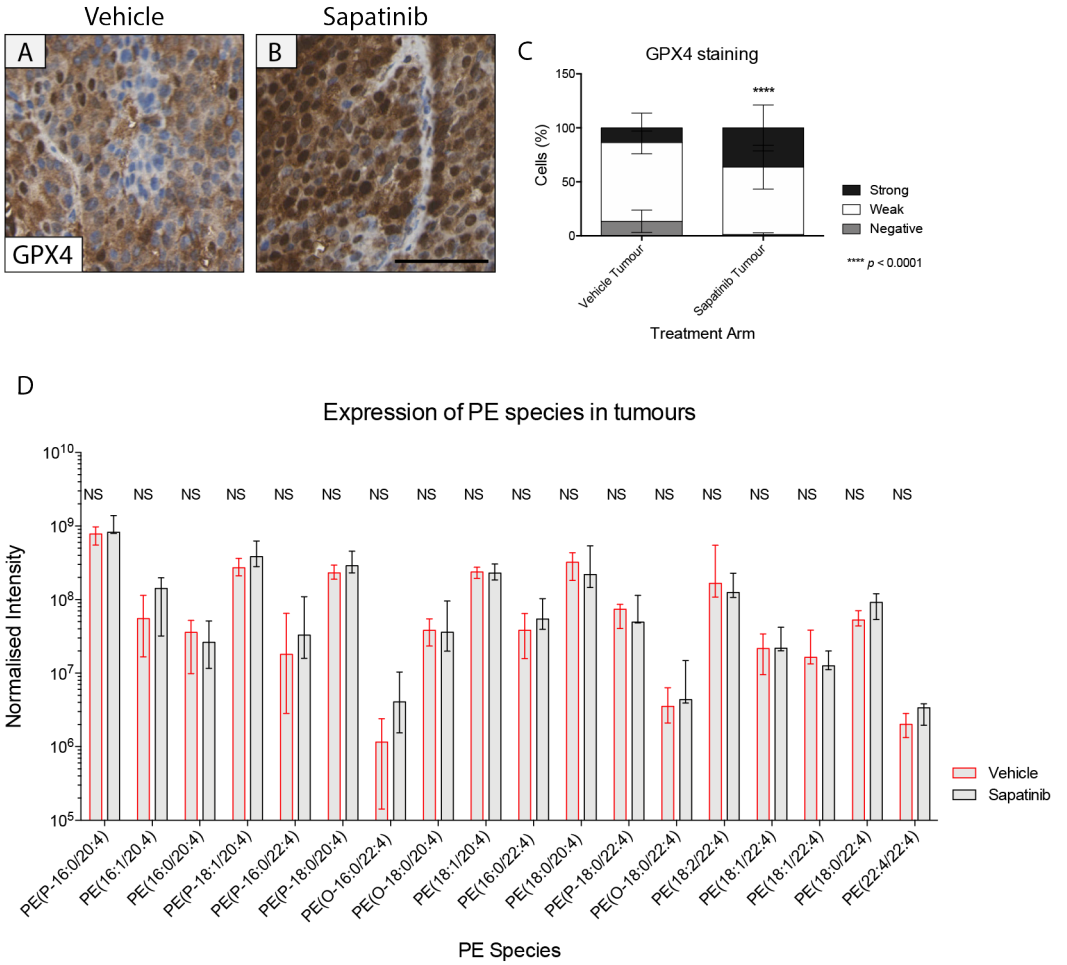


**Figure 6.7. Sapatinib-treated tumours have increased GPX4.** Representative IHC staining of **(A–B)** glutathione peroxidase 4 (GPX4) in vehicle-treated (n=25) and sapatinib-treated (n=8) tumours. Scale bar: 50 $\mu$m. Quantification of **(C)** GPX4 by Definiens Architect. Results presented as mean $\pm$ standard deviation. Two-tailed Mann-Whitney test, p<0.0001=****. **(D)** Assessment of phosphatidylethanolamine (PE) lipid species in vehicle-treated (n=4) and sapatinib-treated (n=5) tumours by liquid chromatography-tandem mass spectroscopy (LC-MS/MS). Peak detection and lipid identification were performed as described in Wills et al.[156] Results presented as median $\pm$ interquartile range. Multiple *t*-tests, not significant = NS. Detailed results can be found in table A.12.

## 6.3 Sapatinib and lapatinib induce ferroptotic cell death

Ferroptosis is a form of caspase-independent, regulated cell death.[223] As there are no protein markers identified which indicate if cells are dying via ferroptosis,[250] rescue by iron chelation (deferoxamine; DFO) or prevention of lipid ROS accumulation by trapping peroxyl radicals (ferrostatin) are used to verify ferroptotic cell death *in vitro*.[276,277] Despite not indicating the development of ferroptosis as the process can be reversed at this point, cyclooxygenase 2 (COX2) is used to indicate cells entering the start of the ferroptotic pathway.[272,278]

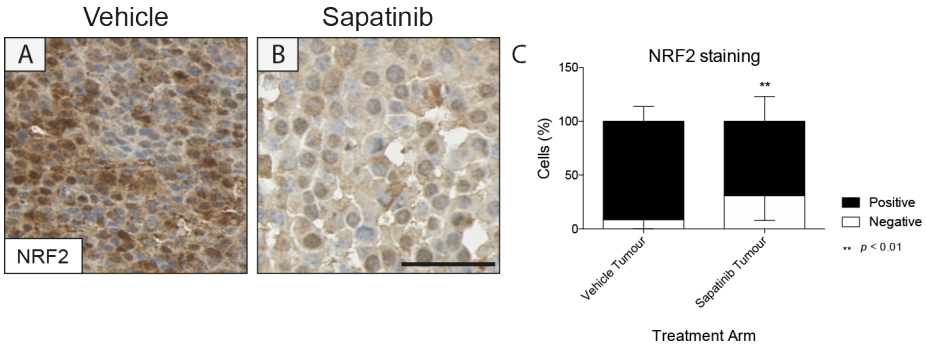


**Figure 6.8. Sapatinib-treated tumours have less NRF2.** **(A–B)** Representative immunohistochemical (IHC) staining of nuclear factor erythroid 2–related factor 2 (NRF2) (vehicle: n=20; sapatinib: n=9). Scale bar: 50 $\mu$m. **(C)** Quantification of NRF2 by Definiens Architect. Results presented as mean $\pm$ standard deviation. Two-tailed Mann-Whitney test, $p$<0.01=**. Detailed results can be found in table A.12.

Therefore, to identify if responding tumours from the iron-deficient diet experiment are undergoing apoptosis or ferroptosis, IHC was performed for cleaved caspase 3, the irreversible step of apoptosis,[219] and COX2. Analysis of progressing and responding tumours by IHC revealed no difference in levels of cleaved caspase 3 in each treatment group and responding tumours (fig 6.9 A–E and K).

However, increased COX2 was seen in sapatinib-treated iron-low control diet tumours that were progressive or responding (fig 6.9 F–J and L). Despite increased COX2 in sapatinib-treated mice on a iron-low control diet, this could not be seen in sapatinib-treated mice on an iron-deficient diet. This may be due to less iron in the labile iron pool, thus a reduced incidence of iron-dependent ferroptosis occurring compared with tumours from mice on a iron-low control diet.

Due to the increased COX2 in sapatinib-treated tumours on a iron-low control diet, we established if SKBR3 cells were susceptible to ferroptosis, to allow modulation of ferroptosis *in vitro* and study the effects of sapatinib and lapatinib. Cells were treated with erastin, which inactivates system $x_c^-$, leading to ferroptotic cell death.[279] Treatment with erastin revealed that SKBR3 cells are susceptible to ferroptosis, which can be rescued by co-treatment with DFO, which chelates iron, or ferrostatin, which traps peroxyl radicals (fig 6.10 A).[276,277]

To investigate if HER2-targeting agents could be inducing ferroptotic cell death, SKBR3 cells were treated with sapatinib or lapatinib in combination with DFO or ferrostatin.

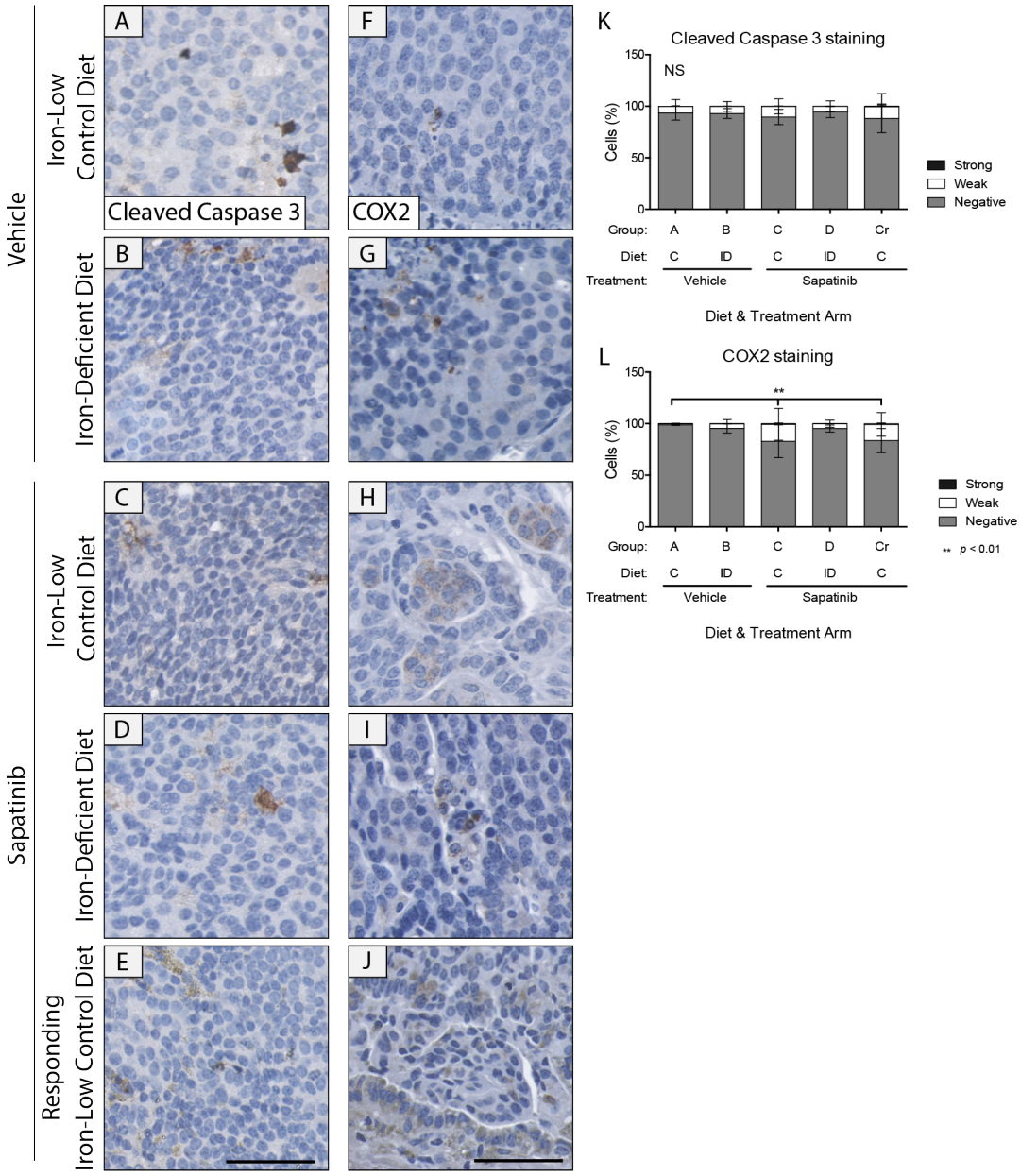


**Figure 6.9. Responding tumours from sapatinib-treated mice on a iron-low control diet have increased COX2.** MMTV-NIC-PTEN$^{+/-}$ mice on a control (C) or iron-deficient (ID) diet were treated with vehicle or sapatinib. Drug treatment began four days after the diet commenced. Representative immunohistochemical staining of **(A–E)** cleaved caspase 3 (iron-low control diet, vehicle; group A, n=6; iron-deficient diet, vehicle: group B, n=6; iron-low control diet, sapatinib: group C, n=5; iron-deficient diet, sapatinib: group D, n=5; responding tumours, iron-low control diet, sapatinib; group Cr, n=6) and **(F–J)** cyclooxygenase 2 (COX2; Group A: n=6; group B: n=5; group C: n=6; group D: n=7; group Cr: n=6) in index tumours. Scale bar: 50 $\mu$m. Quantification of **(K)** cleaved caspase 3 and **(L)** COX2 by Definiens Architect. All groups compared with iron-low control diet, vehicle-treated tumours. Results presented as mean $\pm$ standard deviation. Kruskal-Wallis test, Dunn's post-hoc test, not significant = NS, $p$<0.01=**. Detailed results can be found in table A.11.

**Table 6.1.** GI50 values to sapatinib and lapatinib of SKBR3 cells in the presence or absence of DFO and ferrostatin.

| | **Drug** | |
|---|---|---|
| **Cell Line** | Sapatinib (M) | Lapatinib (M) |
| SKBR3 | $5.83 \times 10^{-12}$ | $1.12 \times 10^{-12}$ |
| SKBR3 plus DFO | $5.49 \times 10^{-7}$ | $7.36 \times 10^{-10}$ |
| SKBR3 plus ferrostatin | $4.74 \times 10^{-7}$ | $7.87 \times 10^{-10}$ |

GI50: Growth inhibition 50%; DFO: deferoxamine

Increased resistance to sapatinib and lapatinib was seen with both DFO and ferrostatin by assessing cell viability (table 6.1). Additionally, cell death analyses showed that both sapatinib- and lapatinib-induced cell death was partially rescued by anti-ferroptotic agents (fig 6.10 A).

As mentioned previously, a key indicator of ferroptosis is lipid peroxidation. To ascertain if sapatinib and lapatinib increased levels of oxidised lipids, SKBR3 cells treated with erastin, sapatinib or lapatinib were stained with C11 BODIPY dye. This has an altered emission spectrum upon binding to oxidised lipids.[280] FACS analysis showed a lower mean RFI ratio 695:530 in SKBR3 cells treated with erastin for 24 or 48 hours compared with DMSO control, as expected. The ratio in erastin-treated cells was similar to that in cells treated with sapatinib and lapatinib (fig 6.10 B; mean ratio 695:530 [SD]; DMSO: 35.83 [$\pm$4.02]; erastin 24 hours: 8.36 [$\pm$1.72]; erastin 48 hours: 11.26 [$\pm$8.30]; sapatinib 48 hours: 15.05 [$\pm$0.37]; lapatinib: 14.15 [$\pm$6.76]; $p<0.01$).

To confirm that sapatinib- and lapatinib-induced cell death was caspase-independent, SKBR3 cells were treated with sapatinib or lapatinib in the presence or absence of pan-caspase inhibitor benzyloxycarbonyl-phenylalanyl-alanyl-fluoromethyl ketone (Z-VAD-FMK).[281] There was a small but non-significant rescue of sapatinib-induced cell death in Z-VAD-FMK treated cells. However, there was no rescue of lapatinib-induced cell death with Z-VAD-FMK (fig 6.11 A).

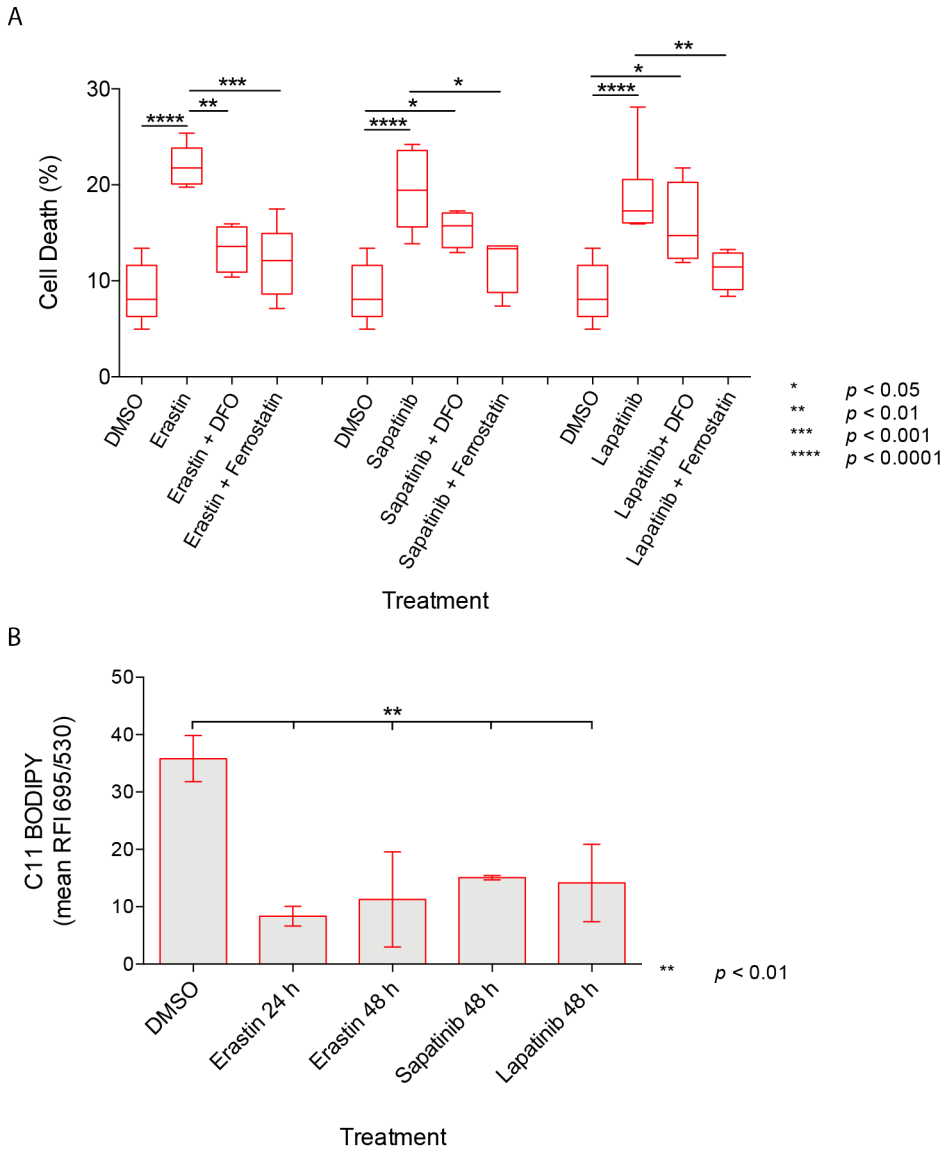


**Figure 6.10. Sapatinib and lapatinib induce ferroptotic cell death in SKBR3 cells.** SKBR3 cells were treated for 48 hours with dimethyl sulfoxide (DMSO; 0.01%), erastin (10 $\mu$M), sapatinib (0.67 $\mu$M) or lapatinib (5 $\mu$M) in the presence or absence of deferoxamine (DFO; 100 $\mu$M) or ferrostatin (5 $\mu$M). **(A)** Cells were stained with propidium iodide and percentage of cell death was analysed using a Tali Image Cytometer. Results presented as box and whisker plot, minimum of four biological repeats. All conditions were compared with DMSO control and single agent treatments. One-way ANOVA, Bonferroni's post-hoc test, $p$<0.05=*, $p$<0.01=**, $p$<0.001=***, $p$<0.0001=****. **(B)** Cells were incubated with 2.5 $\mu$M C11 BODIPY 581/591 for 30 minutes then analysed by flow cytometry. Dead cells were excluded by gating based on forward and side scatter. The ratio of geometric mean relative fluorescence intensity (RFI) 695/530 was calculated. Results presented as bar chart $\pm$ standard deviation, minimum of two biological repeats. One-way ANOVA, Bonferroni's post-hoc test, $p$<0.01=**. Detailed results can be found in table A.13.

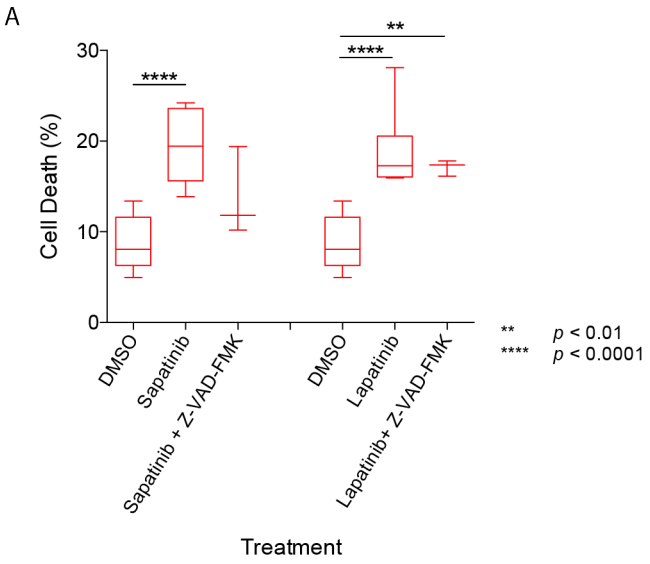


**Figure 6.11. Caspase inhibition does not rescue sapatinib- or lapatinib-induced cell death in SKBR3 cells.** SKBR3 human epidermal growth factor receptor 2 (HER2)-positive breast cancer cells were treated for 48 hours with dimethyl sulfoxide (DMSO; 0.01%), sapatinib (0.67 $\mu$M) or lapatinib (5 $\mu$M) in the presence or absence of pan-caspase inhibitor benzyloxycarbonyl-phenylalanyl-alanyl-fluoromethyl ketone (Z-VAD-FMK; 20 $\mu$M). **(A)** Cells were stained with propidium iodide and percentage of cell death was analysed using a Tali Image Cytometer. Results presented as box and whisker plot, minimum of three biological repeats. All conditions were compared with DMSO control and single agent treatments. One-way ANOVA, Bonferroni's post-hoc test, $p$<0.01=**, $p$<0.0001=****. Detailed results can be found in table A.13.

## 6.4 HO-1-overexpressing cells have increased resistance to HER2-targeted therapies

HO-1 was consistently upregulated in sapatinib-treated tumours (fig 4.8), but its expression was altered in response to an iron-deficient diet (fig 5.6). To further clarify the role of HO-1 in response to HER2-targeted therapies, SKBR3 cells overexpressing HO-1 were made. Overexpression of HO-1 was confirmed by western blot (fig 6.12 A).

To establish if HO-1 overexpression increased cell viability, GI50 values to sapatinib and lapatinib were determined. This revealed that overexpression of HO-1 resulted in increased GI50 values against both sapatinib and lapatinib. However, co-treatment of HO-1-overexpressing cells with DFO or ferrostatin did not further increase GI50 values to sapatinib and lapatinib (table 6.2), suggesting that ferroptosis was not involved in the HO-1-dependent cytoprotection following treatment with sapatinib and lapatinib.

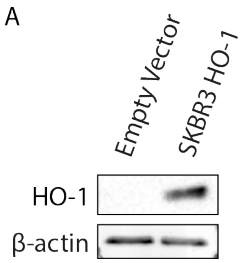


**Figure 6.12. HO-1 expression in SKBR3 cells.** SKBR3 human epidermal growth factor receptor 2 (HER2)-positive breast cancer cell line was stably transfected with a plasmid containing the heme oxygenase-1 (*HO-1*) gene or an empty plasmid. **(A)** Representative western blot analysis (n=2) of HO-1. *B*-actin was used as a loading control.

**Table 6.2.** GI50 values to sapatinib and lapatinib of SKBR3 cells overexpressing HO-1.

| | **Drug** | |
|---|---|---|
| **Cell Line** | Sapatinib (M) | Lapatinib (M) |
| SKBR3 | $5.83x10^{-12}$ | $1.12x10^{-12}$ |
| SKBR3 HO-1 | $9.53x10^{-7}$ | $4.31x10^{-8}$ |
| SKBR3 HO-1 plus DFO | $9.91x10^{-7}$ | $5.08x10^{-8}$ |
| SKBR3 HO-1 plus ferrostatin | $1.04x10^{-6}$ | $2.04x10^{-8}$ |

GI50: Growth inhibition 50%; HO-1: heme oxygenase-1; DFO: deferoxamine

Furthermore, HO-1 cells were resistant to erastin-induced ferroptosis, while empty vector cells were still susceptible (fig 6.13).

HO-1 cells were still undergoing similar levels of cell death as empty vector cells in response to sapatinib and lapatinib (fig 6.14 A and B). This difference between cell viability and cell death read out was expected, as the main mechanism of action of sapatinib and lapatinib is growth arrest.[282] As cytoprotective agents, DFO and ferrostatin would prevent cell death but not growth arrest, leading to increased cell viability as there would be less cell death thus more cells able to proliferate. Additionally, DFO and ferrostatin were unable to rescue cell death in HO-1 cells and did not rescue empty vector cells to the same extent seen in SKBR3 cells (fig 6.10 A). Since cell death could not be rescued by anti-ferroptotic agents, cells were co-treated with Z-VAD-FMK to ascertain if the death was caspase-dependent. This did not rescue death in HO-1 cells, but did result in some decrease in empty vector cells, similar to that seen in SKBR3 cells (fig 6.15 A).

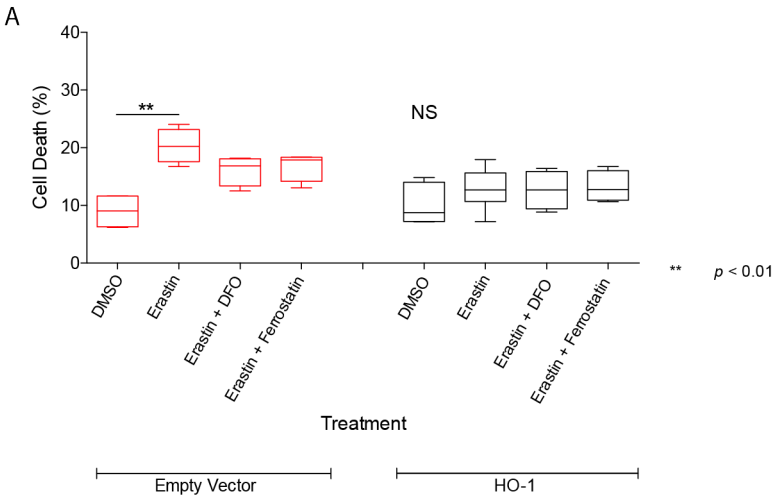


**Figure 6.13. HO-1-overexpressing cells are resistant to erastin-induced cell death.**SKBR3 human epidermal growth factor receptor 2 (HER2)-positive breast cancer cell line was stably transfected with a plasmid containing the heme oxygenase-1 (*HO-1*) gene or an empty plasmid and were treated for 48 hours with dimethyl sulfoxide (DMSO; 0.01%), **(A)** erastin (10 $\mu$M), in the presence of absence of deferoxamine (DFO; 100 $\mu$M) or ferrostatin (5 $\mu$M). Cells were stained with propidium iodide and percentage of cell death was analysed using a Tali Image Cytometer. Results presented as box and whisker plot, minimum of four biological repeats. All conditions were compared with DMSO control and single agent treatments. One-way ANOVA, Bonferroni's post-hoc test, $p$<0.01=**. Detailed results can be found in table A.13.

To further understand the type of cell death occurring, caspase 3 and 7 activity, associated with apoptotic cell death, was analysed in HO-1 and empty vector cells treated with DMSO, erastin, sapatinib and lapatinib. This showed decreased activity relative to DMSO controls in all treatments in both cell lines (fig 6.15 B), indicating that apoptosis was not occurring in response to treatment.

### 6.4.1 Inhibition of autophagy increases sapatinib- and lapatinib-induced cell death

HO-1 has been shown to increase levels of autophagy as a resistance mechanism in chronic myeloid leukaemia, breast cancer and ovarian cancer.[249–251] This was also seen in SKBR3 cells overexpressing HO-1 (fig 6.16 A), consistent with the mouse model where increased HO-1 correlated with increased autophagic flux (fig 6.1). The contribution of autophagy to resistance to sapatinib and lapatinib was investigated further.

Firstly, chemical inhibition of autophagy was confirmed by western blot. 3-methyladenine (3-MA) blocks phagophores maturing into autophagosomes, whereas bafilomycin A1

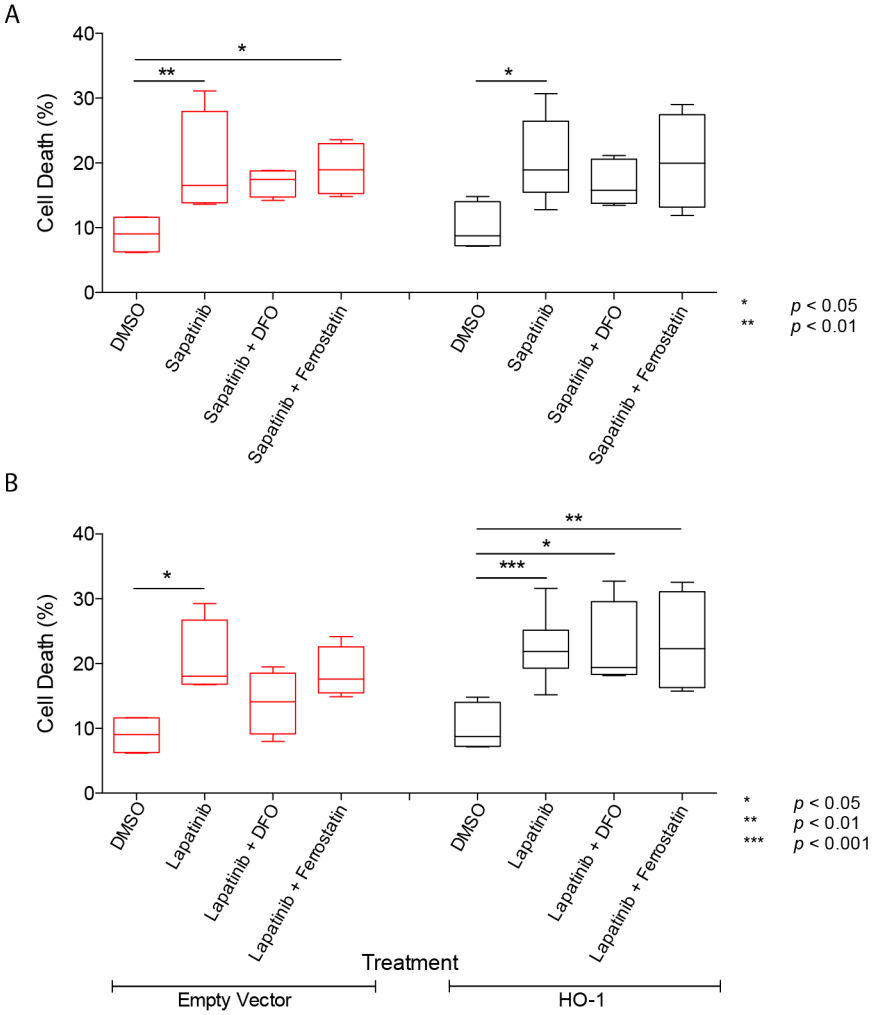


**Figure 6.14. HO-1-overexpressing cells still experience similar levels of cell death due to sapatinib and lapatinib.** SKBR3 human epidermal growth factor receptor 2 (HER2)-positive breast cancer cell line was stably transfected with a plasmid containing the heme oxygenase-1 (*HO-1*) gene or an empty plasmid and were treated for 48 hours with dimethyl sulfoxide (DMSO; 0.01%), **(A)** sapatinib (0.67 $\mu$M) or **(B)** lapatinib (5 $\mu$M) in the presence of absence of deferoxamine (DFO; 100 $\mu$M) or ferrostatin (5 $\mu$M). Cells were stained with propidium iodide and percentage of cell death was analysed using a Tali Image Cytometer. Results presented as box and whisker plot, minimum of four biological repeats. All conditions were compared with DMSO control and single agent treatments. One-way ANOVA, Bonferroni's post-hoc test, $p$<0.05=*, $p$<0.01=**, $p$<0.001=***. Detailed results can be found in table A.13.

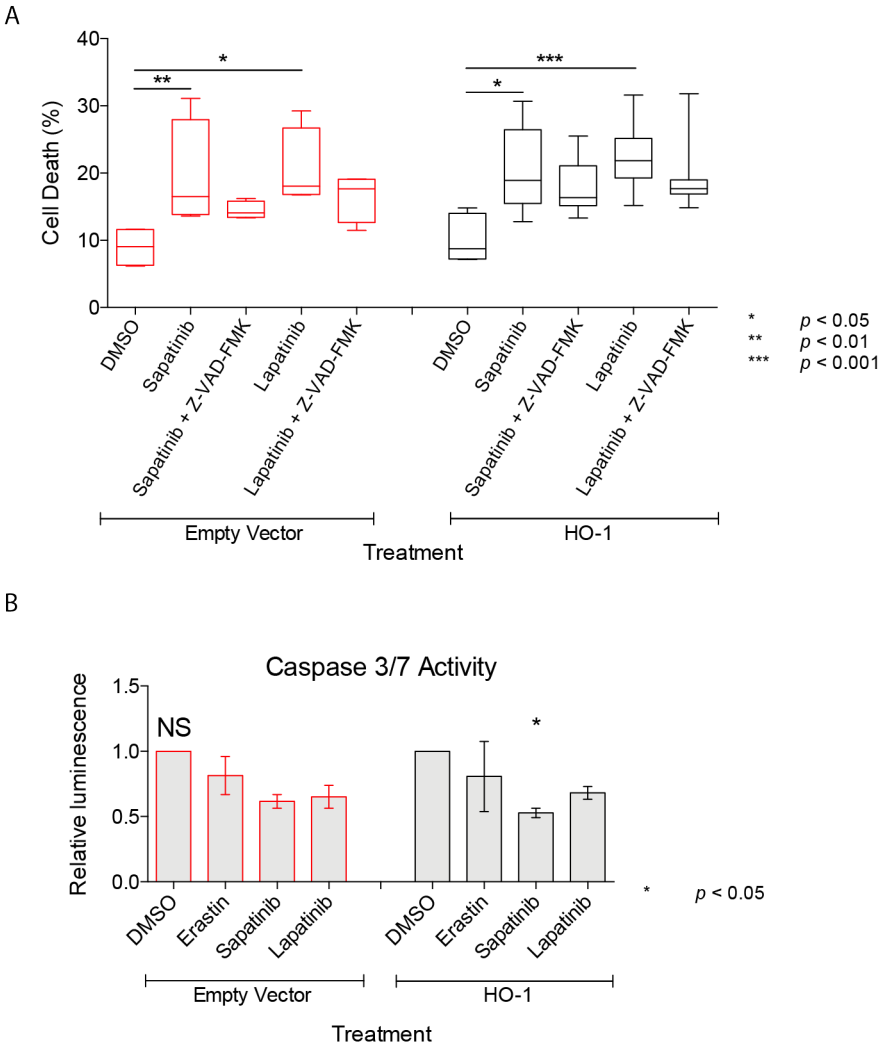


**Figure 6.15. Caspase inhibition does not rescue sapatinib- or lapatinib induced death in HO-1-overexpressing SKBR3 cells.** SKBR3 human epidermal growth factor receptor 2 (HER2)-positive breast cancer cell line was stably transfected with a plasmid containing the heme oxygenase-1 (*HO-1*) gene or an empty plasmid. **(A)** Cells were treated for 48 hours with dimethyl sulfoxide (DMSO; 0.01%), sapatinib (0.67 $\mu$M) or lapatinib (5 $\mu$M) in the presence of pan-caspase inhibitor benzyloxycarbonyl-phenylalanyl-fluoromethyl ketone (Z-VAD-FMK; 20 $\mu$M). Cells were stained with propidium iodide and percentage of cell death was analysed using a Tali Image Cytometer. Results presented as box and whisker plot, minimum of four biological repeats. All conditions were compared with DMSO control and single agent treatments. One-way ANOVA, Bonferroni's post-hoc test, $p$<0.05=*, $p$<0.01=**, $p$<0.001=***. **(B)** Caspase 3 and 7 activity was assessed in empty vector and HO-1-overexpressing cells treated with DMSO (0.01%), erastin (10 $\mu$M), sapatinib (0.67 $\mu$M) and lapatinib (5 $\mu$M) for 48 hours. Results presented as bar chart $\pm$ standard deviation, from 3 biological repeats. Kruskal-Wallis test, Dunn's post-hoc test, not significant = NS, $p$<0.05=*. Detailed results can be found in table A.13.

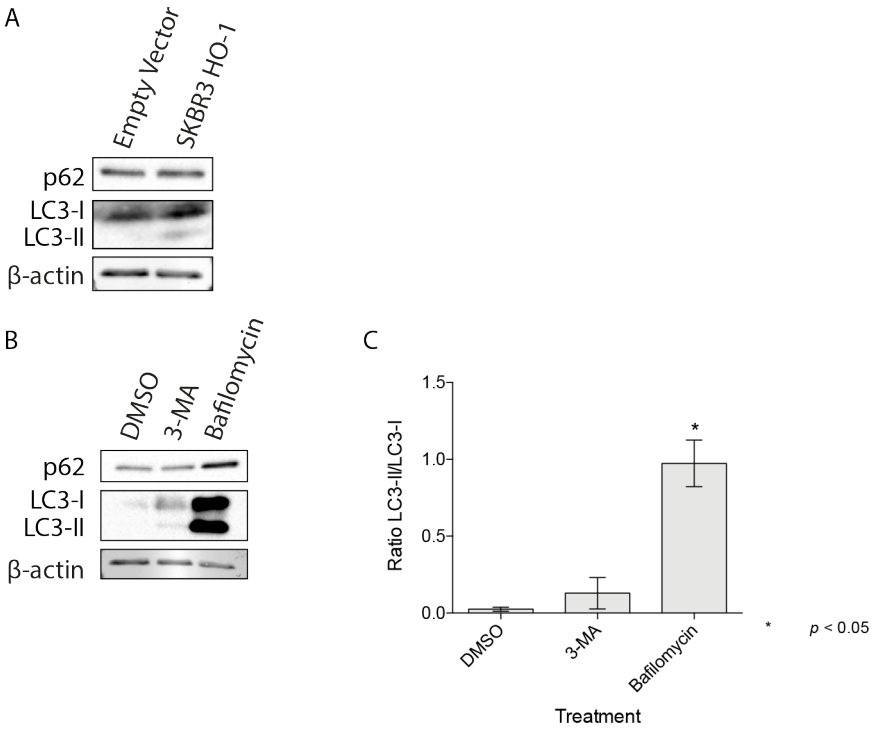


**Figure 6.16. Chemical inhibition of autophagy is successful in HO-1-overexpressing SKBR3 cells.** SKBR3 human epidermal growth factor receptor 2 (HER2)-positive breast cancer cell line was stably transfected with a plasmid containing the heme oxygenase-1 (*HO-1*) gene or an empty plasmid. **(A)** Representative western blot analysis (n=2) of sequestosome 1 (p62) and microtubule-associated proteins 1A/1B light chain 3B (LC3B). *B*-actin was used as a loading control. Cells were treated for 48 hours with dimethyl sulfoxide (DMSO; 0.01%), 3-methyladenine (3-MA; 5 mM) or bafilomycin A1 (bafilomycin; 5 nM). **(B)** Representative western blots, from three biological repeats, of p62 and LC3B. *B*-actin was used as a loading control. **(C)** Quantification of LC3BII:LC3BI. Results presented as bar graph, mean ± standard deviation. Kruskal-Wallis test, Dunn's post-hoc test, $p<0.05$=*.

inhibits autophagosomes fusing with lysosomes, thus preventing their acidification.[283,284] Both 3-MA and bafilomycin A1 were able to successfully inhibit autophagy (fig 6.16). Increased LC3BI can be seen after 3-MA treatment, compared with DMSO control, which is in accordance with 3-MA inhibiting autophagosome formation.[283] Bafilomycin A1 increased levels of LC3BI and LC3BII (fig 6.16 A), resulting in a higher ratio of LC3BII:LC3BI (fig 6.16 B) consistent with inhibition of autophagosomes fusing to lysosomes.[284] Bafilomycin A1 treatment also increased p62 levels compared with DMSO, indicating blockage of autophagy, whereas this cannot be seen after 3-MA treatment.

HO-1 and empty vector cells were co-treated with 3-MA or bafilomycin A1 and erastin. This showed that HO-1 cells, previously resistant to erastin-induced ferroptotic cell death (fig 6.14 A), had increased susceptibility when co-treated with either 3-MA or

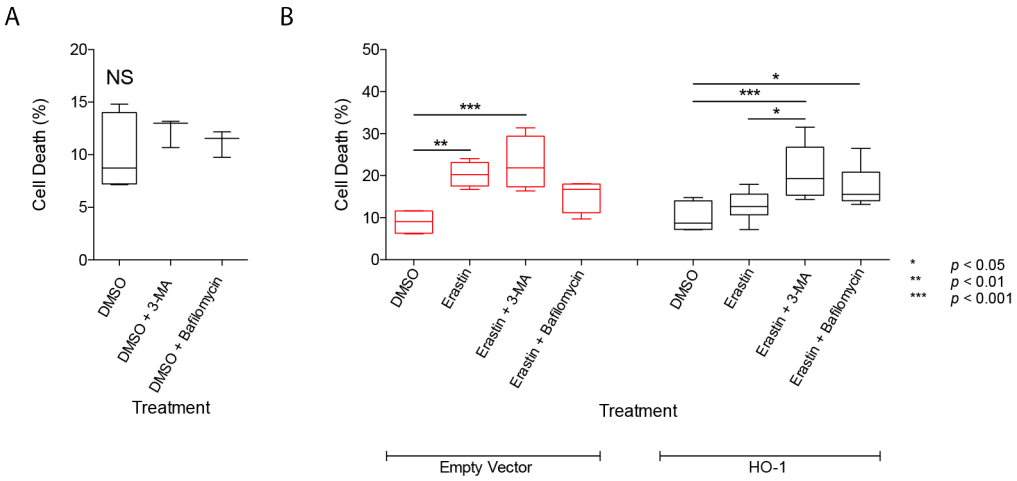


**Figure 6.17. Inhibition of autophagy increases ferroptotic cell death in HO-1-overexpressing SKBR3 cells.** SKBR3 human epidermal growth factor receptor 2 (HER2)-positive breast cancer cell line was stably transfected with a plasmid containing the heme oxygenase-1 (*HO-1*) gene or an empty plasmid. Cells were treated for 48 hours with **(A)** dimethyl sulfoxide (DMSO; 0.01%) or **(B)** erastin (10 $\mu$M) in the presence of absence of autophagy inhibitors 3-methyladenine (3-MA, 5 mM) or bafilomycin A1 (bafilomycin; 5 nM). Cells were stained with propidium iodide and percentage of cell death was analysed using a Tali Image Cytometer. Results presented as box and whisker plot, minimum of three biological repeats. All conditions were compared with DMSO control and single agent treatments. One-way ANOVA, Bonferroni's post-hoc test, not significant = NS, $p$<0.05=*, $p$<0.01=**, $p$<0.001=***. Detailed results can be found in table A.14.

bafilomycin A1 (fig 6.17 B). When exposed to 3-MA and bafilomycin A1 alone, no difference in cell death could be seen in HO-1-overexpressing cells (fig 6.17 A).

No significant difference in cell death was seen in empty vector cells co-treated with erastin and 3-MA or bafilomycin, compared with erastin alone. Treatment of HO-1-overexpressing cells with 3-MA or bafilomycin alone had no effect, but when combined with erastin significantly enhanced cell death. Therefore, resistance to ferroptosis by HO-1 is dependent on autophagy induction.

Co-treatment of empty vector cells with sapatinib or lapatinib and 3-MA or bafilomycin A1 resulted in little change in cell death (fig 6.18 A and B). In HO-1 cells, autophagy inhibition resulted in significantly increased cell death in response to both sapatinib and lapatinib (fig 6.18 A and B). Thus, in the context of HO-1-overexpression, autophagy is essential to maintain resistance.

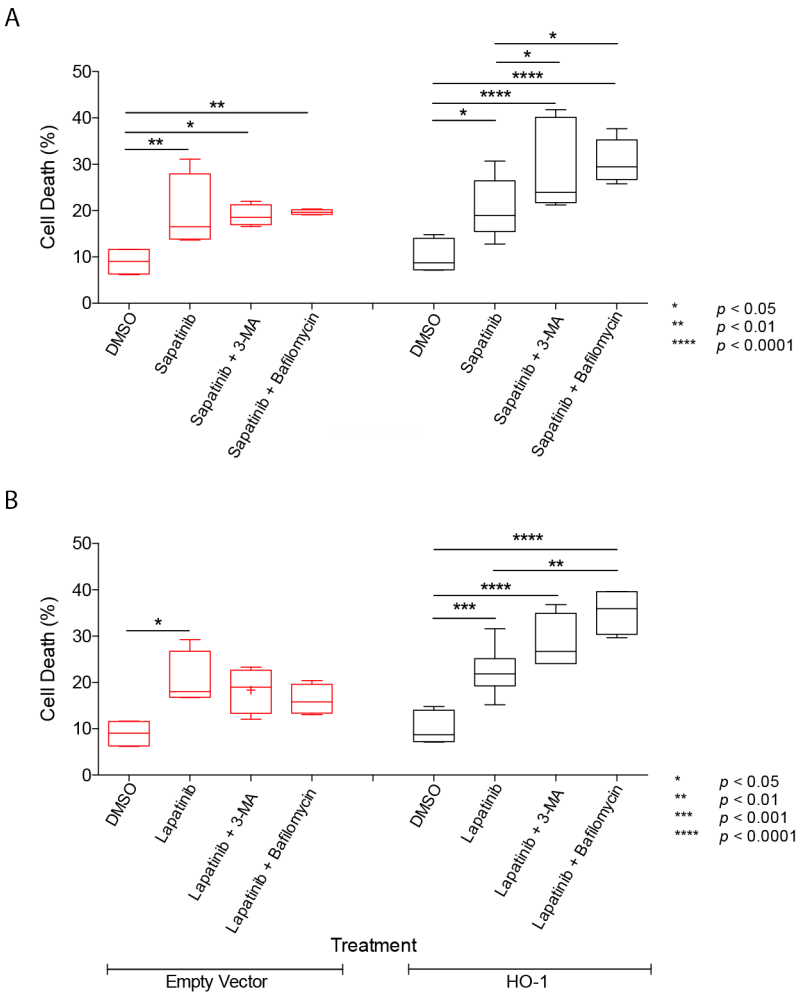


**Figure 6.18. Inhibition of autophagy increases sapatinib- and lapatinib-induced cell death in HO-1-overexpressing SKBR3 cells.** SKBR3 human epidermal growth factor receptor 2 (HER2)-positive breast cancer cell line was stably transfected with a plasmid containing the heme oxygenase-1 (*HO-1*) gene or an empty plasmid. Cells were treated for 48 hours with **(A)** sapatinib (0.67 $\mu$M) or **(B)** lapatinib (5 $\mu$M) in the presence of absence of autophagy inhibitors 3-methyladenine (3-MA, 5 mM) or bafilomycin A1 (bafilomycin; 5 nM). Cells were stained with propidium iodide and percentage of cell death was analysed using a Tali Image Cytometer. Results presented as box and whisker plot, minimum of three biological repeats. All conditions were compared with DMSO control and single agent treatments. One-way ANOVA, Bonferroni's post-hoc test, not significant = NS, $p$<0.05=*, $p$<0.01=**, $p$<0.001=***, $p$<0.0001=****. Detailed results can be found in table A.14.

## 6.5 Discussion

Altered iron metabolism and increased levels of HO-1 have been evidenced in many cancer types as a mechanism of resistance.[136–140,199,232,249–251,285] Increased ferrous iron within cells can lead to ferroptotic cell death through increased lipid peroxidation.[223] However, HO-1 can counteract increased oxidative damage,[286] and has been shown to protect against ferroptosis.[235] The results presented here show that HO-1 upregulation resulted in resistance to HER2-targeted therapies, sapatinib and lapatinib and that resistance is reliant on autophagy induction. Additionally, both agents can induce ferroptotic cell death in HER2-positive breast cancer cells.

### 6.5.1 Apoptotic cell death does not occur in response to sapatinib or lapatinib

Many pathways can be induced by HER2 signalling, including suppression of apoptosis through activation of AKT.[179] Inhibition of HER2 results in activation of the apoptotic pathway, through a lack of AKT and ERK signalling.[179,221] However, upon addition of lapatinib, both BT474 and SKBR3 human HER2 breast cancer cell lines have increased levels of Bcl-xL.[221] Results from a clinical trial support this, as no increase in apoptosis markers were evidenced in patients whose tumours were responding to treatment.[287]

This is in accordance with results presented in this chapter, which show no detectable cleaved caspase 3 upon treatment with sapatinib or lapatinib *in vitro* (fig 6.11 B), despite cell death. Additionally, treatment with pan-caspase inhibitor Z-VAD-FMK failed to rescue sapatinib- and lapatinib-induced cell death. Tumours responding to sapatinib treatment (fig 6.9 A–E and K) also showed no increase in cleaved caspase 3, despite a consistent reduction in volume over a minimum of 7 days. This indicates that our *in vitro* and *in vivo* models evidence that sapatinib and lapatinib do not induce caspase-dependent cell death, in accordance with the literature.[221,287]

However, it is unknown how HO-1-overexpressing cells are dying *in vitro* in response to sapatinib and lapatinib. Other methods of regulated cell death include caspase-dependent necrosis (caspase 8) and pyroptosis (caspase 1), although this would have been inhibited

by Z-VAD-FMK, as a broad spectrum pan-caspase inhibitor.[219,281] It is possible that these cells are undergoing accidental cell death — an instantaneous, catastrophic form of cell death which can result from cells being exposed to severe physical, chemical or mechanical insults.[219] Further investigation should focus on how this subset of cells are dying, which may allow a better understanding of how HO-1-induced resistance to HER2-targeted therapies can be overcome.

### 6.5.2 Sapatinib and lapatinib induce ferroptosis

SRC tyrosine kinase inhibitor, sorafenib, has been shown to induce ferroptosis *in vitro* in cell lines from a variety of cancer types.[288,289] The mechanism by which sorafenib is thought to induce ferroptosis is similar to erastin: inhibiting system $x_c^-$ and therefore glutathione synthesis. Both studies investigated other tyrosine kinase inhibitors, including lapatinib and concluded that they were unable to induce ferroptosis in the cell lines tested in the same way as sorafenib.

These results contradict the findings presented here which show that reduced viability and cell death caused by sapatinib and lapatinib can be rescued by iron chelator DFO and lipophilic antioxidant ferrostatin, indicating that cells are dying by ferroptosis (table 6.1; fig 6.10 A). Further supporting this conclusion is the lipid peroxidation seen after treatment with sapatinib and lapatinib, which is similar to that in cells treated with erastin (fig 6.10 B). Increased levels of COX2 in sapatinib-treated progressing and responding tumours (fig 6.9 F–J and L) provides further evidence for induction of ferroptosis, as COX2 has been identified as a marker of ferroptosis.[272,278]

In both published studies assessing the ferroptotic potential of lapatinib, no HER2-positive cell lines were used.[288,289] This indicates that HER2-targeting tyrosine kinase inhibitors may induce ferroptosis downstream of HER2, rather than by a tyrosine kinase-independent mechanism seen with sorafenib. A study by Ma et al.[290] showed that lapatinib was able to induce ferroptotic cell death in HER2-positive breast cancer cell line SKBR3 and triple-negative breast cancer cell line MDA-MB-231 in combination with a lysosome disrupting agent, siramesine.

The group showed that lapatinib treatment increased expression of transferrin receptor, whilst siramesine reduced expression of ferroportin. This suggests that lapatinib is capable of inducing ferroptosis in a HER2-independent manner, but only in combination with another agent.[290] However, in our studies we have seen no increase in transferrin receptor in response to sapatinib treatment (fig 4.12, 5.9). As such, in our system sapatinib and lapatinib may be inducing ferroptosis in both a HER2-dependent and HER2-indepedent manner. However, this has not been investigated as part of this work.

### 6.5.3 Dietary iron modulation represents a novel way to study ferroptosis *in vivo*

Thus far, no *in vivo* or *ex vivo* cancer model has evidenced ferroptosis, despite many *in vitro* studies.[223,288,290–292] Treatment of MMTV-NIC-PTEN$^{+/-}$ mice with an iron-deficient diet was able to alter tumours' response to sapatinib, resulting in fewer responding tumours in mice on an iron-deficient diet, compared with iron-low control diet mice (fig 5.4).

*In vivo* models of ferroptosis have so far been limited. Recently, models of ischemia-reperfusion injury, such as stroke, myocardial infarction and acute kidney injury, have evidenced ferroptosis *in vivo* and *ex vivo*.[293–296] Using ferroptosis inhibitors, these groups were able to show that ischemia-reperfusion injuries undergo ferroptotic cell death and inhibition of ferroptosis could reduce the injury sustained.[293–295]

Altering dietary iron intake *in vivo* is a novel method to modulate ferroptosis. Many features of dementia are consistent with ferroptosis: decreased cortical GSH, increased cortical iron and lipoxygenase activity and elevated lipid peroxidation products.[297] Using a GEMM in which *Gpx4* was conditionally knocked out, Hambright et al.[298] evidenced that forebrain neurons are susceptible to ferroptosis and that the features observed were consistent with this.

Despite not studying ferroptosis, Pino et al.[242] showed changes in lipid peroxidation after long-term iron deficiency in the brain. This provides good supporting evidence to suggest that an iron-deficient diet in MMTV-NIC-PTEN$^{+/-}$ mice is capable of modulating

cellular iron metabolism within tumours, as dietary iron modulation was able to show alterations in key changes associated with ferroptosis, such as lipid peroxidation.

### 6.5.4 Regulation of HO-1 is NRF2-independent

Treatment with trastuzumab or pertuzumab have been shown to result in generation of ROS in HER2-expressing ovarian cancer cell lines.[267] GSH depletion and reduced NRF2 signalling were also noted as a result of HER2 inhibition. A reduction in nuclear NRF2 was seen in MMTV-NIC-PTEN$^{+/-}$ tumours treated with sapatinib in accordance with the literature (fig 6.8 A, B and E),[252,267,299] although no GSH depletion was seen in our system (fig 6.6). Both HO-1 and GPX4, which are regulated by NRF2, were increased in sapatinib-treated mice (fig 4.8, 6.7).[252,267,299] However, HO-1 and GPX4 are also regulated in an NRF2-independent manner,[300,301] which is likely the case in our model.

In the literature, HO-1 can be induced via several different pathways.[249–251] Such pathways include NRF2-dependent, SRC/STAT3-dependent and MAPK-dependent regulation of HO-1-induced autophagy.[249,250,302] Sapatinib-treated tumours also displayed similar levels of ERK phosphorylation despite HER2 inhibition (fig 4.5, 4.6). This suggests that HO-1 may be regulated via the MAPK pathway in our model.

### 6.5.5 HO-1 mediates resistance to HER2-targeted therapies and is dependent on autophagy

Consistent with observations in many cancer types and therapies,[249–256] our data display a clear and novel role for HO-1 in resistance to sapatinib and lapatinib. HO-1-overexpressing cells were 5-fold more resistant to sapatinib-induced and 4-fold more resistant to lapatinib-induced growth inhibition than SKBR3 cells (table 6.2).

The mechanisms underlying resistance mediated by HO-1 involve induction of autophagy, response to oxidative stress or a combination of both.[249–256] This is consistent with our findings: HO-1 resulted in increased autophagy (fig 6.16). Inhibiting autophagy and exposing HO-1 expressing cells to HER2-targeted therapies resulted in increased

cell death, while having no deleterious effect on control cells (fig 6.18 B and C). In addition, while tumours responding to sapatinib had increased HO-1, there was no evidence of LC3B-positive puncta (fig 6.2), indicative of a lack of autophagy, suggesting that HO-1-mediated resistance is dependent on increased autophagic flux.

However, an iron-deficient diet was sufficient to induce autophagy without increased expression of HO-1. This may have been linked to increased degradation of ferritin to increase cellular iron levels.[260] Thus, when tumours from mice on an iron-deficient diet are initially exposed to sapatinib, autophagy induction may have already occurred, mitigating the need for HO-1. Therefore, irrespective of the mechanism of induction, increased autophagy protected cells from the effects of sapatinib. This is in contention with the literature, which evidences a mixed role for autophagy in ferroptosis. Although ferroptosis is still ill-defined, thus the exact role of autophagy cannot be determined to be supportive of ferroptosis or suppressive.[219,297]

### 6.5.6 Summary

Overall, our findings indicate that HER2-targeted agents sapatinib and lapatinib induce ferroptosis *in vitro* and *in vivo*. We have shown that expression of HO-1, an iron-deficient diet and anti-ferroptotic agents are able to maintain a resistant phenotype in response to sapatinib. Additionally, resistance due to increased HO-1 is reliant on autophagy induction, inhibition of which increases sapatinib- and lapatinib-induced cell death. However, an iron-deficient diet increases autophagic flux independently of HO-1, resulting in resistance to HER2-targeted therapies prior to treatment.

# Chapter 7

# Discussion

Targeted therapies against HER2 have revolutionised treatment options for patients with HER2-positive breast cancer. Despite this, development of resistance remains a key problem; approximately half of patients experience *de novo* resistance, while 70% of those that initially responded will develop acquired resistance within two years of treatment.[69–71]

Many *in vitro* studies have uncovered resistance mechanisms including: epitope masking, lineage changes, mutations in HER2, downstream pathway activation and bypass RTK activation. However, translating these findings into the clinic and therapeutically targeting them has proven difficult or unreliable.[22,93,96,131] With this in mind, the aims of this thesis were:

- Understand the link between EMT and resistance to HER2-targeted therapy previously identified in the Brunton lab.[84]

- Use a mouse model of HER2-driven mammary cancer to identify novel mechanisms of resistance to HER2-targeted therapy.

The first aim was addressed by analysing the expression of several EMT-associated transcription factors to understand how EMT was being maintained at a transcriptional level. Consistent with the literature, we showed that ZEB1 and ZEB2 were highly expressed in sapatinib-resistant tumours that had undergone EMT, compared with those that maintained an epithelial phenotype.[85,171,172] Analysis of patient data confirmed that this finding translated to the clinic and that patients with high expression of ZEB1 had worse RFS than those with low expression.

Generation of drug resistant lines *in vitro* did not recapitulate the phenotype seen *in vivo*, which may be due to discordance between the *PTEN* status of the *in vivo* and *in vitro* models. Transient overexpression of *ZEB1* did not induce overt EMT and despite a trend towards lower levels of HER2 protein and transcript, did not give rise to loss of HER2. The lack of pro-inflammatory cytokines, which would be present *in vivo* may have prevented a full program of EMT being induced.

However, loss of HER2 did induce some features of EMT; increased *ZEB1* and migratory capacity were seen. These results contradict the literature, which shows that EMT can

drive loss of HER2.[90,157] Although without external factors such as pro-inflammatory cytokines, the full program of EMT may not be realised by loss of HER2 alone.

The second aim was addressed using a proteomics approach to identify differentially regulated proteins in sapatinib-treated tumours compared with vehicle-treated tumours. This revealed increased levels of proteins associated with cellular iron homeostasis: HO-1 and ceruloplasmin. Further investigation revealed extracellular iron deposition and increased levels of iron exporter ferroportin in sapatinib-treated tumours.

As iron is known to impact tumour growth, we then looked at the effect of altering dietary iron intake on the development of resistance to sapatinib. This showed that an iron-deficient diet can reduce the time taken for tumours to progress on sapatinib. Additionally, these tumours did not upregulate HO-1, despite tumours from mice on a iron-low control diet treated with sapatinib showing increases similar to the previous *in vivo* experiment.

Assessment of ferroptosis induction by HER2-targeting agents revealed increased COX2, a marker of ferroptosis induction,[272,278] in sapatinib-treated mice fed an iron-deficient diet. *In vitro* studies supported this, showing higher levels of lipid peroxidation, associated with ferroptotic cell death, after treatment with sapatinib and lapatinib. This finding has not been evidenced in the literature,[288,289] but increased ROS and GSH depletion have been shown after treatment with trastuzumab and pertuzumab, supporting our findings.[267] Additionally, studies have shown no increase in apoptosis markers in regressing tumours,[221,287] which is also supported by our data.

Overexpression of HO-1 showed that this rendered cells resistant to sapatinib, lapatinib and erastin, which is known to induce ferroptosis. Further investigation of HO-1 revealed a correlation with increased autophagic flux in sapatinib-treated tumours, which was also seen in tumours from mice fed iron-deficient diets regardless of treatment arm. Increased autophagic flux was confirmed in the HO-1-overexpressing cells *in vitro*. Furthermore, inhibition of autophagy was able to resensitise cells to HER2-targeted therapies and erastin. Expression of HO-1 driving resistance via autophagy is noted in the literature,[249–251] but these data are the first evidence of this mechanism in response to HER2-targeted therapies.

Although HO-1 expression was able to increase cell viability, the same level of cell death as SKBR3 or empty vector cells could be seen after treatment with sapatinib and lapatinib. Furthermore, this couldn't be rescued by anti-ferroptotic agents, as seen in SKBR3 and empty vector cells, or a pan-caspase inhibitor. This raises the question of how these cells are dying and if this could be exploited to overcome resistance in patients.

## 7.1 Future work

The results presented in this thesis have partially fulfilled the aims set out above. However, my findings have raised additional questions which will be the focus of future work.

### 7.1.1 Why did *in vitro* models fail to replicate EMT and loss of HER2?

In chapter 3, generation of resistant cell lines, overexpression of *ZEB1* and knockdown of *ERBB2* failed to accurately represent the resistant fragment-derived tumours which had undergone EMT. This limitation resulted in the question of how EMT and loss of HER2 were linked remaining unanswered. However, some EMT-like features were evidenced in *ERBB2* knockdown cells, despite not undergoing overt EMT. Future studies should utilise these cells, treating them with pro-inflammatory cytokines, such as IL-6 and TGF-$\beta$ which have been noted in the literature to induce EMT in response to targeted therapies, maintaining a positive feedback loop.

The experiments mentioned above will address how EMT can be induced by loss of HER2, but performing these experiments will not answer how cells initially lost expression of HER2. As material from the fragment-derived tumours is limited, other *in vitro* techniques will need to be utilised to address this question. Initial work on SKBR3 cells with CRISPR knockout of *PTEN* has begun; FACS analysis has shown that they have lower levels of HER2 on the cell surface compared with parental SKBR3 cells. This may be transient, but further characterisation will confirm this.

Treating SKBR3 PTEN$^{-/-}$ cells with sapatinib and lapatinib to generate resistant lines may give rise to cell lines with loss of HER2, better representing the *in vivo* loss. Furthermore, if these cell lines are generated using 3D culture methods, co-culture or treatment with pro-inflammatory cytokines, to mimic the TME, it may encourage a switch to a mesenchymal phenotype with concurrent loss of HER2.

### 7.1.2 What effect would iron overload have on the development of resistance?

In chapter 5, mice fed an iron-deficient diet had tumours that progressed more quickly and were less likely to respond to sapatinib than tumours from mice fed a iron-low control diet. Studies have shown that patients presenting with FID, sometimes associated with iron-deficiency anaemia, have worse ECOG scores and lower OS than those without FID.[239] A question that was not answered as part of this thesis is how a diet rich in iron would affect tumour development and progression in sapatinib-treated mice.

However, iron is often associated with increasing tumour growth and proliferation, thus providing an iron rich diet may not have the opposite effect as an iron-deficient diet on the development of resistance.[227,243–246] Therefore, before progressing with further *in vivo* studies, this should be explored by supplementing cells with iron in conjunction with sapatinib and lapatinib treatments to ascertain if this is likely to enhance cell death or, conversely, proliferation *in vitro*.

### 7.1.3 How does an iron-deficient diet drive autophagy?

As seen in chapter 6, expression of HO-1 and increased autophagic flux were correlated in tumours progressing on sapatinib treatment. However, similar levels of LC3B-positive puncta were seen in mice fed an iron-deficient diet, irrespective of treatment regimen and did not correlate with HO-1 expression. In the literature, recycling of iron-containing proteins and ferritin complexes is performed differently in iron deficiency compared with iron sufficiency. Ferritin degradation is dependent on the acidic environment of lysosomes; when iron is sufficiently available within cells, this process is independent

of autophagy. However, in iron-deficient conditions, ferritin is targeted for lysosomal degradation via autophagy.[260,303]

We have shown that iron chelation with DFO can increase cell viability and decrease cell death in response to sapatinib and lapatinib. To investigate this further, autophagy induction should be studied in SKBR3 cells in the presence or absence of iron chelation. This will provide confirmation that altering iron availability can induce autophagy, which provides protection from HER2-targeted therapies. Uncovering the mechanisms governing autophagy in our systems, we will be able to gain a better understanding of how this may be targeted clinically. Due to the lack of clinically-approved specific inhibitors of autophagy, this is of particular importance.[304]

### 7.1.4 How are HO-1-overexpressing cells dying *in vitro*?

Despite increased viability, HO-1-overexpressing cells experienced levels of cell death similar to SKBR3 and empty vector cells (fig 6.14 6.15). Iron chelation and pan-caspase inhibitor Z-VAD-FMK failed to rescue sapatinib- and lapatinib-induced death, indicating that these cells are not dying by ferroptosis or apoptosis.

As a pan-caspase inhibitor, Z-VAD-FMK would be expected to inhibit pyroptosis and necroptosis in addition to apoptosis, although there are conflicting studies showing enhanced activation of caspase 8 after Z-VAD-FMK treatment.[219] However, treatment did not increase cell death, thus it can be assumed this did not occur in our system.

More in depth analysis of caspase activation would rule out caspase-dependent cell death mechanisms.[219] Autophagic cell death could be occurring, due to inappropriately increased autophagy resulting in enhanced degradation rather than a protective mechanism. However, inhibition of autophagy increased cell death, therefore this method of cell death is unlikely to be occuring in our system.

The most likely form of cell death occurring is accidental cell death.[219] Providing evidence for this will rely on ruling out other cell death mechanisms. By understanding the mechanisms involved, it may be possible to enhance cell death, thus overcoming resistance and restoring sensitivity to HER2-targeted therapies. Although concentrations

of sapatinib and lapatinib exceeded the concentration required for target inhibition, they were similar to concentrations seen in plasma and patients tumours, therefore maintaining clinical relevance.[61,162–164]

### 7.1.5 Are these changes seen in patients?

The findings presented in chapters 4–6 indicate a novel role for dietary iron and HO-1 in inducing autophagy to overcome ferroptosis caused by HER2-targeted therapies and resistance to these agents. However, if these mechanisms are not observed in the clinic, the findings presented here would have limited significance.

Trastuzumab is first-line treatment for patients presenting with HER2-positive breast cancer. Studies with trastuzumab and pertuzumab have shown increased ROS generation and GSH depletion after treatment *in vitro*,[267] which are indicative of ferroptosis. This indicates that our findings that sapatinib and lapatinib induce ferroptosis are likely to be applicable across all HER2-targeted therapies.

With this in mind, analysis of patient material will allow further validation of our findings. Work is currently ongoing analysing gene expression data in matched pre- and post-trastuzumab treatment patient samples. This will allow interrogation of a wide range of genes associated with cellular iron homeostasis to support the results presented here. However, several studies have shown that HO-1 is regulated post-transcriptionally by miR-377, miR-217 and embryonic lethal abnormal vision (ELAV) RNA-binding proteins.[305,306] As such, this analysis will likely not highlight HO-1, although other proteins involved in iron homeostasis may be indicated.

Therefore, analysis of patient material for iron deposition, HO-1 expression and the presence of LC3B-positive puncta may give a better indication of how these findings may be translated to the clinic. If these results were able to be linked to pathology reports including iron and haemoglobin levels, this would provide further significance to our findings.

## 7.2 Wider implications

The results presented in this thesis have so far focused on their relevance to resistance to HER2-targeted therapies. However, they may have wider implications in other fields.

### 7.2.1 Dietary iron modulation

In our study, we showed modulation of the development of resistance by utilising an iron deficient diet. This reduced the number of tumours responding to sapatinib treatment, which were shown to have increased COX2, a marker of ferroptosis. Together with the *in vitro* data presented in chapter 6, this supported the hypothesis that HER2-targeted therapies induced ferroptosis. These data are the first indication that susceptibility to ferroptosis can be affected by dietary modulation of iron. Ferroptosis has been implicated in a wide range of pathologies including degenerative brain diseases, ischemia-reperfusion-induced injuries and kidney disease.

Degenerative brain diseases such as Alzheimer's and Parkinson's disease are caused by the loss of synaptic neurons.[236] There is mounting evidence linking disease progression to increased iron deposition and ferroptosis.[242,297] Supporting this, inducible deletion of *Gpx4* in adult mice resulted in increased neuronal loss in the hippocampus together with astrogliosis, which is seen in patients with Alzheimer's.[298]

A clinical trial administering iron chelator deferiprone showed lower levels of iron deposits in the substantia nigra and improved motor scores in patients with beginning treatment earlier compared with those who started later.[307] With this in mind, administering an iron-deficient diet to patients with degenerative brain diseases such as Alzheimer's or Parkinson's could reduce the rate of disease progression and improve patient outcomes.

In chapter 6, we evidenced increased autophagy as a result of an iron deficient diet. Impairment of autophagy has been shown in both patients and models of Alzheimer's and Parkinson's disease.[308–311] Several studies have investigated autophagy induction to increase the removal of extracellular plaques consisting of $\beta$-amyloid, tau and $\alpha$-

synuclein aggregates.[308,310,311] Thus, dietary iron modulation may serve a dual purpose in alleviating the symptoms and progression of degenerative brain diseases.

Ischemia-reperfusion-induced injuries include myocardial infarction, stroke and peripheral vascular disease. Nutrient starvation is a key feature of these injuries, resulting in amino acid deprivation.[296] A recent study showed that organ injury as a result of ischemia-reperfusion was mediated by glutaminolysis and transferrin and that reversal of these processes, or treatment with DFO or ferrostatin, could reduce cell death caused by ischemia-reperfusion.[296] Thus, in patients that are deemed to have an increased risk of myocardial infarction or stroke, adherence to an iron-deficient diet could reduce injuries sustained in an acute event.

Acute kidney injury, if unresolved, can progress to chronic kidney disease. Acute injury can be caused by a range of factors, including ischemia-reperfusion, toxic substances or obstruction of the urinary tract.[235] In these instances, the proximal tubule becomes increasingly sensitive to injury and cell death. A recent study showed that this cell death occurred by ferroptosis and that *ex vivo* treatment of proximal tubules with iron chelating agents attenuated cell death.[235,312] Therefore, in patients presenting with acute kidney injury, an iron-deficient diet may represent a novel way to minimise proximal tubule cell death.

### 7.2.2 Autophagic flux induced by HO-1

Direct inhibition of autophagy has proved difficult so far, thus targeting upstream proteins resulting in increased autophagy could represent a good avenue to prevent autophagy induction. Chloroquine, an anti-malarial, is the main clinically-approved autophagy inhibitor. However prolonged exposure to chloroquine at clinically relevant concentrations for autophagy inhibition results in severe side effects.[304] Although it is currently indicated for treatment of systemic lupus erythematosus and rheumatoid arthritis, this does not rely on autophagy inhibition and uses much lower doses than those required to inhibit autophagy.[313]

A derivative of chloroquine, hydroxychloroquine, has shown promising in phase I and II clinical trials. However, treatment frequently results in dose-limiting fatigue and

gastrointestinal side effects. Similar to chloroquine treatment, hydroxychloroquine at higher doses for longer periods of time results in severe toxicities.[314–316]

Pantoprazole, a proton pump inhibitor approved for gastro-oesophageal reflux, has recently been investigated at higher doses as an autophagy inhibitor.[317,318] Despite effectively inhibiting autophagy, higher doses give rise to similar adverse events as hydroxychloroquine.[317] Therefore, despite being clinically-approved, pantoprazole faces the same challenges as other autophagy inhibitors.

In our model, autophagy was induced due to HO-1 expression both *in vivo* and *in vitro*. Other studies have also shown this mechanism of induction in several cancer types.[249–251] With this in mind, inhibition of HO-1 may provide a novel way in which to inhibit autophagy without the adverse events commonly seen due to off-target effects.[304,314]

Metalloporphyrins show good inhibition of HO-1 *in vitro*, but this has failed to translate to the clinic. Inhibition of HO-1 with zinc protoporphyrin IX showed good anti-tumour effects *in vivo*. However, when combined with chemotherapy agents, it was unable to enhance their anti-tumour effects, despite potentiating toxicities.[319]

Conversely, autophagy induction has been shown to have a protective effect from chemotherapy-induced damage to the proximal tubules of the kidneys.[304] Recent studies have linked this damage and cell death to ferroptosis, which can be mitigated by expression of HO-1.[235,312] Further understanding the link between HO-1 and autophagy could aid in selectively increasing autophagy in the kidneys, minimising damage, while maintaining autophagy inhibition in tumours.

Studies have looked at induction of HO-1 through dietary supplements or administration of hemin. However, these trials have so far failed to show any clinical benefit due to HO-1 expression as a result of the interventions applied.[320,321] Despite this, HO-1 induction remains a promising avenue for treating acute kidney and ischemia-reperfusion injuries.

## 7.3 Summary and conclusions

In this study, we explored the mechanisms governing a previously uncovered link between EMT and HER2 loss and the role of HO-1 and iron in response to HER2-targeted therapies. To achieve this, we utilised two mouse models of HER2-positive breast cancer; one GEMM which develops HER2-driven mammary tumours and one allogeneic model using tumour fragments derived from the GEMM. To confirm results from the *in vivo* models, a range of *in vitro* models were utilised.

In a fragment-derived tumour mouse model, we showed that expression of ZEB1 and ZEB2 maintained EMT *in vivo*. Furthermore, loss of HER2 induced some properties associated with EMT: increased expression of *ZEB1* and migration. Although, the mechanism behind loss of HER2 *in vivo* is still unknown.

In another mouse model of HER2-positive breast cancer, we demonstrated a link between resistance to HER2-targeted therapies and ferroptosis, which was modulated by altering dietary iron intake. This resistance was also associated with HO-1 expression, which correlated with increased autophagic flux. However, dietary iron modulation did not increase HO-1, with tumours showing increased autophagy induction in response to an iron-deficient diet regardless of treatment arm.

In conclusion, the results presented within this thesis support the hypothesis of ferroptotic cell death in response to HER2-targeted therapies, which may be mitigated by expression of HO-1 or administration of an iron-deficient diet to induce autophagy. With a better understanding of these processes, they could be exploited in the clinic to overcome therapy resistance.

# Appendix A

# Detailed results

**Table A.1.** Chapter 3 fragment-derived tumour results

| | **Vehicle** | **Sapatinib** | **Sapatinib-EMT** |
|---|---|---|---|
| Figure 3.2 | | | |
| ZEB1, % (95% CI) | 87.5 (62.23–94.17) | 95.26 (88.28–96.30) | 45.87 (37.03–51.38) |
| ZEB2, % (95% CI) | 80.21 (68.05–92.57) | 78.21 (66.63–86.95) | 50.29 (40.51–60.06) |
| SNAIL, % (95% CI) | 19.44 (14.79–51.13) | 22.38 (17.19–50.96) | 16.11 (11.97–16.56) |
| SLUG, % (95% CI) | 11.08 (3.04–30.01) | 9.34 (5.67–33.85) | 8.78 (4.81–56.76) |
| TWIST, % (95% CI) | 0.85 (0.30–5.78) | 1.12 (0.84–1.41) | 1.20 (048–1.92) |

**Table A.2.** Chapter 3 resistant cell line results

| | **SKBR3** | **SapR-A** | **SapR-B** | **LapR-A** | **LapR-B** |
|---|---|---|---|---|---|
| Figure 3.8 | | | | | |
| Confluency, % (95% CI) | 36.97 (27.33–59.90) | 22.45 (22.28–47.32) | 37.51 (17.20–45.44) | 26.01 (23.67–31.28) | 40.78 (37.49–55.29) |
| Figure 3.9 | | | | | |
| Wound closure, % (95% CI) | 19.50 (13.12–19.66) | 26.06 (14.26–45.47) | 35.82 (11.60–40.79) | 11.01 (6.40–18.75) | 23.78 (12.00–32.58) |
| Figure 3.12 | | | | | |
| *ERBB2*, $\Delta$CT (95% CI) | 6.36 (5.36–7.91) | 7.96 (7.33–8.88) | 6.44 (4.66–7.58) | 6.15 (5.11–7.31) | 6.12 (4.99–9.91) |
| Figure 3.13 | | | | | |
| HER2-negative cells, % (95% CI) | 5.70 (2.70–5.90) | 2.65 (2.40–2.90) | 2.35 (1.40–3.30) | 10.55 (6.30–14.80) | 8.25 (3.50–13.00) |

**Table A.3.** Chapter 3 *ZEB1*-overexpressing cell line results

| | **Empty vector** | ***ZEB1*-overexpressing** | **Significance** |
|---|---|---|---|
| Figure 3.15 | | | |
| *ERBB2*, ΔCT (95% CI) | 2.91 (2.83–4.40) | 3.71 (3.35–4.90) | NS |

**Table A.4.** Chapter 3 *ERBB2* shRNA cell line results

| | **Empty vector** | ***ERBB2* shRNA** | **Significance** |
|---|---|---|---|
| Figure 3.16 | | | |
| *ERBB2*, ΔCT (95% CI) | 3.12 (1.12–3.37) | 9.49 (9.11–10.13) | 0.0001 |
| *ERBB3*, ΔCT (95% CI) | 5.34 (4.13–5.74) | 5.64 (4.82–7.36) | NS |
| Figure 3.17 | | | |
| *ZEB1*, ΔCT (95% CI) | ND | 17.26 (16.96–17.55) | 0.0001 |
| *ZEB2*, ΔCT (95% CI) | 19.76 (14.26–23.17) | 18.32 (14.21–19.21) | NS |
| *SNAIL*, ΔCT (95% CI) | 11.44 (8.57–11.52) | 12.13 (11.51–12.31) | NS |
| *SLUG*, ΔCT (95% CI) | 9.15 (8.40–10.09) | 6.27 (5.73–6.35) | 0.01 |
| Figure 3.18 | | | |
| Confluency, % (95% CI) | 29.33 (13.79–37.49) | 14.25 (3.81–20.79) | 0.0001 |
| Figure 3.19 | | | |
| Wound closure, % (95% CI) | 39.14 (37.04–44.01) | 91.26 (89.93–100.00 | 0.01 |

**Table A.5.** Chapter 4 results

| | Vehicle | Sapatinib | Significance |
|---|---|---|---|
| Figure 4.2 | | | |
| Tumour, % of section (95% CI) | 81.02 (76.49–87.02) | 76.46 (65.43–89.33) | NS |
| Cell area, $\mu m^2$ (95% CI) | 89.30 (86.59–91.93) | 94.61 (91.09–97.18) | 0.05 |
| Nuclear area, $\mu m^2$ (95% CI) | 57.05 (56.33–58.10) | 62.76 (59.86–64.68) | 0.01 |
| Figure 4.3 | | | |
| HER2, % (95% CI) | 79.54 (70.72–85.80) | 78.3 (55.57–91.31) | NS |
| Vimentin, % (95% CI) | 2.91 (1.59–5.93) | 2.56 (1.63–8.38) | NS |
| $\beta$-catenin, % (95% CI) | 58.72 (51.66–65.37) | 84.09 (66.11–88.11) | NS |
| Figure 4.4 | | | |
| Ki-67, % (95% CI) | 21.97 (13.95–39.88) | 69.93 (29.32–91.19) | 0.0006 |
| PTEN, % (95% CI) | 94.73 (89.84–97.18) | 93.28 (84.28–98.25) | NS |
| Figure 4.5 | | | |
| phospho-AKT, % (95% CI) | 80.18 (64.37–87.20) | 36.45 (31.29–80.83) | 0.05 |
| phospo-ERK, % (95% CI) | 63.75 (54.93–73.13) | 63.22 (35.01–89.43) | NS |
| Figure 4.6 | | | |

Continued on the next page

| | | | |
|---|---|---|---|
| c-Myc, $\log_{10}$ RFI (SD) | 2.492 (±0.01) | 2.487 (±0.03) | 0.05 |
| phospho-AKT, $\log_{10}$ RFI (SD) | 1.643 (±0.43) | 2.747 (±0.47) | 0.01 |
| phospho-PLC-$\gamma$1, $\log_{10}$ RFI (SD) | 1.746 (±0.19) | 2.002 (±0.11) | 0.05 |
| phospho-ERK, $\log_{10}$ RFI (SD) | 3.251 (±0.2116) | 3.464 (±0.1304) | NS |
| phospho-SMAD1/5, $\log_{10}$ RFI (SD) | 1.409 (±0.32) | 0.8102 (±0.39) | 0.05 |
| phospho-SMAD1/5 : SMAD1+SMAD5 (95% CI) | 0.004686 (0.0008255–0.01188) | 0.002526 (0.001509–0.007842) | NS |
| Figure 4.10 | | | |
| *Cp*, ΔCT (95% CI) | 0.63 ((3.07)–4.51) | 1.82 ((5.55)–5.58) | NS |
| *Fth*, ΔCT (95% CI) | 2.00 ((2.83)–1.19) | 1.97 ((4.14)–(0.33)) | NS |
| *Ftl*, ΔCT (95% CI) | 1.824 ((3.92)–0.74) | 2.37 ((4.10)–(0.20)) | NS |
| *Ho-1*, ΔCT (95% CI) | 3.47 ((0.93)–4.64) | 0.40 ((1.46)–4.77) | NS |
| Figure 4.11 | | | |
| Total iron, ng/$\mu$g protein (95% CI) | 2.59 (1.40–4.60) | 2.30 (1.75–4.68) | NS |
| Ferrous ($Fe^{2+}$) iron, ng/$\mu$g protein (95% CI) | 2.26 (1.22–3.07) | 2.22 (1.60–2.98) | NS |
| Ferric iron ($Fe^{3+}$) iron, ng/$\mu$g protein (95% CI) | 0.18 (0.04–1.80) | 0.51 (0.08–1.23) | NS |
| Figure 4.12 | | | |
| Transferrin receptor, % (95% CI) | 49.63 (40.06–60.01) | 59.40 (13.61–87.62) | NS |
| DMT-1, % (95% CI) | 98.02 (93.55–99.33) | 98.35 (96.53–99,86) | NS |
| Ferroportin, % (95% CI) | 98.30 (94.49–99.18) | 99.73 (97.17–99.93) | 0.01 |

**Table A.6.** Chapter 4 results

| | Non-tumour | | | Tumour | | |
|---|---|---|---|---|---|---|
| | Vehicle | Sapatinib | Significance | Vehicle | Sapatinib | Significance |
| Figure 4.6 | | | | | | |
| Nuclear phospho-SMAD1/5/8, % (95% CI) | 23.88 (16.67–31.06) | 28.58 (22.27–44.42) | NS | 46.35 (39.40–57.89) | 56.57 (32.58–75.82) | NS |
| Figure 4.8 | | | | | | |
| Ceruloplasmin, % (95% CI) | 33.96 (17.89–49.78) | 59.16 (26.47–72.97) | NS | 53.07 (36.82–69.46) | 86.38 (58.16–92.31) | 0.05 |

Continued on the next page

| | Non-tumour | | | Tumour | | |
|---|---|---|---|---|---|---|
| | Vehicle | Sapatinib | Significance | Vehicle | Sapatinib | Significance |
| Ferritin heavy chain, % (95% CI) | 83.91 (80.68–87.29) | 91.45 (80.68–95.86) | NS | 83.98 (74.97–88.77) | 93.12 (82.63–98.54) | NS |
| Ferritin light chain, % (95% CI) | 98.49 (98.17–98.81) | 98.57 (97.98–99.23) | NS | 85.92 (76.13–90.89) | 91.00 (58.76–97.30) | NS |
| HO-1, % (95% CI) | 23.06 (13.76–32.12) | 27.14 (21.99–46.82) | NS | 14.31 (8.88–26.17) | 50.61 (23.81–73.39) | 0.01 |
| Figure 4.9 | | | | | | |
| Nuclear ferritin heavy chain, % (95% CI) | 91.25 (88.45–94.08) | 95.11 (93.10–96.74) | NS | 79.13 (71.21–89.03) | 91.87 (71.67–98.34) | NS |
| Nuclear ferritin light chain, % (95% CI) | 82.99 (82.93–86.26) | 87.66 (83.09–89.22) | NS | 15.60 (13.62–17.82) | 29.82 (17.97–34.55) | NS |
| Nuclear HO-1 | 32.42 (22.14–40.77) | 34.86 (20.53–48.36) | NS | 14.18 (8.04–35.84) | 48.58 (17.54–57.83) | 0.05 |
| Figure 4.11 | | | | | | |
| Ferric ($Fe^{3+}$) iron, % (95% CI) | 1.53 (1.00–3.91) | 14.39 (3.42–33.83) | 0.001 | 2.16 (1.17–3.93) | 4.42 (0.61–21.61) | NS |
| Three-day treatment | | | | | | |
| Figure 4.14 | | | | | | |
| Ferric ($Fe^{3+}$) iron, % (95% CI) | 0.21 (0.10–1.01]) | 0.23 (0.07–0.99) | NS | 0.18 (0.03–3.79) | 0.47 (0.21–0.87) | NS |
| Fragment-derived tumour experiment | | | | | | |
| Figure 4.16 | | | | | | |
| Ferric ($Fe^{3+}$) iron, % (95% CI) | 3.01 (0.89–17.33) | 14.97 (9.77–43.90) | NS | 2.00 (0.29–8.17) | 6.15 (3.13–14.36) | NS |

**Table A.7.** Chapter 4 results: three-day treatment

| | Vehicle | Sapatinib | Significance |
|---|---|---|---|
| Figure 4.13 | | | |
| Ceruloplasmin, % (95% CI) | 51.48 (33.74–80.09) | 74.12 (45.91–92.97) | NS |
| Ferritin heavy chain, % (95% CI) | 85.40 (41.57–97.56) | 96.41 (85.85–98.54) | 0.05 |
| Ferritin light chain, % (95% CI) | 29.09 (14.57–51.53) | 64.82 (38.63–81.96) | 0.01 |
| HO-1, % (95% CI) | 67.36 (36.95–78.41) | 81.64 (51.20–96.45) | NS |

Continued on the next page

| | | | |
|---|---|---|---|
| Figure 4.14 | | | |
| Transferrin receptor, % (95% CI) | 59.64 (22.10–99.72) | 89.60 (53.70–96.25) | NS |
| DMT-1, % (95% CI) | 46.99 (4.26–63.66) | 41.99 (23.57–70.45) | NS |
| Ferroportin, % (95% CI) | 40.21 (17.13–69.80) | 67.00 (43.28–76.10) | 0.05 |

**Table A.8.** Chapter 4 results: fragment-derived tumours

| | Vehicle | Sapatinib | Significance |
|---|---|---|---|
| Figure 4.15 | | | |
| Ceruloplasmin, % (95% CI) | 61.84 (15.68–75.97) | 64.82 (20.59–76.26) | NS |
| Ferritin heavy chain, % (95% CI) | 82.63 (78.54–97.86) | 93.48 (88.57–98.40) | NS |
| Ferritin light chain, % (95% CI) | 49.23 (8.81–71.91) | 28.81 (14.28–54.83) | NS |
| HO-1, % (95% CI) | 53.52 (44.60–75.59) | 63.63 (40.31–64.61) | NS |
| Figure 4.16 | | | |
| Transferrin receptor, % (95% CI) | 88.78 (7.53–99.02) | 43.78 (23.38–64.57) | NS |
| DMT-1, % (95% CI) | 99.40 (99.19–100.00) | 99.65 (99.40–99.91) | NS |
| Ferroportin, % (95% CI) | 87.86 (65.96–98.67) | 92.92 (91.04–94.79) | NS |

**Table A.9.** Chapter 5 results

| | Vehicle | | Sapatinib | | |
|---|---|---|---|---|---|
| | Iron-low control diet | Iron-deficient diet | Iron-low control diet | Iron-deficient diet | Significance |
| Figure 5.5 | | | | | |
| Total iron, ng/$\mu$g protein (95% CI) | 22.43 (21.47–25.86) | 19.12 (16.08–20.46) | 26.20 (20.63–27.84) | 21.54 (18.92–24.67) | NS |
| Ferrous ($Fe^{2+}$) iron, ng/$\mu$g protein (95% CI) | 22.41 (21.46–24.37) | 17.72 (15.51–19.23) | 25.79 (20.53–27.18) | 19.64 (18.46–24.21) | NS |
| Ferric iron ($Fe^{3+}$) iron, ng/$\mu$g protein (95% CI) | 0.02 (0.01–1.49) | 1.23 (0.57–1.40) | 0.41 (0.10–0.66) | 0.46 (0.45–1.91) | NS |

**Table A.10.** Chapter 5 results

| | Vehicle | | Sapatinib | | | |
|---|---|---|---|---|---|---|
| | Iron-low control diet | Iron-deficient diet | Iron-low control diet | Iron-deficient diet | Iron-low control diet, responding tumours | Significance |
| Figure 5.6 | | | | | | |
| Ceruloplasmin, % (95% CI) | 60.29 (38.45–96.55) | 91.40 (69.04–94.37) | 81.99 (81.53–93.93) | 88.81 (59.39–93.44) | 77.02 (59.39–88.09) | NS |
| HO-1, % (95% CI) | 10.18 (6.35–27.58) | 10.52 (5.76–34.33) | 16.57 (14.00–66.32) | 21.84 (3.89–49.88) | 40.61 (14.48–65.72) | 0.05 |
| Figure 5.7 | | | | | | |
| Ferritin heavy chain, % (95% CI) | 82.78 (35.91–95.52) | 73.51 (63.06–84.17) | 94.05 (46.38–97.66) | 89.03 (56.08–98.50) | 94.99 (90.06–99.95) | NS |
| Ferritin light chain, % (95% CI) | 30.04 (10.48–52.34) | 20.47 (16.48–24.87) | 61.45 (27.08–82.85) | 50.91 (18.94–75.55) | 81.82 (45.53–94.57) | NS |
| Figure 5.8 | | | | | | |

Continued on the next page

| | Vehicle | | Sapatinib | | | |
|---|---|---|---|---|---|---|
| | Iron-low control diet | Iron-deficient diet | Iron-low control diet | Iron-deficient diet | Iron-low control diet, responding tumours | Significance |
| Ferric ($Fe^{3+}$) iron non-tumour, % (95% CI) | 0.51 (0.23–1.63) | 2.69 (0.56–5.57) | 10.23 (5.43–17.08) | 7.67 (0.53–24.35) | 19.46 (2.71–35.09) | 0.05 |
| Ferric ($Fe^{3+}$) iron tumour, % (95% CI) | 3.13 (2.00–4.15) | 6.82 (1.74–8.60) | 15.23 (5.91–24.65) | 24.36 (1.90–58.49) | 29.88 (3.38–70.92) | 0.05 |
| Figure 5.9 | | | | | | |
| Transferrin receptor, % (95% CI) | 91.71 (69.68–99.53) | 92.88 (85.83–95.42) | 93.47 (51.06–98.52) | 92.34 (90.69–98.47) | 95.88 (54.71–99.62) | NS |
| DMT-1, % (95% CI) | 90.96 (33.53–95.49) | 89.56 (77.30–89.63) | 96.32 (88.38–97.92) | 88.38 (64.50–91.57) | 98.09 (60.50–98.67) | NS |
| Ferroportin, % (95% CI) | 96.79 (84.35–99.86) | 97.93 (93.16–99.49) | 88.77 (66.26–99.83) | 91.27 (71.67–98.85) | 99.37 (76.46–99.75) | NS |



**Table A.11.** Chapter 6 iron-deficient diet experiment results

| | Vehicle | | Sapatinib | | | |
|---|---|---|---|---|---|---|
| | Iron-low control diet | Iron-deficient diet | Iron-low control diet | Iron-deficient diet | Iron-low control diet, responding tumours | Significance |
| Figure 6.2 | | | | | | |
| p62 , % (95% CI) | 52.32 (23.58–81.94) | 87.81 (81.88–97.86) | 77.70 (2.807–97.47 | 46.72 (41.22–79.09) | 76.47 (63.64–96.08) | 0.05 |
| Figure 6.9 | | | | | | |
| Cleaved caspase 3, % (95% CI) | 3.28 (3.08–16.21) | 9.37 (4.71–14.12) | 10.51 (1.35–19.63) | 19.98 (10.26–16.21) | 9.57 (1.68–27.46) | NS |

Continued on the next page

| | Vehicle | | Sapatinib | | | |
|---|---|---|---|---|---|---|
| | Iron-low control diet | Iron-deficient diet | Iron-low control diet | Iron-deficient diet | Iron-low control diet, responding tumours | Significance |
| COX2, % (95% CI) | 1.11 (0.41–1.89) | 3.51 (0.44–13.08) | 11.41 (0.98–44.48) | 4.96 (1.21–8.90) | 17.23 (2.82–28.08) | 0.01 |

**Table A.12.** Chapter 6 spontaneous tumour results

| | Vehicle | Sapatinib | Significance |
|---|---|---|---|
| Figure 6.1 | | | |
| p62, % (95% CI) | 69.88 (52.65–85.71) | 31.59 (18.97–69.80) | 0.05 |
| Figure 6.4 | | | |
| NCOA4, % (95% CI) | 95.14 (93.38–96.81) | 95.20 (80.89–96.86) | NS |
| Figure 6.5 | | | |
| CD31-positive vessels, mean (SD) | 2.94 (±1.22) | 2.88 (±2.31) | NS |
| Figure 6.7 | | | |
| G6PDH, slope (95% CI) | 0.03973 (0.01444–0.04502) | 0.02483 (0.00901–0.04066) | NS |
| GSH:GSSG, median (95% CI) | 0.6186 (0.2980–5.689) | 0.4666 (0.0009–1.2710) | NS |
| GPX4, % (95% CI) | 88.60 (79.52–95.40) | 99.40 (95.05–99.82) | 0.0001 |
| Figure 6.8 | | | |
| NRF2, % (95% CI) | 98.05 (86.40–99.50) | 71.36 (46.39–92.96) | 0.01 |

**Table A.13.** Chapter 6 cell death results

| Mean cell death, % (±SD) | SKBR3 | Empty vector | HO-1-overexpressing |
|---|---|---|---|
| Figure 6.10, 6.13 | | | |
| DMSO | 8.67 (±2.95) | 8.99 (±3.00) | 10.41 (±3.53) |
| Erastin | 21.93 (±2.19) | 20.33 (±2.99) | 13.05 (±3.30) |
| Erastin+DFO | 13.37 (±2.44) | 16.07 (±2.59) | 12.66 (±3.34) |
| Erastin+ferrostatin | 11.84 (±3.80) | 16.8 (±2.53) | 13.22 (±2.70) |
| Figure 6.10, 6.14 | | | |
| Sapatinib | 19.50 (±3.84) | 19.44 (±8.06) | 20.01 (±5.97) |
| Sapatinib+DFO | 15.42 (±1.90) | 17.00 (±2.17) | 16.91 (±3.48) |
| Sapatinib+ferrostatin | 11.90 (±3.04) | 19.07 (±4.01) | 20.20 (±7.37) |
| Lapatinib | 19.16 (±4.31) | 20.52 (±5.92) | 22.19 (±4.70) |
| Lapatinib+DFO | 15.77 (±4.29) | 13.91 (±4.85) | 22.42 (±6.91) |
| Lapatinib+ferrostatin | 11.13 (±2.03) | 18.56 (±3.94) | 23.23 (±7.81) |
| Figure 6.11, 6.15 | | | |
| Sapatinib+Z-VAD-FMK | 13.81 (±4.92) | 14.43 (±1.31) | 17.77 (±4.17) |
| Lapatiib+Z-VAD-FMK | 17.11 (±0.87) | 16.46 (±3.59) | 19.29 (±5.67) |

**Table A.14.** Chapter 6 autophagy cell death results

| Mean cell death, % (±SD) | Empty vector | HO-1-overexpressing |
|---|---|---|
| Figure 6.17 | | |

Continued on the next page

| | | |
|---|---|---|
| DMSO+3-MA | - | 12.30 (±1.39) |
| DMSO+Bafilomycin | - | 11.17 (±1.26) |
| Erastin+3-MA | 22.86 (±6.37) | 20.55 (±6.45) |
| Erastin+Bafilomycin | 15.33 (±3.90) | 17.38 (±4.61) |
| Figure 6.18 | | |
| Sapatinib+3-MA | 18.92 (±2.29) | 29.54 (±9.80) |
| Sapatinib+Bafilomycin | 19.68 (±0.52) | 30.69 (±4.70) |
| Lapatinib+3-MA | 18.34 (±4.86) | 28.57 (±6.03) |
| Lapatinib+Bafilomycin | 16.28 (3±.26) | 35.31 (±5.04) |

# Appendix B

# Hits identified by proteomics

**Table B.1.** Proteins identified by proteomics that were significantly and 2-fold differentially regulated between vehicle- and sapatinib-treated tumours

| **Gene name** | **Ratio** | ***p*-value** |
|---|---|---|
| Tprkb | -4.140654502 | $1.87x10^{-05}$ |
| A2mp | -3.835752326 | 0.022993765 |
| Dpysl5 | -3.80018804 | 0.019213191 |
| Mtx2 | -3.65358671 | 0.017941552 |
| Plin2 | -3.647423782 | 0.030408404 |
| Tarsl2 | -3.550573966 | 0.004089219 |
| Fundc2 | -3.543543301 | 0.015554104 |
| Acss2 | -3.442544687 | 0.040324609 |
| Alkbh5 | -3.381192421 | 0.041815904 |
| Lsm5 | -3.377436219 | 0.044627289 |
| Pycr1 | -3.292224379 | 0.017164936 |
| Tubb6 | -3.106586454 | 0.042591931 |
| Ncln | -3.0606184 | 0.025224162 |
| Ero1l | -3.060352529 | 0.042480726 |
| Dnajc10 | -3.042829366 | 0.042928806 |
| Fads3 | -3.025610556 | 0.004956993 |
| Cnep1r1 | -2.915836262 | 0.009856324 |
| Clca3a2 | -2.857213953 | 0.000778377 |
| Trove2 | -2.840116679 | 0.048521229 |
| Slc25a13 | -2.829876351 | 0.041433872 |
| Afap1l1 | -2.788051995 | 0.043984844 |

Continued on the next page

| | | |
|---|---|---|
| Espn | -2.765162387 | 0.035360429 |
| Trmt10c | -2.750101456 | 0.037922252 |
| Lss | -2.740644538 | 0.046238066 |
| Csn3 | -2.702609829 | 0.030334867 |
| Gramd4 | -2.653558582 | 0.018840986 |
| Psen1 | -2.555381618 | 0.034132534 |
| Nup133 | -2.421013472 | 0.039396113 |
| Usp48 | -2.350740759 | 0.036837596 |
| Gng10 | -2.222421367 | 0.039773832 |
| Map3k7 | -2.085450448 | 0.024521763 |
| Ddah1 | -1.731553734 | 0.002769104 |
| Slc2a1 | -1.637354217 | 0.00871054 |
| Pmvk | -1.547385 | 0.026141123 |
| Krt19 | -1.514035799 | 0.047157156 |
| Fam162a | -1.472902688 | 0.001025414 |
| Pc | -1.378241551 | 0.005112338 |
| Hk2 | -1.285176369 | 0.00950782 |
| Rtn1 | -1.246881442 | 0.000893418 |
| Mcm3 | -1.227975251 | 0.025799524 |
| Fasn | -1.049043334 | 0.024014181 |
| Hsp90b1 | -1.045168779 | 0.00255196 |
| Higd1a | -1.026020692 | 0.014691129 |
| Tmem258 | -0.994778224 | 0.021946338 |
| Slc25a1 | -0.985998361 | 0.017897019 |
| Hm13 | -0.980500199 | 0.041184013 |
| Mov10 | -0.97510695 | 0.024437272 |
| Rfc4 | -0.94016502 | 0.033638177 |
| Dcakd | -0.919500666 | 0.038380083 |
| Sfxn1 | -0.914584782 | 0.005614952 |
| Myh10 | -0.905694606 | 0.006675558 |
| Dstn | -0.895256974 | 0.008039821 |
| Hspa5 | -0.840841174 | 0.002669093 |
| Rpl31 | -0.819793228 | 0.041823111 |
| Pdia6 | -0.795422921 | 0.015639296 |
| Crabp2 | -0.789243936 | 0.019632056 |

Continued on the next page

| | | |
|---|---|---|
| Ppme1 | -0.787082689 | 0.039606514 |
| Dnajb11 | -0.786730486 | 0.004045689 |
| Rps9 | -0.753561352 | 0.020001843 |
| Rpl18 | -0.747516754 | 0.044048727 |
| Spcs2 | -0.744956451 | 0.03784557 |
| Rpl18a | -0.736032107 | 0.024648109 |
| Vbp1 | -0.731765778 | 0.004878754 |
| Creld2 | -0.717182351 | 0.031885349 |
| Hist1h2ah | -0.672104071 | 0.046835135 |
| Canx | -0.667498384 | 0.006955488 |
| Hyou1 | -0.651732035 | 0.018693286 |
| Rab10 | -0.646440292 | 0.005110041 |
| Ndufv1 | -0.643377039 | 0.024479454 |
| Atp6v0a1 | -0.641568138 | 0.040421099 |
| Gapdh | -0.634472999 | 0.037487392 |
| Rpl26 | -0.589029734 | 0.032884945 |
| Plod3 | -0.559231539 | 0.029526867 |
| Coro1c | -0.5531035 | 0.008532186 |
| Stt3b | -0.550778545 | 0.002625545 |
| Kif1c | -0.540552901 | 0.02147534 |
| Pdia4 | -0.518925767 | 0.011813703 |
| Rps11 | -0.515223751 | 0.04834537 |
| Dlst | -0.508884008 | 0.028490738 |
| Pccb | -0.506183818 | 0.009672262 |
| Gorasp2 | -0.494201152 | 0.013422886 |
| Calr | -0.490313283 | 0.003982758 |
| Ndufs3 | -0.478120336 | 0.032336965 |
| Pdia3 | -0.47782483 | 0.018161556 |
| Aifm1 | -0.475705035 | 0.040036568 |
| Syne1 | -0.457937508 | 0.037594377 |
| Ppib | -0.410924953 | 0.028656938 |
| Lrpap1 | -0.348812453 | 0.047313947 |
| Immt | -0.31985922 | 0.015251323 |
| Spag9 | 0.276273801 | 0.031615638 |
| Add1 | 0.415045674 | 0.022724124 |

Continued on the next page

| | | |
|---|---|---|
| Rpl19 | 0.421612892 | 0.039760627 |
| Snap29 | 0.437631504 | 0.027970371 |
| Eif3j2 | 0.445761868 | 0.040958946 |
| Arhgdia | 0.505554062 | 0.006709223 |
| Ctsd | 0.621405547 | 0.027542594 |
| Ctsb | 0.629171769 | 0.011788847 |
| Pdxk | 0.672679225 | 0.032936387 |
| Blvra | 0.678335979 | 0.003547624 |
| Samhd1 | 0.743122057 | 0.040508912 |
| Cndp2 | 0.807779786 | 0.013054586 |
| Ahnak | 0.815764731 | 0.016508851 |
| Steap4 | 0.866741264 | 0.034259287 |
| Prdx5 | 0.951874243 | 0.028186803 |
| Ppl | 1.145586758 | 0.008370363 |
| Cp | 1.199858399 | 0.013992181 |
| Hcls1 | 1.212055712 | 0.043316416 |
| Gstm1 | 1.243939776 | 0.03883327 |
| Aspn | 1.358273909 | 0.011637499 |
| Prelp | 1.551294077 | 0.03605453 |
| Ace | 1.560094641 | 0.011401202 |
| Ighm | 1.711461984 | 0.025440829 |
| Hmox1 | 1.84987713 | 0.013763124 |
| IgHv | 2.046662467 | 0.014241301 |
| Fth1 | 2.081573232 | 0.007845305 |
| Agl | 2.799453657 | 0.043309924 |
| Pomp | 2.810996431 | 0.044563148 |
| Mpi | 2.927850005 | 0.013695408 |
| Lypla2 | 3.113790573 | 0.018403069 |
| Cd74 | 3.302844393 | 0.022427556 |
| Ftl1 | 3.446259738 | 0.009523485 |
| Casp8 | 3.631757878 | 0.046474779 |
| Katnal2 | 4.648614928 | 0.012564172 |

# Appendix C

# Publications

Paper 1: Use of a genetically engineered mouse model as a preclinical tool for HER2 breast cancer.
Helen Creedon, Lucy A. Balderstone, Morwenna Muir, Jozef Balla, Laura Gomez-Cuadrado, **Natasha Tracey**, Joseph Loane, Teresa Klinowska, William J. Muller and Valerie G. Brunton

For this paper, I worked on the revisions. The ZEB1 staining presented in figure 7 is my work.

Paper 2: Mouse models of metastasis: progress and prospects.
Laura Gomez-Cuadrado,* **Natasha Tracey**,* Ruoyu Ma, Binzhi Qian, and Valerie G. Brunton

*Joint first authors

For this review paper, I made substantial contributions to the text and the editing, and made figure 3.

© 2016. Published by The Company of Biologists Ltd | Disease Models & Mechanisms (2016) 9, 131-140 doi:10.1242/dmm.023143

RESEARCH ARTICLE

# Use of a genetically engineered mouse model as a preclinical tool for HER2 breast cancer

**Helen Creedon[1], Lucy A. Balderstone[1,*], Morwenna Muir[1], Jozef Balla[1], Laura Gomez-Cuadrado[1], Natasha Tracey[1], Joseph Loane[2], Teresa Klinowska[3], William J. Muller[4] and Valerie G. Brunton[1,‡]**

## ABSTRACT

Resistance to human epidermal growth factor receptor 2 (HER2)-targeted therapies presents a major clinical problem. Although preclinical studies have identified a number of possible mechanisms, clinical validation has been difficult. This is most likely to reflect the reliance on cell-line models that do not recapitulate the complexity and heterogeneity seen in human tumours. Here, we show the utility of a genetically engineered mouse model of HER2-driven breast cancer (MMTV-NIC) to define mechanisms of resistance to the pan-HER family inhibitor AZD8931. Genetic manipulation of MMTV-NIC mice demonstrated that loss of phosphatase and tensin homologue (PTEN) conferred *de novo* resistance to AZD8931, and a tumour fragment transplantation model was established to assess mechanisms of acquired resistance. Using this approach, 50% of tumours developed resistance to AZD8931. Analysis of the resistant tumours showed two distinct patterns of resistance: tumours in which reduced membranous HER2 expression was associated with an epithelial-to-mesenchymal transition (EMT) and resistant tumours that retained HER2 expression and an epithelial morphology. The plasticity of the EMT phenotype was demonstrated upon re-implantation of resistant tumours that then showed a mixed epithelial and mesenchymal phenotype. Further AZD8931 treatment resulted in the generation of secondary resistant tumours that again had either undergone EMT or retained their original epithelial morphology. The data provide a strong rationale for basing therapeutic decisions on the biology of the individual resistant tumour, which can be very different from that of the primary tumour and will be specific to individual patients.

**KEY WORDS: HER2, Breast cancer, Resistance, Epithelial-to-mesenchymal transition**

## INTRODUCTION

Human epidermal growth factor receptor 2 (HER2) gene amplification and/or protein overexpression occurs in around 20% of breast cancers and is associated with poor prognosis. Several drugs capable of specifically targeting the HER2 pathway have been developed for use in both early and late HER2-positive disease and have had a significant impact on the treatment of HER2-positive breast cancer (Arteaga et al., 2012); these include antibodies directed against HER2, such as trastuzumab and pertuzumab, and small molecule tyrosine kinase inhibitors that target the kinase activity of HER2 and HER1, such as lapatinib. Although initial response rates to the current HER2-targeted therapies are good, resistance is inevitable. Further tyrosine kinase inhibitors, including AZD8931 (sapatinib) and neratinib, have been developed in an attempt to improve efficacy rates and the duration of response. Preclinical studies have identified numerous mechanisms of both *de novo* and acquired resistance (Creedon et al., 2014; Rexer and Arteaga, 2012), although their clinical validation has been more difficult, which reflects the inability of the conventional cell-based approaches to model the complexity of the human disease adequately.

The limitation of conventional cell culture and mouse xenograft studies is well recognized as an obstacle to the effective translation of preclinical findings into clinical benefit (Sharpless and Depinho, 2006). Use of genetically engineered models in which tumours develop *in situ* in the context of an intact microenvironment is a viable alternative for preclinical assessment of both drug response and mechanisms of resistance (van Miltenburg and Jonkers, 2012). Generation of autochthonous tumours driven by cell-specific expression of oncogenic drivers or loss of tumour suppressors relevant to human tumours gives rise to tumours in which the histopathology and disease progression also recapitulate many aspects of the human disease, providing more relevant models with which to study drug response.

Here, we describe the use of a HER2-driven model of mammary tumorigenesis as a preclinical tool to study response and resistance mechanisms in HER2-positive breast cancer. We have used the MMTV-NIC (Neu-IRES-Cre) model (Ursini-Siegel et al., 2008), which employs a bicistronic transcript to co-express activated ErbB2/Neu (HER2) with MMTV-Cre recombinase, resulting in the formation of activated ErbB2/Neu-driven mammary tumours. The advantage of this model is that the coupling of activated ErbB2/Neu with Cre recombinase in the same cell means that Cre-negative tumour cells are not generated, allowing the efficient Cre-mediated deletion of additional conditional alleles (Schade et al., 2009). This allows validation of potential mechanisms of *de novo* resistance, such as loss of phosphatase and tensin homologue (PTEN). Loss of PTEN and subsequent activation of the phosphoinositide 3-kinase (PI3K) pathway has been identified as a key determinant of trastuzumab sensitivity and has been associated with poorer overall survival in trastuzumab-treated patients (Berns et al., 2007; Esteva et al., 2010; Nagata et al., 2004), although the impact on lapatinib resistance remains unclear (Xia et al., 2007). Here, we have coupled loss of PTEN with HER2 activation in the MMTV-NIC model and demonstrate that loss of PTEN is associated with *de novo* resistance to the small molecule tyrosine kinase inhibitor sapatinib

[1]Edinburgh Cancer Research UK Centre, University of Edinburgh, Crewe Road South, Edinburgh EH4 2XR, UK. [2]Pathology Department, Western General Hospital, Edinburgh EH4 2ZD, UK. [3]AstraZeneca Oncology iMed, Alderley Park, Macclesfield SK10 4TG, UK. [4]Goodman Cancer Research Center, McGill University, Montreal, Canada H3A 1A3.
*Present address: AstraZeneca Innovative Medicines & Early Development, Darwin Building, Cambridge Science Park, Cambridge CB4 0FZ, UK.

[‡]Author for correspondence (v.brunton@ed.ac.uk)



**Received 2 September 2015; Accepted 23 December 2015**

Disease Models & Mechanisms (2016) 9, 131-140 doi:10.1242/dmm.023143

(AZD8931). We also show the utility of the model for identifying mechanisms of acquired resistance to HER2-targeted therapy and identify the induction of an epithelial-to-mesenchymal transition (EMT) in a subpopulation of AZD8931-resistant tumours.

## RESULTS

### Loss of PTEN confers resistance to AZD8931

Initial experiments were carried out to determine whether the MMTV-NIC model was sensitive to the HER family tyrosine kinase inhibitor AZD8931. As loss of PTEN and activation of the PI3K signalling pathway have previously been reported to confer resistance to trastuzumab, cohorts of both MMTV-NIC PTEN$^{+/+}$ and MMTV-NIC PTEN$^{+/-}$ mice were used. Both MMTV-NIC PTEN$^{+/+}$ and MMTV-NIC PTEN$^{+/-}$ mice developed on average four tumours per mouse with 100% penetrance. As described previously, loss of PTEN accelerated tumour onset in the MMTV-NIC mice (Schade et al., 2009). The median age of tumour onset was 102 days in the MMTV-NIC PTEN$^{+/-}$ cohort compared with 150 days in the MMTV-NIC PTEN$^{+/+}$ cohort ($P$=0.0001, Gehan–Breslow–Wilcoxon test; Fig. S1A). Western blot analysis of tumours showed reduced expression of PTEN and increased phosphorylation of Akt in tumours taken from the MMTV-NIC PTEN$^{+/-}$ mice, consistent with increased signalling through the PI3K pathway (Fig. S1B).

To assess the response to AZD8931, we randomized cohorts of MMTV-NIC PTEN$^{+/+}$ and MMTV-NIC PTEN$^{+/-}$ mice to treatment with either AZD8931 or vehicle. Median survival in the vehicle arm of the MMTV-NIC PTEN$^{+/+}$ cohort after the start of treatment was 35 days (range 10-39 days), compared with 18 days (range 11-24 days) in vehicle-treated MMTV-NIC PTEN$^{+/-}$ mice. Drug treatment was stopped at 40 days, when all vehicle-treated animals were sacrificed because of tumour burden. At this time, none of the drug-treated animals had to be sacrificed because of tumour burden (Fig. 1A,B). When we looked at the growth of the individual index tumours (defined as the largest tumour at the time of sacrifice) in the different cohorts after 40 days, we saw that all AZD8931-treated MMTV-NIC PTEN$^{+/+}$ tumours initially responded to treatment and two out of five tumours fully resolved. The growth of a further two tumours was inhibited, whereas the final tumour initially responded but after 17 days of drug treatment became insensitive, and after 40 days of treatment its volume had increased by 134.2%. By comparison, the tumours in the vehicle-treated arm continued to grow throughout the experiment, and the median percentage change in tumour volume was an increase of 294.6% (Fig. 1C). By contrast, all but one of five AZD8931-treated MMTV-NIC PTEN$^{+/-}$ tumours became rapidly insensitive to AZD8931, and by day 40 all AZD8931-treated tumours had grown beyond their initial starting volume, with a median percentage change in tumour volume of 131.1%. As expected, all vehicle-treated tumours continued to grow steadily throughout the experiment, with a median percentage change in tumour volume of 415.1% (Fig. 1D). In summary, AZD8931 resulted in tumour shrinkage in the majority of MMTV-NIC PTEN$^{+/+}$ animals, but although it slowed tumour growth in MMTV-NIC PTEN$^{+/-}$ animals it did not cause tumour resolution. We also noted that by day 40 there were fewer additional tumours in both the MMTV-NIC PTEN$^{+/+}$ and MMTV-NIC PTEN$^{+/-}$ animals treated with AZD8931, and although this did not reach statistical significance the reduction in tumour burden was greater in the MMTV-NIC PTEN$^{+/+}$ mice, consistent with the increased sensitivity of the MMTV-NIC PTEN$^{+/+}$ tumours to AZD8931 (median values for tumours per mouse: MMTV-NIC PTEN$^{+/+}$, vehicle=5; MMTV-NIC PTEN$^{+/+}$, AZD8931=1; MMTV-NIC PTEN$^{+/-}$, vehicle=6; MMTV-NIC PTEN$^{+/-}$, AZD8931=3; $P$=0.1025, Kruskal–Wallis). This illustrates the significant heterogeneity in response to AZD8931 between the two different cohorts and demonstrates that loss of PTEN, leading to activation of the PI3K pathway, confers *de novo* resistance to AZD8931.

As there was little residual tissue from the AZD8931-treated MMTV-NIC PTEN$^{+/+}$ animals at the completion of the experiment, additional cohorts of both MMTV-NIC PTEN$^{+/+}$ and MMTV-NIC PTEN$^{+/-}$ mice were treated with vehicle or AZD8931 for 3 days and effects on HER family signalling pathways assessed. There was a reduction in phosphorylation of HER2 and HER3 in MMTV-NIC PTEN$^{+/+}$ and MMTV-NIC PTEN$^{+/-}$ tumours following treatment with AZD8931 compared with vehicle-treated animals, although this did not reach statistical significance after histoscoring (Fig. 1E). This reflects the heterogeneous expression and activation of both HER2 and HER3 in the tumours (Fig. S1C). No significant epidermal growth factor receptor (EGFR/HER1) expression was detected in the MMTV-NIC tumours, so it was not possible to assess effects on EGFR activation (results not shown). We used reverse-phase protein arrays to look at downstream signalling to Akt, mitogen-activated protein kinase (MAPK) and S6 in the AZD8931-treated tumours and found that their activation was significantly inhibited in MMTV-NIC PTEN$^{+/+}$ and MMTV-NIC PTEN$^{+/-}$ tumours (Fig. 1F). Immunohistochemical analysis showed that pAkt was confined to the tumour cells and not expressed in the surrounding stroma, whereas pMAPK was also expressed in the stroma, and the reduced expression of pMAPK might therefore also reflect reduced activation of MAPK in the surrounding stroma (Fig. S1D). Thus short-term treatment with AZD8931 inhibits HER family signalling in both tumour types, and therefore, the differential response of the MMTV-NIC PTEN$^{+/+}$ and MMTV-NIC PTEN$^{+/-}$ tumours does not reflect an inability of the drug to inhibit the target in the different tumours.

### Establishment of orthotopic transplanted tumours

The multifocal nature of the MMTV-NIC model means that it is not possible to study mechanisms of acquired drug resistance. We therefore established whether the MMTV-NIC PTEN tumours could be orthotopically transplanted into syngeneic wild-type FVB/N mice to provide a more tractable model for drug-resistance studies. We were able to establish tumours after transplantation of tumour fragments from MMTV-NIC PTEN$^{+/-}$ tumours but not from MMTV-NIC PTEN$^{+/+}$ tumour fragments. Examination of sections stained with haematoxylin and eosin (H&E) from the fragment-derived MMTV-NIC PTEN$^{+/-}$ tumours confirmed the presence of highly mitotic, grade 3 carcinomas, which were indistinguishable from tumours that developed in the parental MMTV-NIC PTEN$^{+/-}$ model (Fig. 2A). Both parental and fragment-derived tumours demonstrated inter-and intratumoral heterogeneity in HER2 expression (Fig. 2B) and, consistent with the frequent observation of mitotic figures on H&E sections, a high percentage of nuclei stained positively for Ki67 in both parental and fragment-derived tumours (Fig. 2C). The orthotopic transplantation model therefore provides a useful tool by circumventing problems associated with the multifocal nature of the genetically engineered model.

Initial studies to determine the suitability of the MMTV-NIC transplantation model for drug-efficacy studies were carried out using the taxane paclitaxel, whose role in the management of both early and metastatic breast cancer is well established (Gajria et al., 2010; Ghersi et al., 2005). Paclitaxel treatment resulted in a statistically significant increase in overall survival of mice bearing fragment-derived tumours. Median overall survival was increased

Disease Models & Mechanisms (2016) 9, 131-140 doi:10.1242/dmm.023143

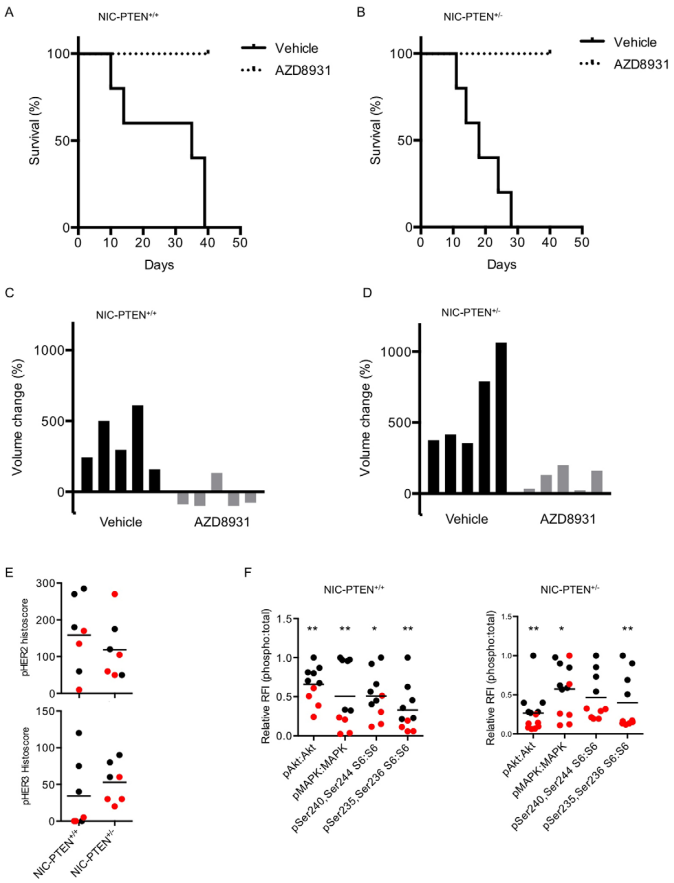


**Fig. 1. PTEN status determines the sensitivity to AZD8931.** Cohorts of MMTV-NIC-PTEN$^{+/+}$ and NIC-PTEN$^{+/-}$ mice were randomized to treatment with daily AZD8931 or vehicle, and the tumour response was monitored. (A) Overall survival in vehicle- ($n$=5) and AZD8931-treated ($n$=5) NIC-PTEN$^{+/+}$ mice ($P$=0.0043, Gehan–Breslow–Wilcoxon test). (B) Overall survival in vehicle- ($n$=5) and AZD8931-treated ($n$=5) NIC-PTEN$^{+/-}$ mice ($P$=0.0039, Gehan–Breslow–Wilcoxon test). (C) Waterfall plot of percentage tumour volume change over duration of experiment in NIC-PTEN$^{+/+}$ vehicle- and AZD8931-treated animals ($P$=0.0079, Mann–Whitney $U$-test). (D) Waterfall plot of percentage tumour volume change over duration of experiment in NIC-PTEN$^{+/-}$ vehicle- and AZD8931-treated animals ($P$=0.0079, Mann–Whitney $U$-test). Vehicle-treated mice were sacrificed when the tumour burden reached the maximal permitted size, at 10-39 days for MMTV-NIC PTEN$^{+/+}$ mice and 11-24 days for MMTV-NIC PTEN$^{+/-}$ mice. AZD8931 treatment was stopped at 40 days, when all vehicle-treated animals were sacrificed because of tumour burden. (E) Immunohistochemical analysis was performed on paraffin-embedded sections of AZD8931- and vehicle-treated tumours with pTyr 1221/1222 HER2 and pTyr 1289 HER3 antibodies. Membranous histoscore calculated as the sum of the product of the percentage of cells stained by the intensity graded from 0 to 3, where 1=weak, 2=moderate and 3=strong staining [histoscore=(% *1)+(% *2)+(% *3)]. pTyr 1221/1222 HER2 staining: NIC-PTEN$^{+/+}$, $P$=0.48; NIC-PTEN$^{+/-}$, $P$=1.0; and pTyr1289 HER3 staining: NIC-PTEN$^{+/+}$, $P$=0.20; NIC-PTEN$^{+/-}$, $P$=0.07; Mann–Whitney $U$-test comparing vehicle- and AZD8931-treated tumours. Black data points represent vehicle-treated tumours. Red data points represent AZD8931-treated tumours. Bars represent mean value for each genotype. (F) Reverse-phase protein array analysis was performed on lysate from AZD8931- (red data points) and vehicle-treated (black data points) NIC-PTEN$^{+/+}$ and NIC-PTEN$^{+/-}$ tumours. The ratio of phospho:total protein relative fluorescence intensity (RFI) value is presented and normalized to the maximal value in each data set. *$P$≤0.05 and **$P$≤0.01 comparing vehicle and AZD8931 for each antibody, Mann–Whitney $U$-test.

from 14 days in vehicle-treated animals (range 7-14 days) to 24 days (range 24-24 days) in drug-treated animals ($P$=0.03, Gehan–Breslow–Wilcoxon test). Looking at the response of individual tumours to treatment, we found that although paclitaxel slowed tumour growth, it did not result in tumour shrinkage (Fig. 2D).

Disease Models & Mechanisms (2016) 9, 131-140 doi:10.1242/dmm.023143

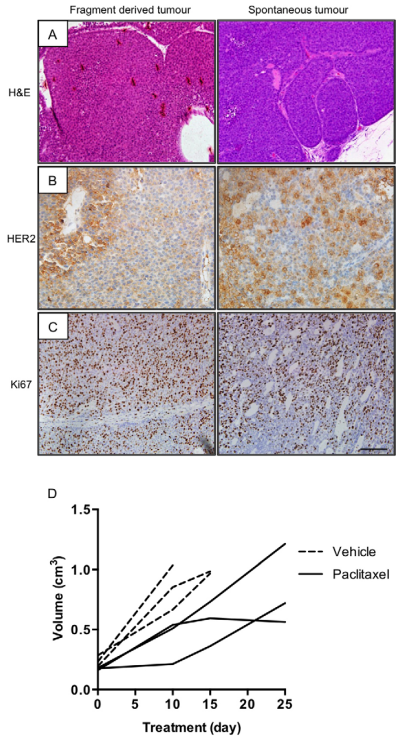


**Fig. 2. Transplantation of NIC-PTEN$^{+/-}$ fragments generated tumours that were indistinguishable from the parental tumours.** (A) Representative H&E images of fragment-derived and spontaneous tumours from NIC-PTEN$^{+/-}$ mice. (B,C) Representative images of HER2 (B) and Ki67 (C) expression in fragment-derived and spontaneous tumours. Scale bar: 100 µm. (D) Growth rate of vehicle- ($n$=3) and paclitaxel-treated ($n$=3) fragment-derived tumours.

### Development of resistance to AZD8931

We next determined whether the MMTV-NIC tumours could be used to model acquired resistance to AZD8931. We generated tumour fragments from three MMTV-NIC PTEN$^{+/-}$ donor mice. From each mouse, donor tumour fragments were then transplanted into cohorts of six wild-type FVB/N mice. After the development of established tumours, mice were randomized to treatment with either vehicle ($n$=3) or AZD8931 ($n$=3). AZD8931 treatment resulted in an initial inhibition of tumour growth in all mice. When tumours had regressed to $\leq$0.1 cm$^3$, AZD8931 treatment was stopped. After the subsequent regrowth of the tumour, treatment was then resumed when tumours reached $\geq$0.3 cm$^3$. This cycle was repeated until tumours either resolved or became resistant and were able to continue growing in the presence of ongoing treatment. The resistant tumours originated from different donors, and the duration of treatment required for the individual tumours to become resistant varied between individual tumours (Fig. 3A).

Histopathological examination of the matched AZD8931-naïve and -resistant tumours revealed that although all the AZD8931-naïve tumours were histologically indistinguishable from each other (Fig. 3B,C) there were significant differences in the AZD8931-resistant tumours (Fig. 3D,E). Although some of the resistant tumours had the same histopathological phenotype as their matched naïve tumour (Fig. 3D), a subset of resistant tumours had a more pleomorphic appearance and were composed of spindle cells, suggestive of tumours undergoing EMT (Fig. 3E).

Loss of cell surface E-cadherin is an established marker of EMT, and although strong membranous expression of E-cadherin was seen in all drug-naïve tumours, loss of E-cadherin in the resistant tumours was associated with the conversion to a spindle cell morphology (Fig. 4A-D), with the resistant tumours that had not undergone the morphological change retaining expression of E-cadherin (Fig. 4I-L). This loss of E-cadherin was accompanied by expression of the mesenchymal marker vimentin in the resistant spindle cell tumours (Fig. 4E,F), indicating that these resistant tumours had undergone EMT. HER2 expression was preserved in the resistant tumours that had retained the histopathological features of the drug-naïve tumours (Fig. 4O,P), but total loss of membranous HER2 expression was seen in the resistant spindle cell tumours (Fig. 4G,H).

To establish whether the resistant phenotype was stable, fragments from one individual resistant tumour were re-implanted into cohorts of wild-type FVB/N mice. After the development of established tumours, mice were randomized to treatment with either vehicle or AZD8931. AZD8931 treatment prevented the growth of one tumour, although tumour regression did not occur (Fig. 5A, red growth curve, 'AZD8931 responsive'). The remaining three tumours responded initially to AZD8931, although resistance did develop over time (Fig. 5A, black growth curves, 'AZD8931 resistant'). The onset of secondary resistance was faster than in the original drug-naïve tumour fragments (compare Figs 3A and 5A).

The vehicle-treated tumours were all highly mitotic, containing rounded cells with pleomorphic nuclei (Fig. 5B). The tumour whose growth was inhibited by AZD8931 had mild to moderately pleomorphic nuclei and no mitoses (Fig. 5C). The resistant tumours had distinct morphologies; two of the tumours were composed of highly mitotic spindle cells with similar histology to those seen in the primary resistant tumours that had undergone EMT (compare Fig. 5E,F with Fig. 3C), whereas the remaining resistant tumour had a papillary architecture with moderate/marked nuclear pleomorphism (Fig. 5D). As we had previously demonstrated a reduction in pAkt and pMAPK after acute treatment with AZD8931 (Fig. 1F), we looked at activation of Akt and MAPK following development of resistance to AZD8931 (Fig. 5G-P). Chronic exposure to AZD8931 did not reduce pAkt and pMAPK levels, although one AZD89231 resistant tumour showed an overall reduction in pMAPK staining, with only small pockets of pMAPK-positive cells scattered throughout the tumour (Fig. 5N).

Further analysis of the tumours revealed that all vehicle-treated tumours expressed both E-cadherin and vimentin (Fig. 6A). The AZD8931-responsive tumour was also both E-cadherin and vimentin positive, although the number of vimentin-positive tumour cells was much lower than in the vehicle-treated tumours (Fig. 6B). As with the primary resistant tumours, the two spindle cell AZD8931-resistant tumours had lost E-cadherin and were strongly vimentin positive. Strikingly, this was associated with loss of membranous HER2 expression (Fig. 6D,E). The remaining AZD8931-resistant tumour resembled the vehicle-treated tumours, being both E-cadherin and vimentin positive (Fig. 6C). Thus, the

Disease Models & Mechanisms (2016) 9, 131-140 doi:10.1242/dmm.023143

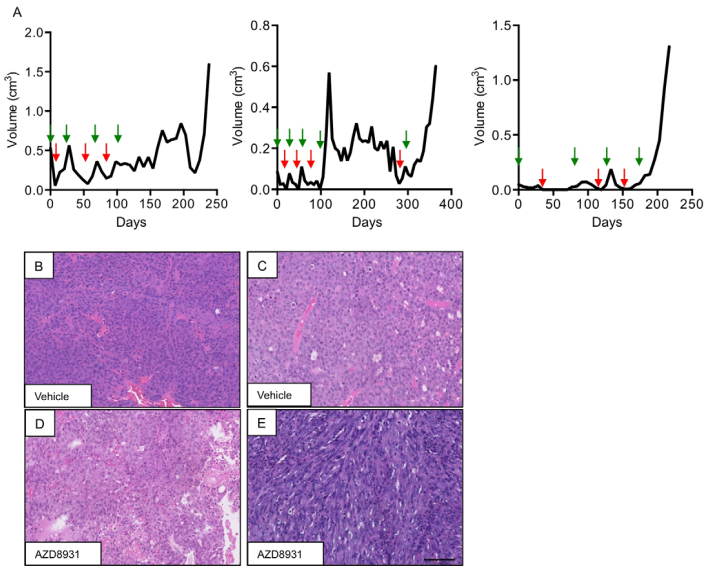


**Fig. 3. Generation of fragment-derived tumours with acquired resistance to AZD8931.** (A) Representative growth curves of three independent NIC-PTEN$^{+/-}$ tumour fragments treated with AZD8931. Repeated cycles of AZD8931 were administered to facilitate the selection of tumours with acquired resistance to AZD8931. Green arrows indicate the start of treatment and red arrows indicate when treatment was stopped. (B,C) Representative H&E images of AZD8931-naïve (vehicle) and AZD8931-resistant tumours. (D) AZD8931-resistant tumour phenotypically indistinguishable from AZD8931-naïve tumour. (E) AZD8931-resistant tumour consisting of spindle-shaped cells. Scale bar: 100 µm.

development of resistance to AZD8931 in a subpopulation of tumours is linked to increased expression of markers associated with the induction of EMT and loss of membranous HER2.

In order to explore further the mechanisms of EMT induction in the resistant tumours, we looked at expression of Zeb1, which is a known transcriptional regulator of EMT. Upregulation of nuclear Zeb1 was seen only in the resistant spindle cell tumours, consistent with a Zeb1-regulated induction of EMT (Fig. 7).

## DISCUSSION

It is widely acknowledged that the use of conventional xenograft models for preclinical drug testing has limited predictive clinical value. Use of genetically engineered mouse models provides a useful alternative, in which drug response and resistance can be evaluated in situations that more faithfully recapitulate the human disease (Olive et al., 2009; Singh et al., 2010; Wang et al., 2012). Here, we show that the MMTV-NIC model has utility in assessing efficacy and resistance mechanisms of HER2-targeted therapies. Comparison of tumours with the same genotype demonstrated heterogeneity in the rate and extent of response to AZD8931, despite the use of predefined genetic mutations to drive tumour development. This variation in therapeutic response has been described previously in other genetically engineered models (Rottenberg et al., 2007) and contrasts with the more uniform response seen in xenograft studies (Becher and Holland, 2006). This is an important advance because it enables us more accurately to recapitulate the behaviour of human tumours and is most probably a result of the random acquisition of secondary mutations during tumour development and progression in these models. In addition, we show, for the first time, that acquired resistance to a HER2-targeted therapy can be modelled in MMTV-NIC tumours. The majority of studies exploring resistance to HER2-directed therapies have used cell-line-based approaches and, although numerous resistance mechanisms have been identified *in vitro*, clinical validation has proved challenging. The use of genetically engineered models to explore resistance mechanisms offers a more physiologically relevant system, with tumours developing resistance whilst exposed to ongoing *in vivo* selection pressures. Therefore, any resistance strategies identified might be more predictive of clinically relevant resistance mechanisms.

We identified PTEN loss as an important determinant of *de novo* AZD8931 resistance. Loss of PTEN and subsequent activation of the PI3K pathway has been identified as a key determinant of trastuzumab sensitivity and has been associated with poorer overall survival in trastuzumab-treated patients (Berns et al., 2007; Esteva et al., 2010; Nagata et al., 2004), although the impact on lapatinib resistance remains unclear (Xia et al., 2007). Like lapatinib, AZD8931 is a dual inhibitor of both HER2 and HER1; however, it has a unique profile of activity, being a more effective inhibitor of HER family signalling than lapatinib, resulting in a distinct profile of anti-tumour activity (Hickinson et al., 2010). Current trials are underway to determine whether the more effective simultaneous inhibition of HER family signalling provided by AZD8931 could have clinical benefit (Tjulandin et al., 2014); therefore,

Disease Models & Mechanisms (2016) 9, 131-140 doi:10.1242/dmm.023143

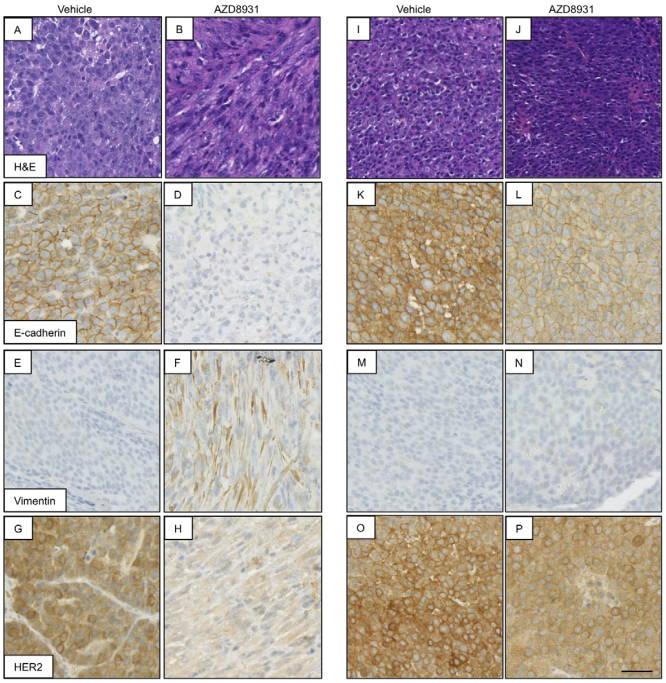


**Fig. 4. AZD8931 resistance is associated with EMT in a subpopulation of tumours.** Analysis of AZD8931-naïve (vehicle) and AZD8931-resistant tumours showing representative images of H&E staining and immunohistochemical analysis of E-cadherin, vimentin and HER2. Scale bar: 50 µm. (A-H) AZD8931-resistant spindle cell tumour and corresponding vehicle-treated tumour. (I-P) AZD8931-resistant tumour phenotypically indistinguishable from AZD8931-naïve (vehicle) tumour and corresponding vehicle-treated tumour.

understanding potential mechanisms of resistance to AZD8931 is required. Both MMTV-NIC PTEN$^{+/+}$ and MMTV-NIC PTEN$^{+/-}$ tumours displayed reduced Akt activity after treatment with AZD8931, although in both models there was still evidence of residual activity following AZD8931 treatment. Incomplete inhibition of Akt signalling is a well-established mechanism of resistance to HER2-targeted therapies (Rexer and Arteaga, 2012) and is likely to contribute to the continued tumour progression in the MMTV-NIC PTEN$^{+/-}$ model. In support of this, we saw no reduction in pAkt in AZD8931-resistant MMTV-NIC PTEN$^{+/-}$ tumours following chronic drug treatment. Other studies have shown that combination therapy using a HER2 monoclonal antibody and an Akt inhibitor inhibited growth of MMTV-NIC PTEN$^{-/-}$ tumours that were resistant to treatment with either drug alone (Wang et al., 2012). Taken together, this supports the use of Akt inhibitors in combination with HER2-targeted therapies, and a number of clinical trials are currently underway to evaluate the use of trastuzumab and/or lapatinib with Akt inhibitors.

One of the major advantages of using the MMTV-NIC tumours for modelling drug resistance was the generation of resistant tumours with distinct molecular phenotypes, which recapitulates in part the heterogeneity seen in the clinic. This provides a strong rationale for basing therapeutic decisions on the biology of the individual resistant tumour, which might be very different from that of the primary tumour. For example, the observation that a subset of our resistant tumours no longer expressed high levels of membranous HER2 could have a significant impact on future treatments. To date, major advances in overcoming clinical resistance to trastuzumab have focused on alternative strategies for targeting HER2 signalling, either by combining drugs that target different HER family receptors or through use of drug-antibody conjugates, such as trastuzumab-emtansine. As it is rarely mandatory to re-biopsy tumours at the time of entry into clinical trials, patients whose tumours no longer express HER2 risk being exposed to the toxicity of treatments that might not be anticipated to be effective.

Several *in vitro* studies have shown that resistance to lapatinib and trastuzumab is associated with induction of EMT (Creedon et al., 2014; Kim et al., 2013; Korkaya et al., 2012; Oliveras-Ferraros et al., 2012), and our finding that a subset of the resistant tumours have undergone EMT indicates that targeting pathways that regulate EMT might be effective in a subpopulation of resistant tumours (Singh and Settleman, 2010). Interestingly, the generation of mixed vimentin- and E-cadherin-positive tumours following re-implantation of an AZD8931-resistant tumour shows that the induction of EMT is not binary and that the tumours are highly plastic and can respond to microenvironmental factors that can affect their EMT status. The initial response of the re-implanted resistant tumour fragments to AZD8931 most probably reflects this plasticity, with the reversion to a more epithelial phenotype and the concomitant re-expression of HER2 conferring initial drug sensitivity. Although we have shown that the induction of EMT is associated with acquired resistance to AZD8931, induction of EMT

Disease Models & Mechanisms (2016) 9, 131-140 doi:10.1242/dmm.023143

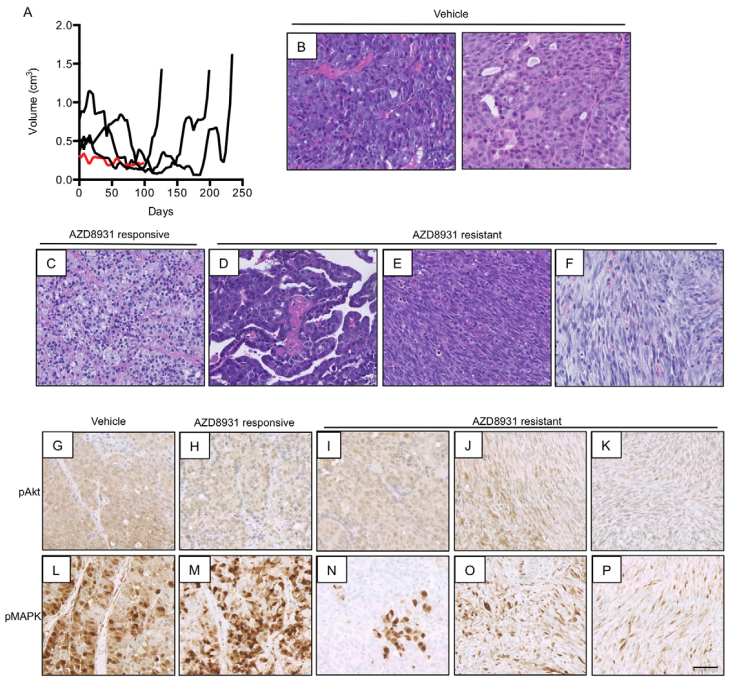


**Fig. 5. Generation of secondary resistance in NIC-PTEN$^{+/-}$ tumour fragments.** (A) Growth curves of NIC-PTEN$^{+/-}$ AZD8931-resistant tumour fragments following treatment with repeated cycles of AZD8931. Black lines represent tumours that developed resistance to AZD8931. Red line represents tumour with growth inhibited by AZD8931. Treatment was stopped after 90 days because of lack of tumour growth. (B) Representative H&E staining of vehicle-treated tumours. (C-F) H&E staining of AZD8931-treated tumours. (C) AZD8931-responsive tumour (red line in A) with growth inhibited by AZD893. (D) AZD8931-resistant tumour that has retained the morphology of the AZD8931-naïve (vehicle) tumours. (E,F) AZD8931-resistant tumours with a spindle cell morphology. (G-P) Immunohistochemical analysis of pAkt (G-K) and pMAPK (L-P) in vehicle- and AZD8931-treated tumours. Scale bar: 50 µm.

in HER2-driven mouse mammary tumours via expression of an activating PI3K mutation was associated with *de novo* resistance to HER2-targeted therapies (Hanker et al., 2013), whereas *in vitro* studies showed that expression of transcription factors that drive EMT was causally related to *de novo* trastuzumab resistance (Oliveras-Ferraros et al., 2012).

One of the main challenges for the future is the identification of effective drug combinations to combat resistance to HER2-targeted therapies. Use of the transplantable tumour model described here provides a powerful preclinical tool with which to test potential novel drug combinations in resistant tumours, studies which to date rely on use of resistant cell lines established *in vitro*. For example, exploitation of the molecular differences in resistant tumours that have undergone EMT might provide alternative combination strategies for overcoming resistance in these tumours.

## MATERIALS AND METHODS

### Animals

MMTV-NIC mice expressing an oncogenic ErbB2/Neu allele and Cre recombinase under the control of the MMTV promoter were generated as previously described (Ursini-Siegel et al., 2008) and inter-crossed with floxed *Pten* (strain C;129S4-*Pten*$^{tm1Hwu}$/J; Jackson Laboratory) mice to generate either MMTV-NIC PTEN$^{+/+}$ or MMTV-NIC PTEN$^{+/-}$ progeny on a FVB/N background. Genotyping was carried out by Transnetyx (Cordova, TN, USA). All experiments were conducted in compliance with UK Home Office guidelines. Nulliparous females were monitored twice weekly, using manual palpation, for tumour formation. The greatest tumour dimension and its perpendicular measurement were recorded, and when tumours had reached their maximal size (1.5 cm in one direction) as determined by Home Office regulations, mice were sacrificed. Tumours were then collected and fixed in 10% neutral buffered formalin. Tumours used for the generation of fragments were washed in ice-cold PBS and cut into 1 mm$^3$ fragments and any macroscopic necrotic areas removed and then centrifuged at 450 ***g*** for 1 min. The supernatant, containing fibrous and necrotic material, was removed and the remaining fragments were suspended in cryopreservation buffer (50% Dulbecco's modified Eagle's medium, 45% fetal bovine serum and 5% dimethyl sulfoxide) and stored at −80°C. At the time of transplantation, fragments were defrosted at room temperature, washed in PBS and inserted into the fourth mammary fat pad.

For drug studies using AZD8931 (AstraZeneca Oncology iMed, Alderley Park, Macclesfield, UK), treatment was commenced when mice had at least one tumour ≥0.1 cm$^3$ (index tumour) and continued until complete resolution of the index tumour or until the animal was sacrificed because of tumour size ≥1.5 cm (in any direction). Mice were dosed daily with

Disease Models & Mechanisms (2016) 9, 131-140 doi:10.1242/dmm.023143

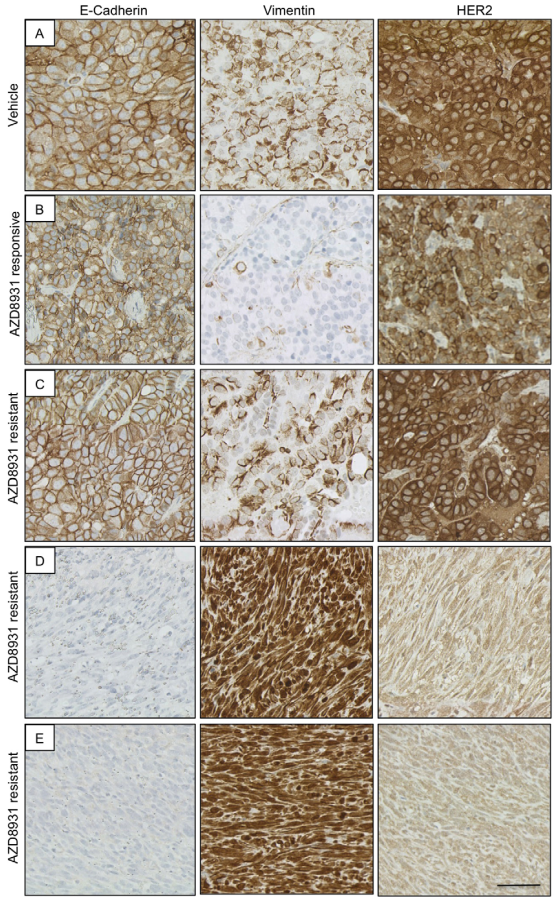


**Fig. 6. Development of EMT in AZD8931-resistant tumours.** Immunohistochemical analysis of E-cadherin, vimentin and HER2 in (A) vehicle- and (B-E) AZD8931-treated tumours. (B) AZD8931-responsive tumour with growth inhibited by AZD8931. (C) AZD8931-resistant tumour that has retained the morphology of the AZD8931-naïve (vehicle) tumours. (D,E) AZD8931-resistant tumours with a spindle cell morphology. Scale bar: 50 µm.

vehicle (1% Tween 80 in PBS) or AZD8931 (100 mg/kg) suspended in 1% Tween 80 (in PBS) by oral gavage. To generate tumours that were resistant to AZD8931, an intermittent drug treatment schedule was performed. After transplantation of tumour fragments, tumours were allowed to grow to ≥0.1 $cm^3$ before treatment with AZD8931 as above was started. When tumours regressed to <0.1 $cm^3$, AZD8931 treatment was stopped and tumours were monitored twice weekly. If the tumour regrew, treatment was then restarted when tumours reached ≥0.3 $cm^3$. This cycle was repeated until tumours developed resistance, and mice were sacrificed when the maximal tumour size (1.5 cm in any direction) was reached as permitted

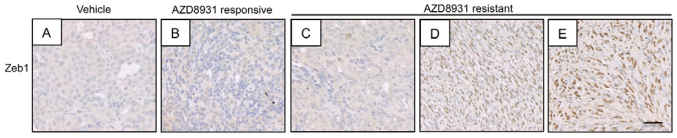


**Fig. 7. Nuclear Zeb1 expression in spindle cell AZD8931-resistant tumours.** Immunohistochemical analysis of Zeb1 in (A) vehicle- and (B-E) AZD8931-treated tumours. (B) AZD8931-responsive tumour with growth inhibited by AZD8931. (C) AZD8931-resistant tumour that has retained the morphology of the AZD8931-naïve (vehicle) tumours. (D,E) AZD8931-resistant tumours with a spindle cell morphology. Scale bar: 50 µm.

under UK Home Office regulations. For drug studies using paclitaxel, treatment was commenced when mice had at least one tumour ≥0.15 $cm^3$ (index tumour) and continued until the animal was sacrificed because of tumour size or when the experiment was terminated 72 h after the fourth dose of paclitaxel. Mice were dosed weekly with vehicle (cremaphor EL: ethanol, 1:1, v:v) or paclitaxel (10 mg/kg) suspended in cremaphor EL: ethanol by intraperitoneal injection.

### Immunohistochemistry

Immunohistochemistry of formalin-fixed, paraffin-embedded tissues was performed as described previously (Karim et al., 2013). Primary antibodies used were as follows: HER2 (Invitrogen; catalogue no. AHO1011; 1:1000), pY1221/1222 HER2 (catalogue no. 2243; 1:400; Cell Signaling, UK), pY1289 HER3 (catalogue no. 4791; 1:100; Cell Signaling, UK), Ki67 (Vector; catalogue no. VP-RM04; 1:500), E-cadherin (catalogue no. 3195, 1:5000; Cell Signaling, UK), vimentin (catalogue no. 5741; 1:100; Cell Signaling, UK), pS473 Akt (catalogue no. 4060; 1:50; Cell Signaling, UK) and pT202/Y204 MAPK (catalogue no. 4370; 1:400; Cell Signaling, UK).

### Western blotting

Western blot analysis was performed as described previously (Karim et al., 2013). Primary antibodies used were HER2 (catalogue no. 2248; 1:1000; Cell Signaling, UK), pS473 Akt (catalogue no. 4060; 1:1000; Cell Signaling, UK), Akt (catalogue no. 9272; 1:1000; Cell Signaling, UK), PTEN (catalogue no. 9552; 1:1000; Cell Signaling, UK) and β-actin (catalogue no. A4700; Sigma, UK; 1:5000).

### Reverse-phase protein array analysis

Tumours were washed with PBS and lysed in 1% Triton X-100, 50 mM HEPES (pH 7.4), 150 mM sodium chloride, 1.5 mM magnesium chloride, 1 mM EGTA, 100 mM sodium fluoride, 10 mM sodium pyrophosphate, 1 mM sodium vanadate and 10% glycerol, supplemented with cOmplete ULTRA protease inhibitor and PhosSTOP phosphatase inhibitor cocktails (Sigma, UK). Cleared lysates were serially diluted to produce a dilution series comprising four serial twofold dilutions of each sample, which were spotted onto nitrocellulose-coated slides (Grace Bio-Labs, supplied by Sigma, UK) in triplicate in conditions of constant 70% humidity using the Aushon 2470 array platform (Aushon Biosystems, Billerica, MA, USA). Slides were hydrated in blocking buffer (Thermo Fisher Scientific, UK) and then incubated with primary antibodies (all 1:250; all from Cell Signaling, UK). Bound antibodies were detected by incubation with anti-rabbit DyLight 800-conjugated secondary antibody (New England BioLabs, UK). An InnoScan 710-IR scanner (Innopsys, Carbonne, France) was used to read the slides, and images were acquired at the highest gain without saturation of the fluorescence signal. The relative fluorescence intensity of each sample replicate was quantified using Mapix software (Innopsys).

The linear fit of the dilution series of each sample was determined for each primary antibody, from which median relative fluorescence intensities were calculated, and samples with $R^2$<0.8 in all three replicates were excluded. Signal intensities were normalized by global sample median normalization (Guo et al., 2012).

#### Competing interests

T.K. and L.A.B. are employees of AstraZeneca. All other authors have no competing interests.

#### Author contributions

H.C., L.A.B., M.M., J.B., N.T. and L.G.-C. carried out the experiments and analysed the data. J.L. carried out the histological evaluation and contributed to writing the manuscript. T.K. provided intellectual input and contributed to writing the manuscript. W.J.M. provided the mouse lines and intellectual input. H.C. and V.G.B. conceived and designed the experiments and wrote the manuscript.

#### Funding

This work was supported by Cancer Research UK grants [C157/A15703, C157/A9148 and C6088/A12063] and a Medical Research Council/AstraZeneca Case Award [G0900184-4/1].

#### Supplementary information

Supplementary information available online at
http://dmm.biologists.org/lookup/suppl/doi:10.1242/dmm.023143/-/DC1

#### References

**Arteaga, C. L., Sliwkowski, M. X., Osborne, C. K., Perez, E. A., Puglisi, F. and Gianni, L.** (2012). Treatment of HER2-positive breast cancer: current status and future perspectives. *Nat. Rev. Clin. Oncol.* **9**, 16-32.

**Becher, O. J. and Holland, E. C.** (2006). Genetically engineered models have advantages over xenografts for preclinical studies. *Cancer Res.* **66**, 3355-3359.

**Berns, K., Horlings, H. M., Hennessy, B. T., Madiredjo, M., Hijmans, E. M., Beelen, K., Linn, S. C., Gonzalez-Angulo, A. M., Stemke-Hale, K., Hauptmann, M. et al.** (2007). A functional genetic approach identifies the PI3K pathway as a major determinant of trastuzumab resistance in breast cancer. *Cancer Cell* **12**, 395-402.

**Creedon, H., Byron, A., Main, J., Hayward, L., Klinowska, T. and Brunton, V. G.** (2014). Exploring mechanisms of acquired resistance to HER2 (human epidermal growth factor receptor 2)-targeted therapies in breast cancer. *Biochem. Soc. Trans.* **42**, 822-830.

**Esteva, F. J., Guo, H., Zhang, S., Santa-Maria, C., Stone, S., Lanchbury, J. S., Sahin, A. A., Hortobagyi, G. N. and Yu, D.** (2010). PTEN, PIK3CA, p-AKT, and p-p70S6K status: association with trastuzumab response and survival in patients with HER2-positive metastatic breast cancer. *Am. J. Pathol.* **177**, 1647-1656.

**Gajria, D., Seidman, A. and Dang, C.** (2010). Adjuvant taxanes: more to the story. *Clin. Breast Cancer* **10** Suppl. 2, S41-S49.

**Ghersi, D., Wilcken, N. and Simes, R. J.** (2005). A systematic review of taxane-containing regimens for metastatic breast cancer. *Br. J. Cancer* **93**, 293-301.

**Guo, H., Liu, W., Ju, Z., Tamboli, P., Jonasch, E., Mills, G. B., Lu, Y., Hennessy, B. T. and Tsavachidou, D.** (2012). An efficient procedure for protein extraction from formalin-fixed, paraffin-embedded tissues for reverse phase protein arrays. *Proteome Sci.* **10**, 56.

**Hanker, A. B., Pfefferle, A. D., Balko, J. M., Kuba, M. G., Young, C. D., Sanchez, V., Sutton, C. R., Cheng, H., Perou, C. M., Zhao, J. J. et al.** (2013). Mutant PIK3CA accelerates HER2-driven transgenic mammary tumors and induces resistance to combinations of anti-HER2 therapies. *Proc. Natl. Acad. Sci. USA* **110**, 14372-14377.

**Hickinson, D. M., Klinowska, T., Speake, G., Vincent, J., Trigwell, C., Anderton, J., Beck, S., Marshall, G., Davenport, S., Callis, R. et al.** (2010). AZD8931, an equipotent, reversible inhibitor of signaling by epidermal growth factor receptor, ERBB2 (HER2), and ERBB3: a unique agent for simultaneous ERBB receptor blockade in cancer. *Clin. Cancer Res.* **16**, 1159-1169.

**Karim, S. A., Creedon, H., Patel, H., Carragher, N. O., Morton, J. P., Muller, W. J., Evans, T. R. J., Gusterson, B., Sansom, O. J. and Brunton, V. G.** (2013). Dasatinib inhibits mammary tumour development in a genetically engineered mouse model. *J. Pathol.* **230**, 430-440.

**Kim, H.-P., Han, S.-W., Song, S.-H., Jeong, E.-G., Lee, M.-Y., Hwang, D., Im, S.-A., Bang, Y.-J. and Kim, T.-Y.** (2013). Testican-1-mediated epithelial-mesenchymal transition signaling confers acquired resistance to lapatinib in HER2-positive gastric cancer. *Oncogene* **33**, 3334-3341.

**Korkaya, H., Kim, G.-I., Davis, A., Malik, F., Henry, N. L., Ithimakin, S., Quraishi, A. A., Tawakkol, N., D'Angelo, R., Paulson, A. K. et al.** (2012). Activation of an IL6 inflammatory loop mediates trastuzumab resistance in HER2+ breast cancer by expanding the cancer stem cell population. *Mol. Cell* **47**, 570-584.

**Nagata, Y., Lan, K.-H., Zhou, X., Tan, M., Esteva, F. J., Sahin, A. A., Klos, K. S., Li, P., Monia, B. P., Nguyen, N. T. et al.** (2004). PTEN activation contributes to tumor inhibition by trastuzumab, and loss of PTEN predicts trastuzumab resistance in patients. *Cancer Cell* **6**, 117-127.

**Olive, K. P., Jacobetz, M. A., Davidson, C. J., Gopinathan, A., McIntyre, D., Honess, D., Madhu, B., Goldgraben, M. A., Caldwell, M. E., Allard, D. et al.** (2009). Inhibition of Hedgehog signaling enhances delivery of chemotherapy in a mouse model of pancreatic cancer. *Science* **324**, 1457-1461.

**Oliveras-Ferraros, C., Corominas-Faja, B., Cufi, S., Vazquez-Martin, A., Martin-Castillo, B., Iglesias, J. M., Lopez-Bonet, E., Martin, A. G. and Menendez, J. A.** (2012). Epithelial-to-mesenchymal transition (EMT) confers primary resistance to trastuzumab (Herceptin). *Cell Cycle* **11**, 4020-4032.

**Rexer, B. N. and Arteaga, C. L.** (2012). Intrinsic and acquired resistance to HER2-targeted therapies in HER2 gene-amplified breast cancer: mechanisms and clinical implications. *Crit. Rev. Oncog.* **17**, 1-16.

**Rottenberg, S., Nygren, A. O. H., Pajic, M., van Leeuwen, F. W. B., van der Heijden, I., van de Wetering, K., Liu, X., de Visser, K. E., Gilhuijs, K. G., van Tellingen, O. et al.** (2007). Selective induction of chemotherapy resistance of mammary tumors in a conditional mouse model for hereditary breast cancer. *Proc. Natl. Acad. Sci. USA* **104**, 12117-12122.

**Schade, B., Rao, T., Dourdin, N., Lesurf, R., Hallett, M., Cardiff, R. D. and Muller, W. J.** (2009). PTEN deficiency in a luminal ErbB-2 mouse model results in dramatic acceleration of mammary tumorigenesis and metastasis. *J. Biol. Chem.* **284**, 19018-19026.

**Sharpless, N. E. and DePinho, R. A.** (2006). The mighty mouse: genetically engineered mouse models in cancer drug development. *Nat. Rev. Drug Discov.* **5**, 741-754.
**Singh, A. and Settleman, J.** (2010). EMT, cancer stem cells and drug resistance: an emerging axis of evil in the war on cancer. *Oncogene* **29**, 4741-4751.
**Singh, M., Lima, A., Molina, R., Hamilton, P., Clermont, A. C., Devasthali, V., Thompson, J. D., Cheng, J. H., Bou Reslan, H., Ho, C. C. K. et al.** (2010). Assessing therapeutic responses in Kras mutant cancers using genetically engineered mouse models. *Nat. Biotech.* **28**, 585-593.
**Tjulandin, S., Moiseyenko, V., Semiglazov, V., Manikhas, G., Learoyd, M., Saunders, A., Stuart, M. and Keilholz, U.** (2014). Phase I, dose-finding study of AZD8931, an inhibitor of EGFR (erbB1), HER2 (erbB2) and HER3 (erbB3) signaling, in patients with advanced solid tumors. *Invest. New Drugs* **32**, 145-153.
**Ursini-Siegel, J., Hardy, W. R., Zuo, D., Lam, S. H. L., Sanguin-Gendreau, V., Cardiff, R. D., Pawson, T. and Muller, W. J.** (2008). ShcA signalling is essential for tumour progression in mouse models of human breast cancer. *EMBO J.* **27**, 910-920.
**van Miltenburg, M. H. and Jonkers, J.** (2012). Using genetically engineered mouse models to validate candidate cancer genes and test new therapeutic approaches. *Curr. Opin. Genet. Dev.* **22**, 21-27.
**Wang, Q., Li, S.-H., Wang, H., Xiao, Y., Sahin, O., Brady, S. W., Li, P., Ge, H., Jaffee, E. M., Muller, W. J. et al.** (2012). Concomitant targeting of tumor cells and induction of T-cell response synergizes to effectively inhibit trastuzumab-resistant breast cancer. *Cancer Res.* **72**, 4417-4428.
**Xia, W., Husain, I., Liu, L., Bacus, S., Saini, S., Spohn, J., Pry, K., Westlund, R., Stein, S. H. and Spector, N. L.** (2007). Lapatinib antitumor activity is not dependent upon phosphatase and tensin homologue deleted on chromosome 10 in ErbB2-overexpressing breast cancers. *Cancer Res.* **67**, 1170-1175.

© 2017. Published by The Company of Biologists Ltd | Disease Models & Mechanisms (2017) 10, 1061-1074 doi:10.1242/dmm.030403

REVIEW

# Mouse models of metastasis: progress and prospects

**Laura Gómez-Cuadrado[1,*], Natasha Tracey[1,*], Ruoyu Ma[2], Binzhi Qian[2,3] and Valerie G. Brunton[1,‡]**


## ABSTRACT

Metastasis is the spread of cancer cells from a primary tumor to distant sites within the body to establish secondary tumors. Although this is an inefficient process, the consequences are devastating as metastatic disease accounts for >90% of cancer-related deaths. The formation of metastases is the result of a series of events that allow cancer cells to escape from the primary site, survive in the lymphatic system or blood vessels, extravasate and grow at distant sites. The metastatic capacity of a tumor is determined by genetic and epigenetic changes within the cancer cells as well as contributions from cells in the tumor microenvironment. Mouse models have proven to be an important tool for unraveling the complex interactions involved in the metastatic cascade and delineating its many stages. Here, we critically appraise the strengths and weaknesses of the current mouse models and highlight the recent advances that have been made using these models in our understanding of metastasis. We also discuss the use of these models for testing potential therapies and the challenges associated with the translation of these findings into the provision of new and effective treatments for cancer patients.


**KEY WORDS: Cancer, Metastasis, Mouse models, Stroma**

## Introduction

Metastasis, the process of tumor cell migration from the primary site to distant organs, remains the major cause of cancer-related deaths, despite therapeutic advances in recent years (Steeg, 2016). This highlights the urgent need to better understand the mechanisms that underlie metastasis and to identify new therapeutic strategies and drug targets to treat metastatic disease. A number of excellent review articles have covered the exciting new advances in our understanding of the genetic and molecular events that govern metastatic spread (Lambert et al., 2017; Massagué and Obenauf, 2016; Sethi and Kang, 2011; Turajlic and Swanton, 2016; Valastyan and Weinberg, 2011), which will not be covered in detail here. In this Review, we discuss the different mouse models of metastasis that are currently used, and focus on how they have contributed to the field thus far. We consider their strengths and weaknesses and the technological advances that are driving the development of more refined models, which have the potential to impact on the translation and development of better therapeutic interventions. We first provide an overview of the metastatic process.

[1]Edinburgh Cancer Research Centre, Institute for Genetics and Molecular Medicine, Edinburgh, EH4 2XR, UK. [2]MRC Centre for Reproductive Health, Queen's Medical Research Institute, University of Edinburgh, Edinburgh, UK. [3]Edinburgh Cancer Research UK Centre, Queen's Medical Research Institute, Edinburgh, EH16 4TJ, UK.
*These authors contributed equally to this work

‡Author for correspondence (v.brunton@ed.ac.uk)

V.G.B., 0000-0002-7778-8794



## The metastatic cascade

Metastasis is a multistep process, as illustrated in Fig. 1. The first step of the metastatic cascade is local invasion at the primary tumor site. This process is initiated by the activation of signaling pathways that regulate cytoskeletal dynamics, loss of adhesion amongst tumor cells and turnover of the surrounding extracellular matrix (ECM) (Friedl and Alexander, 2011). This allows the tumor cells to migrate away from the primary tumor and infiltrate into surrounding tissues. To initiate the spread to secondary sites, the tumor cells must then intravasate (see Glossary, Box 1) into the blood circulation or lymphatic system. Dispersal of tumor cells in the lymphatic system leads to lymph node metastasis in the first instance, while distal metastasis usually requires tumor cells to disseminate via the blood circulation (hematogenous) with the choice of a tumor cell to use either lymphatic or hematogenous dissemination, governed by a number of factors (Chiang et al., 2016; Wong and Hynes, 2006). In this article, we will focus on hematogenous metastasis.

After entry into the circulation, tumor cells can disseminate widely throughout the body and are known as circulating tumor cells (CTCs) (see Glossary, Box 1). CTCs have the potential to serve as prognostic markers of metastasis and survival, as has been discussed extensively in recent reviews (Alix-Panabierès and Pantel, 2013; Plaks et al., 2013). On reaching distal organs, surviving tumor cells can be intercepted in small capillaries or actively adhere to larger blood vessels and extravasate through paracellular or transcellular transendothelial migration (see Glossary, Box 1) (Reymond et al., 2013), prior to colonization (see Glossary, Box 1). This process can be promoted by alterations induced by secreted factors and extracellular vesicles derived from the primary tumor, before the establishment of metastases (McAllister and Weinberg, 2014). These alterations involve fibroblasts, endothelial cells and immune cells, especially bone marrow-derived immature myeloid cells, which can collectively establish a pre-metastatic niche (Box 2) that provides an environment favoring the recruitment of CTCs and their subsequent growth (Liu and Cao, 2016; Peinado et al., 2017).

Once settled in the metastatic organ, tumor cells are referred to as disseminated tumor cells (DTCs) (see Glossary, Box 1). DTCs can be present for years or decades and stay in a latent state as single cells or micrometastases (Massagué and Obenauf, 2016). This tumor dormancy may result from single DTCs entering a quiescent state or may be due to inadequate vascularization or immune clearance of micrometastases (Gay and Malanchi, 2017). Eventually, clinically relevant macrometastases (see Glossary, Box 1) arise from the outgrowth of DTCs, a process termed colonization (see Glossary, Box 1).

## Models of metastasis

In this section, we provide an overview of the main mouse models of metastatic cancer that are currently in use, from mice generated using transplantable cancer cells and tumors to genetically engineered mouse models (GEMMS) (see Glossary, Box 1) (Francia et al., 2011; Kabeer et al., 2016; Kersten et al., 2016; Saxena and Christofori, 2013). These mouse models are classified

Disease Models & Mechanisms (2017) 10, 1061-1074 doi:10.1242/dmm.030403

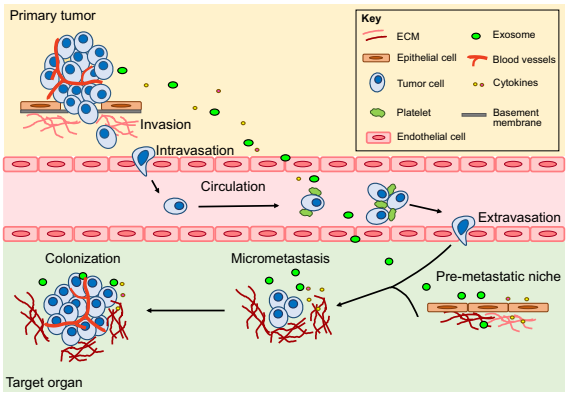


**Fig. 1. Metastatic cascade.** Metastasis is a multistep process. Initially, tumor cells migrate into adjacent tissues, referred to as local invasion. This involves breakdown of the basement membrane and invasion into the surrounding ECM. Intravasation then allows cells to enter the circulation. In blood vessels, CTCs exist as single cells or clusters, coated with platelets. They need to survive shear stress and evade clearance by the immune system to successfully reach distant organs. Tumor cells then attach to endothelial cells, which facilitates their extravasation. After settling in the metastatic target organ, tumor cells must survive in this foreign environment and establish micrometastases. These DTCs can remain dormant for many years before proliferating into large macrometastases in a process termed colonization. The primary site also regulates the development of metastasis via secretion of factors (such as cytokines and exosomes) that can prime a pre-metastatic niche (Box 2) and support survival of DTCs. See Glossary in Box 1 for an explanation of key terms.

and summarized in Table 1, and examples of models that have been used are listed in Table 2.

## Transplantation models

### Spontaneous models of metastasis

Spontaneous metastasis models allow the spread of cells from a primary tumor to secondary sites to be followed in animals that have received ectopic or orthotopic (see Glossary, Box 1) transplants of cancer cells or tissue. The advantage of these models is that they allow the entire metastatic cascade to be modeled. However, although ectopic subcutaneous transplantation of multiple cell or tumor types is widely used to monitor tumor growth as it induces rapid tumor growth in the highly vascularized skin, and tumor development can be monitored easily through the use of caliper measurements, metastasis is not often seen in these models and tends to be restricted to allograft models (see below) such as the B16 melanoma and Lewis lung carcinoma model (Table 2). Orthotopic studies are able to better recapitulate human cancers by enabling interactions with the tissue of origin, which can impact on the initial invasion and intravasation and may reflect the increased metastatic spread seen in orthotopic models (Francia et al., 2011; Kellar et al., 2015) (Table 2). This is dependent on the ability to implant tumor cells in the orthotopic site from which the original tumor was derived, which has been successful for a number of tumor types including mammary, pancreatic, lung and colon (Table 2). In some models, there is a long latency, and resection of the primary tumor is needed to allow development of metastases; this is only possible for certain cancers, such as mammary tumors and melanoma (Coffelt et al., 2015; Cruz-Munoz et al., 2008). However, models in which resection of the primary tumor is possible have the benefit of allowing potential adjuvant therapies to be tested.

### Experimental models of metastasis

Experimental models of metastasis are used to evaluate the capacity of cancer cells to arrest, extravasate and grow in particular organs in ectopic sites following intravascular injection. Different sites of vascular injection in the mouse, including the lateral tail vein, intra-portal, intra-carotid and intra-cardiac, define the site of colonization (reviewed in Khanna and Hunter, 2005). For example, injection into the tail vein leads to the formation of lung metastases, which reflects the rapid trapping of cells within the microvasculature of the lung minutes after injection. Intra-cardiac injection allows wider dissemination of cancer cells and is commonly used to model bone and brain metastasis. Other models include intra-peritoneal injection to model the local dissemination of ovarian cancer or intra-splenic injection of colon cancer cells leading to metastasis formation within the liver. A drawback of experimental metastasis models is that they do not recapitulate the first steps of the metastatic cascade, and only reflect homing of tumor cells circulating in the bloodstream to a limited set of secondary organs. Despite this, they have been instrumental in elucidation of tumor-host interactions required for the initial arrest and colonization at metastatic sites, as discussed below.

Both allograft and xenograft (see Glossary, Box 1) transplantation models are used in spontaneous and experimental metastasis assays and the characteristics of these models are explained in further detail below.

### Allografts

Allograft transplantation models are generated by the transplantation of mouse-derived cancer cells and tumors into mice. The use of genetically identical syngeneic (see Glossary, Box 1) models, to prevent graft versus host reactions, allows investigation of the immune system in cancer progression and identification of new therapeutic opportunities (Serrels et al., 2015).

Fidler (1973) described the first syngeneic mouse model of metastasis and provided the first demonstration that the metastatic potential of tumor cells could be enhanced through *in vivo* selection. B16 melanoma tumor cells are derived from a spontaneous melanoma that developed in the common C57BL/6 strain of laboratory mice. B16 cells with enhanced metastatic properties were generated after several rounds of *in vivo* selection by subcutaneous injection of melanoma cancer cells into the syngeneic C57BL/6J mouse. The occurrence of metastasis to the lungs increases significantly with the clonally selected tumor lines derived from successive pulmonary metastases (Fidler, 1973).

### Xenografts

In contrast to allograft models, xenografts involve human cancer cells and tumors. Human tissue must be introduced into

Disease Models & Mechanisms (2017) 10, 1061-1074 doi:10.1242/dmm.030403

**Box 1. Glossary**

**Allograft:** The transplant of cells or organs from one individual to another individual of the same species.
**Cancer-associated fibroblast (CAF):** Fibroblasts found within or in close proximity to a tumor. Usually derived from normal fibroblasts but can also be formed from pericytes (contractile cells that line capillaries) and smooth muscle cells, among other cell types.
**Circulating tumor cell (CTC):** Tumor cells that have left the primary tumor and entered the circulatory system.
**Colonization:** The processes (e.g. survival and proliferation) which allow disseminated tumor cells to form large macrometastases.
**Cre recombinase/*loxP*:** Cre recombinase enzymatically removes sequences that are flanked (floxed) by inserted *loxP* sequences.
**CRISPR/Cas9:** Gene-editing technology that enables precise genomic modifications. This technology can be used to generate gene modifications, deletions and insertions, by using a synthetic guide RNA to introduce a double-strand break at specific sites in DNA, mediated by Cas9 endonuclease.
**Disseminated tumor cell (DTC):** Tumor cells that have settled in distant organs away from the primary tumor site after exiting the circulatory system.
**Ectopic:** The transplantation of a cell type to a location in which it is not found under normal physiological circumstances.
**Epithelial-to-mesenchymal transition (EMT):** Loss of cell-cell adhesion complexes and cell polarity by an epithelial cell, and the gain of an invasive, migratory, mesenchymal phenotype.
**Exosome:** Extracellular vesicles that are released from cells after the fusion of multivesicular bodies with the plasma membrane.
**Extracellular matrix (ECM):** The acellular support surrounding tissues.
**Extravasation:** The process by which a tumor cell leaves the circulatory system and enters a secondary site away from the primary tumor.
**Genetically engineered mouse model (GEMM):** A mouse with a genome altered by genetic engineering techniques, including gene deletion, mutation or addition. This can be performed in a tissue- or cell-specific manner and may also be inducible.
**Immunocompromised mice:** Mice in which specific elements of the immune system have been removed to allow engraftment of human material.
**Integrin:** Transmembrane receptor protein that cells use to adhere and respond to the extracellular matrix.
**Intravasation:** The process by which a tumor cell leaves the primary tumor and enters the circulation.
**Invadopodium:** Actin-rich protrusion present at the membrane of invasive cancer cells that extends and degrades the extracellular matrix.
**Micrometastasis:** Small clusters of cancer cells in secondary organs that are too small to detect through screening.
**Organoids (tumor):** three-dimensional cultures of tumor cells.
**Orthotopic:** The transplantation of a cell type or organ to a location in which it would be found under normal physiological circumstances.
**Patient-derived xenograft (PDX):** A model in which human patient tumor material is implanted into an immunocompromised host, most commonly the mouse.
**Seeding:** In the context of metastasis, seeding refers to the process whereby tumor cells 'seed' new tumors in distant organs. Originally described in Stephen Paget's 'seed and soil' hypothesis of cancer metastasis (Paget, 1989). The seeding process includes tumor cell adherence to the blood vessel in the distal organ, extravasation, migration to the tissue parenchyma, and survival.
**Syngeneic:** In transplantation biology, this refers to individuals or tissues that are genetically identical or closely related, allowing the transplantation of tissues from the strain of origin into immunocompetent mice.
**Transendothelial migration:** Movement of tumor cells through the endothelial barrier either paracellularly (through the endothelial cell junctions) or transcellularly (through the endothelial cell body).
**Tumor-associated macrophage (TAM):** A macrophage found within or in close proximity to a tumor that actively promotes tumor growth through the secretion of cytokines and chemokines.
**Tumor microenvironment:** All elements that make up the surroundings of the tumor, including other cell types, vasculature and the extracellular matrix.
**Xenograft:** The transplant of cells or organs from one species into an individual of a different species.

immunocompromised (see Glossary, Box 1) or immune-deficient mice in order to prevent rejection by the host. An advantage of these tumor models is that the donor cells are human in origin; however, the key drawback is lack of the host adaptive immune system, which is now recognized to contribute to many aspects of primary tumor growth and metastatic spread (Hanahan and Weinberg, 2011). The use of xenograft mouse models in metastatic studies has been restricted to studies in which highly metastatic variants have been derived through *in vivo* selection (e.g. MDA-MB-231 breast cancer cells, KM12 colon carcinoma cells and WM239A melanoma cells), which overcome the problem of limited metastatic potential (Table 2). This method has also been used extensively to identify gene expression signatures that regulate organ-specific patterns of breast cancer metastasis (Bos et al., 2009; Kang et al., 2003; Minn et al., 2005).

Cancer cell lines often fail to retain the characteristics of the original tumor when cultured *in vitro*. Therefore, they do not reflect the phenotypic and genetic heterogeneity of human cancers and, consequently, xenograft models are poor predictors of clinical responses (Kersten et al., 2016). Patient-derived xenografts (PDXs) (see Glossary, Box 1) have emerged as a potential solution to this problem (reviewed in Whittle et al., 2015). PDXs are generated from resected tumors, propagated directly in immunocompromised mice following orthotopic or subcutaneous injection, avoiding *in vitro* selection pressures. PDXs have been shown to reflect the diversity of human cancer, recapitulating the histology and the metastatic characteristics of the original tumor (DeRose et al., 2011; Eyre et al., 2016; Hiroshima et al., 2016; Julien et al., 2012; Puig et al., 2013). Other studies show that the site and frequency of PDX metastasis may vary from that seen in the patient and the engraftment rate is relatively low. Furthermore, the lack of an intact immune system and the presence of mouse stroma mean that PDXs are not an ideal model for studying the role of the tumor microenvironment in disease progression (Jackson and Thomas, 2017; Pompili et al., 2016; Whittle et al., 2015). To overcome these limitations, humanized xenograft mouse models are being developed, in which the human components of the tumor microenvironment, such as immune cells, peripheral blood and stromal tissue have been engrafted (Bankert et al., 2011; Cassidy et al., 2015; Kuperwasser et al., 2005; Morton et al., 2016). There are also challenges associated with these mice, however, including the technical difficulty of increasing the spectrum of immune cells engrafted while reducing the mouse innate immune response (Shultz et al., 2012). The impact that these humanized mouse models will have on research into metastasis remains unclear at present.

### Genetically engineered mouse models

Genetically engineered mouse models (GEMMs) (see Glossary, Box 1) display *de novo* tumor progression and metastasis formation, usually in an immune-competent tumor microenvironment. This enables both the tumor cell-autonomous and stromal influences on

Disease Models & Mechanisms (2017) 10, 1061-1074 doi:10.1242/dmm.030403

**Box 2. Pre-metastatic niche**

Pre-metastatic niches are organ-specific supportive biological environments that support survival of CTCs in distal organs and promote metastatic outgrowth. The formation of the pre-metastatic niche is governed by secreted factors from the primary tumor, including growth factors and inflammatory cytokines and chemokines. Recent studies found that tumor-derived exosomes can also promote niche establishment and determine organ specificity in some types of cancer; however, whether it is a common feature for pre-metastatic niche formation remains unclear. These tumor-derived secreted factors induce changes in distant pre-metastatic sites while also mobilizing bone marrow-derived cells, the recruitment of which – along with a number of other types of immune cell – to the niche leads to remodeling of the local environment and formation of the pre-metastatic niche. This involves interactions with local resident stromal cells, such as endothelial cells, macrophages and fibroblasts, and also the extracellular matrix, which all cooperate to form a permissive environment for tumor outgrowth. For example, activated fibroblasts remodel the ECM by secreting matrix components such as fibronectin and metalloproteinases that break down existing ECM. Increased fibronectin in the niche enhances adhesion of recruited bone marrow-derived cells. Lysyl oxidase, an enzyme that cross-links collagen and elastins in the ECM, is also important in the formation of the pre-metastatic niche; by remodeling the ECM, this enzyme enhances myeloid cell infiltration. For further information, readers are directed to two reviews on the formation and role of the pre-metastatic niche (Liu and Cao, 2016; Peinado et al., 2017).

all stages of the metastatic cascade to be modeled, making GEMMs an invaluable resource for studying metastasis. Their use in cancer research has been widely reviewed (Kabeer et al., 2016; Kersten et al., 2016; Saxena and Christofori, 2013). Here, we provide an overview of the models available and discuss their potential for modeling metastatic disease.

The first transgenic models used tissue-specific promoters, such as the mammary-specific MMTV promoter, to drive expression of oncogenes such as *v-ErbB2* and *v-HRas* (Muller et al., 1988; Sinn et al., 1987). This was followed by the generation of tumor suppressor gene knockout mice (e.g. *Trp53*) that have a predisposition to tumor formation (Donehower et al., 1992). Although these models have given insight into many fundamental aspects of cancer biology, it is difficult to model sporadic cancer development seen in humans due to lack of tissue specificity of gene knockouts and control of transgene expression in specific cell lineages (Kersten et al., 2016).

More advanced models allow conditional activation of oncogenes and/or inactivation of tumor suppressor genes in somatic cells. The Cre recombinase/*loxP* system (see Glossary, Box 1) is used widely for this. Using this system, genes that are flanked by *loxP* recombination sites are deleted following activation of Cre recombinase (Gu et al., 1993). Use of tissue-specific promoters to drive Cre recombinase expression, combined with expression of oncogenes that are known to be associated with development of human tumors in those tissues, has resulted in the generation of models that recapitulate many of the molecular characteristics and histopathological features of the human disease (Hingorani et al., 2003; Holen et al., 2017; Jackson et al., 2001; Shibata et al., 1997). These have been invaluable in dissecting the complexities of human cancer and its progression.

Further control can be achieved by using regulatable systems such as the Cre-ER system, in which the hormone-binding domain of the estrogen receptor (ER) is fused to Cre recombinase: treatment of mice with the estrogen analogue tamoxifen leads to activation of Cre recombinase in a temporal manner (Lewandoski, 2001). The tetracycline-inducible system also permits the switching on or off (Tet-On/Tet-Off system) of a specific gene of interest in a tissue- and time-specific manner following administration of doxycyline (Gunther et al., 2002). This temporal and spatial control of gene activation and inactivation is useful for overcoming unwanted effects that could impact on organ-specific development or result in embryonic lethality, as seen upon deletion of the *Rb1* tumor suppressor (Lee et al., 1992). These models can also be used to address the importance of genetic changes at specific times during tumor progression.

An important limitation of GEMMs is the low incidence of metastatic spread that often does not reflect the organ tropism seen in the human disease (Kabeer et al., 2016; Kersten et al., 2016). Although identification of the most appropriate tissue-specific

**Table 1. Strengths and weaknesses of mouse models of metastasis**

| Type of model | Strengths | Weaknesses |
|---|---|---|
| Tumor transplantation: spontaneous metastasis | Metastatic disease development from primary tumor site mimics human disease progression<br>Models all stages of the metastatic cascade<br>Immunocompetent host if allograft<br>Low cost | Mouse microenvironment<br>Applicable to limited number of cell lines<br>Poor tropism of metastasis in reference to the clinical setting<br>Asynchronous metastatic development<br>Removal of primary tumor to allow development of metastases can be performed only on certain tumor types such as breast, prostate, pancreas and ectopic transplants<br>Immunocompromised host if xenograft |
| Tumor transplantation: experimental metastasis | Rapid and reproducible development of metastases<br>Site-specific development of metastases<br>Applicable to a wide number of cell lines and tumor models<br>Immunocompetent host if allograft<br>Low cost | Mouse microenvironment<br>Only models late stages of the metastatic cascade<br>Immunocompromised host if xenograft |
| GEMM | Metastatic spread of spontaneous *de novo* tumors, mimicking human disease<br>Tumors develop in natural microenvironment<br>Tumors display genetic heterogeneity<br>Tumors resemble the molecular and histopathological characteristics of the human disease<br>Models have the potential to model all stages of the metastatic cascade<br>Immunocompetent host | Mouse rather than human microenvironment<br>Genetics (promoter and oncogenes) often not truly representative of the human disease<br>Promoters not well defined to a specific lineage<br>Can have low penetrance and long latency of metastatic disease development<br>Poor tropism of metastasis in reference to the clinical setting<br>Extensive breeding programs often required (cost and time implications)<br>Asynchronous metastatic development |

**Table 2. Examples of commonly used models of metastasis**

| Classification | Tumor type | Cells/tumors transplanted in mice or genotypic details of GEMM strain | Site of metastasis | References |
|---|---|---|---|---|
| **Spontaneous metastasis** | | | | |
| Allograft, orthotopic | Melanoma | Mouse B16 cells (C57BL/6 mice) | Lungs | (Fidler, 1973) |
| Allograft, orthotopic | Mammary | Mouse *K14Cre; Cdh1$^{F/F}$; Trp53$^{F/F}$* (KEP) cell line and tumor fragments (FVB mice) | Lungs, lymph nodes, liver, spleen, gastrointestinal and urogenital tract, pancreas, mesenterium and peritoneum | (Coffelt et al., 2015; Derksen et al., 2006; Doornebal et al., 2013) |
| | | Mouse 4T1 cells (BALB/c mice) | Lungs and liver | (Aslakson and Miller, 1992) |
| Allograft, ectopic (subcutaneous) | Lung | Mouse Lewis lung carcinoma (LLC1) cells (C57B1 mice) | Lungs | (Bertram and Janik, 1980) |
| Xenograft, orthotopic | Mammary | Human MDA-MB-231 cells (NOD/SCID mice) | Lungs, liver, lymph nodes | (Munoz et al., 2006) |
| | | Human SUM1315 cells (NOD/SCID mice) | Lung and human bone implant | (Kuperwasser et al., 2005) |
| Xenograft, orthotopic | Colon | Human HCT116, SW-620, DLD-1 cells (Swiss Nu/Nu) | Peritoneum, diaphragm, lymph nodes, pancreas, liver and lungs | (Céspedes et al., 2007) |
| Xenograft, orthotopic | Melanoma | Human 113/6-4L melanoma cells derived from WM239A (CB17-SCID mice) | Central nervous system | (Cruz-Munoz et al., 2008) |
| PDXs, orthotopic | Mammary | Primary breast tumors and metastases [NOD/SCID mice and NOD/SCID *Il2rg$^{-/-}$* (NSG) mice] | Lung, lymph nodes, peritoneum | (DeRose et al., 2011) |
| PDXs, ectopic (subcutaneous) | Mammary | Primary breast tumors and metastases [NOD/SCID *Il2rg$^{-/-}$* (NSG) mice)] | Lung | (Eyre et al., 2016) |
| PDXs, orthotopic | Cervical | Primary HER2-expressing cervical tumor (athymic nu/nu nude mice) | Lung, lymph nodes, peritoneum, liver | (Hiroshima et al., 2016) |
| PDXs, orthotopic | Colon | Primary colorectal tumors and liver metastases (NOD/SCID mice) | Liver, lung, abdominal cavity | (Puig et al., 2013) |
| PDXs, ectopic (subcutaneous) and orthotopic | Colon | Primary colorectal tumors, peritoneal carcinoses and metastases (Swiss nude and CB17-SCID mice) | Hepatic, splenic, and mesenteric lymph node | (Julien et al., 2012) |
| PDXs, ectopic (intraperitoneal) | Ovarian | Primary ovarian tumors [NOD/SCID *Il2rc$^{null}$* (NSG) mice] | Lung | (Bankert et al., 2011) |
| **Experimental metastasis** | | | | |
| Intra-venous | Mammary | Human MDA-MB-231 cells | Lung | (Minn et al., 2005) |
| | Mammary | Mouse Met-1 cells | Lung | (Qian et al., 2011) |
| | Melanoma | Human A7 and mouse B16 cells | Lung | (Gil-Bernabe et al., 2012) |
| | Melanoma | Mouse B16 cells | Lung | (Hiratsuka et al., 2002, 2006; Kaplan et al., 2005) |
| | Lung | Mouse Lewis lung carcinoma (LLC) cells | Lung | (Hiratsuka et al., 2002, 2006; Kaplan et al., 2005) |
| Intra-cardiac | Mammary | Human MDA-MB-231 cells | Brain | (Bos et al., 2009) |
| | Mammary | Human MDA-MB-231 cells | Bone | (Kang et al., 2003) |
| | Prostate | Mouse RM1 cells | Bone | (Jung et al., 2013) |
| Intra-iliac artery | Mammary | Human MDA-MB-231, MCF-7, MDA-MB-361 cells | Bone | (Wang et al., 2015) |
| Intra-splenic | Colon | Human KM12 cells | Lymph nodes and liver | (Morikawa et al., 1988) |
| Intra-tibial | Prostate | Human PC-3 cells | Bone | (Fisher et al., 2002) |
| Intra-peritoneal | Ovary | Human SKOV3 and ES2 cells +/– adipose-derived mesenchymal stem cells derived from omentum | Mesentery | (Chu et al., 2015) |
| **GEMM** | | | | |
| Spontaneous metastasis | Mammary | MMTV-PyMT | Lungs and lymph nodes | (Guy et al., 1992) |
| Spontaneous metastasis | Mammary | MMTV-*Erbb2* | Lungs and lymph nodes | (Muller et al., 1988) |
| Conditional, Cre-*loxP* | Pancreatic | KPC [Lox-Stop-Lox (LSL)-*Kras$^{G12D}$*; LSL-*Trp53$^{R172H}$*; *Pdx1-Cre*] model | Liver, lung, pleural nodules and peripancreatic lymph node | (Hingorani et al., 2005) |
| Conditional, Cre-*loxP* and Flp-FRT | Pancreatic | *R26$^{CAG-CreERT2}$*; *FSF-R26$^{CAG-CreERT2}$* | Liver and lungs | (Schönhuber et al., 2014) |

promoters and the correct combination of genetic alterations has provided more representative models (Derksen et al., 2006; Hingorani et al., 2003), tumor spread to some metastatic sites has been more difficult to model. For example, it has been challenging to model the development of bone metastases, a common site of secondary lesions in prostate and breast cancer (Rampetsreiter et al., 2011). A second drawback of GEMMs is that in many cases the long latency requires mice to be sacrificed due to primary tumor burden before metastatic lesions have developed. This can be overcome by removal of the primary tumor, after which the subsequent development of metastases can be monitored (Coffelt et al., 2015; Doornebal et al., 2013).

## Applications of mouse models in metastatic research

Despite the limitations discussed above, mouse models have made important contributions to our understanding of cancer progression

Disease Models & Mechanisms (2017) 10, 1061-1074 doi:10.1242/dmm.030403

and metastasis. Here, we highlight some recent advances in which mouse models have been instrumental in defining the key drivers and features of metastatic cancer. We also outline the usefulness of these models as preclinical drug development tools.

### Stromal cell interactions at the primary tumor site

*In vivo* metastasis models are important tools to investigate the interaction of tumor cells with tumor-associated stromal components. Within this complex microenvironment, several immune cell populations have been shown to promote tumor invasion and metastasis (Fig. 2) and GEMMs and syngeneic models, both of which have intact immune systems, have provided many valuable insights into how the immune system regulates metastatic progression. Macrophages are often the most abundant infiltrating immune cells in the tumor. These tumor-associated macrophages (TAMs) (see Glossary, Box 1) play multiple roles in promoting cancer metastasis and are associated with metastasis and poor prognosis (Kitamura et al., 2015; Qian and Pollard, 2010). Intra-vital imaging studies have proven useful in elucidating the complex role of TAMs. In a spontaneous GEMM of mammary cancer, MMTV-PyMT (Table 2), cancer cells invade surrounding tissues together with TAMs (Wyckoff, 2004). In this process, TAMs secrete epidermal growth factor (EGF) to activate the EGF receptor on cancer cells, and enhance their motility and invasive potential by increasing invadopodium formation and ECM degradation (Zhou et al., 2014). Reciprocally, tumor cells produce colony-stimulating factor 1 (CSF1) to recruit and activate TAMs. Ablation of this paracrine signal loop significantly inhibited tumor cell invasion in MMTV-PyMT tumors and subsequent lung metastasis without affecting primary tumor growth (Wang et al., 2009). Intra-vital imaging of MMTV-PyMT tumors has also illustrated that tumor cell intravasation occurs in association with perivascular TAMs

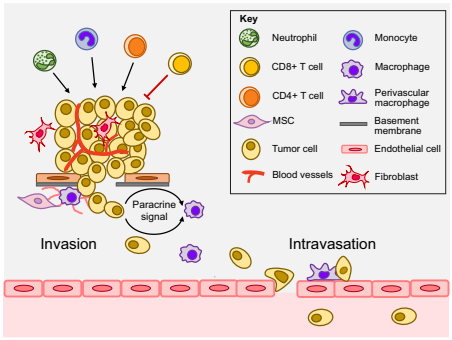


**Fig. 2. Stromal influences in the primary tumor.** Stromal cells such as MSCs, fibroblasts and myeloid cells (including monocytes, macrophages and neutrophils) promote metastasis and modulate the tumor microenvironment. MSCs remodel the ECM and support invasion. Macrophages can promote tumor invasion via several paracrine signaling factors. For example, in response to tumor cell-derived CSF1, TAMs secrete EGF, which is permissive for tumor cell invasion and migration. A subset of $CD4^+$ T cells contributes to tumor progression, while $CD8^+$ T cells mainly mediate anti-tumor immune responses. During intravasation, perivascular macrophages interact with tumor cells directly to help subsequent tumor cells to transit the endothelial barrier and initiate the journey of metastatic dissemination. See Glossary in Box 1 for an explanation of key terms.

(Wyckoff et al., 2007). Via direct interactions, invasive tumor cells, perivascular macrophages and endothelial cells form micro-anatomic structures within the tumor (termed 'tumor microenvironment for metastasis' or 'TMEM') (Pignatelli et al., 2014). The frequency with which these TMEMs occur has been shown to predicate metastasis of $ER^+$ breast cancer in a case-control study with >3700 patient samples (Rohan et al., 2014). These TMEM structures control tumor cell intravasation by transiently increasing local vascular permeability in a vascular endothelial growth factor (VEGF)-dependent manner, as illustrated by recent studies using high-resolution two-photon intra-vital microscopy (Harney et al., 2015). These data strongly indicate that the local tumor microenvironment and macrophage interactions play a central role in promotion of tumor cell intravasation, and highlight the importance of using intra-vital microscopy to visualize these processes.

Neutrophils have also been shown to contribute to invasion and metastasis. Using a combination of GEMM and transplant models of melanoma, UV radiation was shown to promote neutrophil infiltration through secretion of high-mobility group protein B1 (HMGB1) derived from UV-damaged keratinocytes. This neutrophil recruitment led to enhanced tumor migration and invasion resulting in distal metastasis (Bald et al., 2014). More recently, a role for neutrophils in the pre-metastatic niche within the lung was established using the MMTV-PyMT model (Wculek and Malanchi, 2015). This was mediated through secretion of leukotrienes from neutrophils in the pre-metastatic niche, which promoted metastatic formation. In the KPC (Lox-Stop-Lox (LSL)-$Kras^{G12D}$; LSL-$Trp53^{R172H}$; *Pdx1-Cre*) GEMM of pancreatic cancer, where mutations in *Kras* and *Trp53* drive the development of spontaneous pancreatic ductal adenocarcinomas (Gopinathan et al., 2015), neutrophils have also been shown to promote metastasis (Steele et al., 2016).

Among adaptive immune cells, Th2 cells, $CD4^+$ T helper cells expressing Type 2 cytokines [e.g. interleukin (IL) 4, IL10], have been shown to promote tumor progression via activation of humoral immunity and inflammation (Shurin et al., 1999). Using the MMTV-PyMT model, it was found that $CD4^+$ T helper cells can induce alternative activation of TAMs and secretion of EGF, to directly promote tumor invasion and egress from the primary tumor as a result of IL4 activation (DeNardo et al., 2009). By utilizing existing and emerging mouse models, future experiments could uncover the role of other lymphocyte populations in tumor progression and invasion.

Coffelt et al. (2015) used a GEMM of invasive lobular breast cancer, the *K14Cre;* $Cdh1^{F/F}$; $Trp53^{F/F}$ (KEP) model, and transplanted tumor fragments from this KEP model into recipient mice. Metastatic development was monitored following resection of the primary tumor, and the authors observed that systemic expansion of neutrophils significantly promoted spontaneous metastasis to the lungs and lymph nodes by suppressing a $CD8^+$ T cell-mediated anti-tumor immune response (Coffelt et al., 2015). Mechanistically, this involves IL17 expression from γδ T cells that leads to expansion of neutrophils via granulocyte colony stimulating factor (G-CSF). IL17 derived from a subset of $CD4^+$ T helper cells has also been shown to promote anti-tumor immune responses through the recruitment of dendritic cells and cytotoxic cells in several murine tumor models (reviewed in Zou and Restifo, 2010). Thus, the role of IL17 in metastasis may be dependent on the cancer type and/or specific tissue environment.

Cells of mesenchymal origin, most notably mesenchymal stem cells (MSCs) and cancer-associated fibroblasts (CAFs) (see

Glossary, Box 1) can also promote metastasis through direct interaction with tumor cells. For example, MSCs have been shown to promote peritoneal dissemination of ovarian cancer cells via activation of the matrix metalloproteinases (MMPs) MMP2 and MMP9 (Chu et al., 2015). In xenograft and allograft models of prostate cancer, chemokine (C-X-C motif) ligand 16 (CXCL16)/CXC receptor 6 (CXCR6) chemokine signaling promotes recruitment of bone marrow-derived MSCs and their differentiation into CAFs, which in turn promote prostate tumor cell invasion and metastasis through production of chemokines such as CXCL12 (Jung et al., 2013; Mognetti et al., 2013) and chemokine (C-C motif) ligand 5 (CCL5) (Luo et al., 2015). CAF-derived MMPs can promote ECM remodeling and tumor cell invasion (Kalluri and Zeisberg, 2006), and in an orthotopic model of colon cancer, CAFs promote formation of distal metastases through secretion of the glycoprotein stanniocalcin 1 (STC1) which regulates intravasation of the tumor cells (Pena et al., 2013). CAFs can also generate mechanical pressure and paracrine signaling to promote tumor invasion and metastasis (Karagiannis et al., 2012), and through remodeling of the ECM (Kaushik et al., 2016).

In summary, *in vivo* metastasis models have provided important insights into the interactions of tumor and stromal cells that contribute significantly to tumor invasion and metastasis. Of note, only a minority of cancer cells are migratory, as revealed by intra-vital imaging studies across multiple tumor models, even in aggressive tumors (Condeelis et al., 2005; Scheele et al., 2016). Thus, specific interactions of the tumor microenvironment with these migratory tumor cells could be attractive targets to treat metastatic disease.

## Systemic influence on metastasis

The metastatic process is not only influenced by cell-cell interactions within the adjacent primary tumor microenvironment but also systemic alterations induced by the presence of tumor cells. Experimental metastasis assays in tumor-bearing animals have been key in demonstrating that primary tumor-derived systemic factors, such as cytokines and immune cell chemoattractants, can alter metastatic target tissues and influence the subsequent seeding (see Glossary, Box 1) of tumor cells in these tissues (Hiratsuka et al., 2002, 2006; Kaplan et al., 2005). More recently, elegant mouse experiments again using experimental metastasis models have shown that tumor-derived exosomes (see Glossary, Box 1) induce pro-metastatic progenitor cells in the bone marrow through receptor tyrosine kinase MET signaling (Peinado et al., 2012), and that exosomal integrins (see Glossary, Box 1) can direct organ-specific colonization by priming the metastatic niche (Box 2) (Hoshino et al., 2015). Such advances will impact on how we can harness the ability to measure specific systemic factors in clinical samples to allow more careful monitoring of tumor progression.

Systemic influences can also promote colonization after metastatic seeding. For example, a study using an esophageal cancer model showed that lung metastatic colonization (following tail vein injection of tumor cells) can be significantly promoted by distal tumors in an insulin growth factor (IGF)-II-dependent manner (Li et al., 2014). Using a xenograft model in which human breast cancer cell lines with different tumorigenic potential were injected contralaterally into the same mouse, pro-angiogenic cytokines secreted by human luminal breast cancer cells have been shown to mobilize pro-angiogenic vascular endothelial growth factor receptor 2 $(VEGFR2)^{+}$ bone marrow-derived cells into distal tumors to promote angiogenesis (Kuznetsov et al., 2012). However, systemic influences can also be anti-metastatic. Using human prostate and breast cancer cells, and a combination of spontaneous and experimental metastasis models, an earlier study suggested that the presence of a primary tumor can inhibit metastatic seeding. This was mediated through secretion of prosaposin (a precursor of saposins, which function as cofactors for sphingolipid hydrolases), which stimulates expression of the angiogenic factor thrombospondin-1 in lung stromal cells (Kang et al., 2009). Thus, models that faithfully mimic systemic influences in patients are required to better understand the influence of secreted factors on metastasis.

Immune rejection is a key factor that limits the efficiency of tumor engraftment in immune-competent preclinical models, even when the tumor and host are both from the same syngeneic background (Dunn et al., 2006). It is probably not surprising that immune suppression generated by established tumors enhances engraftment efficiency of subsequent (secondary) tumors (Mullen et al., 1985; Reilly et al., 2000). Careful experiment design is essential to study tumor-tumor and tumor-host interaction in these models.

## Role of epithelial-to-mesenchymal transition in metastasis

Epithelial-to-mesenchymal transition (EMT) (see Glossary, Box 1) is a developmental program that occurs during embryogenesis (Thiery et al., 2009). It involves the loss of cell-cell adhesions, apical-basal polarity and the conversion to a mesenchymal phenotype that is typified by increased motility and invasiveness and plays a role in the invasion of tumor cells, an early event in the metastatic cascade (Valastyan and Weinberg, 2011). It is tightly controlled by a number of pathways that activate the EMT transcription factors Snail, Slug, Twist, Zeb1 and Zeb2 (Thiery et al., 2009). However, there is debate concerning the extent to which EMT contributes to the different stages of the metastatic cascade, much of which has arisen from difficulties in demonstrating that mesenchymal cells persist in metastatic lesions (Lambert et al., 2017; Yeung and Yang, 2017). This is confounded by the inherent plasticity exhibited by tumor cells and the reversibility of the EMT program. Since the use of Cre recombinase technology has become more prevalent, the opportunity to study EMT in mouse models and address these issues has advanced greatly. Prior to this, GEMMs to address the causal connection between EMT and metastasis implicated in *in vitro* studies were lacking.

Utilizing Cre recombinase to perform lineage-tracing experiments has provided useful insights into the contribution of EMT to the metastatic process (Fig. 3). One such study involved the widely used KPC model. In these mice, EMT was identified in premalignant lesions, and the process was found to be associated with invasion of the surrounding basement membrane (Rhim et al., 2012). In addition, inflammation enhanced EMT and entry of tumor cells into the circulation. However, using the same KPC model, direct involvement of EMT in the metastatic process was not supported; conditional deletion of *Snai1* or *Twist1*, the genes that encode Snail and Twist, respectively, in the primary tumor resulted in a reduced number of cells undergoing EMT, but this had no impact on the metastatic spread (Zheng et al., 2015). More recently, it was shown that loss of Zeb1 in the KPC model is sufficient to significantly reduce metastatic spread (Krebs et al., 2017). This highlights the specificity and lack of redundancy between EMT transcription factors in controlling metastatic spread in this model.

Using mammary tumor models driven by MMTV-PyMT or human epidermal growth factor receptor 2 (HER2) oncogenes, Fischer and colleagues also established that EMT and metastasis might not be as intricately linked as first thought (Fischer et al., 2015). By using a mesenchymal-specific (Fsp1) promoter to drive

Disease Models & Mechanisms (2017) 10, 1061-1074 doi:10.1242/dmm.030403

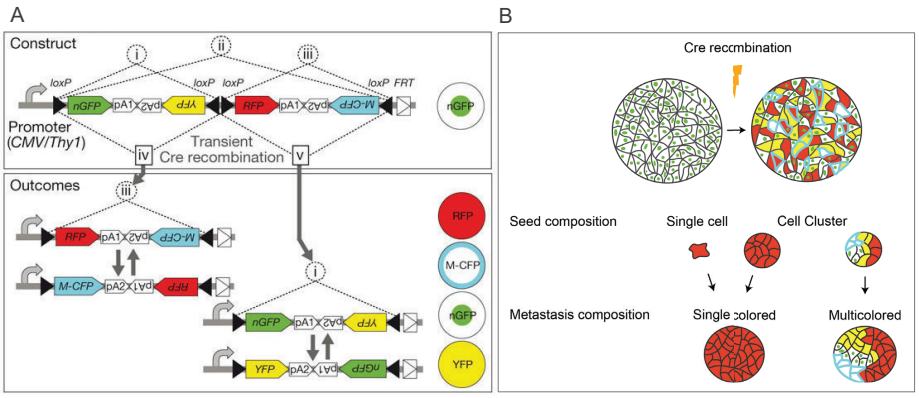


**Fig. 3. Lineage tracing allows identification of the clonal nature of metastatic lesions.** (A) The *Brainbow-2.1* construct contains two tandem invertible DNA segments, each flanked by *loxP* sequences (indicated with black arrowheads). Inversion (i-iii) and excision (iv,v) recombination events create four expression possibilities, with the fluorescent protein that follows the promoter being uniquely expressed. Expression of the different fluorescent proteins at different ratios within each cell provides a unique color combination for each cell. Adapted from Livet et al. (2007), with permission from Macmillan Publishers Ltd. (B) Cre-mediated recombination during primary tumorigenesis allows identification of metastatic lesions of a single color, indicating derivation from single cells or clusters from a single cell, or multicolored cell clusters consisting of many different colored cells.

Cre recombinase-dependent expression of a green fluorescent protein (GFP) reporter, they observed no enrichment of tumor cells expressing GFP in the metastatic site, and thus no indication of an EMT, although there was an enrichment of GFP-expressing CTCs. A key limitation of this study is the reliance on a single 'EMT-associated' promoter to drive the Cre recombinase, as EMT is controlled and characterized by a plethora of transcriptional changes. In addition, it does not address the inherent plasticity and reversibility within the system: EMT does not represent an on-off switch but is a continuum with many cells expressing both epithelial and mesenchymal markers at a given time. Indeed, in a model of HER2-driven mammary cancer, early dissemination of tumor cells was associated with a partial EMT, wherein some epithelial cell properties were retained (Harper et al., 2016).

The use of intra-vital imaging has helped unravel the complexities associated with tumor cell plasticity and metastatic spread. In the MMTV-PyMT mammary tumor model, Beerling and colleagues used a fluorescent epithelial marker (E-cadherin-CFP) combined with intra-vital imaging to show that EMT is a reversible, plastic process and that mesenchymal cells that reach secondary sites can rapidly regain an epithelial phenotype (Beerling et al., 2016). In contrast with many other studies, it was possible to demonstrate this plasticity *in vivo* without experimental modulation of genes commonly thought to regulate EMT. Models that are able to accurately recapitulate the metastatic cascade without experimental gene modulation are key tools in uncovering the events involved, but in a way that reflects *in situ* processes as closely as possible. The use of lineage tracing to assess the contribution of EMT to metastasis has the potential to help uncover the gene signature of cells that are able to colonize secondary sites.

### Unraveling the polyclonal nature of metastasis

The increasing use of deep-sequencing analysis has helped elucidate the evolutionary history of metastatic lesions and has shed light on whether metastatic dissemination follows a linear or parallel model (Turajlic and Swanton, 2016). Evidence from a HER2-driven mouse mammary tumor model supports a parallel model of evolution and also highlights the importance of mouse models in demonstrating that early disseminated tumor cells are critical to the formation of metastatic lesions (Hosseini et al., 2016). Lineage tracing of CTCs and clusters of CTCs has also proven invaluable in the investigation of the origins of these clusters and single cells. By using a convertible double-fluorescent mammary tumor model, *ROSA*$^{mT/mG}$*; MMTV-PyMT*, from which organoids (see Glossary, Box 1) were injected into the mammary fat pad of nonfluorescent hosts, Cheung et al. (2016) evidenced the polyclonal origin of a lesion in the lung, showing that it contained at least two separate clones based on the fluorescent reporters present. They found multicolored cell clusters at all stages of the metastatic cascade, including local disseminated and CTC clusters. The advent of Brainbow-2.1 (Livet et al., 2007) has allowed the detailed tracing of multiple cells by utilizing Cre recombinase and the stochastic expression of four fluorescent proteins from multiple copies of a single transgene, which can generate up to 90 distinguishable colors when multiple copies of Brainbow-2.1 are present per cell, due to the differential expression of each transgene (Fig. 3). By combining the transgene with Cre recombinase placed under tissue-specific promoters, it will be possible to more fully assess the clonal heterogeneity of a metastatic lesion using imaging alone (Fig. 3) or in combination with deep-sequencing techniques. One such example of this is Prorainbow, a novel fluorescently labeled mouse strain (*PB-Cre4;* *Pkd1*$^{lox/lox}$*;* *Pten*$^{lox/lox}$*;* *CMV-XFP/+*) that can be used to model prostate cancer (Fang et al., 2015). Although this model has not yet been used to look at the metastatic process, initial characterization indicates that it is an extremely promising advance in technology to allow assessment of metastatic colonization in many different mouse models.

### Arrest, extravasation and colonization at distant organs

Experimental metastasis assays have illustrated that multiple stromal components can be hijacked by tumor cells in the process of metastatic seeding, as detailed below. Platelets play an important role in facilitating metastatic dissemination. In addition to protecting cells in the bloodstream from natural killer (NK) cells, interaction of platelet integrins with collagen at specific regions of the endothelium may help tumor cell adherence at secondary organs and determine the site of metastatic tumor cell extravasation (Gay and Felding-Habermann, 2011; Ruggeri and Mendolicchio, 2007). A recent study identified that platelets promote tumor cell extravasation through adenosine triphosphate (ATP)-dependent activation of the endothelial P2Y2 receptor, which opens the vessel barrier to enable tumor cell extravasation and metastatic seeding (Schumacher et al., 2013). This was identified by utilizing both spontaneous and experimental metastasis models in syngeneic C57BL/6J mice. The utility of experimental metastasis models in studying these early events when tumor cells first reach the metastatic site was further highlighted by another group, who were able to show that metastatic seeding is promoted by coagulation pathways, in particular tissue factor (TF). By imaging myeloid-tumor cell interactions within the lung following intravenous injection of tumor cells, they demonstrated that TF-induced platelet clots attract recruitment of bone marrow-derived macrophages to support the survival of metastatic melanoma cells and inhibit NK cell-mediated destruction of micrometastases in the lung (Gil-Bernabe et al., 2012).

Using both spontaneous and experimental lung metastasis models of breast cancer, a distinct population of metastasis-associated macrophages (MAMs) has been characterized in the target organ (lung). Depletion of these MAMs using transgenic CD11b-diphtheria toxin receptor (DTR) mice significantly reduces metastatic seeding and persistent growth of breast cancer cells (Qian et al., 2011). One caveat of this approach is that administration of diphtheria toxin to CD11b-DTR mice selectively kills CD11b-expressing monocytes as well as macrophages (Stoneman et al., 2007). However, *ex vivo* intact lung imaging in the same model revealed that macrophages (and not monocytes) directly contact the extravasating tumor cells, and depletion of these macrophages significantly reduces the number of tumor cells that complete extravasation (Qian et al., 2009).

Adhesion signaling also plays an important role in the survival of tumor cells within the metastatic niche. Using an innovative method of experimental bone metastasis in which breast cancer cells were injected into the iliac artery of mice (both allograft and xenograft models), Wang et al. (2015) showed that bone seeding of multiple human and murine breast cancer cells is dependent on heterotypic adherens junctions between cancer cells and osteogenic cells. Thus, a number of models and experimental approaches have demonstrated the importance of the interaction of tumor cells with stromal cells in the metastatic niche that is required to support the outgrowth of secondary tumors.

### Dormancy in the metastatic niche

Metastases can arise from DTCs many years after the initial treatment and/or surgical removal of the primary tumor. This is because at the time of diagnosis, metastatic spread has already occurred but the resulting DTCs have entered a state of quiescence (Sosa et al., 2014). These metastases may be resistant to current therapies that are directed at proliferating cells; therefore, targeting dormant DTCs or preventing their reactivation from dormancy may be of clinical benefit. The factors that control tumor dormancy are poorly understood, but using a spontaneous model of breast cancer metastasis, DTCs were found to reside on the microvasculature of different organs and subsequent *in vitro* experiments demonstrated that distinct endothelial niches can induce dormancy through the secretion of thrombospondin-1 (Ghajar et al., 2013). A gain-of-function screen in an allograft model of mouse mammary carcinoma identified the bone morphogenetic protein (BMP) inhibitor Coco as a mediator of DTC reactivation (Gao et al., 2012). Coco stimulated the proliferation of DTC in the lungs through induction of a discrete gene expression signature that was associated with relapse to the lung but not to other organs where BMP is not active. This highlights the organ specificity of signals that control reactivation of DTCs in the metastatic niche. Bragado et al. (2013) provided further support to this by tracing spontaneous DTCs following subcutaneous transplantation of a head and neck squamous cell carcinoma cell line. They showed that transforming growth factor beta 2 (TGFβ2) signaling in the bone marrow initiates tumor dormancy, while the low levels of TGFβ2 signaling found in the lungs prevented long-term dormancy, resulting in outgrowth of metastatic lesions (Bragado et al., 2013). These studies support the concept of dormancy-permissive and -restrictive microenvironments that determine whether DTCs divide or remain quiescent. The collection and analysis of CTCs and DTCs from patients at different stages of the metastatic journey will provide important information and clinical validation of the functional regulators linked to the emergence of overt metastatic disease. This should provide an iterative framework for the further refinement of mouse models.

### Therapeutics and translation

Although mouse models have been invaluable in enhancing our understanding of the biology that drives the metastatic cascade, their utility as preclinical drug development tools is less well defined. The approval rate of oncology drugs remains poor, with recent research indicating that only 7.5% of oncology drugs that entered phase I clinical development, and 33.2% of drugs that entered phase III trials, were eventually approved (Toniatti et al., 2014). This highlights the need for more predictive and improved preclinical mouse models. The majority of preclinical studies that support clinical evaluation rely on the use of established cell lines grown ectopically in immune-deficient mice. These cell lines show limited tumor heterogeneity, and combined with the lack of appropriate human stroma and an intact immune system (Table 1), this contributes to the poor clinical predictivity of these models (Singh and Ferrara, 2012; Toniatti et al., 2014). In most studies, regression of primary tumor growth is used as an endpoint and no consideration is given to effects on metastatic disease (in most cases metastatic disease is not even modeled). By contrast, the majority of early clinical trials will involve patients with advanced metastatic disease and as the genetic and epigenetic landscape of metastases differ from the primary tumor, which is reflected in the response to treatment, identifying the most effective way to model this will have an impact on drug development programs. The ability to model this in preclinical models is challenging, but the resistance of metastatic disease to current therapies and the realization that >90% of cancer-related mortality is due to metastatic disease progression highlights the need for new approaches to be considered. In addition to developing improved models, a better understanding of how best to implement currently available models could provide benefits (Francia et al., 2011; Steeg, 2016). For example, experimental metastasis models have been used widely, but what needs to be considered is the cell population that is being targeted in these models. Do they reflect the outgrowth of latent tumor cells or the subsequent growth of macrometastatic lesions?

Such nuances are currently difficult to address in most models and are not often considered when carrying out drug intervention studies.

Despite the limitations associated with the use of established cell lines in immune-deficient animals, they can provide important insights into the potential clinical activity of drugs, for which differential responses to therapies have been reported between primary and metastatic lesions, thus reflecting what is seen in the clinic (Francia et al., 2011). Another important consideration is how closely we can recapitulate clinically relevant intervention strategies. Surgical removal of the primary tumor followed by adjuvant treatment to prevent recurrence is widely used in clinical practice. Spontaneous metastasis models that utilize cell lines (xenograft, allograft) are particularly amenable to modeling adjuvant treatments, although they are limited to a few models where the primary tumor can be easily resected (e.g. Cruz-Munoz et al., 2008; Ebos et al., 2009). Although these experiments can be technically challenging and time-consuming, they have provided useful insight into the activity of drugs in the clinical setting. For example, studies with transplantable models have helped to unravel the effects of anti-angiogenic therapies in the adjuvant setting (Kerbel et al., 2013) and shed light on the possible mechanisms responsible for the disappointing results of recent Phase III clinical trials in metastatic breast cancer (Bridgeman et al., 2017).

The benefits of GEMMs in generating tumors that develop in the organ of origin (autochthonous) in immune competent hosts has led to their adoption for preclinical assessment of drug response and mechanisms of resistance (Gopinathan et al., 2015; van Miltenburg and Jonkers, 2012). GEMMs are very useful for studying early and late stages of disease, and studies showing the clinical predictivity of lung and pancreatic cancer GEMMs to chemotherapy are encouraging (Singh et al., 2010), but this needs to be more widely validated in other models and the impact on metastatic disease evaluated. These models are often limited by growth of the primary tumor, which necessitates cull of the animals and thus true effects on metastasis-associated survival cannot be monitored (Karim et al., 2013). Most GEMMs are not amenable to resection of the primary tumor and thus dissecting effects on primary tumor growth from specific effects on metastatic disease are complicated, as neoadjuvant and adjuvant studies cannot be carried out although excision of primary pancreatic tumors in the KPC model is being trialed (Gopinathan et al., 2015). In addition, in the context of mammary tumors, the development of transplantation models in which fragments of tumors are re-implanted into recipient mice allows resection of the primary tumor and the subsequent monitoring of metastatic spread. This reduces the latency and variability in metastatic dissemination making this approach more amenable to drug studies. This opens up the possibility of using these models for testing adjuvant therapies and importantly for assessing the potential of new immunotherapies (Coffelt et al., 2015).

PDX models are also predicted to be a major advance in preclinical testing platforms as they recapitulate the tumor heterogeneity that plays such an important role in tumor biology, including response to therapy. A number of therapeutic studies have demonstrated their value in linking response with genetic alterations and identifying mechanisms of resistance and biomarkers, while use of humanized mice recipients will further enhance their value as we look at the potential for testing immunotherapies (Byrne et al., 2017). However, the cost and length of time required to conduct studies in PDX models is restrictive and, as yet, their utility in assessing effects on metastatic spread is not clear. Although spontaneous metastases do develop, this is limited to a relatively small number of PDX models, with orthotopic injection of tumor fragments being more successful in modeling metastatic spread (Pompili et al., 2016). Moreover, the asynchronous development of metastatic disease in these models would require large cohorts of animals, which further increases the cost of such studies. Generation of PDX from primary tumors and metastatic sites from the same patient that can be transplanted orthotopically would allow direct evaluation of drugs in the metastatic setting.

The increasing use of imaging modalities that allow noninvasive longitudinal monitoring of metastases will help more accurate detection and quantification of metastatic disease in deep tissue sites. This technology is thus likely to enhance the usability of GEMMs and PDXs. Recent advances in preclinical magnetic resonance imaging (MRI), computed tomography (CT), positron emission tomography (PET) and single-photon emission computed tomography (SPECT) are showing promise (Fleten et al., 2017; Marien et al., 2017; Sanches et al., 2015; Taromi et al., 2016).

A greater understanding of the pathways that drive metastatic spread and what is achievable in the clinical setting gives hope that anti-metastatic therapies will be viable in the future. For example, targeting metastatic colonization, which is often the rate-limiting step in the metastatic cascade holds great potential, but it will be important to provide robust preclinical evidence of activity in appropriate animal models that accurately reflect the clinical scenario in which the therapy will ultimately be tested in. Careful thought to clinical trial design with appropriate primary endpoints is also essential.

## Future outlook

Mouse models have been essential in advancing our understanding of the biological processes that drive tumor progression. However, metastatic cancer remains the main cause of cancer-related deaths, with new treatments desperately needed. Increasing our understanding of what drives metastatic spread is key to achieving this goal. This will require the further development and refinement of mouse models to more faithfully mimic human disease and progression.

A number of technological advances have allowed the further development of GEMMs. These include combined use of the Cre-*loxP* and Flp-FRT systems (Schönhuber et al., 2014) that allow sequential activation or inactivation of genes, thereby enabling human disease progression to be mimicked more closely, which may provide more representative metastatic progression models. This also opens up the possibility of targeting both tumor and stromal cells in the same model, which is an important consideration when studying metastatic progression. In addition, the CRISPR/Cas9 gene editing system (see Glossary, Box 1) has been used to successfully introduce targeted mutations in GEMMs, enabling more rapid validation and characterization of putative cancer genes that are being uncovered by the large-scale sequencing efforts currently underway using human tissue samples (Annunziato et al., 2016; Chiou et al., 2015; Sánchez-Rivera et al., 2014; Weber et al., 2015). It is hoped that this will help in the design of better GEMMs that more readily recapitulate the metastatic tropism seen in human disease. The development of humanized mouse models that incorporate human-derived stromal components, including CAFs and immune cell populations, will help with regards to metastasis to particular sites (Shultz et al., 2012). For example, human bone discs and engineered human bone environments have been used to model bone metastases (Holen et al., 2015; Wright et al., 2016). RNA interference and CRISPR/Cas9 screens have been used to identify metastatic drivers in *in vivo* transplantation models (Chen et al., 2015; Murugaesu et al., 2014); the validation of these and

improvements in such screening approaches will help in the development of future GEMMs.

The design of more biologically relevant *in vitro* models that try to recapitulate the complexity of the tumor microenvironment is a major area of ongoing research. Models include co-culture of tumor cells with different stromal cell types and 3D engineered matrixes, with developments in 3D bioprinting and microfluidics platforms having the potential to significantly impact on the design and reconstruction of the complex tumor microenvironment (Albritton and Miller, 2017). Coupled with the use of high-resolution real-time imaging, microfluidics devices have been used to study different components of the metastatic cascade such as intra- and extravasation (Jeon et al., 2015; Zervantonakis et al., 2012). The design of these models could be geared towards addressing specific questions about the biology that drives metastatic behavior. Importantly, such *in vitro* models have the potential to be used as drug screening platforms and could guide the preclinical testing of new agents in mouse models.

Advances in intra-vital imaging have shown great potential for elucidation of the close interplay between tumor and host cells (Cuccarese et al., 2017; Hawkins et al., 2016; Headley et al., 2016; Lee et al., 2015; Szulczewski et al., 2016), and fundamental aspects of the metastatic process. For example, use of a Cre recombinase-driven reporter system has allowed the visualization of extracellular vesicle exchange between tumor cells and has provided further insight into the biological consequences and potential impact on metastatic potential (Zomer et al., 2015). The use of optical windows to allow imaging in the metastatic niche provides both spatial and temporal information on the behavior of cancer cells; another major advance (Entenberg et al., 2015; Headley et al., 2016; Ritsma et al., 2012; Rodriguez-Tirado et al., 2016). The ability of such imaging approaches to shed light on the localization and activity of drugs within the tumor microenvironment (Dubach et al., 2016; Junankar et al., 2015; Tipping et al., 2016) also provides a more sophisticated platform for evaluation of new therapies.

Although much is known about the biological pathways that control the individual steps in the metastatic cascade, a number of important questions remain. Uncovering the underlying mechanisms that govern the enormous diversity in the onset and target organs affected in patients and identifying whether there are common mechanisms at play will be important. In addition, understanding the fundamental differences between primary and secondary tumors and the drivers of metastatic colonization is essential to identifying strategies for targeting metastatic disease, and would have a major impact on the survival of cancer patients. The technological advances in the generation of mouse models that better mimic human disease, combined with advances in imaging, will allow for the translation of such research into meaningful treatments.

**Competing interests**

The authors declare no competing or financial interests.

**Funding**

L.G.-C. is supported by a Cancer Research UK Edinburgh Centre training grant (C157/A25186). N.T. is funded by a Medical Research Council (MRC) training grant (MR/K50080X/1). R.M. is partially funded by a University of Edinburgh Global Research Scholarship. B.Q. is partially funded by a Cancer Research UK Career Development Fellowship (C49791/A17367) and a European Research Council Starting Grant (716379). Part of the work was undertaken in the MRC Centre for Reproductive Health, which is funded by a MRC Centre grant (MR/N022556/1). V.G.B. is partially funded by Cancer Research UK (C157/A15703) and the European Research Council (29440).

**References**

**Albritton, J. L. and Miller, J. S.** (2017). 3D bioprinting: improving *in vitro* models of metastasis with heterogeneous tumor microenvironments. *Dis. Model. Mech.* **10**, 3-14.

**Alix-Panabierès, C. and Pantel, K.** (2013). Circulating tumor cells: liquid biopsy of cancer. *Clin. Chem.* **59**, 110-118.

**Annunziato, S., Kas, S. M., Nethe, M., Yücel, H., Del Bravo, J., Pritchard, C., Bin Ali, R., van Gerwen, B., Siteur, B., Drenth, A. P. et al.** (2016). Modeling invasive lobular breast carcinoma by CRISPR/Cas9-mediated somatic genome editing of the mammary gland. *Genes Dev.* **30**, 1470-1480.

**Aslakson, C. J. and Miller, F. R.** (1992). Selective events in the metastatic process defined by analysis of the sequential dissemination of subpopulations of a mouse mammary tumor. *Cancer Res.* **52**, 1399-1405.

**Bald, T., Landsberg, J., Lopez-Ramos, D., Renn, M., Glodde, N., Jansen, P., Gaffal, E., Steitz, J., Tolba, R., Kalinke, U. et al.** (2014). Immune cell-poor melanomas benefit from PD-1 blockade after targeted type I IFN activation. *Cancer Discov.* **4**, 674-687.

**Bankert, R. B., Balu-Iyer, S. V., Odunsi, K., Shultz, L. D., Kelleher, R. J., Barnas, J. L., Simpson-Abelson, M., Parsons, R. and Yokota, S. J.** (2011). Humanized mouse model of ovarian cancer recapitulates patient solid tumor progression, ascites formation, and metastasis. *PLoS ONE* **6**, e24420.

**Beerling, E., Seinstra, D., de Wit, E., Kester, L., van der Velden, D., Maynard, C., Schäfer, R., van Diest, P., Voest, E., van Oudenaarden, A. et al.** (2016). Plasticity between epithelial and mesenchymal states unlinks EMT from metastasis-enhancing stem cell capacity. *Cell Rep.* **14**, 2281-2288.

**Bertram, J. S. and Janik, P.** (1980). Establishment of a cloned line of Lewis Lung Carcinoma cells adapted to cell culture. *Cancer Lett.* **11**, 63-73.

**Bos, P. D., Zhang, X. H.-F., Nadal, C., Shu, W., Gomis, R. R., Nguyen, D. X., Minn, A. J., van de Vijver, M. J., Gerald, W. L., Foekens, J. A. et al.** (2009). Genes that mediate breast cancer metastasis to the brain. *Nature* **459**, 1005-1009.

**Bragado, P., Estrada, Y., Parikh, F., Krause, S., Capobianco, C., Farina, H. G., Schewe, D. M. and Aguirre-Ghiso, J. A.** (2013). TGF-β2 dictates disseminated tumour cell fate in target organs through TGF-β-RIII and p38α/β signalling. *Nat. Cell Biol.* **15**, 1351-1361.

**Bridgeman, V. L., Vermeulen, P. B., Foo, S., Bilecz, A., Daley, F., Kostaras, E., Nathan, M. R., Wan, E., Frentzas, S., Schweiger, T. et al.** (2017). Vessel co-option is common in human lung metastases and mediates resistance to anti-angiogenic therapy in preclinical lung metastasis models. *J. Pathol.* **241**, 362-374.

**Byrne, A. T., Alférez, D. G., Amant, F., Annibali, D., Arribas, J., Biankin, A. V., Bruna, A., Budinská, E., Caldas, C., Chang, D. K. et al.** (2017). Interrogating open issues in cancer precision medicine with patient-derived xenografts. *Nat. Rev. Cancer* **17**, 254-268.

**Cassidy, J. W., Caldas, C. and Bruna, A.** (2015). Maintaining tumor heterogeneity in patient-derived tumor xenografts. *Cancer Res.* **75**, 2963-2968.

**Céspedes, M. V., Espina, C., García-Cabezas, M. A., Trias, M., Boluda, A., Gómez del Pulgar, M. T., Sancho, F. J., Nistal, M., Lacal, J. C. and Mangues, R.** (2007). Orthotopic microinjection of human colon cancer cells in nude mice induces tumor foci in all clinically relevant metastatic sites. *Am. J. Pathol.* **170**, 1077-1085.

**Chen, S., Sanjana, N. E., Zheng, K., Shalem, O., Lee, K., Shi, X., Scott, D. A., Song, J., Pan, J. Q., Weissleder, R. et al.** (2015). Genome-wide CRISPR screen in a mouse model of tumor growth and metastasis. *Cell* **160**, 1246-1260.

**Cheung, K. J., Padmanaban, V., Silvestri, V., Schipper, K., Cohen, J. D., Fairchild, A. N., Gorin, M. A., Verdone, J. E., Pienta, K. J., Bader, J. S. et al.** (2016). Polyclonal breast cancer metastases arise from collective dissemination of keratin 14-expressing tumor cell clusters. *Proc. Natl. Acad. Sci. USA* **113**, E854-E863.

**Chiang, S. P. H., Cabrera, R. M. and Segall, J. E.** (2016). Tumor cell intravasation. *Am. J. Physiol. Cell Physiol.* **311**, C1-C14.

**Chiou, S.-H., Winters, I. P., Wang, J., Naranjo, S., Dudgeon, C., Tamburini, F. B., Brady, J. J., Yang, D., Grüner, B. M., Chuang, C.-H. et al.** (2015). Pancreatic cancer modeling using retrograde viral vector delivery and in vivo CRISPR/Cas9-mediated somatic genome editing. *Genes Dev.* **29**, 1576-1585.

**Chu, Y., Tang, H., Guo, Y., Guo, J., Huang, B., Fang, F., Cai, J. and Wang, Z.** (2015). Adipose-derived mesenchymal stem cells promote cell proliferation and invasion of epithelial ovarian cancer. *Exp. Cell Res.* **337**, 16-27.

**Coffelt, S. B., Kersten, K., Doornebal, C. W., Weiden, J., Vrijland, K., Hau, C.-S., Verstegen, N. J. M., Ciampricotti, M., Hawinkels, L. J. A. C., Jonkers, J. et al.** (2015). IL-17-producing γδ T cells and neutrophils conspire to promote breast cancer metastasis. *Nature* **522**, 345-348.

**Condeelis, J., Singer, R. H. and Segall, J. E.** (2005). THE GREAT ESCAPE: when cancer cells hijack the genes for chemotaxis and motility. *Annu. Rev. Cell Dev. Biol.* **21**, 695-718.

**Cruz-Munoz, W., Man, S., Xu, P. and Kerbel, R. S.** (2008). Development of a preclinical model of spontaneous human melanoma central nervous system metastasis. *Cancer Res.* **68**, 4500-4505.

**Cuccarese, M. F., Dubach, J. M., Pfirschke, C., Engblom, C., Garris, C., Miller, M. A., Pittet, M. J. and Weissleder, R.** (2017). Heterogeneity of macrophage infiltration and therapeutic response in lung carcinoma revealed by 3D organ imaging. *Nat. Commun.* **8**, 14293.

**DeNardo, D. G., Barreto, J. B., Andreu, P., Vasquez, L., Tawfik, D., Kolhatkar, N. and Coussens, L. M.** (2009). CD4+ T cells regulate pulmonary metastasis of mammary carcinomas by enhancing protumor properties of macrophages. *Cancer Cell* **16**, 91-102.

**Derksen, P. W. B., Liu, X., Saridin, F., van der Gulden, H., Zevenhoven, J., Evers, B., van Beijnum, J. R., Griffioen, A. W., Vink, J., Krimpenfort, P. et al.** (2006). Somatic inactivation of E-cadherin and p53 in mice leads to metastatic lobular mammary carcinoma through induction of anoikis resistance and angiogenesis. *Cancer Cell* **10**, 437-449.

**DeRose, Y. S., Wang, G., Lin, Y.-C., Bernard, P. S., Buys, S. S., Ebbert, M. T. W., Factor, R., Matsen, C., Milash, B. A., Nelson, E. et al.** (2011). Tumor grafts derived from women with breast cancer authentically reflect tumor pathology, growth, metastasis and disease outcomes. *Nat. Med.* **17**, 1514-1520.

**Donehower, L. A., Harvey, M., Slagle, B. L., McArthur, M. J., Montgomery, C. A., Butel, J. S. and Bradley, A.** (1992). Mice deficient for p53 are developmentally normal but susceptible to spontaneous tumours. *Nature* **356**, 215-221.

**Doornebal, C. W., Klarenbeek, S., Braumuller, T. M., Klijn, C. N., Ciampricotti, M., Hau, C.-S., Hollmann, M. W., Jonkers, J. and de Visser, K. E.** (2013). A preclinical mouse model of invasive lobular breast cancer metastasis. *Cancer Res.* **73**, 353-363.

**Dubach, J. M., Kim, E., Yang, K., Cuccarese, M., Giedt, R. J., Meimetis, L. G., Vinegoni, C. and Weissleder, R.** (2016). Quantitating drug-target engagement in single cells in vitro and in vivo. *Nat. Chem. Biol.* **13**, 168-173.

**Dunn, G. P., Koebel, C. M. and Schreiber, R. D.** (2006). Interferons, immunity and cancer immunoediting. *Nat. Rev. Immunol.* **6**, 836-846.

**Ebos, J. M. L., Lee, C. R., Cruz-Munoz, W., Bjarnason, G. A., Christensen, J. G. and Kerbel, R. S.** (2009). Accelerated metastasis after short-term treatment with a potent inhibitor of tumor angiogenesis. *Cancer Cell* **15**, 232-239.

**Entenberg, D., Rodriguez-Tirado, C., Kato, Y., Kitamura, T., Pollard, J. W. and Condeelis, J.** (2015). In vivo subcellular resolution optical imaging in the lung reveals early metastatic proliferation and motility. *IntraVital* **4**, 1-11.

**Eyre, R., Alférez, D. G., Spence, K., Kamal, M., Shaw, F. L., Simões, B. M., Santiago-Gómez, A., Sarmiento-Castro, A., Bramley, M., Absar, M. et al.** (2016). Patient-derived mammosphere and xenograft tumour initiation correlates with progression to metastasis. *J. Mammary Gland Biol. Neoplasia.* **21**, 99-109.

**Fang, X., Gyabaah, K., Nickkholgh, B., Cline, J. M. and Balaji, K. C.** (2015). Novel in vivo model for combinatorial fluorescence labeling in mouse prostate. *Prostate* **75**, 988-1000.

**Fidler, I. J.** (1973). Selection of successive tumour lines for metastasis. *Nat. New Biol.* **242**, 148-149.

**Fischer, K. R., Durrans, A., Lee, S., Sheng, J., Li, F., Wong, S. T. C., Choi, H., El Rayes, T., Ryu, S., Troeger, J. et al.** (2015). Epithelial-to-mesenchymal transition is not required for lung metastasis but contributes to chemoresistance. *Nature* **527**, 472-476.

**Fisher, J. L., Schmitt, J. F., Howard, M. L., Mackie, P. S., Choong, P. F. and Risbridger, G. P.** (2002). An in vivo model of prostate carcinoma growth and invasion in bone. *Cell Tissue Res.* **307**, 337-345.

**Fleten, K. G., Bakke, K. M., Mælandsmo, G. M., Abildgaard, A., Redalen, K. R. and Flatmark, K.** (2017). Use of non-invasive imaging to monitor response to aflibercept treatment in murine models of colorectal cancer liver metastases. *Clin. Exp. Metastasis* **34**, 51-62.

**Francia, G., Cruz-Munoz, W., Man, S., Xu, P. and Kerbel, R. S.** (2011). Mouse models of advanced spontaneous metastasis for experimental therapeutics. *Nat. Rev. Cancer* **11**, 135-141.

**Friedl, P. and Alexander, S.** (2011). Cancer invasion and the microenvironment: plasticity and reciprocity. *Cell* **147**, 992-1009.

**Gao, H., Chakraborty, G., Lee-Lim, A. P., Mo, Q., Decker, M., Vonica, A., Shen, R., Brogi, E., Brivanlou, A. H. and Giancotti, F. G.** (2012). The BMP inhibitor coco reactivates breast cancer cells at lung metastatic sites. *Cell* **150**, 764-779.

**Gay, L. J. and Felding-Habermann, B.** (2011). Contribution of platelets to tumour metastasis. *Nat. Rev. Cancer* **11**, 123-134.

**Gay, L. J. and Malanchi, I.** (2017). The sleeping ugly: tumour microenvironment's act to make or break the spell of dormancy. *Biochim. Biophys. Acta Rev. Cancer* **1868**, 231-238.

**Ghajar, C. M., Peinado, H., Mori, H., Matei, I. R., Evason, K. J., Brazier, H., Almeida, D., Koller, A., Hajjar, K. A., Stainier, D. Y. R. et al.** (2013). The perivascular niche regulates breast tumour dormancy. *Nat. Cell Biol.* **15**, 807-817.

**Gil-Bernabe, A. M., Ferjancic, S., Tlalka, M., Zhao, L., Allen, P. D., Im, J. H., Watson, K., Hill, S. A., Amirkhosravi, A., Francis, J. L. et al.** (2012). Recruitment of monocytes/macrophages by tissue factor-mediated coagulation is essential for metastatic cell survival and premetastatic niche establishment in mice. *Blood* **119**, 3164-3175.

**Gopinathan, A., Morton, J. P., Jodrell, D. I. and Sansom, O. J.** (2015). GEMMs as preclinical models for testing pancreatic cancer therapies. *Dis. Model. Mech.* **8**, 1185-1200.

**Gu, H., Zou, Y.-R. and Rajewsky, K.** (1993). Independent control of immunoglobulin switch recombination at individual switch regions evidenced through Cre-loxP-mediated gene targeting. *Cell* **73**, 1155-1164.

**Gunther, E. J., Belka, G. K., Wertheim, G. B. W., Wang, J., Hartman, J. L., Boxer, R. B. and Chodosh, L. A.** (2002). A novel doxycycline-inducible system for the transgenic analysis of mammary gland biology. *FASEB J.* **16**, 283-292.

**Guy, C. T., Webster, M. A., Schaller, M., Parsons, T. J., Cardiff, R. D. and Muller, W. J.** (1992). Expression of the neu protooncogene in the mammary epithelium of transgenic mice induces metastatic disease. *Proc. Natl. Acad. Sci. USA* **89**, 10578-10582.

**Hanahan, D. and Weinberg, R. A.** (2011). Hallmarks of cancer: the next generation. *Cell* **144**, 646-674.

**Harney, A. S., Arwert, E. N., Entenberg, D., Wang, Y., Guo, P., Qian, B.-Z., Oktay, M. H., Pollard, J. W., Jones, J. G. and Condeelis, J. S.** (2015). Real-time imaging reveals local, transient vascular permeability, and tumor cell intravasation stimulated by TIE2hi macrophage-derived VEGFA. *Cancer Discov.* **5**, 932-943.

**Harper, K. L., Sosa, M. S., Entenberg, D., Hosseini, H., Cheung, J. F., Nobre, R., Avivar-Valderas, A., Nagi, C., Girnius, N., Davis, R. J. et al.** (2016). Mechanism of early dissemination and metastasis in Her2+ mammary cancer. *Nature* **540**, 588-592.

**Hawkins, E. D., Duarte, D., Akinduro, O., Khorshed, R. A., Passaro, D., Nowicka, M., Straszkowski, L., Scott, M. K., Rothery, S., Ruivo, N. et al.** (2016). T-cell acute leukaemia exhibits dynamic interactions with bone marrow microenvironments. *Nature* **538**, 518-522.

**Headley, M. B., Bins, A., Nip, A., Roberts, E. W., Looney, M. R., Gerard, A. and Krummel, M. F.** (2016). Visualization of immediate immune responses to pioneer metastatic cells in the lung. *Nature* **531**, 513-517.

**Hingorani, S. R., Petricoin, E. F., Maitra, A., Rajapakse, V., King, C., Jacobetz, M. A., Ross, S., Conrads, T. P., Veenstra, T. D., Hitt, B. A. et al.** (2003). Preinvasive and invasive ductal pancreatic cancer and its early detection in the mouse. *Cancer Cell* **4**, 437-450.

**Hingorani, S. R., Wang, L., Multani, A. S., Combs, C., Deramaudt, T. B., Hruban, R. H., Rustgi, A. K., Chang, S. and Tuveson, D. A.** (2005). Trp53R172H and Kras G12D cooperate to promote chromosomal instability and widely metastatic pancreatic ductal adenocarcinoma in mice. *Cancer Cell* **7**, 469-483.

**Hiratsuka, S., Nakamura, K., Iwai, S., Murakami, M., Itoh, T., Kijima, H., Shipley, J. M., Senior, R. M. and Shibuya, M.** (2002). MMP9 induction by vascular endothelial growth factor receptor-1 is involved in lung-specific metastasis. *Cancer Cell* **2**, 289-300.

**Hiratsuka, S., Watanabe, A., Aburatani, H. and Maru, Y.** (2006). Tumour-mediated upregulation of chemoattractants and recruitment of myeloid cells predetermines lung metastasis. *Nat. Cell Biol.* **8**, 1369-1375.

**Hiroshima, Y., Maawy, A., Zhang, Y., Zhang, N. and Murakami, T.** (2016). Patient-derived mouse models of cancer need to be orthotopic in order to evaluate targeted anti-metastatic therapy. *Oncotarget* **7**, 71696-71702.

**Holen, I., Nutter, F., Wilkinson, J. M., Evans, C. A., Avgoustou, P. and Ottewell, P. D.** (2015). Human breast cancer bone metastasis in vitro and in vivo: a novel 3D model system for studies of tumour cell-bone cell interactions. *Clin. Exp. Metastasis* **32**, 689-702.

**Holen, I., Speirs, V., Morrissey, B. and Blyth, K.** (2017). In vivo models in breast cancer research: progress, challenges and future directions. *Dis. Model. Mech.* **10**, 359-371.

**Hoshino, A., Costa-Silva, B., Shen, T.-L., Rodrigues, G., Hashimoto, A., Tesic Mark, M., Molina, H., Kohsaka, S., Di Giannatale, A., Ceder, S. et al.** (2015). Tumour exosome integrins determine organotropic metastasis. *Nature* **527**, 329-335.

**Hosseini, H., Obradović, M. M. S., Hoffmann, M., Harper, K. L., Sosa, M. S., Werner-Klein, M., Nanduri, L. K., Werno, C., Ehrl, C., Maneck, M. et al.** (2016). Early dissemination seeds metastasis in breast cancer. *Nature* **540**, 552-558.

**Jackson, S. J. and Thomas, G. J.** (2017). Human tissue models in cancer research: looking betond the mouse. *Dis Model Mech.* **10**, 939-942.

**Jackson, E. L., Willis, N., Mercer, K., Bronson, R. T., Crowley, D., Montoya, R., Jacks, T. and Tuveson, D. A.** (2001). Analysis of lung tumor initiation and progression using conditional expression of oncogenic K-ras. *Genes Dev.* **15**, 3243-3248.

**Jeon, J. S., Bersini, S., Gilardi, M., Dubini, G., Charest, J. L., Moretti, M. and Kamm, R. D.** (2015). Human 3D vascularized organotypic microfluidic assays to study breast cancer cell extravasation. *Proc. Natl. Acad. Sci. USA* **112**, 214-219.

**Julien, S., Merino-Trigo, A., Lacroix, L., Pocard, M., Goeré, D., Mariani, P., Landron, S., Bigot, L., Nemati, F., Dartigues, P. et al.** (2012). Characterization of a large panel of patient-derived tumor xenografts representing the clinical heterogeneity of human colorectal cancer. *Clin. Cancer Res.* **18**, 5314-5328.

**Junankar, S., Shay, G., Jurczyluk, J., Ali, N., Down, J., Pocock, N., Parker, A., Nguyen, A., Sun, S., Kashemirov, B. et al.** (2015). Real-time intravital imaging establishes tumor-associated macrophages as the extraskeletal target of bisphosphonate action in cancer. *Cancer Discov.* **5**, 35-42.

**Jung, Y., Kim, J. K., Shiozawa, Y., Wang, J., Mishra, A., Joseph, J., Berry, J. E., McGee, S., Lee, E., Sun, H. et al.** (2013). Recruitment of mesenchymal stem cells into prostate tumours promotes metastasis. *Nat. Commun.* **4**, 1795.

**Kabeer, F., Beverly, L. J., Darrasse-Jèze, G. and Podsypanina, K.** (2016). Methods to study metastasis in genetically modified mice. *Cold Spring Harb. Protoc.* **2016**, pdb.top069948.

**Kalluri, R. and Zeisberg, M.** (2006). Fibroblasts in cancer. *Nat. Rev. Cancer* **6**, 392-401.
**Kang, Y., Siegel, P. M., Shu, W., Drobnjak, M., Kakonen, S. M., Cordon-Cardo, C., Guise, T. A. and Massague, J.** (2003). A multigenic program mediating breast cancer metastasis to bone. *Cancer Cell* **3**, 537-549.
**Kang, S.-Y., Halvorsen, O. J., Gravdal, K., Bhattacharya, N., Lee, J. M., Liu, N. W., Johnston, B. T., Johnston, A. B., Haukaas, S. A., Aamodt, K. et al.** (2009). Prosaposin inhibits tumor metastasis via paracrine and endocrine stimulation of stromal p53 and Tsp-1. *Proc. Natl. Acad. Sci. USA* **106**, 12115-12120.
**Kaplan, R. N., Riba, R. D., Zacharoulis, S., Bramley, A. H., Vincent, L., Costa, C., MacDonald, D. D., Jin, D. K., Shido, K., Kerns, S. A. et al.** (2005). VEGFR1-positive haematopoietic bone marrow progenitors initiate the pre-metastatic niche. *Nature* **438**, 820-827.
**Karagiannis, G. S., Poutahidis, T., Erdman, S. E., Kirsch, R., Riddell, R. H. and Diamandis, E. P.** (2012). Cancer-associated fibroblasts drive the progression of metastasis through both paracrine and mechanical pressure on cancer tissue. *Mol. Cancer Res.* **10**, 1403-1418.
**Karim, S. A., Creedon, H., Patel, H., Carragher, N. O., Morton, J. P., Muller, W. J., Evans, T. R. J., Gusterson, B., Sansom, O. J. and Brunton, V. G.** (2013). Dasatinib inhibits mammary tumour development in a genetically engineered mouse model. *J. Pathol.* **230**, 430-440.
**Kaushik, S., Pickup, M. W. and Weaver, V. M.** (2016). From transformation to metastasis: deconstructing the extracellular matrix in breast cancer. *Cancer Metastasis Rev.* **35**, 655-667.
**Kellar, A., Egan, C. and Morris, D.** (2015). Preclinical murine models for lung cancer: clinical trial applications. *Biomed Res. Int.* **2015**, 621324.
**Kerbel, R. S., Guerin, E., Francia, G., Xu, P., Lee, C. R., Ebos, J. M. L. and Man, S.** (2013). Preclinical recapitulation of antiangiogenic drug clinical efficacies using models of early or late stage breast cancer metastatis. *The Breast* **22**, S57-S65.
**Kersten, K., de Visser, K. E., van Miltenburg, M. H. and Jonkers, J.** (2016). Genetically engineered mouse models in oncology research and cancer medicine. *EMBO Mol. Med.* **9**, 135-153.
**Khanna, C. and Hunter, K.** (2005). Modeling metastasis in vivo. *Carcinogenesis* **26**, 513-523.
**Kitamura, T., Qian, B.-Z. and Pollard, J. W.** (2015). Immune cell promotion of metastasis. *Nat. Rev. Immunol.* **15**, 73-86.
**Krebs, A. M., Mitschke, J., Lasierra Losada, M., Schmalhofer, O., Boerries, M., Busch, H., Boettcher, M., Mougiakakos, D., Reichardt, W., Bronsert, P. et al.** (2017). The EMT-activator Zeb1 is a key factor for cell plasticity and promotes metastasis in pancreatic cancer. *Nat. Cell Biol.* **19**, 518-529.
**Kuperwasser, C., Dessain, S., Bierbaum, B. E., Garnet, D., Sperandio, K., Gauvin, G. P., Naber, S. P., Weinberg, R. A. and Rosenblatt, M.** (2005). A mouse model of human breast cancer metastasis to human bone. *Cancer Res.* **65**, 6130-6138.
**Kuznetsov, H. S., Marsh, T., Markens, B. A., Castano, Z., Greene-Colozzi, A., Hay, S. A., Brown, V. E., Richardson, A. L., Signoretti, S., Battinelli, E. M. et al.** (2012). Identification of luminal breast cancers that establish a tumor-supportive macroenvironment defined by proangiogenic platelets and bone marrow-derived cells. *Cancer Discov.* **2**, 1150-1165.
**Lambert, A. W., Pattabiraman, D. R. and Weinberg, R. A.** (2017). Emerging biological principles of metastasis. *Cell* **168**, 670-691.
**Lee, E. Y.-H. P., Chang, C.-Y., Hu, N., Wang, Y.-C. J., Lai, C.-C., Herrup, K., Lee, W.-H. and Bradley, A.** (1992). Mice deficient for Rb are nonviable and show defects in neurogenesis and haematopoiesis. *Nature* **359**, 288-294.
**Lee, M., Downes, A., Chau, Y.-Y., Serrels, B., Hastie, N., Elfick, A., Brunton, V., Frame, M. and Serrels, A.** (2015). In vivo imaging of the tumor and its associated microenvironment using combined CARS / 2-photon microscopy. *IntraVital* **4**, e1055430.
**Lewandoski, M.** (2001). Conditional control of gene expression in the mouse. *Nat. Rev. Genet.* **2**, 743-755.
**Li, B., Tsao, S. W., Chan, K. W., Ludwig, D. L., Novosyadlyy, R., Li, Y. Y., He, Q. Y. and Cheung, A. L. M.** (2014). Id1-induced IGF-II and its autocrine/endocrine promotion of esophageal cancer progression and chemoresistance–implications for IGF-II and IGF-IR-targeted therapy. *Clin. Cancer Res.* **20**, 2651-2662.
**Liu, Y. and Cao, X.** (2016). Characteristics and significance of the pre-metastatic niche. *Cancer Cell* **30**, 668-681.
**Livet, J., Weissman, T. A., Kang, H., Draft, R. W., Lu, J., Bennis, R. A., Sanes, J. R. and Lichtman, J. W.** (2007). Transgenic strategies for combinatorial expression of fluorescent proteins in the nervous system. *Nature* **450**, 56-62.
**Luo, J., Lee, S. O., Yun, C., Yang, R. and Chang, C.** (2015). Infiltrating bone marrow mesenchymal stem cells (BM-MSCs) increase prostate cancer cell invasion via altering the CCL5/HIF2α/androgen receptor signals. *Oncotarget* **6**, 27555-27565.
**Marien, E., Hillen, A., Vanderhoydonc, F., Swinnen, J. V. and Vande Velde, G.** (2017). Longitudinal microcomputed tomography-derived biomarkers for lung metastasis detection in a syngeneic mouse model: added value to bioluminescence imaging. *Lab. Investig.* **97**, 24-33.
**Massagué, J. and Obenauf, A. C.** (2016). Metastatic colonization by circulating tumour cells. *Nature* **529**, 298-306.
**McAllister, S. S. and Weinberg, R. A.** (2014). The tumour-induced systemic environment as a critical regulator of cancer progression and metastasis. *Nat. Cell Biol.* **16**, 717-727.
**Minn, A. J., Gupta, G. P., Siegel, P. M., Bos, P. D., Shu, W., Giri, D. D., Viale, A., Olshen, A. B., Gerald, W. L. and Massagué, J.** (2005). Genes that mediate breast cancer metastasis to lung. *Nature* **436**, 518-524.
**Mognetti, B., Montagna, G., La, Perrelli, M. G., Pagliaro, P. and Penna, C.** (2013). Bone marrow mesenchymal stem cells increase motility of prostate cancer cells via production of stromal cell-derived factor-1 α. *J. Cell. Mol. Med.* **17**, 287-292.
**Morikawa, K., Walker, S. M., Nakajima, M., Jessup, J. M. and Fidler, I. J.** (1988). Influence of organ environment on the growth, selection and metastasis of human colon carcinoma cells in nude mice. *Cancer Res.* **48**, 6863-6871.
**Morton, J. J., Bird, G., Refaeli, Y. and Jimeno, A.** (2016). Humanized mouse xenograft models: Narrowing the tumor-microenvironment gap. *Cancer Res.* **76**, 6153-6158.
**Mullen, C. A., Urban, J. L., Van Waes, C., Rowley, D. A. and Schreiber, H.** (1985). Multiple cancers. Tumor burden permits the outgrowth of other cancers. *J. Exp. Med.* **162**, 1665-1682.
**Muller, W. J., Sinn, E., Pattengale, P. K., Wallace, R. and Leder, P.** (1988). Single-step induction of mammary adenocarcinoma in transgenic mice bearing the activated c-neu oncogene. *Cell* **54**, 105-115.
**Munoz, R., Man, S., Shaked, Y., Lee, C. R., Wong, J., Francia, G. and Kerbel, R. S.** (2006). Highly efficacious nontoxic preclinical treatment for advanced metastatic breast cancer using combination oral UFT-cyclophosphamide metronomic chemotherapy. *Cancer Res.* **66**, 3386-3391.
**Murugaesu, N., Iravani, M., van Weverwijk, A., Ivetic, A., Johnson, D. A., Antonopoulos, A., Fearns, A., Jamal-Hanjani, M., Sims, D., Fenwick, K. et al.** (2014). An in vivo functional screen identifies ST6GalNAc2 Sialyltransferase as a breast cancer metastasis suppressor. *Cancer Discov.* **4**, 304-317.
**Paget, S.** (1989). The distribution of secondary growths in cancer of the breast. *Cancer Metastasis Rev.* **8**, 98-101.
**Peinado, H., Alečković, M., Lavotshkin, S., Matei, I., Costa-Silva, B., Moreno-Bueno, G., Hergueta-Redondo, M., Williams, C., García-Santos, G., Ghajar, C. M. et al.** (2012). Melanoma exosomes educate bone marrow progenitor cells toward a pro-metastatic phenotype through MET. *Nat. Med.* **18**, 883-891.
**Peinado, H., Zhang, H., Matei, I. R., Costa-Silva, B., Hoshino, A., Rodrigues, G., Psaila, B., Kaplan, R. N., Bromberg, J. F., Kang, Y. et al.** (2017). Pre-metastatic niches: organ-specific homes for metastases. *Nat. Rev. Cancer* **17**, 302-317.
**Pena, C., Cespedes, M. V., Lindh, M. B., Kiflemariam, S., Mezheyeuski, A., Edqvist, P.-H., Hagglof, C., Birgisson, H., Bojmar, L., Jirstrom, K. et al.** (2013). STC1 expression by cancer-associated fibroblasts drives metastasis of colorectal cancer. *Cancer Res.* **73**, 1287-1297.
**Pignatelli, J., Goswami, S., Jones, J. G., Rohan, T. E., Pieri, E., Chen, X., Adler, E., Cox, D., Maleki, S., Bresnick, A. et al.** (2014). Invasive breast carcinoma cells from patients exhibit MenaINV- and macrophage-dependent transendothelial migration. *Sci. Signal.* **7**, ra112-ra112.
**Plaks, V., Koopman, C. D. and Werb, Z.** (2013). Circulating tumor cells. *Science* **341**, 1186-1188.
**Pompili, L., Porru, M., Caruso, C., Biroccio, A. and Leonetti, C.** (2016). Patient-derived xenografts: a relevant preclinical model for drug development. *J. Exp. Clin. Cancer Res.* **35**, 189.
**Puig, I., Chicote, I., Tenbaum, S. P., Arqués, O., Herance, J. R., Gispert, J. D., Jimenez, J., Landolfi, S., Caci, K., Allende, H. et al.** (2013). A personalized preclinical model to evaluate the metastatic potential of patient-derived colon cancer initiating cells. *Clin. Cancer Res.* **19**, 6787-6801.
**Qian, B.-Z. and Pollard, J. W.** (2010). Macrophage diversity enhances tumor progression and metastasis. *Cell* **141**, 39-51.
**Qian, B.-Z. Deng, Y., Im, J. H., Zou, Y., Li, J., Lang, R. A. and Pollard, J. W.** (2009). A distinct macrophage population mediates metastatic breast cancer cell extravasation, establishment and growth. *PLoS ONE* **4**, e6562.
**Qian, B.-Z., Li, J., Zhang, H., Kitamura, T., Zhang, J., Campion, L. R., Kaiser, E. A., Snyder, L. A. and Pollard, J. W.** (2011). CCL2 recruits inflammatory monocytes to facilitate breast-tumour metastasis. *Nature* **475**, 222-225.
**Rampetsreiter, P., Casanova, E. and Eferl, R.** (2011). Genetically modified mouse models of cancer invasion and metastasis. *Drug Discov. Today Dis. Model.* **8**, 67-74.
**Reilly, R. T., Gottlieb, M. B., Ercolini, A. M., Machiels, J. P., Kane, C. E., Okoye, F. I., Muller, W. J., Dixon, K. H. and Jaffee, E. M.** (2000). HER-2/neu is a tumor rejection target in tolerized HER-2/neu transgenic mice. *Cancer Res.* **60**, 3569-3576.
**Reymond, N., d'Água, B. B. and Ridley, A. J.** (2013). Crossing the endothelial barrier during metastasis. *Nat. Rev. Cancer* **13**, 858-870.
**Rhim, A. D., Mirek, E. T., Aiello, N. M., Maitra, A., Bailey, J. M., McAllister, F., Reichert, M., Beatty, G. L., Rustgi, A. K., Vonderheide, R. H. et al.** (2012). EMT and dissemination precede pancreatic tumor formation. *Cell* **148**, 349-361.
**Ritsma, L., Steller, E. J. A., Beerling, E., Loomans, C. J. M., Zomer, A., Gerlach, C., Vrisekoop, N., Seinstra, D., van Gurp, L., Schafer, R. et al.** (2012). Intravital microscopy through an abdominal imaging window reveals a pre-micrometastasis stage during liver metastasis. *Sci. Transl. Med.* **4**, 158ra145.

**Rodriguez-Tirado, C., Kitamura, T., Kato, Y., Pollard, J. W., Condeelis, J. S. and Entenberg, D.** (2016). Long-term high-resolution intravital microscopy in the lung with a vacuum stabilized imaging window. *J. Vis. Exp.* **57**, 742-768.
**Rohan, T. E., Xue, X., Lin, H.-M., D'Alfonso, T. M., Ginter, P. S., Oktay, M. H., Robinson, B. D., Ginsberg, M., Gertler, F. B., Glass, A. G. et al.** (2014). Tumor microenvironment of metastasis and risk of distant metastasis of breast cancer. *JNCI J. Natl. Cancer Inst.* **106**, dju136.
**Ruggeri, Z. M. and Mendolicchio, G. L.** (2007). Adhesion mechanisms in platelet function. *Circ. Res.* **100**, 1673-1685.
**Sanches, P. G., Peters, S., Rossin, R., Kaijzel, E. L., Que, I., Löwik, C. W. G. M. and Grüll, H.** (2015). Bone metastasis imaging with SPECT/CT/MRI: a preclinical toolbox for therapy studies. *Bone* **75**, 62-71.
**Sánchez-Rivera, F. J., Papagiannakopoulos, T., Romero, R., Tammela, T., Bauer, M. R., Bhutkar, A., Joshi, N. S., Subbaraj, L., Bronson, R. T., Xue, W. et al.** (2014). Rapid modelling of cooperating genetic events in cancer through somatic genome editing. *Nature* **516**, 428-431.
**Saxena, M. and Christofori, G.** (2013). Rebuilding cancer metastasis in the mouse. *Mol. Oncol.* **7**, 283-296.
**Scheele, C. L. G. J., Maynard, C. and van Rheenen, J.** (2016). Intravital insights into heterogeneity, metastasis, and therapy responses. *Trends in Cancer* **2**, 205-216.
**Schönhuber, N., Seidler, B., Schuck, K., Veltkamp, C., Schachtler, C., Zukowska, M., Eser, S., Feyerabend, T. B., Paul, M. C., Eser, P. et al.** (2014). A next-generation dual-recombinase system for time- and host-specific targeting of pancreatic cancer. *Nat. Med.* **20**, 1340-1347.
**Schumacher, D., Strilic, B., Sivaraj, K. K., Wettschureck, N. and Offermanns, S.** (2013). Platelet-derived nucleotides promote tumor-cell transendothelial migration and metastasis via P2Y2 receptor. *Cancer Cell* **24**, 130-137.
**Serrels, A., Lund, T., Serrels, B., Byron, A., McPherson, R. C., von Kriegsheim, A., Gómez-Cuadrado, L., Canel, M., Muir, M., Ring, J. E. et al.** (2015). Nuclear FAK controls chemokine transcription, tregs, and evasion of anti-tumor immunity. *Cell* **163**, 160-173.
**Sethi, N. and Kang, Y.** (2011). Unravelling the complexity of metastasis — molecular understanding and targeted therapies. *Nat. Rev. Cancer* **11**, 735-748.
**Shibata, H., Toyama, K., Shioya, H., Ito, M., Hirota, M., Hasegawa, S., Matsumoto, H., Takano, H., Akiyama, T., Toyoshima, K. et al.** (1997). Rapid colorectal adenoma formation initiated by conditional targeting of the Apc gene. *Science* **278**, 120-123.
**Shultz, L. D., Brehm, M. A., Garcia-Martinez, J. V. and Greiner, D. L.** (2012). Humanized mice for immune system investigation: progress, promise and challenges. *Nat. Rev. Immunol.* **12**, 786-798.
**Shurin, M. R., Lu, L., Kalinski, P., Stewart-Akers, A. M. and Lotze, M. T.** (1999). Th1/Th2 balance in cancer, transplantation and pregnancy. *Springer Semin. Immunopathol.* **21**, 339-359.
**Singh, M. and Ferrara, N.** (2012). Modeling and predicting clinical efficacy for drugs targeting the tumor milieu. *Nat. Biotechnol.* **30**, 648-657.
**Singh, M., Lima, A., Molina, R., Hamilton, P., Clermont, A. C., Devasthali, V., Thompson, J. D., Cheng, J. H., Bou Reslan, H., Ho, C. C. K. et al.** (2010). Assessing therapeutic responses in Kras mutant cancers using genetically engineered mouse models. *Nat. Biotechnol.* **28**, 585-593.
**Sinn, E., Muller, W., Pattengale, P., Tepler, I., Wallace, R. and Leder, P.** (1987). Coexpression of MMTV/v-Ha-ras and MMTV/c-myc genes in transgenic mice: synergistic action of oncogenes in vivo. *Cell* **49**, 465-475.
**Sosa, M. S., Bragado, P. and Aguirre-Ghiso, J. A.** (2014). Mechanisms of disseminated cancer cell dormancy: an awakening field. *Nat. Rev. Cancer* **14**, 611-622.
**Steeg, P. S.** (2016). Targeting metastasis. *Nat. Rev. Cancer* **16**, 201-218.
**Steele, C. W., Karim, S. A., Leach, J. D. G., Bailey, P., Upstill-Goddard, R., Rishi, L., Foth, M., Bryson, S., McDaid, K., Wilson, Z. et al.** (2016). CXCR2 inhibition profoundly suppresses metastases and augments immunotherapy in pancreatic ductal adenocarcinoma. *Cancer Cell* **29**, 832-845.
**Stoneman, V., Braganza, D., Figg, N., Mercer, J., Lang, R., Goddard, M. and Bennett, M.** (2007). Monocyte/macrophage suppression in CD11b diphtheria toxin receptor transgenic mice differentially affects atherogenesis and established plaques. *Circ. Res.* **100**, 884-893.
**Szulczewski, J. M., Inman, D. R., Entenberg, D., Ponik, S. M., Aguirre-Ghiso, J., Castracane, J., Condeelis, J., Eliceiri, K. W. and Keely, P. J.** (2016). In vivo visualization of stromal macrophages via label-free FLIM-based metabolite imaging. *Sci. Rep.* **6**, 25086.
**Taromi, S., Kayser, G., von Elverfeldt, D., Reichardt, W., Braun, F., Weber, W. A., Zeiser, R. and Burger, M.** (2016). An orthotopic mouse model of small cell lung cancer reflects the clinical course in patients. *Clin. Exp. Metastasis* **33**, 651-660.
**Thiery, J. P., Acloque, H., Huang, R. Y. J. and Nieto, M. A.** (2009). Epithelial-mesenchymal transitions in development and disease. *Cell* **139**, 871-890.
**Tipping, W. J., Lee, M., Serrels, A., Brunton, V. G. and Hulme, A. N.** (2016). Stimulated Raman scattering microscopy: an emerging tool for drug discovery. *Chem. Soc. Rev.* **45**, 2075-2089.
**Toniatti, C., Jones, P., Graham, H., Pagliara, B. and Draetta, G.** (2014). Oncology drug discovery: planning a turnaround. *Cancer Discov.* **4**, 397-404.
**Turajlic, S. and Swanton, C.** (2016). Metastasis as an evolutionary process. *Science* **352**, 169-175.
**Valastyan, S. and Weinberg, R. A.** (2011). Tumor metastasis: molecular insights and evolving paradigms. *Cell* **147**, 275-292.
**van Miltenburg, M. H. and Jonkers, J.** (2012). Using genetically engineered mouse models to validate candidate cancer genes and test new therapeutic approaches. *Curr. Opin. Genet. Dev.* **22**, 21-27.
**Wang, S., Yuan, Y., Liao, L., Kuang, S.-Q., Tien, J. C.-Y., O'Malley, B. W. and Xu, J.** (2009). Disruption of the SRC-1 gene in mice suppresses breast cancer metastasis without affecting primary tumor formation. *Proc. Natl. Acad. Sci. USA* **106**, 151-156.
**Wang, H., Yu, C., Gao, X., Welte, T., Muscarella, A. M., Tian, L., Zhao, H., Zhao, Z., Du, S., Tao, J. et al.** (2015). The osteogenic niche promotes early-stage bone colonization of disseminated breast cancer cells. *Cancer Cell* **27**, 193-210.
**Wculek, S. K. and Malanchi, I.** (2015). Neutrophils support lung colonization of metastasis-initiating breast cancer cells. *Nature* **528**, 413-417.
**Weber, J., Öllinger, R., Friedrich, M., Ehmer, U., Barenboim, M., Steiger, K. and Heid, I.** (2015). CRISPR/Cas9 somatic multiplex-mutagenesis for high-throughput functional cancer genomics in mice. *Proc. Natl. Acad. Sci. USA* **112**, 13982-13987.
**Whittle, J. R., Lewis, M. T., Lindeman, G. J. and Visvader, J. E.** (2015). Patient-derived xenograft models of breast cancer and their predictive power. *Breast Cancer Res.* **17**, 17.
**Wong, S. Y. and Hynes, R. O.** (2006). Lymphatic or hematogenous dissemination: how does a metastatic tumor cell decide? *Cell Cycle* **5**, 812-817.
**Wright, L. E., Ottewell, P. D., Rucci, N., Peyruchaud, O., Pagnotti, G. M., Chiechi, A., Buijs, J. T. and Sterling, J. A.** (2016). Murine models of breast cancer bone metastasis. *Bonekey Rep.* **5**, 1-11.
**Wyckoff, J.** (2004). A paracrine loop between tumor cells and macrophages is required for tumor cell migration in mammary tumors. *Cancer Res.* **64**, 7022-7029.
**Wyckoff, J. B., Wang, Y., Lin, E. Y., Li, J.-F., Goswami, S., Stanley, E. R., Segall, J. E., Pollard, J. W. and Condeelis, J.** (2007). Direct visualization of macrophage-assisted tumor cell intravasation in mammary tumors. *Cancer Res.* **67**, 2649-2656.
**Yeung, K. T. and Yang, J.** (2017). Epithelial-mesenchymal transition in tumor metastasis. *Mol. Oncol.* **11**, 28-39.
**Zervantonakis, I. K., Hughes-Alford, S. K., Charest, J. L., Condeelis, J. S., Gertler, F. B. and Kamm, R. D.** (2012). Three-dimensional microfluidic model for tumor cell intravasation and endothelial barrier function. *Proc. Natl. Acad. Sci. USA* **109**, 13515-13520.
**Zheng, X., Carstens, J. L., Kim, J., Scheible, M., Kaye, J., Sugimoto, H., Wu, C.-C., Lebleu, V. S. and Kalluri, R.** (2015). Epithelial-to-mesenchymal transition is dispensable for metastasis but induces chemoresistance in pancreatic cancer. *Nature* **527**, 525-530.
**Zhou, Z. N., Sharma, V. P., Beaty, B. T., Roh-Johnson, M., Peterson, E. A., Van Rooijen, N., Kenny, P. A., Wiley, H. S., Condeelis, J. S. and Segall, J. E.** (2014). Autocrine HBEGF expression promotes breast cancer intravasation, metastasis and macrophage-independent invasion in vivo. *Oncogene* **33**, 3784-3793.
**Zomer, A., Maynard, C., Verweij, F. J., Kamermans, A., Schäfer, R., Beerling, E., Schiffelers, R. M., de Wit, E., Berenguer, J., Ellenbroek, S. I. J. et al.** (2015). In vivo imaging reveals extracellular vesicle-mediated phenocopying of metastatic behavior. *Cell* **161**, 1046-1057.
**Zou, W. and Restifo, N. P.** (2010). T(H)17 cells in tumour immunity and immunotherapy. *Nat. Rev. Immunol.* **10**, 248-256.

# References


[1] Stewart B. W and Wild C. P. World Cancer Report 2014. **2014**.

[2] Sinn H.-P and Kreipe H. A Brief Overview of the WHO Classification of Breast Tumors, 4th Edition, Focusing on Issues and Updates from the 3rd Edition. *Breast Care*, 8(2):149–154, **2013**. doi: 10.1159/000350774.

[3] Li C. I, Uribe D. J, and Daling J. R. Clinical characteristics of different histologic types of breast cancer. *British Journal of Cancer*, 93(9):1046–1052, **2005**. doi: 10.1038/sj.bjc.6602787.

[4] Allison K. H. Molecular Pathology of Breast Cancer. *American Journal of Clinical Pathology*, 138(6):770–780, **2012**. doi: 10.1309/AJCPIV9IQ1MRQMOO.

[5] Hammond M. E. H, Hayes D. F, Dowsett M, Allred D. C, Hagerty K. L, Badve S, Fitzgibbons P. L, Francis G, Goldstein N. S, Hayes M, Hicks D. G, Lester S, Love R, Mangu P. B, McShane L, Miller K, Osborne C. K, Paik S, Perlmutter J, Rhodes A, Sasano H, Schwartz J. N, Sweep F. C, Taube S, Torlakovic E. E, Valenstein P, Viale G, Visscher D, Wheeler T, Williams R. B, Wittliff J. L, and Wolff A. C. American Society of Clinical Oncology/College of American Pathologists Guideline Recommendations for Immunohistochemical Testing of Estrogen and Progesterone Receptors in Breast Cancer. *Journal of Clinical Oncology*, 28(16):2784–2795, **2010**. doi: 10.1200/JCO.2009.25.6529.

[6] Byrski T, Dent R, Blecharz P, Foszczynska-Kloda M, Gronwald J, Huzarski T, Cybulski C, Marczyk E, Chrzan R, Eisen A, Lubinski J, and Narod S. A. Results of a phase II open-label, non-randomized trial of cisplatin chemotherapy in patients with BRCA1-positive metastatic breast cancer. *Breast cancer research : BCR*, 14(4):R110, **2012**. doi: 10.1186/bcr3231.

[7] Tutt A, Robson M, Garber J. E, Domchek S. M, Audeh M. W, Weitzel J. N, Friedlander M, Arun B, Loman N, Schmutzler R. K, Wardley A, Mitchell G, Earl H, Wickens M, and Carmichael J. Oral poly(ADP-ribose) polymerase inhibitor olaparib in patients with BRCA1 or BRCA2 mutations and advanced breast cancer: a proof-of-concept trial. *The Lancet*, 376(9737):235–244, **2010**. doi: 10.1016/S0140-6736(10)60892-6.

[8] Cappuzzo F. The Human Epidermal growth factor Receptor (HER) family: structure and function. In *Guide to Targeted Therapies: EGFR mutations in NSCLC*, chapter 2, pages 7–18. Springer International Publishing, Switzerland, **2014**. ISBN 978-3-319-03058-6. doi: 10.1007/978-3-319-03059-3.

[9] Kokai Y, Dobashi K, Weiner D. B, Myers J. N, Nowell P. C, and Greene M. I. Phosphorylation process induced by epidermal growth factor alters the oncogenic and cellular neu (NGL) gene products. *Proceedings of the National Academy of Sciences*, 85(15):5389–5393, **1988**. doi: 10.1073/pnas.85.15.5389.

[10] Garrett T. P, McKern N. M, Lou M, Elleman T. C, Adams T. E, Lovrecz G. O, Kofler M, Jorissen R. N, Nice E. C, Burgess A. W, and Ward C. W. The Crystal Structure of a Truncated ErbB2 Ectodomain Reveals an Active Conformation, Poised to Interact with Other ErbB Receptors. *Molecular Cell*, 11(2):495–505, **2003**. doi: 10.1016/S1097-2765(03)00048-0.

[11] Wieduwilt M. J and Moasser M. M. The epidermal growth factor receptor family: Biology driving targeted therapeutics. *Cellular and Molecular Life Sciences*, 65(10):1566–1584, **2008**. doi: 10.1007/s00018-008-7440-8.

[12] Yarden Y and Ullrich A. Molecular analysis of signal transduction by growth factors. *Biochemistry*, 27(9):3113–3119, **1988**. doi: 10.1021/bi00409a001.

[13] Domin J and Waterfield M. D. Using structure to define the function of phosphoinositide 3-kinase family members. *FEBS letters*, 410(1):91–5, **1997**.

[14] Karagöz G. E and Rüdiger S. G. Hsp90 interaction with clients. *Trends in Biochemical Sciences*, 40(2):117–125, **2015**. doi: 10.1016/j.tibs.2014.12.002.

[15] Sawai A, Chandarlapaty S, Greulich H, Gonen M, Ye Q, Arteaga C. L, Sellers W, Rosen N, and Solit D. B. Inhibition of Hsp90 Down-regulates Mutant Epidermal Growth Factor Receptor (EGFR) Expression and Sensitizes EGFR Mutant Tumors to Paclitaxel. *Cancer Research*, 68(2): 589–596, **2008**. doi: 10.1158/0008-5472.CAN-07-1570.

[16] Bertelsen V and Stang E. The Mysterious Ways of ErbB2/HER2 Trafficking. *Membranes*, 4(3): 424–46, **2014**. doi: 10.3390/membranes4030424.

[17] Citri A, Gan J, Mosesson Y, Vereb G, Szollosi J, and Yarden Y. Hsp90 restrains ErbB-2/HER2 signalling by limiting heterodimer formation. *EMBO reports*, 5(12):1165–1170, **2004**. doi: 10.1038/sj.embor.7400300.

[18] Zhang X, Loijens J. C, Boronenkov I. V, Parker G. J, Norris F. A, Chen J, Thum O, Prestwich G. D, Majerus P. W, and Anderson R. A. Phosphatidylinositol-4-phosphate 5-Kinase Isozymes Catalyze the Synthesis of 3-Phosphate-containing Phosphatidylinositol Signaling Molecules. *Journal of Biological Chemistry*, 272(28):17756–17761, **1997**. doi: 10.1074/jbc.272.28.17756.

[19] Maehama T and Dixon J. E. The Tumor Suppressor, PTEN/MMAC1, Dephosphorylates the Lipid Second Messenger, Phosphatidylinositol 3,4,5-Trisphosphate. *Journal of Biological Chemistry*, 273(22):13375–13378, **1998**. doi: 10.1074/jbc.273.22.13375.

[20] Walker K. S, Deak M, Paterson A, Hudson K, Cohen P, and Alessi D. R. Activation of protein kinase B $\beta$ and $\gamma$ isoforms by insulin in vivo and by 3-phosphoinositide-dependent protein kinase-1 in vitro: comparison with protein kinase B $\alpha$. *Biochemical Journal*, 331(1):299–308, **1998**. doi: 10.1042/bj3310299.

[21] Sarbassov D. D. Phosphorylation and Regulation of Akt/PKB by the Rictor-mTOR Complex. *Science*, 307(5712):1098–1101, **2005**. doi: 10.1126/science.1106148.

[22] De Luca A, Maiello M. R, D'Alessio A, Pergameno M, and Normanno N. The RAS/RAF/MEK/ERK and the PI3K/AKT signalling pathways: role in cancer pathogenesis and implications for therapeutic approaches. *Expert Opinion on Therapeutic Targets*, 16(sup2): S17–S27, **2012**. doi: 10.1517/14728222.2011.639361.

[23] Hales E. C, Orr S. M, Larson Gedman A, Taub J. W, and Matherly L. H. Notch1 Receptor Regulates AKT Protein Activation Loop (Thr 308 ) Dephosphorylation through Modulation of the PP2A Phosphatase in Phosphatase and Tensin Homolog (PTEN)-null T-cell Acute Lymphoblastic Leukemia Cells. *Journal of Biological Chemistry*, 288(31):22836–22848, **2013**. doi: 10.1074/jbc.M113.451625.

[24] Brognard J, Sierecki E, Gao T, and Newton A. C. PHLPP and a Second Isoform, PHLPP2, Differentially Attenuate the Amplitude of Akt Signaling by Regulating Distinct Akt Isoforms. *Molecular Cell*, 25(6):917–931, **2007**. doi: 10.1016/J.MOLCEL.2007.02.017.

[25] Chardin P, Camonis J, Gale N, Aelst van L, Schlessinger J, Wigler M, and Bar-Sagi D. Human Sos1: a guanine nucleotide exchange factor for Ras that binds to GRB2. *Science*, 260(5112): 1338–1343, **1993**. doi: 10.1126/science.8493579.

[26] Robbins D. J, Cheng M, Zhen E, Vanderbilt C. A, Feig L. A, and Cobb M. H. Evidence for a Ras-dependent extracellular signal-regulated protein kinase (ERK) cascade. *Proceedings of the National Academy of Sciences of the United States of America*, 89(15):6924–8, **1992**.

[27] Avruch J. MAP kinase pathways: The first twenty years. *Biochimica et Biophysica Acta (BBA) - Molecular Cell Research*, 1773(8):1150–1160, **2007**. doi: 10.1016/j.bbamcr.2006.11.006.

[28] Rodriguez-Viciana P, Warne P. H, Dhand R, Vanhaesebroeck B, Gout I, Fry M. J, Waterfield M. D, and Downward J. Phosphatidylinositol-3-OH kinase direct target of Ras. *Nature*, 370(6490): 527–532, **1994**. doi: 10.1038/370527a0.

[29] Therrien M, Chang H. C, Solomon N. M, Karim F. D, Wassarman D. a, and Rubin G. M. KSR, a novel protein kinase required for RAS signal transduction. *Cell*, 83(6):879–88, **1995**. doi: 0092-8674(95)90204-X[pii].

[30] Kim H. J and Bar-Sagi D. Modulation of signalling by Sprouty: a developing story. *Nature Reviews Molecular Cell Biology*, 5(6):441–450, **2004**. doi: 10.1038/nrm1400.

[31] Keyse S. M. Dual-specificity MAP kinase phosphatases (MKPs) and cancer. *Cancer and Metastasis Reviews*, 27(2):253–261, **2008**. doi: 10.1007/s10555-008-9123-1.

[32] Baselga J, Norton L, Albanell J, Kim Y. M, and Mendelsohn J. Recombinant humanized anti-HER2 antibody (Herceptin) enhances the antitumor activity of paclitaxel and doxorubicin against HER2/neu overexpressing human breast cancer xenografts. *Cancer research*, 58(13):2825–31, **1998**. doi: 10.1158/0008-5472.CAN-16-2269.

[33] Harbeck N, Beckmann M. W, Rody A, Schneeweiss A, Müller V, Fehm T, Marschner N, Gluz O, Schrader I, Heinrich G, Untch M, and Jackisch C. HER2 dimerization inhibitor pertuzumab - Mode of action and clinical data in breast cancer. *Breast Care*, 8(1):49–55, **2013**. doi: 10.1159/000346837.

[34] Xia W, Mullin R. J, Keith B. R, Liu L.-H, Ma H, Rusnak D. W, Owens G, Alligood K. J, and Spector N. L. Anti-tumor activity of GW572016: a dual tyrosine kinase inhibitor blocks EGF activation of EGFR/erbB2 and downstream Erk1/2 and AKT pathways. *Oncogene*, 21(41): 6255–6263, **2002**. doi: 10.1038/sj.onc.1205794.

[35] Rabindran S. K, Discafani C. M, Rosfjord E. C, Baxter M, Floyd M. B, Golas J, Hallett W. A, Johnson B. D, Nilakantan R, Overbeek E, Reich M. F, Shen R, Shi X, Tsou H.-R, Wang Y.-F, and Wissner A. Antitumor Activity of HKI-272, an Orally Active, Irreversible Inhibitor of the HER-2 Tyrosine Kinase. *Cancer Research*, 64(11):3958–3965, **2004**. doi: 10.1158/0008-5472.CAN-03-2868.

[36] Barlaam B, Anderton J, Ballard P, Bradbury R. H, Hennequin L. F. A, Hickinson D. M, Kettle J. G, Kirk G, Klinowska T, Lambert-Van Der Brempt C, Trigwell C, Vincent J, and Ogilvie D. Discovery of AZD8931, an equipotent, reversible inhibitor of signaling by EGFR, HER2, and HER3 receptors. *ACS Medicinal Chemistry Letters*, 4(8):742–746, **2013**. doi: 10.1021/ml400146c.

[37] Genentech. Herceptin, Trastuzumab FDA Fact Sheet, 2000.

[38] Scheuer W, Friess T, Burtscher H, Bossenmaier B, Endl J, and Hasmann M. Strongly Enhanced Antitumor Activity of Trastuzumab and Pertuzumab Combination Treatment on HER2-Positive Human Xenograft Tumor Models. *Cancer Research*, 69(24):9330–9336, **2009**. doi: 10.1158/0008-5472.CAN-08-4597.

[39] Arnould L, Gelly M, Penault-Llorca F, Benoit L, Bonnetain F, Migeon C, Cabaret V, Fermeaux V, Bertheau P, Garnier J, Jeannin J.-F, and Coudert B. Trastuzumab-based treatment of HER2-positive breast cancer: an antibody-dependent cellular cytotoxicity mechanism? *British Journal of Cancer*, 94(2):259–267, **2006**. doi: 10.1038/sj.bjc.6602930.

[40] Kono K, Kawaida H, Takahashi A, Sugai H, Mimura K, Miyagawa N, Omata H, and Fujii H. CD4(+)CD25high regulatory T cells increase with tumor stage in patients with gastric and esophageal cancers. *Cancer Immunology, Immunotherapy*, 55(9):1064–1071, **2006**. doi: 10.1007/s00262-005-0092-8.

[41] Junttila T. T, Li G, Parsons K, Phillips G. L, and Sliwkowski M. X. Trastuzumab-DM1 (T-DM1) retains all the mechanisms of action of trastuzumab and efficiently inhibits growth of lapatinib insensitive breast cancer. *Breast Cancer Research and Treatment*, 128(2):347–356, **2011**. doi: 10.1007/s10549-010-1090-x.

[42] Verma S, Goyal S, Kumari A, Singh A, Jamal S, and Grover A. Structural investigations on mechanism of lapatinib resistance caused by HER-2 mutants. *PLOS ONE*, 13(2):e0190942, **2018**. doi: 10.1371/journal.pone.0190942.

[43] Ballard P, Swaisland H. C, Malone M. D, Sarda S, Ghiorghiu S, and Wilbraham D. Metabolic disposition of AZD8931, an oral equipotent inhibitor of EGFR, HER2 and HER3 signalling, in rat, dog and man. *Xenobiotica*, 44(12):1083–1098, **2014**. doi: 10.3109/00498254.2014.938257.

[44] Castellino S, O'Mara M, Koch K, Borts D. J, Bowers G. D, and MacLauchlin C. Human metabolism of lapatinib, a dual kinase inhibitor: Implications for hepatotoxicity. *Drug Metabolism and Disposition*, 40(1):139–150, **2012**. doi: 10.1124/dmd.111.040949.

[45] Genentech. Pertuzumab prescribing information, 2012.

[46] Gianni L, Pienkowski T, Im Y. H, Roman L, Tseng L. M, Liu M. C, Lluch A, Staroslawska E, Haba-Rodriguez de la J, Im S. A, Pedrini J. L, Poirier B, Morandi P, Semiglazov V, Srimuninnimit V, Bianchi G, Szado T, Ratnayake J, Ross G, and Valagussa P. Efficacy and safety of neoadjuvant pertuzumab and trastuzumab in women with locally advanced, inflammatory, or early HER2-positive breast cancer (NeoSphere): A randomised multicentre, open-label, phase 2 trial. *The Lancet Oncology*, 13(1):25–32, **2012**. doi: 10.1016/S1470-2045(11)70336-9.

[47] Gianni L, Pienkowski T, Im Y.-H, Tseng L.-M, Liu M.-C, Lluch A, Starosławska E, Haba-Rodriguez de la J, Im S.-A, Pedrini J. L, Poirier B, Morandi P, Semiglazov V, Srimuninnimit V, Bianchi G. V, Magazzù D, McNally V, Douthwaite H, Ross G, and Valagussa P. 5-year analysis of neoadjuvant pertuzumab and trastuzumab in patients with locally advanced, inflammatory, or early-stage HER2-positive breast cancer (NeoSphere): a multicentre, open-label, phase 2 randomised trial. *The Lancet Oncology*, 17(6):791–800, **2016**. doi: 10.1016/S1470-2045(16)00163-7.

[48] Waddell T, Kotsori A, Constantinidou A, Yousaf N, Ashley S, Parton M, Allen M, Starling N, Papadopoulos P, O'Brien M, Smith I, and Johnston S. Trastuzumab beyond progression in HER2-positive advanced breast cancer: The Royal Marsden experience. *British Journal of Cancer*, 104(11):1675–1679, **2011**. doi: 10.1038/bjc.2011.138.

[49] Fujimoto-Ouchi K, Sekiguchi F, Yamamoto K, Shirane M, Yamashita Y, and Mori K. Preclinical study of prolonged administration of trastuzumab as combination therapy after disease progression during trastuzumab monotherapy. *Cancer Chemotherapy and Pharmacology*, 66(2):269–276, **2010**. doi: 10.1007/s00280-009-1160-0.

[50] National Institute for Health and Care Excellence. Advanced breast cancer: diagnosis and treatment. Technical report, 2017.

[51] Denduluri N, Somerfield M. R, Eisen A, Holloway J. N, Hurria A, King T. A, Lyman G. H, Partridge A. H, Telli M. L, Trudeau M. E, and Wolff A. C. Selection of Optimal Adjuvant Chemotherapy Regimens for Human Epidermal Growth Factor Receptor 2 (HER2) –Negative and Adjuvant Targeted Therapy for HER2-Positive Breast Cancers: An American Society of Clinical Oncology Guideline Adaptation of the Cancer C. *Journal of Clinical Oncology*, 34(20):2416–2427, **2016**. doi: 10.1200/JCO.2016.67.0182.

[52] Novartis. Lapatinib prescribing information, 2007.

[53] Schwartzberg L. S, Franco S. X, Florance A, O'Rourke L, Maltzman J, and Johnston S. Lapatinib plus Letrozole as First-Line Therapy for HER-2+ Hormone Receptor-Positive Metastatic Breast Cancer. *The Oncologist*, 15(2):122–129, **2010**. doi: 10.1634/theoncologist.2009-0240.

[54] Blackwell K. L, Burstein H. J, Storniolo A. M, Rugo H. S, Sledge G, Aktan G, Ellis C, Florance A, Vukelja S, Bischoff J, Baselga J, and O'Shaughnessy J. Overall Survival Benefit With Lapatinib in Combination With Trastuzumab for Patients With Human Epidermal Growth Factor Receptor 2–Positive Metastatic Breast Cancer: Final Results From the EGF104900 Study. *Journal of Clinical Oncology*, 30(21):2585–2592, **2012**. doi: 10.1200/JCO.2011.35.6725.

[55] FDA. Kadcyla (trastuzumab emtansine) prescribing information, 2013.

[56] Verma S, Miles D, Gianni L, Krop I. E, Welslau M, Baselga J, Pegram M, Oh D.-Y, Diéras V, Guardino E, Fang L, Lu M. W, Olsen S, and Blackwell K. Trastuzumab Emtansine for HER2-Positive Advanced Breast Cancer. *New England Journal of Medicine*, 367(19):1783–1791, **2012**. doi: 10.1056/NEJMoa1209124.

[57] FDA. Nerlynx (neratinib) prescribing information, 2017.

[58] Committee for Medicinal Products for Human Use. Refusal of the marketing authorisation for Nerlynx (neratinib). Technical report, 2018.

[59] Chan A, Delaloge S, Holmes F. A, Moy B, Iwata H, Harvey V. J, Robert N. J, Silovski T, Gokmen E, Minckwitz von G, Ejlertsen B, Chia S. K, Mansi J, Barrios C. H, Gnant M, Buyse M, Gore I, Smith J, Harker G, Masuda N, Petrakova K, Zotano A. G, Iannotti N, Rodriguez G, Tassone P, Wong A, Bryce R, Ye Y, Yao B, and Martin M. Neratinib after trastuzumab-based adjuvant therapy in patients with HER2-positive breast cancer (ExteNET): A multicentre, randomised, double-blind, placebo-controlled, phase 3 trial. *The Lancet Oncology*, 17(3):367–377, **2016**. doi: 10.1016/S1470-2045(15)00551-3.

[60] Kurata T, Tsurutani J, Fujisaka Y, Okamoto W, Hayashi H, Kawakami H, Shin E, Hayashi N, and Nakagawa K. Inhibition of EGFR, HER2 and HER3 signaling with AZD8931 alone and in combination with paclitaxel: Phase I study in Japanese patients with advanced solid malignancies and advanced breast cancer. *Investigational New Drugs*, 32(5):946–954, **2014**. doi: 10.1007/s10637-014-0112-7.

[61] Tjulandin S, Moiseyenko V, Semiglazov V, Manikhas G, Learoyd M, Saunders A, Stuart M, and Keilholz U. Phase I, dose-finding study of AZD8931, an inhibitor of EGFR (erbB1), HER2 (erbB2) and HER3 (erbB3) signaling, in patients with advanced solid tumors. *Investigational New Drugs*, 32(1):145–153, **2014**. doi: 10.1007/s10637-013-9963-6.

[62] Ghiorghiu S. Assess the Efficacy of AZD8931 in Combination With Paclitaxel Versus Paclitaxel Alone in Patients With Gastric Cancer. Technical report, AstraZeneca, 2014.

[63] Hickinson D. M, Klinowska T, Speake G, Vincent J, Trigwell C, Anderton J, Beck S, Marshall G, Davenport S, Callis R, Mills E, Grosios K, Smith P, Barlaam B, Wilkinson R. W, and Ogilvie D. AZD8931, an equipotent, reversible inhibitor of signaling by epidermal growth factor receptor, ERBB2 (HER2), and ERBB3: a unique agent for simultaneous ERBB receptor blockade in cancer. *Clinical Cancer Research*, 16(4):1159–69, **2010**. doi: 10.1158/1078-0432.CCR-09-2353.

[64] Guarneri V, Dieci M. V, Barbieri E, Piacentini F, Omarini C, Ficarra G, Bettelli S, and Conte P. F. Loss of HER2 positivity and prognosis after neoadjuvant therapy in HER2-positive breast cancer patients. *Annals of Oncology*, 24(12):2990–2994, **2013**. doi: 10.1093/annonc/mdt364.

[65] Mittendorf E. A, Wu Y, Scaltriti M, Meric-bernstam F, Hunt K. K, Dawood S, Esteva F. J, Buzdar A. U, Chen H, Eksambi S, Hortobagyi G. N, Baselga J, and Gonzalez-angulo A. M. Loss of HER2 Amplification Following Trastuzumab-Based Neoadjuvant Systemic Therapy and Survival Outcomes. *Clinical Cancer Research*, 15(23):7381–7389, **2009**. doi: 10.1158/1078-0432.CCR-09-1735.

[66] Lower E. E, Glass E, Blau R, and Harman S. HER-2/neu expression in primary and metastatic breast cancer. *Breast Cancer Research and Treatment*, 113(2):301–306, **2009**. doi: 10.1007/s10549-008-9931-6.

[67] Lower E, Khan S, Kennedy D, and Baughman R. Discordance of the estrogen receptor and HER-2/neu in breast cancer from primary lesion to first and second metastatic site. *Breast Cancer: Targets and Therapy*, Volume 9:515–520, **2017**. doi: 10.2147/BCTT.S137709.

[68] De Gregorio A, Friedl T. W, Huober J, Scholz C, De Gregorio N, Rack B, Trapp E, Alunni-Fabbroni M, Riethdorf S, Mueller V, Schneeweiss A, Pantel K, Meier-Stiegen F, Jaeger B, Hartkopf A, Taran F.-A, Fasching P. A, Janni W, and Fehm T. Discordance in Human Epidermal Growth Factor Receptor 2 (HER2) Phenotype Between Primary Tumor and Circulating Tumor Cells in Women With HER2-Negative Metastatic Breast Cancer. *JCO Precision Oncology*, 2(1):1–12, **2017**. doi: 10.1200/PO.17.00023.

[69] Narayan M, Wilken J. A, Harris L. N, Baron A. T, Kimbler K. D, and Maihle N. J. Trastuzumab-Induced HER Reprogramming in "Resistant" Breast Carcinoma Cells. *Cancer Research*, 69(6):2191–2194, **2009**. doi: 10.1158/0008-5472.CAN-08-1056.

[70] Vu T and Claret F. X. Trastuzumab: updated mechanisms of action and resistance in breast cancer. *Frontiers in oncology*, 2(June):62, **2012**. doi: 10.3389/fonc.2012.00062.

[71] Gajria D and Chandarlapaty S. HER2-amplified breast cancer: mechanisms of trastuzumab resistance and novel targeted therapies. *Expert Review of Anticancer Therapy*, 11(2):263–275, **2011**. doi: 10.1586/era.10.226.

[72] Wang Y.-C, Morrison G, Gillihan R, Guo J, Ward R. M, Fu X, Botero M. F, Healy N. A, Hilsenbeck S. G, Phillips G. L, Chamness G. C, Rimawi M. F, Osborne C. K, and Schiff R. Different mechanisms for resistance to trastuzumab versus lapatinib in HER2- positive breast cancers - role of estrogen receptor and HER2 reactivation. *Breast Cancer Research*, 13(6):R121, **2011**. doi: 10.1186/bcr3067.

[73] Nagy P, Friedländer E, Tanner M, Kapanen A. I, Carraway K. L, Isola J, and Jovin T. M. Decreased accessibility and lack of activation of ErbB2 in JIMT-1, a herceptin-resistant, MUC4-expressing breast cancer cell line. *Cancer research*, 65(2):473–82, **2005**.

[74] Sáez R, Molina M. A, Ramsey E. E, Rojo F, Keenan E. J, Albanell J, Lluch A, Garcia-Conde J, Baselga J, and Clinton G. M. p95HER-2 predicts worse outcome in patients with HER-2-positive breast cancer. *Clinical Cancer Research*, 12(2):424–431, **2006**. doi: 10.1158/1078-0432.CCR-05-1807.

[75] Sperinde J, Jin X, Banerjee J, Penuel E, Saha A, Diedrich G, Huang W, Leitzel K, Weidler J, Ali S. M, Fuchs E. M, Singer C. F, Köstler W. J, Bates M, Parry G, Winslow J, and Lipton A. Quantitation of p95HER2 in paraffin sections by using a p95-specific antibody and correlation with outcome in a cohort of trastuzumab-treated breast cancer patients. *Clinical Cancer Research*, 16(16):4226–4235, **2010**. doi: 10.1158/1078-0432.CCR-10-0410.

[76] Molina M. A, Sáez R, Ramsey E. E, Garcia-Barchino M.-J, Rojo F, Evans A. J, Albanell J, Keenan E. J, Lluch A, García-Conde J, Baselga J, and Clinton G. M. NH(2)-terminal truncated HER-2 protein but not full-length receptor is associated with nodal metastasis in human breast cancer. *Clinical cancer research : an official journal of the American Association for Cancer Research*, 8(2):347–53, **2002**.

[77] Tanner M, Kapanen A. I, Junttila T, Raheem O, Grenman S, Elo J, Elenius K, and Isola J. Characterization of a novel cell line established from a patient with Herceptin-resistant breast cancer. *Molecular cancer therapeutics*, 3(12):1585–92, **2004**. doi: 3/12/1585[pii].

[78] Mani S. A, Guo W, Liao M.-J, Eaton E. N, Ayyanan A, Zhou A. Y, Brooks M, Reinhard F, Zhang C. C, Shipitsin M, Campbell L. L, Polyak K, Brisken C, Yang J, and Weinberg R. A. The Epithelial-Mesenchymal Transition Generates Cells with Properties of Stem Cells. *Cell*, 133(4): 704–715, **2008**. doi: 10.1016/j.cell.2008.03.027.

[79] Pályi-Krekk Z, Barok M, Isola J, Tammi M, Szöllo˝si J, and Nagy P. Hyaluronan-induced masking of ErbB2 and CD44-enhanced trastuzumab internalisation in trastuzumab resistant breast cancer. *European Journal of Cancer*, 43(16):2423–2433, **2007**. doi: 10.1016/j.ejca.2007.08.018.

[80] Liu P. C, Liu X, Li Y, Covington M, Wynn R, Huber R, Hillman M, Yang G, Ellis D, Marando C, Katiyar K, Bradley J, Abremski K, Stow M, Rupar M, Zhuo J, Li Y.-L, Lin Q, Burns D, Xu M, Zhang C, Qian D.-Q, He C, Sharief V, Weng L, Agrios C, Shi E, Metcalf B, Newton R, Friedman S, Yao W, Scherle P. A, Hollis G, and Burn T. C. Identification of ADAM10 as a major source of HER2 ectodomain sheddase activity in HER2 overexpressing breast cancer cells. *Cancer Biology & Therapy*, 5(6):657–664, **2006**. doi: 10.4161/cbt.5.6.2708.

[81] Radisky E. S and Radisky D. C. Matrix Metalloproteinase-Induced Epithelial-Mesenchymal Transition in Breast Cancer. *Journal of Mammary Gland Biology and Neoplasia*, 15(2):201–212, **2010**. doi: 10.1007/s10911-010-9177-x.

[82] Hanahan D and Weinberg R. A. Hallmarks of Cancer: The Next Generation. *Cell*, 144(5):646–674, **2011**. doi: 10.1016/j.cell.2011.02.013.

[83] Marcucci F, Stassi G, and De Maria R. Epithelial–mesenchymal transition: a new target in anticancer drug discovery. *Nature Reviews Drug Discovery*, 15(5):311–325, **2016**. doi: 10.1038/nrd.2015.13.

[84] Creedon H, Balderstone L. A, Muir M, Balla J, Gomez-Cuadrado L, Tracey N, Loane J, Klinowska T, Muller W. J, and Brunton V. G. Use of a genetically engineered mouse model as a preclinical tool for HER2 breast cancer. *Disease models & mechanisms*, 9(2):131–40, **2016**. doi: 10.1242/dmm.023143.

[85] Zhang X, Zhang Z, Zhang Q, Zhang Q, Sun P, Xiang R, Ren G, and Yang S. ZEB1 confers chemotherapeutic resistance to breast cancer by activating ATM. *Cell Death & Disease*, 9(2):57, **2018**. doi: 10.1038/s41419-017-0087-3.

[86] Zheng X, Carstens J. L, Kim J, Scheible M, Kaye J, Sugimoto H, Wu C.-c, Lebleu V. S, and Kalluri R. Epithelial-to-mesenchymal transition is dispensable for metastasis but induces chemoresistance in pancreatic cancer. *Nature*, 527(7579):525–530, **2015**. doi: 10.1038/nature16064.

[87] Ingthorsson S, Andersen K, Hilmarsdottir B, Maelandsmo G. M, Magnusson M. K, and Gudjonsson T. HER2 induced EMT and tumorigenicity in breast epithelial progenitor cells is inhibited by coexpression of EGFR. *Oncogene*, 35(November):1–12, **2015**. doi: 10.1038/onc.2015.489.

[88] Xu H, Tian Y, Yuan X, Liu Y, Wu H, Liu Q, Wu G. S, and Wu K. Enrichment of CD44 in basal-type breast cancer correlates with EMT , cancer stem cell gene profile , and prognosis. pages 431–444, **2016**. doi: 10.2147/OTT.S97192.

[89] Yoshida T, Song L, Bai Y, Kinose F, Li J, Ohaegbulam K. C, Muñoz-Antonia T, Qu X, Eschrich S, Uramoto H, Tanaka F, Nasarre P, Gemmill R. M, Roche J, Drabkin H. A, and Haura E. B. ZEB1 Mediates Acquired Resistance to the Epidermal Growth Factor Receptor-Tyrosine Kinase Inhibitors in Non-Small Cell Lung Cancer. *PLOS ONE*, 11(1):e0147344, **2016**. doi: 10.1371/journal.pone.0147344.

[90] Burnett J. P, Korkaya H, Ouzounova M. D, Jiang H, Conley S. J, Newman B. W, Sun L, Connarn J. N, Chen C.-S, Zhang N, Wicha M. S, and Sun D. Trastuzumab resistance induces EMT to transform HER2+ PTEN to a triple negative breast cancer that requires unique treatment options. *Scientific Reports*, 5(22):15821, **2015**. doi: 10.1038/srep15821.

[91] Korkaya H, Kim G. I, Davis A, Malik F, Henry N. L, Ithimakin S, Quraishi A. A, Tawakkol N, D'Angelo R, Paulson A. K, Chung S, Luther T, Paholak H. J, Liu S, Hassan K. A, Zen Q, Clouthier S. G, and Wicha M. S. Activation of an IL6 Inflammatory Loop Mediates Trastuzumab Resistance in HER2+ Breast Cancer by Expanding the Cancer Stem Cell Population. *Molecular Cell*, 47(4):570–584, **2012**. doi: 10.1016/j.molcel.2012.06.014.

[92] Tang Y, Tang Y, and Cheng Y.-s. miR-34a inhibits pancreatic cancer progression through Snail1-mediated epithelial–mesenchymal transition and the Notch signaling pathway. *Scientific Reports*, 7(November 2016):38232, **2017**. doi: 10.1038/srep38232.

[93] Beg M. S, Brenner A. J, Sachdev J, Borad M, Kang Y.-K, Stoudemire J, Smith S, Bader A. G, Kim S, and Hong D. S. Phase I study of MRX34, a liposomal miR-34a mimic, administered twice weekly in patients with advanced solid tumors. *Investigational New Drugs*, 35(2):180–188, **2017**. doi: 10.1007/s10637-016-0407-y.

[94] Wu F, Li J, Jang C, Wang J, and Xiong J. The role of Axl in drug resistance and epithelial-to-mesenchymal transition of non-small cell lung carcinoma. *International journal of clinical and experimental pathology*, 7(10):6653–61, **2014**.

[95] Lee A.-F, Chen M.-C, Chen C.-J, Yang C.-J, Huang M.-S, and Liu Y.-P. Reverse epithelial-mesenchymal transition contributes to the regain of drug sensitivity in tyrosine kinase inhibitor-resistant non-small cell lung cancer cells. *PLOS ONE*, 12(7):e0180383, **2017**. doi: 10.1371/journal.pone.0180383.

[96] Shen Y, Chen X, He J, Liao D, and Zu X. Axl inhibitors as novel cancer therapeutic agents. *Life Sciences*, 198(December 2017):99–111, **2018**. doi: 10.1016/j.lfs.2018.02.033.

[97] Ogiso H, Ishitani R, Nureki O, Fukai S, Yamanaka M, Kim J.-H, Saito K, Sakamoto A, Inoue M, Shirouzu M, and Yokoyama S. Crystal Structure of the Complex of Human Epidermal Growth Factor and Receptor Extracellular Domains. *Cell*, 110(6):775–787, **2002**. doi: 10.1016/S0092-8674(02)00963-7.

[98] Martino de M, Zhuang D, Klatte T, Rieken M, Rouprêt M, Xylinas E, Clozel T, Krzywinski M, Elemento O, and Shariat S. F. Impact of ERBB2 mutations on in vitro sensitivity of bladder cancer to lapatinib. *Cancer Biology & Therapy*, 15(9):1239–1247, **2014**. doi: 10.4161/cbt.29687.

[99] Kavuri S. M, Jain N, Galimi F, Cottino F, Leto S. M, Migliardi G, Searleman A. C, Shen W, Monsey J, Trusolino L, Jacobs S. A, Bertotti A, and Bose R. HER2 activating mutations are targets for colorectal cancer treatment. *Cancer Discovery*, 5(8):832–841, **2015**. doi: 10.1158/2159-8290.CD-14-1211.

[100] De Yao J. T, Sun D, Galehouse D, Shorten S, Haller N. A, and Rehmus E. H. HER2Δ16 expression in HER2-positive breast cancer. *Journal of Clinical Oncology*, 32(26_suppl):31–31, **2014**. doi: 10.1200/jco.2014.32.26_suppl.31.

[101] Castagnoli L, Iezzi M, Ghedini G. C, Ciravolo V, Marzano G, Lamolinara A, Zappasodi R, Gasparini P, Campiglio M, Amici A, Chiodoni C, Palladini A, Lollini P. L, Triulzi T, Menard S, Nanni P, Tagliabue E, and Pupa S. M. Activated d16HER2 Homodimers and SRC Kinase Mediate Optimal Efficacy for Trastuzumab. *Cancer Research*, 74(21):6248–6259, **2014**. doi: 10.1158/0008-5472.CAN-14-0983.

[102] Finger C, Escher C, and Schneider D. The Single Transmembrane Domains of Human Receptor Tyrosine Kinases Encode Self-Interactions. *Science Signaling*, 2(89):ra56–ra56, **2009**. doi: 10.1126/scisignal.2000547.

[103] Bose R, Kavuri S. M, Searleman A. C, Shen W, Shen D, Koboldt D. C, Monsey J, Goel N, Aronson A. B, Li S, Ma C. X, Ding L, Mardis E. R, and Ellis M. J. Activating HER2 Mutations in HER2 Gene Amplification Negative Breast Cancer. *Cancer Discovery*, 3(2):224–237, **2013**. doi: 10.1158/2159-8290.CD-12-0349.

[104] Wang S. E, Narasanna A, Perez-Torres M, Xiang B, Wu F. Y, Yang S, Carpenter G, Gazdar A. F, Muthuswamy S. K, and Arteaga C. L. HER2 kinase domain mutation results in constitutive phosphorylation and activation of HER2 and EGFR and resistance to EGFR tyrosine kinase inhibitors. *Cancer Cell*, 10(1):25–38, **2006**. doi: 10.1016/j.ccr.2006.05.023.

[105] Shimamura T, Ji H, Minami Y, Thomas R. K, Lowell A. M, Shah K, Greulich H, Glatt K. A, Meyerson M, Shapiro G. I, and Wong K.-K. Non–Small-Cell Lung Cancer and Ba/F3 Transformed Cells Harboring the ERBB2 G776insV_G/C Mutation Are Sensitive to the Dual-Specific Epidermal Growth Factor Receptor and ERBB2 Inhibitor HKI-272. *Cancer Research*, 66(13):6487–6491, **2006**. doi: 10.1158/0008-5472.CAN-06-0971.

[106] Perera S. A, Li D, Shimamura T, Raso M. G, Ji H, Chen L, Borgman C. L, Zaghlul S, Brandstetter K. A, Kubo S, Takahashi M, Chirieac L. R, Padera R. F, Bronson R. T, Shapiro G. I, Greulich H, Meyerson M, Guertler U, Chesa P. G, Solca F, Wistuba I. I, and Wong K.-K. HER2YVMA drives rapid development of adenosquamous lung tumors in mice that are sensitive to BIBW2992 and rapamycin combination therapy. *Proceedings of the National Academy of Sciences*, 106(2):474–479, **2009**. doi: 10.1073/pnas.0808930106.

[107] Forbes S. A, Beare D, Gunasekaran P, Leung K, Bindal N, Boutselakis H, Ding M, Bamford S, Cole C, Ward S, Kok C. Y, Jia M, De T, Teague J. W, Stratton M. R, McDermott U, and Campbell P. J. COSMIC: exploring the world's knowledge of somatic mutations in human cancer. *Nucleic Acids Research*, 43(D1):D805–D811, **2015**. doi: 10.1093/nar/gku1075.

[108] Mishra R, Hanker A. B, and Garrett J. T. Genomic alterations of ERBB receptors in cancer: clinical implications. *Oncotarget*, 8(69):114371–114392, **2017**. doi: 10.18632/oncotarget.22825.

[109] Stern H. M, Gardner H, Burzykowski T, Elatre W, O'Brien C, Lackner M. R, Pestano G. A, Santiago A, Villalobos I, Eiermann W, Pienkowski T, Martin M, Robert N, Crown J, Nuciforo P, Bee V, Mackey J, Slamon D. J, and Press M. F. PTEN Loss Is Associated with Worse Outcome in HER2-Amplified Breast Cancer Patients but Is Not Associated with Trastuzumab Resistance. *Clinical Cancer Research*, 21(9):2065–2074, **2015**. doi: 10.1158/1078-0432.CCR-14-2993.

[110] Dobashi Y, Sato E, Oda Y, Inazawa J, and Ooi A. Significance of Akt activation and AKT gene increases in soft tissue tumors. *Human Pathology*, 45(1):127–136, **2014**. doi: 10.1016/j.humpath.2013.06.024.

[111] Ebbesen S. H, Scaltriti M, Bialucha C. U, Morse N, Kastenhuber E. R, Wen H. Y, Dow L. E, Baselga J, and Lowe S. W. Pten loss promotes MAPK pathway dependency in HER2/neu breast carcinomas. *Proceedings of the National Academy of Sciences*, 113(11):3030–3035, **2016**. doi: 10.1073/pnas.1523693113.

[112] Scheffzek K. The Ras-RasGAP Complex: Structural Basis for GTPase Activation and Its Loss in Oncogenic Ras Mutants. *Science*, 277(5324):333–338, **1997**. doi: 10.1126/science.277.5324.333.

[113] Wan P. T, Garnett M. J, Roe S. M, Lee S, Niculescu-Duvaz D, Good V. M, Project C. G, Jones C. M, Marshall C. J, Springer C. J, Barford D, and Marais R. Mechanism of activation of the RAF-ERK signaling pathway by oncogenic mutations of B-RAF. *Cell*, 116(6):855–867, **2004**. doi: 10.1016/S0092-8674(04)00215-6.

[114] Zhao L and Vogt P. K. Helical domain and kinase domain mutations in p110 of phosphatidylinositol 3-kinase induce gain of function by different mechanisms. *Proceedings of the National Academy of Sciences*, 105(7):2652–2657, **2008**. doi: 10.1073/pnas.0712169105.

[115] Nagata Y, Lan K.-H, Zhou X, Tan M, Esteva F. J, Sahin A. A, Klos K. S, Li P, Monia B. P, Nguyen N. T, Hortobagyi G. N, Hung M.-C, and Yu D. PTEN activation contributes to tumor inhibition by trastuzumab, and loss of PTEN predicts trastuzumab resistance in patients. *Cancer Cell*, 6(2):117–127, **2004**. doi: 10.1016/j.ccr.2004.06.022.

[116] Kirkegaard T, Witton C. J, Edwards J, Nielsen K. V, Jensen L. B, Campbell F. M, Cooke T. G, and Bartlett J. M. Molecular alterations in AKT1, AKT2 and AKT3 detected in breast and prostatic cancer by FISH. *Histopathology*, 56(2):203–211, **2010**. doi: 10.1111/j.1365-2559.2009.03467.x.

[117] Keniry M and Parsons R. The role of PTEN signaling perturbations in cancer and in targeted therapy. *Oncogene*, 27(41):5477–5485, **2008**. doi: 10.1038/onc.2008.248.

[118] Normanno N, Luca A. D, Maiello M. R, Campiglio M, Napolitano M, Mancino M, Carotenuto A, Viglietto G, and Menard S. The MEK/MAPK pathway is involved in the resistance of breast cancer cells to the EGFR tyrosine kinase inhibitor gefitinib. *Journal of Cellular Physiology*, 207 (2):420–427, **2006**. doi: 10.1002/jcp.20588.

[119] Serra V, Scaltriti M, Prudkin L, Eichhorn P. J. A, Ibrahim Y. H, Chandarlapaty S, Markman B, Rodriguez O, Guzman M, Rodriguez S, Gili M, Russillo M, Parra J. L, Singh S, Arribas J, Rosen N, and Baselga J. PI3K inhibition results in enhanced HER signaling and acquired ERK dependency in HER2-overexpressing breast cancer. *Oncogene*, 30(22):2547–2557, **2011**. doi: 10.1038/onc.2010.626.

[120] McGivern N, El-Helali A, Mullan P, McNeish I. A, Harkin D. P, Kennedy R. D, and McCabe N. Activation of MAPK signalling results in resistance to saracatinib (AZD0530) in ovarian cancer. *Oncotarget*, 9(4):4722–4736, **2018**. doi: 10.18632/oncotarget.23524.

[121] Manzano J. L, Layos L, Bugés C, de los Llanos Gil M, Vila L, Martínez-Balibrea E, and Martínez-Cardús A. Resistant mechanisms to BRAF inhibitors in melanoma. *Annals of Translational Medicine*, 4(12):237–237, **2016**. doi: 10.21037/atm.2016.06.07.

[122] Piro G, Carbone C, Cataldo I, Di Nicolantonio F, Giacopuzzi S, Aprile G, Simionato F, Boschi F, Zanotto M, Mina M. M, Santoro R, Merz V, Sbarbati A, Manzoni de G, Scarpa A, Tortora G, and Melisi D. An FGFR3 Autocrine Loop Sustains Acquired Resistance to Trastuzumab in Gastric Cancer Patients. *Clinical Cancer Research*, 22(24):6164–6175, **2016**. doi: 10.1158/1078-0432. CCR-16-0178.

[123] Valabrega G, Capellero S, Cavalloni G, Zaccarello G, Petrelli A, Migliardi G, Milani A, Peraldo-Neia C, Gammaitoni L, Sapino A, Pecchioni C, Moggio A, Giordano S, Aglietta M, and Montemurro F. HER2-positive breast cancer cells resistant to trastuzumab and lapatinib lose reliance upon HER2 and are sensitive to the multitargeted kinase inhibitor sorafenib. *Breast Cancer Research and Treatment*, 130(1):29–40, **2011**. doi: 10.1007/s10549-010-1281-5.

[124] Alexander P. B, Chen R, Gong C, Yuan L, Jasper J. S, Ding Y, Markowitz G. J, Yang P, Xu X, McDonnell D. P, Song E, and Wang X. F. Distinct receptor tyrosine kinase subsets mediate anti-HER2 drug resistance in breast cancer. *Journal of Biological Chemistry*, 292(2):748–759, **2017**. doi: 10.1074/jbc.M116.754960.

[125] Zhang S, Huang W.-C, Li P, Guo H, Poh S.-B, Brady S. W, Xiong Y, Tseng L.-M, Li S.-H, Ding Z, Sahin A. A, Esteva F. J, Hortobagyi G. N, and Yu D. Combating trastuzumab resistance by targeting SRC, a common node downstream of multiple resistance pathways. *Nature Medicine*, 17 (4):461–469, **2011**. doi: 10.1038/nm.2309.

[126] Fang H, Jin J, Huang D, Yang F, and Guan X. PAI-1 induces Src inhibitor resistance via CCL5 in HER2-positive breast cancer cells. *Cancer Science*, 109(6):1949–1957, **2018**. doi: 10.1111/cas.13593.

[127] Beadnell T. C, Mishall K. M, Zhou Q, Riffert S. M, Wuensch K. E, Kessler B. E, Corpuz M. L, Jing X, Kim J, Wang G, Tan A. C, and Schweppe R. E. The Mitogen-Activated Protein Kinase Pathway Facilitates Resistance to the Src Inhibitor Dasatinib in Thyroid Cancer. *Molecular Cancer Therapeutics*, 15(8):1952–1963, **2016**. doi: 10.1158/1535-7163.MCT-15-0702.

[128] Yakes F. M, Chen J, Tan J, Yamaguchi K, Shi Y, Yu P, Qian F, Chu F, Bentzien F, Cancilla B, Orf J, You A, Laird A. D, Engst S, Lee L, Lesch J, Chou Y.-C, and Joly A. H. Cabozantinib (XL184), a Novel MET and VEGFR2 Inhibitor, Simultaneously Suppresses Metastasis, Angiogenesis, and Tumor Growth. *Molecular Cancer Therapeutics*, 10(12):2298–2308, **2011**. doi: 10.1158/1535-7163.MCT-11-0264.

[129] Schlumberger M, Elisei R, Müller S, Schöffski P, Brose M, Shah M, Licitra L, Krajewska J, Kreissl M. C, Niederle B, Cohen E. E. W, Wirth L, Ali H, Clary D. O, Yaron Y, Mangeshkar M, Ball D, Nelkin B, and Sherman S. Overall survival analysis of EXAM, a phase III trial of cabozantinib in patients with radiographically progressive medullary thyroid carcinoma. *Annals of Oncology*, 28(11):2813–2819, **2017**. doi: 10.1093/annonc/mdx479.

[130] Choueiri T. K, Escudier B, Powles T, Mainwaring P. N, Rini B. I, Donskov F, Hammers H, Hutson T. E, Lee J.-L, Peltola K, Roth B. J, Bjarnason G. A, Géczi L, Keam B, Maroto P, Heng D. Y, Schmidinger M, Kantoff P. W, Borgman-Hagey A, Hessel C, Scheffold C, Schwab G. M, Tannir N. M, and Motzer R. J. Cabozantinib versus Everolimus in Advanced Renal-Cell Carcinoma. *New England Journal of Medicine*, 373(19):1814–1823, **2015**. doi: 10.1056/NEJMoa1510016.

[131] Trepel J, Mollapour M, Giaccone G, and Neckers L. Targeting the dynamic HSP90 complex in cancer. *Nature Reviews Cancer*, 10(8):537–549, **2010**. doi: 10.1038/nrc2887.

[132] Modi S, Stopeck A, Linden H, Solit D, Chandarlapaty S, Rosen N, D'Andrea G, Dickler M, Moynahan M. E, Sugarman S, Ma W, Patil S, Norton L, Hannah A. L, and Hudis C. HSP90 Inhibition Is Effective in Breast Cancer: A Phase II Trial of Tanespimycin (17-AAG) Plus Trastuzumab in Patients with HER2-Positive Metastatic Breast Cancer Progressing on Trastuzumab. *Clinical Cancer Research*, 17(15):5132–5139, **2011**. doi: 10.1158/1078-0432.CCR-11-0072.

[133] Papanikolaou G and Pantopoulos K. Iron metabolism and toxicity. *Toxicology and Applied Pharmacology*, 202(2):199–211, **2005**. doi: 10.1016/j.taap.2004.06.021.

[134] Crielaard B. J, Lammers T, and Rivella S. Targeting iron metabolism in drug discovery and delivery. *Nature Reviews Drug Discovery*, 16(6):400–423, **2017**. doi: 10.1038/nrd.2016.248.

[135] Nicolas G, Bennoun M, Devaux I, Beaumont C, Grandchamp B, Kahn A, and Vaulont S. Lack of hepcidin gene expression and severe tissue iron overload in upstream stimulatory factor 2 (USF2) knockout mice. *Proceedings of the National Academy of Sciences*, 98(15):8780–8785, **2001**. doi: 10.1073/pnas.151179498.

[136] Fukushima T, Kawabata H, Nakamura T, Iwao H, Nakajima A, Miki M, Sakai T, Sawaki T, Fujita Y, Tanaka M, Masaki Y, Hirose Y, and Umehara H. Iron chelation therapy with deferasirox induced complete remission in a patient with chemotherapy-resistant acute monocytic leukemia. *Anticancer Research*, 31(5):1741–1744, **2011**.

[137] Whitnall M, Howard J, Ponka P, and Richardson D. R. A class of iron chelators with a wide spectrum of potent antitumor activity that overcomes resistance to chemotherapeutics. *Proceedings of the National Academy of Sciences*, 103(40):14901–14906, **2006**. doi: 10.1073/pnas.0604979103.

[138] Lee S. Y, Slagle-Webb B, Schengrund C.-L, and Connor J. Abstract 4065: Association study between iron and cholesterol for the treatment of drug resistant neuroblastoma. *Cancer Research*, 77(13 Supplement):4065–4065, **2017**. doi: 10.1158/1538-7445.AM2017-4065.

[139] Haro K. J, Sheth A, and Scheinberg D. A. Dysregulation of IRP1-Mediated Iron Metabolism Causes Gamma Ray-specific Radioresistance in Leukemia Cells. *PLoS ONE*, 7(11):1–10, **2012**. doi: 10.1371/journal.pone.0048841.

[140] Liu X, Madhankumar A. B, Slagle-Webb B, Sheehan J. M, Surguladze N, and Connor J. R. Heavy chain ferritin siRNA delivered by cationic liposomes increases sensitivity of cancer cells to chemotherapeutic agents. *Cancer Research*, 71(6):2240–2249, **2011**. doi: 10.1158/0008-5472.CAN-10-1375.

[141] Neve R. M, Chin K, Fridlyand J, Yeh J, Baehner F. L, Fevr T, Clark L, Bayani N, Coppe J.-P, Tong F, Speed T, Spellman P. T, DeVries S, Lapuk A, Wang N. J, Kuo W.-L, Stilwell J. L, Pinkel D, Albertson D. G, Waldman F. M, McCormick F, Dickson R. B, Johnson M. D, Lippman M, Ethier S, Gazdar A, and Gray J. W. A collection of breast cancer cell lines for the study of functionally distinct cancer subtypes. *Cancer Cell*, 10(6):515–527, **2006**. doi: 10.1016/j.ccr.2006.10.008.

[142] Holen I, Speirs V, Morrissey B, and Blyth K. In vivo models in breast cancer research: progress, challenges and future directions. *Disease Models & Mechanisms*, 10(4):359–371, **2017**. doi: 10.1242/dmm.028274.

[143] Fleming J. M, Miller T. C, Meyer M. J, Ginsburg E, and Vonderhaar B. K. Local regulation of human breast xenograft models. *Journal of Cellular Physiology*, 224(3):795–806, **2010**. doi: 10.1002/jcp.22190.

[144] Hoffman R. M. Patient-derived orthotopic xenografts: Better mimic of metastasis than subcutaneous xenografts. *Nature Reviews Cancer*, 15(8):451–452, **2015**. doi: 10.1038/nrc3972.

[145] Rottenberg S, Nygren A. O. H, Pajic M, Leeuwen van F. W. B, Heijden van der I, Wetering van de K, Liu X, Visser de K. E, Gilhuijs K. G, Tellingen van O, Schouten J. P, Jonkers J, and Borst P. Selective induction of chemotherapy resistance of mammary tumors in a conditional mouse model for hereditary breast cancer. *Proceedings of the National Academy of Sciences*, 104(29):12117–12122, **2007**. doi: 10.1073/pnas.0702955104.

[146] Akashi Y, Oda T, Ohara Y, Miyamoto R, Hashimoto S, Enomoto T, Yamada K, Kobayashi A, Fukunaga K, and Ohkochi N. Histological Advantages of the Tumor Graft. *Pancreas*, 42(8):1275–1282, **2013**. doi: 10.1097/MPA.0b013e318296f866.

[147] Muller W. J, Sinn E, Pattengale P. K, Wallace R, and Leder P. Single-step induction of mammary adenocarcinoma in transgenic mice bearing the activated c-neu oncogene. *Cell*, 54(1):105–115, **1988**. doi: 10.1016/0092-8674(88)90184-5.

[148] Ursini-Siegel J, Hardy W. R, Zuo D, Lam S. H. L, Sanguin-Gendreau V, Cardiff R. D, Pawson T, and Muller W. J. ShcA signalling is essential for tumour progression in mouse models of human breast cancer. *The EMBO journal*, 27(6):910–20, **2008**. doi: 10.1038/emboj.2008.22.

[149] Schade B, Rao T, Dourdin N, Lesurf R, Hallett M, Cardiff R. D, and Muller W. J. PTEN deficiency in a luminal ErbB-2 mouse model results in dramatic acceleration of mammary tumorigenesis and metastasis. *Journal of Biological Chemistry*, 284(28):19018–19026, **2009**. doi: 10.1074/jbc.M109.018937.

[150] Creedon H, Byron A, Main J, Hayward L, Klinowska T, and Brunton V. G. Exploring mechanisms of acquired resistance to HER2 (human epidermal growth factor receptor 2)-targeted therapies in breast cancer. *Biochemical Society Transactions*, 42(4):822–830, **2014**. doi: 10.1042/BST20140109.

[151] Ye J, Coulouris G, Zaretskaya I, Cutcutache I, Rozen S, and Madden T. L. Primer-BLAST: A tool to design target-specific primers for polymerase chain reaction. *BMC Bioinformatics*, 13(1):134, **2012**. doi: 10.1186/1471-2105-13-134.

[152] Rappsilber J, Ishihama Y, and Mann M. Stop and Go Extraction Tips for Matrix-Assisted Laser Desorption/Ionization, Nanoelectrospray, and LC/MS Sample Pretreatment in Proteomics. *Analytical Chemistry*, 75(3):663–670, **2003**. doi: 10.1021/ac026117i.

[153] Cox J and Mann M. MaxQuant enables high peptide identification rates, individualized p.p.b.-range mass accuracies and proteome-wide protein quantification. *Nature Biotechnology*, 26(12):1367–1372, **2008**. doi: 10.1038/nbt.1511.

[154] Tyanova S, Temu T, Carlson A, Sinitcyn P, Mann M, and Cox J. Visualization of LC-MS/MS proteomics data in MaxQuant. *Proteomics*, 15(8):1453–1456, **2015**. doi: 10.1002/pmic.201400449.

[155] The UniProt Consortium. UniProt: the universal protein knowledgebase. *Nucleic Acids Research*, 45(D1):D158–D169, **2017**. doi: 10.1093/nar/gkw1099.

[156] Wills J, Edwards-Hicks J, and Finch A. J. AssayR: A Simple Mass Spectrometry Software Tool for Targeted Metabolic and Stable Isotope Tracer Analyses. *Analytical Chemistry*, 89(18):9616–9619, **2017**. doi: 10.1021/acs.analchem.7b02401.

[157] Shi J, Li F, Yao X, Mou T, Xu Z, Han Z, Chen S, Li W, Yu J, Qi X, Liu H, and Li G. The HER4-YAP1 axis promotes trastuzumab resistance in HER2-positive gastric cancer by inducing epithelial and mesenchymal transition. *Oncogene*, 37(22):3022–3038, **2018**. doi: 10.1038/s41388-018-0204-5.

[158] Oliveras-Ferraros C, Corominas-Faja B, Cufi S, Vazquez-Martin A, Martin-Castillo B, Iglesias J. M, López-Bonet E, Martin A. G, and Menendez J. A. Epithelial-to-mesenchymal transition (EMT) confers primary resistance to trastuzumab (Herceptin). *Cell Cycle*, 11(21):4020–4032, **2012**. doi: 10.4161/cc.22225.

[159] Hanker A. B, Pfefferle A. D, Balko J. M, Kuba M. G, Young C. D, Sanchez V, Sutton C. R, Cheng H, Perou C. M, Zhao J. J, Cook R. S, and Arteaga C. L. Mutant PIK3CA accelerates HER2-driven transgenic mammary tumors and induces resistance to combinations of anti-HER2 therapies. *Proceedings of the National Academy of Sciences*, 110(35):14372–14377, **2013**. doi: 10.1073/pnas.1303204110.

[160] Elaskalani O, Razak N. B. A, Falasca M, and Metharom P. Epithelial-mesenchymal transition as a therapeutic target for overcoming chemoresistance in pancreatic cancer. *World Journal of Gastrointestinal Oncology*, 9(1):37, **2017**. doi: 10.4251/wjgo.v9.i1.37.

[161] Győrffy B, Lanczky A, Eklund A. C, Denkert C, Budczies J, Li Q, and Szallasi Z. An online survival analysis tool to rapidly assess the effect of 22,277 genes on breast cancer prognosis using microarray data of 1,809 patients. *Breast Cancer Research and Treatment*, 123(3):725–731, **2010**. doi: 10.1007/s10549-009-0674-9.

[162] Burris H. A, Taylor C. W, Jones S. F, Koch K. M, Versola M. J, Arya N, Fleming R. A, Smith D. A, Pandite L, Spector N, and Wilding G. A phase I and pharmacokinetic study of oral lapatinib administered once or twice daily in patients with solid malignancies. *Clinical Cancer Research*, 15 (21):6702–8, **2009**. doi: 10.1158/1078-0432.CCR-09-0369.

[163] Simonelli M, Zucali P. A, Lorenzi E, Rubino L, De Vincenzo F, De Sanctis R, Perrino M, Mancini L, Di Tommaso L, Rimassa L, Masci G, Zuradelli M, Suter M. B, Bertossi M, Fattuzzo G, Giordano L, Roncalli M. G, and Santoro A. Phase i pharmacokinetic and pharmacodynamic study of lapatinib in combination with sorafenib in patients with advanced refractory solid tumors. *European Journal of Cancer*, 49(5):989–998, **2013**. doi: 10.1016/j.ejca.2012.10.016.

[164] Spector N. L, Robertson F. C, Bacus S, Blackwell K, Smith D. A, Glenn K, Cartee L, Harris J, Kimbrough C. L, Gittelman M, Avisar E, Beitsch P, and Koch K. M. Lapatinib plasma and tumor concentrations and effects on HER receptor phosphorylation in tumor. *PLoS ONE*, 10(11):1–17, **2015**. doi: 10.1371/journal.pone.0142845.

[165] Creedon H. *Use of Genetically Engineered Mouse Models in Preclinical Drug Development*. PhD thesis, University of Edinburgh, **2014**.

[166] Pierceall W. E, Woodard A. S, Morrow J. S, Rimm D, and Fearon E. R. Frequent alterations in E-cadherin and alpha- and beta-catenin expression in human breast cancer cell lines. *Oncogene*, 11(7):1319–26, **1995**.

[167] Wilson J. N, Liu W, Brown A. S, and Landgraf R. Binding-induced, turn-on fluorescence of the EGFR/ERBB kinase inhibitor, lapatinib. *Organic & Biomolecular Chemistry*, 13(17):5006–5011, **2015**. doi: 10.1039/C5OB00239G.

[168] Lo P.-K, Kanojia D, Liu X, Singh U. P, Berger F. G, Wang Q, and Chen H. CD49f and CD61 identify Her2/neu-induced mammary tumor-initiating cells that are potentially derived from luminal progenitors and maintained by the integrin–TGF$\beta$ signaling. *Oncogene*, 31(21):2614–2626, **2012**. doi: 10.1038/onc.2011.439.

[169] Gregory P. A, Bracken C. P, Smith E, Bert A. G, Wright J. A, Roslan S, Morris M, Wyatt L, Farshid G, Lim Y.-Y, Lindeman G. J, Shannon M. F, Drew P. A, Khew-Goodall Y, and Goodall G. J. An autocrine TGF- /ZEB/miR-200 signaling network regulates establishment and maintenance of epithelial-mesenchymal transition. *Molecular Biology of the Cell*, 22(10): 1686–1698, **2011**. doi: 10.1091/mbc.E11-02-0103.

[170] Joseph J. V, Conroy S, Tomar T, Eggens-Meijer E, Bhat K, Copray S, Walenkamp A. M, Boddeke E, Balasubramanyian V, Wagemakers M, Den Dunnen W. F, and Kruyt F. A. TGF-$\beta$ is an inducer of ZEB1-dependent mesenchymal transdifferentiation in glioblastoma that is associated with tumor invasion. *Cell Death and Disease*, 5(10):e1443–14, **2014**. doi: 10.1038/cddis.2014.395.

[171] Zhang P, Wei Y, Wang L, Debeb B. G, Yuan Y, Zhang J, Yuan J, Wang M, Chen D, Sun Y, Woodward W. A, Liu Y, Dean D. C, Liang H, Hu Y, Ang K. K, Hung M.-c, Chen J, and Ma L. ATM-mediated stabilization of ZEB1 promotes DNA damage response and radioresistance through CHK1. *Nature Cell Biology*, 16(9):864–875, **2014**. doi: 10.1038/ncb3013.

[172] Zhang J, Zhou C, Jiang H, Liang L, Shi W, Zhang Q, Sun P, Xiang R, Wang Y, and Yang S. ZEB1 induces ER-$\alpha$ promoter hypermethylation and confers antiestrogen resistance in breast cancer. *Cell Death & Disease*, 8(4):e2732–e2732, **2017**. doi: 10.1038/cddis.2017.154.

[173] Kim H. P, Han S. W, Song S. H, Jeong E. G, Lee M. Y, Hwang D, Im S. A, Bang Y. J, and Kim T. Y. Testican-1-mediated epithelial-mesenchymal transition signaling confers acquired resistance to lapatinib in HER2-positive gastric cancer. *British Dental Journal*, 217(1):3334–3341, **2014**. doi: 10.1038/onc.2013.285.

[174] Ma Y, Zheng X, Zhou J, Zhang Y, and Chen K. ZEB1 promotes the progression and metastasis of cervical squamous cell carcinoma via the promotion of epithelial-mesenchymal transition. 8(9): 11258–11267, **2015**.

[175] O'Shea J, Cremona M, Morgan C, Milewska M, Holmes F, Espina V, Liotta L, O'Shaughnessy J, Toomey S, Madden S. F, Carr A, Elster N, Hennessy B. T, and Eustace A. J. A preclinical evaluation of the MEK inhibitor refametinib in HER2-positive breast cancer cell lines including those with acquired resistance to trastuzumab or lapatinib. *Oncotarget*, 8(49):85120–85135, **2017**. doi: 10.18632/oncotarget.19461.

[176] Wang Q, Liu P, Spangle J. M, Von T, Roberts T. M, Lin N. U, Krop I. E, Winer E. P, and Zhao J. J. PI3K-p110$\alpha$ mediates resistance to HER2-targeted therapy in HER2+, PTEN-deficient breast cancers. *Oncogene*, 35(27):3607–3612, **2016**. doi: 10.1038/onc.2015.406.

[177] Nunes J, Zhang H, Angelopoulos N, Chhetri J, Osipo C, Grothey A, Stebbing J, and Giamas G. ATG9A loss confers resistance to trastuzumab via c-Cbl mediated Her2 degradation. *Oncotarget*, 7(19):27599–612, **2016**. doi: 10.18632/oncotarget.8504.

[178] Yao M, Shang Y.-Y, Zhou Z.-W, Yang Y.-X, Wu Y.-S, Guan L.-F, Wang X.-Y, Zhou S.-F, and Wei X. The research on lapatinib in autophagy, cell cycle arrest and epithelial to mesenchymal transition via Wnt/ErK/PI3K-AKT signaling pathway in human cutaneous squamous cell carcinoma. *Journal of Cancer*, 8(2):220–226, **2017**. doi: 10.7150/jca.16850.

[179] Georgescu M.-M. PTEN Tumor Suppressor Network in PI3K-Akt Pathway Control. *Genes & Cancer*, 1(12):1170–1177, **2010**. doi: 10.1177/1947601911407325.

[180] Jenndahl L. E, Isakson P, and Baeckström D. C-erbB2-induced epithelial-mesenchymal transition in mammary epithelial cells is suppressed by cell-cell contact and initiated prior to E-cadherin downregulation. *International Journal of Oncology*, 27(2):439–448, **2005**.

[181] Liu J. B, Feng C. Y, Deng M, Ge D. F, Liu D. C, Mi J. Q, and Feng X. S. E-cadherin expression phenotypes associated with molecular subtypes in invasive non-lobular breast cancer: Evidence from a retrospective study and meta-analysis. *World Journal of Surgical Oncology*, 15(1):1–13, **2017**. doi: 10.1186/s12957-017-1210-8.

[182] O'Brien N. A, Browne B. C, Chow L, Wang Y, Ginther C, Arboleda J, Duffy M. J, Crown J, O'Donovan N, and Slamon D. J. Activated Phosphoinositide 3-Kinase/AKT Signaling Confers Resistance to Trastuzumab but not Lapatinib. *Molecular Cancer Therapeutics*, 9(6):1489–1502, **2010**. doi: 10.1158/1535-7163.MCT-09-1171.

[183] Dai X, Cheng H, Bai Z, and Li J. Breast Cancer Cell Line Classification and Its Relevance with Breast Tumor Subtyping. *Journal of Cancer*, 8(16):3131–3141, **2017**. doi: 10.7150/jca.18457.

[184] Ellison G, Klinowska T, Westwood R. F. R, Docter E, French T, and Fox J. C. Further evidence to support the melanocytic origin of MDA-MB-435. *Molecular pathology : MP*, 55(5):294–9, **2002**. doi: 10.1136/mp.55.5.294.

[185] Jernström S, Hongisto V, Leivonen S.-K, Due E. U, Tadele D. S, Edgren H, Kallioniemi O, Perälä M, Mælandsmo G. M, and Sahlberg K. K. Drug-screening and genomic analyses of HER2-positive breast cancer cell lines reveal predictors for treatment response. *Breast Cancer: Targets and Therapy*, Volume 9:185–198, **2017**. doi: 10.2147/BCTT.S115600.

[186] Sawada T, Chung Y. S, Nakata B, Kubo T, Kondo Y, Sogabe T, Onoda N, Ogawa Y, Yamada N, and Sowa M. Establishment and characterization of a human breast cancer cell line, OCUB-1. *Human cell*, 7(3):138–44, **1994**.

[187] Balderstone L. A. *Use of fluorescent imaging to monitor drug responses in mouse models of tumourigenesis*. PhD thesis, University of Edinburgh, **2013**.

[188] Liu S, Lee J. S, Jie C, Park M. H, Iwakura Y, Patel Y, Soni M, Reisman D, and Chen H. HER2 Overexpression Triggers an IL1$\alpha$ Proinflammatory Circuit to Drive Tumorigenesis and Promote Chemotherapy Resistance. *Cancer Research*, 78(8):2040–2051, **2018**. doi: 10.1158/0008-5472. CAN-17-2761.

[189] Businaro L, De Ninno A, Schiavoni G, Lucarini V, Ciasca G, Gerardino A, Belardelli F, Gabriele L, and Mattei F. Cross talk between cancer and immune cells: exploring complex dynamics in a microfluidic environment. *Lab Chip*, 13(2):229–239, **2013**. doi: 10.1039/C2LC40887B.

[190] Horie M, Saito A, Yamaguchi Y, Ohshima M, and Nagase T. Three-dimensional Co-culture Model for Tumor-stromal Interaction. *Journal of Visualized Experiments*, (96):1–7, **2015**. doi: 10.3791/52469.

[191] Wells R. G. The role of matrix stiffness in regulating cell behavior. *Hepatology*, 47(4):1394–1400, **2008**. doi: 10.1002/hep.22193.

[192] Edalat F, Bae H, Manoucheri S, Cha J. M, and Khademhosseini A. Engineering Approaches Toward Deconstructing and Controlling the Stem Cell Environment. *Annals of Biomedical Engineering*, 40(6):1301–1315, **2012**. doi: 10.1007/s10439-011-0452-9.

[193] Eisenhauer E. A, Therasse P, Bogaerts J, Schwartz L. H, Sargent D, Ford R, Dancey J, Arbuck S, Gwyther S, Mooney M, Rubinstein L, Shankar L, Dodd L, Kaplan R, Lacombe D, and Verweij J. New response evaluation criteria in solid tumours: Revised RECIST guideline (version 1.1). *European Journal of Cancer*, 45(2):228–247, **2009**. doi: 10.1016/j.ejca.2008.10.026.

[194] Akbani R, Becker K.-F, Carragher N, Goldstein T, Koning de L, Korf U, Liotta L, Mills G. B, Nishizuka S. S, Pawlak M, Petricoin E. F, Pollard H. B, Serrels B, and Zhu J. Realizing the Promise of Reverse Phase Protein Arrays for Clinical, Translational, and Basic Research: A Workshop Report. *Molecular & Cellular Proteomics*, 13(7):1625–1643, **2014**. doi: 10.1074/mcp.O113.034918.

[195] Bragado P, Estrada Y, Parikh F, Krause S, Capobianco C, Farina H. G, Schewe D. M, and Aguirre-Ghiso J. A. TGF-$\beta$2 dictates disseminated tumour cell fate in target organs through TGF-$\beta$-RIII and p38$\alpha/\beta$ signalling. *Nature Cell Biology*, 15(11):1351–1361, **2013**. doi: 10.1038/ncb2861.

[196] Daly A. C, Randall R. A, and Hill C. S. Transforming growth factor beta-induced Smad1/5 phosphorylation in epithelial cells is mediated by novel receptor complexes and is essential for anchorage-independent growth. *Molecular and cellular biology*, 28(22):6889–902, **2008**. doi: 10.1128/MCB.01192-08.

[197] Fei T, Xia K, Li Z, Zhou B, Zhu S, Chen H, Zhang J, Chen Z, Xiao H, Han J.-D. J, and Chen Y.-G. Genome-wide mapping of SMAD target genes reveals the role of BMP signaling in embryonic stem cell fate determination. *Genome Research*, 20(1):36–44, **2010**. doi: 10.1101/gr.092114.109.

[198] Huang D. W, Sherman B. T, and Lempicki R. A. Systematic and integrative analysis of large gene lists using DAVID bioinformatics resources. *Nature Protocols*, 4(1):44–57, **2008**. doi: 10.1038/nprot.2008.211.

[199] Chekhun V. F, Lukyanova N. Y, Burlaka A. P, Bezdenezhnykh N. A, Shpyleva S. I, Tryndyak V. P, Beland F. A, and Pogribny I. P. Iron metabolism disturbances in the MCF-7 human breast cancer cells with acquired resistance to doxorubicin and cisplatin. *International Journal of Oncology*, 43 (5):1481–1486, **2013**. doi: 10.3892/ijo.2013.2063.

[200] Biswas C, Shah N, Muthu M, La P, Fernando A. P, Sengupta S, Yang G, and Dennery P. A. Nuclear heme oxygenase-1 (HO-1) modulates subcellular distribution and activation of Nrf2, impacting metabolic and anti-oxidant defenses. *Journal of Biological Chemistry*, 289(39):26882–26894, **2014**. doi: 10.1074/jbc.M114.567685.

[201] Surguladze N, Thompson K. M, Beard J. L, Connor J. R, and Fried M. G. Interactions and Reactions of Ferritin with DNA. *Journal of Biological Chemistry*, 279(15):14694–14702, **2004**. doi: 10.1074/jbc.M313348200.

[202] Muckenthaler M. U, Rivella S, Hentze M. W, and Galy B. A Red Carpet for Iron Metabolism. *Cell*, 168(3):344–361, **2017**. doi: 10.1016/j.cell.2016.12.034.

[203] Kersten K, Visser de K. E, Miltenburg van M. H, and Jonkers J. Genetically engineered mouse models in oncology research and cancer medicine. *EMBO Molecular Medicine*, 9(2):137–153, **2017**. doi: 10.15252/emmm.201606857.

[204] Fry E. A, Taneja P, and Inoue K. Clinical applications of mouse models for breast cancer engaging HER2/neu. *Integrative Cancer Science and Therapeutics*, 3(5):593–603, **2016**. doi: 10.15761/ICST.1000210.

[205] Knudson A. G. Mutation and Cancer: Statistical Study of Retinoblastoma. *Proceedings of the National Academy of Sciences*, 68(4):820–823, **1971**. doi: 10.1073/pnas.68.4.820.

[206] Wang Z. C, Birkbak N. J, Culhane A. C, Drapkin R, Fatima A, Tian R, Schwede M, Alsop K, Daniels K. E, Piao H, Liu J, Etemadmoghadam D, Miron A, Salvesen H. B, Mitchell G, DeFazio A, Quackenbush J, Berkowitz R. S, Iglehart J. D, Bowtell D. D. L, Australian Ovarian Cancer Study Group f. t. A. O. C. S, and Matulonis U. A. Profiles of genomic instability in high-grade serous ovarian cancer predict treatment outcome. *Clinical Cancer Research*, 18(20):5806–15, **2012**. doi: 10.1158/1078-0432.CCR-12-0857.

[207] Bedard P. L, Hansen A. R, Ratain M. J, and Siu L. L. Tumour heterogeneity in the clinic. *Nature*, 501(7467):355–364, **2013**. doi: 10.1038/nature12627.

[208] Brenton J. D, Aparicio S. A, and Caldas C. Molecular profiling of breast cancer: portraits but not physiognomy. *Breast Cancer Research*, 3(2):77, **2001**. doi: 10.1186/bcr274.

[209] Nguyen L. V, Pellacani D, Lefort S, Kannan N, Osako T, Makarem M, Cox C. L, Kennedy W, Beer P, Carles A, Moksa M, Bilenky M, Balani S, Babovic S, Sun I, Rosin M, Aparicio S, Hirst M, and Eaves C. J. Barcoding reveals complex clonal dynamics of de novo transformed human mammary cells. *Nature*, 528(7581):267–271, **2015**. doi: 10.1038/nature15742.

[210] Yamamoto K. N, Hirota K, Takeda S, and Haeno H. Evolution of Pre-Existing versus Acquired Resistance to Platinum Drugs and PARP Inhibitors in BRCA-Associated Cancers. *PLoS ONE*, 9 (8):e105724, **2014**. doi: 10.1371/journal.pone.0105724.

[211] Yuan Y, Failmezger H, Rueda O. M, Ali H. R, Graf S, Chin S, Schwarz R. F, Curtis C, Dunning M. J, Bardwell H, Johnson N, Doyle S, Turashvili G, Provenzano E, Aparicio S, Caldas C, and Markowetz F. Quantitative Image Analysis of Cellular Heterogeneity in Breast Tumors Complements Genomic Profiling. *Science Translational Medicine*, 4(157):157ra143–157ra143, **2012**. doi: 10.1126/scitranslmed.3004330.

[212] Burrell R. A and Swanton C. Tumour heterogeneity and the evolution of polyclonal drug resistance. *Molecular Oncology*, 8(6):1095–1111, **2014**. doi: 10.1016/j.molonc.2014.06.005.

[213] Housman G, Byler S, Heerboth S, Lapinska K, Longacre M, Snyder N, and Sarkar S. Drug resistance in cancer: An overview. *Cancers*, 6(3):1769–1792, **2014**. doi: 10.3390/cancers6031769.

[214] Bussolati G, Maletta F, Asioli S, Annaratone L, Sapino A, and Marchiò C. "To Be or Not to Be in a Good Shape": Diagnostic and Clinical Value of Nuclear Shape Irregularities in Thyroid and Breast Cancer. In *Adv Exp Med Biol*, volume 773, pages 101–121. **2014**. ISBN 0065-2598 (Print) 0065-2598 (Linking). doi: 10.1007/978-1-4899-8032-8_5.

[215] Kroemer G, Galluzzi L, Vandenabeele P, Abrams J, Alnemri E. S, Baehrecke E. H, Blagosklonny M. V, El-Deiry W. S, Golstein P, Green D. R, Hengartner M, Knight R. A, Kumar S, Lipton S. a, Malorni W, Nuñez G, Peter M. E, Tschopp J, Yuan J, Piacentini M, Zhivotovsky B, and Melino G. Classification of cell death: recommendations of the Nomenclature Committee on Cell Death 2009. *Cell Death and Differentiation*, 16(1):3–11, **2009**. doi: 10.1038/cdd.2008.150.

[216] Bortner C. D and Cidlowski J. A. Apoptotic volume decrease and the incredible shrinking cell. *Cell Death & Differentiation*, 9(12):1307–1310, **2002**. doi: 10.1038/sj.cdd.4401126.

[217] Elmore S. Apoptosis: A Review of Programmed Cell Death. *Toxicologic Pathology*, 35(4):495–516, **2007**. doi: 10.1080/01926230701320337.

[218] Lloyd A. C. The Regulation of Cell Size. *Cell*, 154(6):1194–1205, **2013**. doi: 10.1016/j.cell.2013.08.053.

[219] Galluzzi L, Vitale I, Aaronson S. A, Abrams J. M, Adam D, Agostinis P, Alnemri E. S, Altucci L, Amelio I, Andrews D. W, Annicchiarico-Petruzzelli M, Antonov A. V, Arama E, Baehrecke E. H, Barlev N. A, Bazan N. G, Bernassola F, Bertrand M. J. M, Bianchi K, Blagosklonny M. V, Blomgren K, Borner C, Boya P, Brenner C, Campanella M, Candi E, Carmona-Gutierrez D, Cecconi F, Chan F. K, Chandel N. S, Cheng E. H, Chipuk J. E, Cidlowski J. A, Ciechanover A, Cohen G. M, Conrad M, Cubillos-Ruiz J. R, Czabotar P. E, D'Angiolella V, Dawson T. M, Dawson V. L, De Laurenzi V, De Maria R, Debatin K.-M, DeBerardinis R. J, Deshmukh M, Di Daniele N, Di Virgilio F, Dixit V. M, Dixon S. J, Duckett C. S, Dynlacht B. D, El-Deiry W. S, Elrod J. W, Fimia G. M, Fulda S, García-Sáez A. J, Garg A. D, Garrido C, Gavathiotis E, Golstein P, Gottlieb E, Green D. R, Greene L. A, Gronemeyer H, Gross A, Hajnoczky G, Hardwick J. M, Harris I. S, Hengartner M. O, Hetz C, Ichijo H, Jäättelä M, Joseph B, Jost P. J, Juin P. P, Kaiser W. J, Karin M, Kaufmann T, Kepp O, Kimchi A, Kitsis R. N, Klionsky D. J, Knight R. A, Kumar S, Lee S. W, Lemasters J. J, Levine B, Linkermann A, Lipton S. A, Lockshin R. A, López-Otín C, Lowe S. W, Luedde T, Lugli E, MacFarlane M, Madeo F, Malewicz M, Malorni W, Manic G, Marine J.-C, Martin S. J, Martinou J.-C, Medema J. P, Mehlen P, Meier P, Melino S, Miao E. A, Molkentin J. D, Moll U. M, Muñoz-Pinedo C, Nagata S, Nuñez G, Oberst A, Oren M, Overholtzer M, Pagano M, Panaretakis T, Pasparakis M, Penninger J. M, Pereira D. M, Pervaiz S, Peter M. E, Piacentini M, Pinton P, Prehn J. H, Puthalakath H, Rabinovich G. A, Rehm M, Rizzuto R, Rodrigues C. M, Rubinsztein D. C, Rudel T, Ryan K. M, Sayan E, Scorrano L, Shao F, Shi Y, Silke J, Simon H.-U, Sistigu A, Stockwell B. R, Strasser A, Szabadkai G, Tait S. W, Tang D, Tavernarakis N, Thorburn A, Tsujimoto Y, Turk B, Vanden Berghe T, Vandenabeele P, Vander Heiden M. G, Villunger A, Virgin H. W, Vousden K. H, Vucic D, Wagner E. F, Walczak H, Wallach D, Wang Y, Wells J. A, Wood W, Yuan J, Zakeri Z, Zhivotovsky B, Zitvogel L, Melino G, and Kroemer G. Molecular mechanisms of cell death: recommendations of the Nomenclature Committee on Cell Death 2018. *Cell Death & Differentiation*, 25(3):486–541, **2018**. doi: 10.1038/s41418-017-0012-4.

[220] Segovia-Mendoza M, González-González M. E, Barrera D, Díaz L, and García-Becerra R. Efficacy and mechanism of action of the tyrosine kinase inhibitors gefitinib, lapatinib and neratinib in the treatment of HER2-positive breast cancer: preclinical and clinical evidence. *American journal of cancer research*, 5(9):2531–61, **2015**. doi: 10.1016/j.molcel.2015.05.037.

[221] Faber A. C, Li D, Song Y, Liang M.-C, Yeap B. Y, Bronson R. T, Lifshits E, Chen Z, Maira S.-M, Garcia-Echeverria C, Wong K.-K, and Engelman J. A. Differential induction of apoptosis in HER2 and EGFR addicted cancers following PI3K inhibition. *Proceedings of the National Academy of Sciences*, 106(46):19503–19508, **2009**. doi: 10.1073/pnas.0905056106.

[222] Yu H, Guo P, Xie X, Wang Y, and Chen G. Ferroptosis, a new form of cell death, and its relationships with tumourous diseases. *Journal of Cellular and Molecular Medicine*, 21(4):648–657, **2017**. doi: 10.1111/jcmm.13008.

[223] Dixon S. J, Lemberg K. M, Lamprecht M. R, Skouta R, Zaitsev E. M, Gleason C. E, Patel D. N, Bauer A. J, Cantley A. M, Yang W. S, Morrison B, and Stockwell B. R. Ferroptosis: An

Iron-Dependent Form of Nonapoptotic Cell Death. *Cell*, 149(5):1060–1072, **2012**. doi: 10.1016/j.cell.2012.03.042.

[224] Zhang W and Liu H. T. MAPK signal pathways in the regulation of cell proliferation in mammalian cells. *Cell Research*, 12(1):9–18, **2002**. doi: 10.1038/sj.cr.7290105.

[225] Kirouac D. C, Du J, Lahdenranta J, Onsum M. D, Nielsen U. B, Schoeberl B, and McDonagh C. F. HER2+ Cancer Cell Dependence on PI3K vs. MAPK Signaling Axes Is Determined by Expression of EGFR, ERBB3 and CDKN1B. *PLOS Computational Biology*, 12(4):e1004827, **2016**. doi: 10.1371/journal.pcbi.1004827.

[226] Thomas D. W, Hinchliffe R. F, Briggs C, Macdougall I. C, Littlewood T, and Cavill I. Guideline for the laboratory diagnosis of functional iron deficiency. *British Journal of Haematology*, 161(5):639–648, **2013**. doi: 10.1111/bjh.12311.

[227] Czerwonka M and Tokarz A. Iron in red meat–friend or foe. *Meat Science*, 123:157–165, **2017**. doi: 10.1016/j.meatsci.2016.09.012.

[228] Phipps A. I, Ichikawa L, Bowles E. J, Carney P. A, Kerlikowske K, Miglioretti D. L, and Buist D. S. Defining menopausal status in epidemiologic studies: A comparison of multiple approaches and their effects on breast cancer rates. *Maturitas*, 67(1):60–66, **2010**. doi: 10.1016/j.maturitas.2010.04.015.

[229] Lin H, Yu C. H, Jen C. Y, Cheng C. F, Chou Y, Chang C. C, and Juan S. H. Adiponectin-mediated heme oxygenase-1 induction protects against iron-induced liver injury via a PPAR$\alpha$-dependent mechanism. *American Journal of Pathology*, 177(4):1697–1709, **2010**. doi: 10.2353/ajpath.2010.090789.

[230] Poss K. D and Tonegawa S. Heme oxygenase 1 is required for mammalian iron reutilization. *Proceedings of the National Academy of Sciences*, 94(20):10919–10924, **1997**. doi: 10.1073/pnas.94.20.10919.

[231] Cairo G, Conte D, Bianchi L, Fraquelli M, and Recalcati S. Reduced serum ceruloplasmin levels in hereditary haemochromatosis. *British Journal of Haematology*, 114(1):226–229, **2001**. doi: 10.1046/j.1365-2141.2001.02917.x.

[232] Wu J, Bao L, Zhang Z, and Yi X. Nrf2 induces cisplatin resistance via suppressing the iron export related gene SLC40A1 in ovarian cancer cells. *Oncotarget*, **2017**. doi: 10.18632/oncotarget.19548.

[233] Martin D, Rojo A. I, Salinas M, Diaz R, Gallardo G, Alam J, Ruiz De Galarreta C. M, and Cuadrado A. Regulation of Heme Oxygenase-1 Expression through the Phosphatidylinositol 3-Kinase/Akt Pathway and the Nrf2 Transcription Factor in Response to the Antioxidant Phytochemical Carnosol. *Journal of Biological Chemistry*, 279(10):8919–8929, **2004**. doi: 10.1074/jbc.M309660200.

[234] Doll S and Conrad M. Iron and ferroptosis: A still ill-defined liaison. *IUBMB Life*, 69(6):423–434, **2017**. doi: 10.1002/iub.1616.

[235] Adedoyin O, Boddu R, Traylor A, Lever J. M, Bolisetty S, George J. F, and Agarwal A. Heme oxygenase-1 mitigates ferroptosis in renal proximal tubule cells. *American Journal of Physiology-Renal Physiology*, 314(5):F702–F714, **2018**. doi: 10.1152/ajprenal.00044.2017.

[236] Duijn van S, Nabuurs R. J. A, Duinen van S. G, and Natté R. Comparison of Histological Techniques to Visualize Iron in Paraffin-embedded Brain Tissue of Patients with Alzheimer's Disease. *Journal of Histochemistry and Cytochemistry*, 61(11):785–792, **2013**. doi: 10.1369/0022155413501325.

[237] Lin Q, Weis S, Yang G, Weng Y. H, Helston R, Rish K, Smith A, Bordner J, Polte T, Gaunitz F, and Dennery P. A. Heme oxygenase-1 protein localizes to the nucleus and activates transcription factors important in oxidative stress. *Journal of Biological Chemistry*, 282(28):20621–20633, **2007**. doi: 10.1074/jbc.M607954200.

[238] Cohen G and Sinet P. M. The fenton reaction between ferrous-diethylenetriaminepentaacetic acid and hydrogen peroxide. *FEBS Letters*, 138(2):258–260, **1982**. doi: 10.1016/0014-5793(82)80455-9.

[239] Naoum F. A. Iron deficiency in cancer patients. *Revista Brasileira de Hematologia e Hemoterapia*, 38(4):325–330, **2016**. doi: 10.1016/j.bjhh.2016.05.009.

[240] Gurzau E. S, Neagu C, and Gurzau A. E. Essential metals—case study on iron. *Ecotoxicology and Environmental Safety*, 56(1):190–200, **2003**. doi: 10.1016/S0147-6513(03)00062-9.

[241] Kamei A, Watanabe Y, Kondo K, Okada S, Shinozaki F, Ishijima T, Nakai Y, Kondo T, Arai S, and Abe K. Influence of a Short-Term Iron-Deficient Diet on Hepatic Gene Expression Profiles in Rats. *PLoS ONE*, 8(6):e65732, **2013**. doi: 10.1371/journal.pone.0065732.

[242] Pino J. M. V, Luz da M. H. M, Antunes H. K. M, Giampá S. Q. d. C, Martins V. R, and Lee K. S. Iron-Restricted Diet Affects Brain Ferritin Levels, Dopamine Metabolism and Cellular Prion Protein in a Region-Specific Manner. *Frontiers in Molecular Neuroscience*, 10(May):1–13, **2017**. doi: 10.3389/fnmol.2017.00145.

[243] Jian J, Yang Q, Dai J, Eckard J, Axelrod D, Smith J, and Huang X. Effects of iron deficiency and iron overload on angiogenesis and oxidative stress—a potential dual role for iron in breast cancer. *Free Radical Biology and Medicine*, 50(7):841–847, **2011**. doi: 10.1016/j.freeradbiomed.2010.12.028.

[244] Huang X. Iron overload and its association with cancer risk in humans: evidence for iron as a carcinogenic metal. *Mutation Research/Fundamental and Molecular Mechanisms of Mutagenesis*, 533(1-2):153–171, **2003**. doi: 10.1016/j.mrfmmm.2003.08.023.

[245] Radulescu S, Brookes M. J, Salgueiro P, Ridgway R. A, McGhee E, Anderson K, Ford S. J, Stones D. H, Iqbal T. H, Tselepis C, and Sansom O. J. Luminal Iron Levels Govern Intestinal Tumorigenesis after Apc Loss In Vivo. *Cell Reports*, 2(2):270–282, **2012**. doi: 10.1016/j.celrep.2012.07.003.

[246] Boyd P. W, Watson A. J, Law C. S, Abraham E. R, Trull R, Murdoch R, Bakker D. C. E, Bowle A. R, Buesseler K. O, Chang H, Charette M, Croot P, Downing K, Frew R, Gall M, Hadfield M, Hall J, Harvey M, Jameson G, LaRoche J, Liddlcoat M, Ling R, Maldonade M. T, McKay R. M, Noddler S, Pickmere S, Pridmore R, Rintoul S, Safi K, Sutton P, Strzepek R, Tanneberger K, Turner S, Walte A, and Zeldis J. Phytoplankton bloom upon mesoscale iron fertilization of polar Southern Ocean waters. *Nature*, 407(October):695–702, **2000**.

[247] Hann H.-W. W, Stahlhut M. W, and Menduke H. Iron enhances tumor growth. Observation on spontaneous mammary tumors in mice. *Cancer*, 68(11):2407–10, **1988**.

[248] Ohara T, Noma K, Urano S, Watanabe S, Nishitani S, Tomono Y, Kimura F, Kagawa S, Shirakawa Y, and Fujiwara T. A novel synergistic effect of iron depletion on antiangiogenic cancer therapy. *International Journal of Cancer*, 132(11):2705–2713, **2013**. doi: 10.1002/ijc.27943.

[249] Bao L. J, Jaramillo M. C, Zhang Z. B, Zheng Y. X, Yao M, Zhang D. D, and Yi X. F. Nrf2 induces cisplatin resistance through activation of autophagy in ovarian carcinoma. *International Journal of Clinical and Experimental Pathology*, 7(4):1502–1513, **2014**.

[250] Cao L, Wang J, Ma D, Wang P, Zhang Y, and Fang Q. Heme oxygenase-1 contributes to imatinib resistance by promoting autophagy in chronic myeloid leukemia through disrupting the mTOR signaling pathway. *Biomedicine and Pharmacotherapy*, 78:30–38, **2016**. doi: 10.1016/j.biopha.2015.12.029.

[251] Tan Q, Wang H, Hu Y, Hu M, Li X, Aodengqimuge, Ma Y, Wei C, and Song L. Src/STAT3-dependent heme oxygenase-1 induction mediates chemoresistance of breast cancer cells to doxorubicin by promoting autophagy. *Cancer Science*, 106(8):1023–1032, **2015**. doi: 10.1111/cas.12712.

[252] Kang H. J, Yi Y. W, Hong Y. B, Kim H. J, Jang Y.-J, Seong Y.-S, and Bae I. HER2 confers drug resistance of human breast cancer cells through activation of NRF2 by direct interaction. *Scientific Reports*, 4(1):7201, **2015**. doi: 10.1038/srep07201.

[253] Furfaro A. L, Piras S, Passalacqua M, Domenicotti C, Parodi A, Fenoglio D, Pronzato M. A, Marinari U. M, Moretta L, Traverso N, and Nitti M. HO-1 up-regulation: A key point in high-risk neuroblastoma resistance to bortezomib. *Biochimica et Biophysica Acta - Molecular Basis of Disease*, 1842(4):613–622, **2014**. doi: 10.1016/j.bbadis.2013.12.008.

[254] Lv X, Song D.-m, Niu Y.-h, and Wang B.-s. Inhibition of heme oxygenase-1 enhances the chemosensitivity of laryngeal squamous cell cancer Hep-2 cells to cisplatin. *Apoptosis*, 21(4): 489–501, **2016**. doi: 10.1007/s10495-016-1216-7.

[255] Yin H, Fang J, Liao L, Maeda H, and Su Q. Upregulation of heme oxygenase-1 in colorectal cancer patients with increased circulation carbon monoxide levels, potentially affects chemotherapeutic sensitivity. *BMC Cancer*, 14(1):436, **2014**. doi: 10.1186/1471-2407-14-436.

[256] Chen N, Wu L, Yuan H, and Wang J. ROS/Autophagy/Nrf2 Pathway Mediated Low-Dose Radiation Induced Radio-Resistance in Human Lung Adenocarcinoma A549 Cell. *International Journal of Biological Sciences*, 11(7):833–844, **2015**. doi: 10.7150/ijbs.10564.

[257] Tenhunen R, Marver H. S, and Schmid R. The enzymatic conversion of heme to bilirubin by microsomal heme oxygenase. *Proceedings of the National Academy of Sciences*, 61(2):748–755, **1968**. doi: 10.1073/pnas.61.2.748.

[258] Bothwell T. H. Overview and Mechanisms of Iron Regulation. *Nutrition Reviews*, 53(9):237–245, **2009**. doi: 10.1111/j.1753-4887.1995.tb05480.x.

[259] Kamei A, Watanabe Y, Ishijima T, Uehara M, Arai S, Kato H, Nakai Y, and Abe K. Dietary iron-deficient anemia induces a variety of metabolic changes and even apoptosis in rat liver: a DNA microarray study. *Physiological Genomics*, 42(2):149–156, **2010**. doi: 10.1152/physiolgenomics.00150.2009.

[260] Asano T, Komatsu M, Yamaguchi-Iwai Y, Ishikawa F, Mizushima N, and Iwai K. Distinct Mechanisms of Ferritin Delivery to Lysosomes in Iron-Depleted and Iron-Replete Cells. *Molecular and Cellular Biology*, 31(10):2040–2052, **2011**. doi: 10.1128/MCB.01437-10.

[261] Rusten T. E and Stenmark H. p62, an autophagy hero or culprit? *Nature Cell Biology*, 12(3): 207–209, **2010**. doi: 10.1038/ncb0310-207.

[262] Tanida I, Ueno T, and Kominami E. LC3 and Autophagy. pages 77–88. **2008**. ISBN 9781588298539. doi: 10.1007/978-1-59745-157-4_4.

[263] Puissant A, Fenouille N, and Auberger P. When autophagy meets cancer through p62/SQSTM1. *American journal of cancer research*, 2(4):397–413, **2012**.

[264] Mancias J. D, Wang X, Gygi S. P, Harper J. W, and Kimmelman A. C. Quantitative proteomics identifies NCOA4 as the cargo receptor mediating ferritinophagy. *Nature*, 509(7498):105–109, **2014**. doi: 10.1038/nature13148.

[265] Kaur J and Debnath J. Autophagy at the crossroads of catabolism and anabolism. *Nature Reviews Molecular Cell Biology*, 16(8):461–472, **2015**. doi: 10.1038/nrm4024.

[266] Hoeben A, Landuyt B, Highley M. S, Wildiers H, Van Oosterom A. T, and De Bruijn E. A. Vascular endothelial growth factor and angiogenesis. *Pharmacological reviews*, 56(4):549–580, **2004**. doi: 10.1124/pr.56.4.3.549.

[267] Khalil H. S, Langdon S. P, Goltsov A, Soininen T, Harrison D. J, Bown J, and Deeni Y. Y. A novel mechanism of action of HER2 targeted immunotherapy is explained by inhibition of NRF2 function in ovarian cancer cells. *Oncotarget*, 7(46):75874–75901, **2016**. doi: 10.18632/oncotarget.12425.

[268] Cruickshanks N, Tang Y, Booth L, Hamed H, Grant S, and Dent P. Lapatinib and Obatoclax Kill Breast Cancer Cells through Reactive Oxygen Species-Dependent Endoplasmic Reticulum Stress. *Molecular Pharmacology*, 82(6):1217–1229, **2012**. doi: 10.1124/mol.112.081539.

[269] Furfaro A. L, Traverso N, Domenicotti C, Piras S, Moretta L, Marinari U. M, Pronzato M. A, and Nitti M. The Nrf2/HO-1 Axis in Cancer Cell Growth and Chemoresistance. *Oxidative Medicine and Cellular Longevity*, 2016(Table 1), **2016**. doi: 10.1155/2016/1958174.

[270] Stanton R. C. Glucose-6-phosphate dehydrogenase, NADPH, and cell survival. *IUBMB Life*, 64 (5):362–369, **2012**. doi: 10.1002/iub.1017.

[271] Zitka O, Skalickova S, Gumulec J, Masarik M, Adam V, Hubalek J, Trnkova L, Kruseova J, Eckschlager T, and Kizek R. Redox status expressed as GSH:GSSG ratio as a marker for oxidative stress in paediatric tumour patients. *Oncology Letters*, 4(6):1247–1253, **2012**. doi: 10.3892/ol.2012.931.

[272] Yang W. S, SriRamaratnam R, Welsch M. E, Shimada K, Skouta R, Viswanathan V. S, Cheah J. H, Clemons P. A, Shamji A. F, Clish C. B, Brown L. M, Girotti A. W, Cornish V. W, Schreiber S. L, and Stockwell B. R. Regulation of Ferroptotic Cancer Cell Death by GPX4. *Cell*, 156(1-2): 317–331, **2014**. doi: 10.1016/j.cell.2013.12.010.

[273] Doll S, Proneth B, Tyurina Y. Y, Panzilius E, Kobayashi S, Ingold I, Irmler M, Beckers J, Aichler M, Walch A, Prokisch H, Trümbach D, Mao G, Qu F, Bayir H, Füllekrug J, Scheel C. H, Wurst W, Schick J. A, Kagan V. E, Angeli J. P. F, and Conrad M. ACSL4 dictates ferroptosis sensitivity by shaping cellular lipid composition. *Nature Chemical Biology*, 13(1):91–98, **2017**. doi: 10.1038/nchembio.2239.

[274] Kagan V. E, Mao G, Qu F, Angeli J. P. F, Doll S, Croix C. S, Dar H. H, Liu B, Tyurin V. A, Ritov V. B, Kapralov A. A, Amoscato A. A, Jiang J, Anthonymuthu T, Mohammadyani D, Yang Q, Proneth B, Klein-Seetharaman J, Watkins S, Bahar I, Greenberger J, Mallampalli R. K, Stockwell B. R, Tyurina Y. Y, Conrad M, and Bayır H. Oxidized arachidonic and adrenic PEs navigate cells to ferroptosis. *Nature Chemical Biology*, 13(1):81–90, **2017**. doi: 10.1038/nchembio.2238.

[275] Latunde-Dada G. O. Ferroptosis: Role of lipid peroxidation, iron and ferritinophagy. *Biochimica et Biophysica Acta - General Subjects*, 1861(8):1893–1900, **2017**. doi: 10.1016/j.bbagen.2017.05.019.

[276] Angeli J. P. F, Shah R, Pratt D. A, and Conrad M. Ferroptosis Inhibition: Mechanisms and Opportunities. *Trends in Pharmacological Sciences*, 38(5):489–498, **2017**. doi: 10.1016/j.tips.2017.02.005.

[277] Zilka O, Shah R, Li B, Friedmann Angeli J. P, Griesser M, Conrad M, and Pratt D. A. On the Mechanism of Cytoprotection by Ferrostatin-1 and Liproxstatin-1 and the Role of Lipid Peroxidation in Ferroptotic Cell Death. *ACS Central Science*, 3(3):232–243, **2017**. doi: 10.1021/acscentsci.7b00028.

[278] Xie Y, Hou W, Song X, Yu Y, Huang J, Sun X, Kang R, and Tang D. Ferroptosis: process and function. *Cell Death and Differentiation*, 23(3):369–379, **2016**. doi: 10.1038/cdd.2015.158.

[279] Sato M, Kusumi R, Hamashima S, Kobayashi S, Sasaki S, Komiyama Y, Izumikawa T, Conrad M, Bannai S, and Sato H. The ferroptosis inducer erastin irreversibly inhibits system xc and synergizes with cisplatin to increase cisplatin's cytotoxicity in cancer cells. *Scientific Reports*, 8(1):968, **2018**. doi: 10.1038/s41598-018-19213-4.

[280] Drummen G. P, Liebergen van L. C, Op den Kamp J. A, and Post J. A. C11-BODIPY581/591, an oxidation-sensitive fluorescent lipid peroxidation probe: (micro)spectroscopic characterization and validation of methodology. *Free Radical Biology and Medicine*, 33(4):473–490, **2002**. doi: 10.1016/S0891-5849(02)00848-1.

[281] Garcia-Calvo M, Peterson E. P, Leiting B, Ruel R, Nicholson D. W, and Thornberry N. A. Inhibition of Human Caspases by Peptide-based and Macromolecular Inhibitors. *Journal of Biological Chemistry*, 273(49):32608–32613, **1998**. doi: 10.1074/jbc.273.49.32608.

[282] Chen Z.-l, Shen Y, Li S, Lv M, Yang J, Zhang L.-X, Li C.-L, Lin Y.-y, Yang J, and Wang X. The efficiency and safety of trastuzumab and lapatinib added to neoadjuvant chemotherapy in Her2-positive breast cancer patients: a randomized meta-analysis. *OncoTargets and Therapy*, page 3233, **2016**. doi: 10.2147/OTT.S106055.

[283] Seglen P. O and Gordon P. B. 3-Methyladenine: Specific inhibitor of autophagic/lysosomal protein degradation in isolated rat hepatocytes. *Proceedings of the National Academy of Sciences*, 79(6): 1889–1892, **1982**. doi: 10.1073/pnas.79.6.1889.

[284] Yoshimori T, Yamamoto A, Moriyama Y, Futai M, and Tashiro Y. Bafilomycin A1, a specific inhibitor of vacuolar-type H(+)-ATPase, inhibits acidification and protein degradation in lysosomes of cultured cells. *The Journal of biological chemistry*, 266(26):17707–12, **1991**.

[285] Leung L, Radulovich N, Zhu C.-Q, Organ S, Bandarchi B, Pintilie M, To C, Panchal D, and Tsao M. S. Lipocalin2 Promotes Invasion, Tumorigenicity and Gemcitabine Resistance in Pancreatic Ductal Adenocarcinoma. *PLoS ONE*, 7(10):e46677, **2012**. doi: 10.1371/journal.pone.0046677.

[286] Denat L, Kadekaro A. L, Marrot L, Leachman S. A, and Abdel-Malek Z. A. Melanocytes as Instigators and Victims of Oxidative Stress. *Journal of Investigative Dermatology*, 134(6):1512–1518, **2014**. doi: 10.1038/jid.2014.65.

[287] Leary A, Evans A, Johnston S. R. D, A'Hern R, Bliss J. M, Sahoo R, Detre S, Haynes B. P, Hills M, Harper-Wynne C, Bundred N, Coombes G, Smith I, and Dowsett M. Antiproliferative Effect of Lapatinib in HER2-Positive and HER2-Negative/HER3-High Breast Cancer: Results of the Presurgical Randomized MAPLE Trial (CRUK E/06/039). *Clinical Cancer Research*, 21(13):2932–2940, **2015**. doi: 10.1158/1078-0432.CCR-14-1428.

[288] Lachaier E, Louandre C, Godin C, Saidak Z, Baert M, Diouf M, Chauffert B, and Galmiche A. Sorafenib induces ferroptosis in human cancer cell lines originating from different solid tumors. *Anticancer research*, 34(11):6417–22, **2014**.

[289] Dixon S. J, Patel D, Welsch M, Skouta R, Lee E, Hayano M, Thomas A. G, Gleason C, Tatonetti N, Slusher B. S, and Stockwell B. R. Pharmacological inhibition of cystine-glutamate exchange induces endoplasmic reticulum stress and ferroptosis. *eLife*, 2014(3):1–25, **2014**. doi: 10.7554/eLife.02523.

[290] Ma S, Henson E. S, Chen Y, and Gibson S. B. Ferroptosis is induced following siramesine and lapatinib treatment of breast cancer cells. *Cell Death & Disease*, 7(7):e2307–e2307, **2016**. doi: 10.1038/cddis.2016.208.

[291] Roh J. L, Kim E. H, Jang H. J, Park J. Y, and Shin D. Induction of ferroptotic cell death for overcoming cisplatin resistance of head and neck cancer. *Cancer Letters*, 381(1):96–103, **2016**. doi: 10.1016/j.canlet.2016.07.035.

[292] Zhu S, Zhang Q, Sun X, Zeh H. J, Lotze M. T, Kang R, and Tang D. HSPA5 regulates ferroptotic cell death in cancer cells. *Cancer Research*, 77(8):2064–2077, **2017**. doi: 10.1158/0008-5472.CAN-16-1979.

[293] Li Q, Han X, Lan X, Gao Y, Wan J, Durham F, Cheng T, Yang J, Wang Z, Jiang C, Ying M, Koehler R. C, Stockwell B. R, and Wang J. Inhibition of neuronal ferroptosis protects hemorrhagic brain. *JCI Insight*, 2(7), **2017**. doi: 10.1172/jci.insight.90777.

[294] Linkermann A, Skouta R, Himmerkus N, Mulay S. R, Dewitz C, De Zen F, Prokai A, Zuchtriegel G, Krombach F, Welz P.-S, Weinlich R, Vanden Berghe T, Vandenabeele P, Pasparakis M, Bleich M, Weinberg J. M, Reichel C. A, Bräsen J. H, Kunzendorf U, Anders H.-J, Stockwell B. R, Green D. R, and Krautwald S. Synchronized renal tubular cell death involves ferroptosis. *Proceedings of the National Academy of Sciences*, 111(47):16836–16841, **2014**. doi: 10.1073/pnas.1415518111.

[295] Kim S. E, Zhang L, Ma K, Riegman M, Chen F, Ingold I, Conrad M, Turker M. Z, Gao M, Jiang X, Monette S, Pauliah M, Gonen M, Zanzonico P, Quinn T, Wiesner U, Bradbury M. S, and Overholtzer M. Ultrasmall nanoparticles induce ferroptosis in nutrient-deprived cancer cells and suppress tumour growth. *Nature Nanotechnology*, 11(11):977–985, **2016**. doi: 10.1038/nnano.2016.164.

[296] Gao M, Monian P, Quadri N, Ramasamy R, and Jiang X. Glutaminolysis and Transferrin Regulate Ferroptosis. *Molecular Cell*, 59(2):298–308, **2015**. doi: 10.1016/j.molcel.2015.06.011.

[297] Stockwell B. R, Friedmann Angeli J. P, Bayir H, Bush A. I, Conrad M, Dixon S. J, Fulda S, Gascón S, Hatzios S. K, Kagan V. E, Noel K, Jiang X, Linkermann A, Murphy M. E, Overholtzer M, Oyagi A, Pagnussat G. C, Park J, Ran Q, Rosenfeld C. S, Salnikow K, Tang D, Torti F. M, Torti S. V, Toyokuni S, Woerpel K, and Zhang D. D. Ferroptosis: A Regulated Cell Death Nexus Linking Metabolism, Redox Biology, and Disease. *Cell*, 171(2):273–285, **2017**. doi: 10.1016/j.cell.2017.09.021.

[298] Hambright W. S, Fonseca R. S, Chen L, Na R, and Ran Q. Ablation of ferroptosis regulator glutathione peroxidase 4 in forebrain neurons promotes cognitive impairment and neurodegeneration. *Redox Biology*, 12(January):8–17, **2017**. doi: 10.1016/j.redox.2017.01.021.

[299] Pirpour Tazehkand A, Akbarzadeh M, Velaie K, Sadeghi M. R, and Samadi N. The role of Her2-Nrf2 axis in induction of oxaliplatin resistance in colon cancer cells. *Biomedicine & pharmacotherapy*, 103:755–766, **2018**. doi: 10.1016/j.biopha.2018.04.105.

[300] Kang J, Jeong M. G, Oh S, Jang E. J, Kim H. K, and Hwang E. S. A FoxO1-dependent, but NRF2-independent induction of heme oxygenase-1 during muscle atrophy. *FEBS Letters*, 588(1): 79–85, **2014**. doi: 10.1016/j.febslet.2013.11.009.

[301] Piao M. S, Park J. J, Choi J. Y, Lee D. H, Yun S. J, Lee J. B, and Lee S. C. Nrf2-dependent and Nrf2-independent induction of phase 2 detoxifying and antioxidant enzymes during keratinocyte differentiation. *Archives of Dermatological Research*, 304(5):387–395, **2012**. doi: 10.1007/s00403-012-1215-7.

[302] Ma D, Fang Q, Wang P, Gao R, Wu W, Lu T, Cao L, Hu X, and Wang J. Induction of Heme Oxygenase-1 by Na + -H + Exchanger 1 Protein Plays a Crucial Role in Imatinib-resistant Chronic Myeloid Leukemia Cells. *Journal of Biological Chemistry*, 290(20):12558–12571, **2015**. doi: 10.1074/jbc.M114.626960.

[303] Goodwin J. M, Dowdle W. E, DeJesus R, Wang Z, Bergman P, Kobylarz M, Lindeman A, Xavier R. J, McAllister G, Nyfeler B, Hoffman G, and Murphy L. O. Autophagy-Independent Lysosomal Targeting Regulated by ULK1/2-FIP200 and ATG9. *Cell Reports*, 20(10):2341–2356, **2017**. doi: 10.1016/j.celrep.2017.08.034.

[304] Kimura T, Takabatake Y, Takahashi A, and Isaka Y. Chloroquine in Cancer Therapy: A Double-Edged Sword of Autophagy. *Cancer Research*, 73(1):3–7, **2013**. doi: 10.1158/0008-5472.CAN-12-2464.

[305] Beckman J. D, Chen C, Nguyen J, Thayanithy V, Subramanian S, Steer C. J, and Vercellotti G. M. Regulation of Heme Oxygenase-1 Protein Expression by miR-377 in Combination with miR-217. *Journal of Biological Chemistry*, 286(5):3194–3202, **2011**. doi: 10.1074/jbc.M110.148726.

[306] Amadio M, Scapagnini G, Davinelli S, Calabrese V, Govoni S, and Pascale A. Involvement of ELAV RNA-binding proteins in the post-transcriptional regulation of HO-1. *Frontiers in Cellular Neuroscience*, 8(January):1–5, **2015**. doi: 10.3389/fncel.2014.00459.

[307] Devos D, Moreau C, Devedjian J. C, Kluza J, Petrault M, Laloux C, Jonneaux A, Ryckewaert G, Garçon G, Rouaix N, Duhamel A, Jissendi P, Dujardin K, Auger F, Ravasi L, Hopes L, Grolez G, Firdaus W, Sablonnière B, Strubi-Vuillaume I, Zahr N, Destée A, Corvol J.-C, Pöltl D, Leist M, Rose C, Defebvre L, Marchetti P, Cabantchik Z. I, and Bordet R. Targeting Chelatable Iron as a Therapeutic Modality in Parkinson's Disease. *Antioxidants & Redox Signaling*, 21(2):195–210, **2014**. doi: 10.1089/ars.2013.5593.

[308] Du T.-t, Wang L, Duan C.-l, Lu L.-l, Zhang J.-l, Gao G, Qiu X.-b, Wang X.-m, and Yang H. GBA deficiency promotes SNCA/$\alpha$-synuclein accumulation through autophagic inhibition by inactivated PPP2A. *Autophagy*, 11(10):1803–1820, **2015**. doi: 10.1080/15548627.2015.1086055.

[309] Lachenmayer M. L and Yue Z. Genetic animal models for evaluating the role of autophagy in etiopathogenesis of Parkinson disease. *Autophagy*, 8(12):1837–1838, **2012**. doi: 10.4161/auto.21859.

[310] Alam J and Scheper W. Targeting neuronal MAPK14/p38$\alpha$ activity to modulate autophagy in the Alzheimer disease brain. *Autophagy*, 12(12):2516–2520, **2016**. doi: 10.1080/15548627.2016.1238555.

[311] Ihara Y, Morishima-Kawashima M, and Nixon R. The Ubiquitin-Proteasome System and the Autophagic-Lysosomal System in Alzheimer Disease. *Cold Spring Harbor Perspectives in Medicine*, 2(8):a006361–a006361, **2012**. doi: 10.1101/cshperspect.a006361.

[312] Linkermann A, Stockwell B, and Vanden Berghe T. Heavy metal suicide. *American Journal of Physiology - Renal Physiology*, 313(4):F959–F960, **2017**. doi: 10.1152/ajprenal.00273.2017.

[313] Meinão I, Sato E, Andrade L, Ferraz M, and Atra E. Controlled trial with chloroquine diphosphate in systemic lupus erythematosus. *Lupus*, 5(3):237–241, **1996**. doi: 10.1177/096120339600500313.

[314] Rangwala R, Leone R, Chang Y. C, Fecher L. A, Schuchter L. M, Kramer A, Tan K.-S, Heitjan D. F, Rodgers G, Gallagher M, Piao S, Troxel A. B, Evans T. L, DeMichele A. M, Nathanson K. L, O'Dwyer P. J, Kaiser J, Pontiggia L, Davis L. E, and Amaravadi R. K. Phase I trial of hydroxychloroquine with dose-intense temozolomide in patients with advanced solid tumors and melanoma. *Autophagy*, 10(8):1369–1379, **2014**. doi: 10.4161/auto.29118.

[315] Mahalingam D, Mita M, Sarantopoulos J, Wood L, Amaravadi R. K, Davis L. E, Mita A. C, Curiel T. J, Espitia C. M, Nawrocki S. T, Giles F. J, and Carew J. S. Combined autophagy and HDAC inhibition: A phase I safety, tolerability, pharmacokinetic, and pharmacodynamic analysis of hydroxychloroquine in combination with the HDAC inhibitor vorinostat in patients with advanced solid tumors. *Autophagy*, 10(8):1403–1414, **2014**. doi: 10.4161/auto.29231.

[316] Wolpin B. M, Rubinson D. A, Wang X, Chan J. A, Cleary J. M, Enzinger P. C, Fuchs C. S, McCleary N. J, Meyerhardt J. A, Ng K, Schrag D, Sikora A. L, Spicer B. A, Killion L, Mamon H, and Kimmelman A. C. Phase II and Pharmacodynamic Study of Autophagy Inhibition Using Hydroxychloroquine in Patients With Metastatic Pancreatic Adenocarcinoma. *The Oncologist*, 19 (6):637–638, **2014**. doi: 10.1634/theoncologist.2014-0086.

[317] Tan Q, Joshua A. M, Saggar J. K, Yu M, Wang M, Kanga N, Zhang J. Y, Chen X, Wouters B. G, and Tannock I. F. Effect of pantoprazole to enhance activity of docetaxel against human tumour xenografts by inhibiting autophagy. *British Journal of Cancer*, 112(5):832–840, **2015**. doi: 10.1038/bjc.2015.17.

[318] Brana I, Ocana A, Chen E. X, Razak A. R. A, Haines C, Lee C, Douglas S, Wang L, Siu L. L, Tannock I. F, and Bedard P. L. A phase i trial of pantoprazole in combination with doxorubicin in patients with advanced solid tumors: Evaluation of pharmacokinetics of both drugs and tissue penetration of doxorubicin. *Investigational New Drugs*, 32(6):1269–1277, **2014**. doi: 10.1007/s10637-014-0159-5.

[319] Nowis D, Bugajski M, Winiarska M, Bil J, Szokalska A, Salwa P, Issat T, Was H, Jozkowicz A, Dulak J, Stoklosa T, and Golab J. Zinc protoporphyrin IX, a heme oxygenase-1 inhibitor, demonstrates potent antitumor effects but is unable to potentiate antitumor effects of chemotherapeutics in mice. *BMC Cancer*, 8(1):197, **2008**. doi: 10.1186/1471-2407-8-197.

[320] Thomas R. A. B, Czopek A, Bellamy C. O. C, McNally S. J, Kluth D. C, and Marson L. P. Hemin Preconditioning Upregulates Heme Oxygenase-1 in Deceased Donor Renal Transplant Recipients. *Transplantation*, 100(1):176–183, **2016**. doi: 10.1097/TP.0000000000000770.

[321] Klickovic U, Doberer D, Gouya G, Aschauer S, Weisshaar S, Storka A, Bilban M, and Wolzt M. Human pharmacokinetics of high dose oral curcumin and its effect on heme oxygenase-1 expression in healthy male subjects. *BioMed Research International*, 2014, **2014**. doi: 10.1155/2014/458592.